Thermal Transport and Energy Transfer Mechanisms across Interfaces Composed of Varying Phases of Matter

---

A Dissertation Presented to the
Faculty of the School of Engineering and Applied Science
University of Virginia

In Partial Fulfillment
of the Requirements for the Degree of
Doctor of Philosophy
Materials Science and Engineering

John A. Tomko
December 2020

APPROVAL SHEET

The dissertation is submitted in partial fulfillment of the
requirements for the degree of

Doctor of Philosophy in Materials Science and Engineering

John A. Tomko

This dissertation has been read and approved by the Examining Committee:

Patrick E. Hopkins, Advisor

Mona Zebarjadi, Chair

Liheng Cai

Pamela Norris

Scott G. Walton

Accepted for the School of Engineering and Applied Science:

Craig H. Benson, Dean
School of Engineering and Applied Science

December 2020

Abstract

Through the development of numerous optical metrologies, this work seeks to provide insight to one primary question: How does heat and energy transport occur across interfaces composed of varying phases of matter? The projects within this dissertation consider this question within all four phases of matter: Solid, liquid, gas, and plasma.

The vastly studied case of thermal transport across solid-solid interfaces provides itself to be an ideal test-bed for the development of novel experimental techniques for quantification and understanding of interfacial thermal resistances. Through one of these methods, a tunable mid-infrared pump-probe system, this work demonstrates a unique energy transduction process at metal-semiconductor interfaces, despite over a century of prior investigation; this process is manipulated for the modulation of plasmonic optical properties at ultrafast time-scales. In moving to interfaces composed of non-condensed phases of matter, I subsequently propose the application of these newly-developed techniques to the study of solid-liquid, solid-gas, and solid-plasma interfaces.

In the case of solid-liquid interactions, the vast disparities between nanoscale interactions and macroscale phenomenon are investigated. Additionally, through manipulation of these nanoscale interactions and development of a ‘programmable’ biopolymer, we identify a material system with the largest room temperature thermal switch ratio to-date.

In the solid-gas regime, these investigations extend to a much more fundamental level, seeking to answer the nature of nanoscale heat transfer from a solid to a gas: Is this thermal transport specular or diffusive? This question is elucidated upon by interpretation of ultrafast picosecond ultrasonic experiments with a newly-derived formulation for the acoustic and diffuse mismatch models (AMM and DMM).

Finally, we consider the fourth phase of matter: plasma. While plasmas have long been used for the synthesis and manipulation of materials because of their unique ability to deliver both energy and chemically-active species to the surface of a plasma exposed material

- an attribute that separates them from other approaches to materials processing - this complex nature has greatly inhibited experimental realizations of time-resolved plasma-surface interactions. In this work, I demonstrate that non-contact thermoreflectance methods are particularly well-suited for such investigations and provide a direct measure of the energy transferred from an atmospheric plasma jet to a solid surface. Specifically, these measurements provide a direct measure of the localized, transient thermal response of a a material subjected to an incident plasma flux. In doing so, we demonstrate a regime in which plasma-induced cooling of the surface can be enabled.

Acknowledgements

It is impossible to express the gratitude and appreciation I have for the various mentors, collaborators, family, and friends who have made this dissertation possible. The help and guidance they have provided has certainly played a large role in my success during graduate school.

First and foremost, I would like to thank my advisor, Prof. Patrick Hopkins. Patrick's mentorship and guidance has not only improved my skills as a scientist and researcher, but has also provided a tremendous source of motivation in my own social endeavors and mentoring. At both a professional and personal level, Patrick has been amazing advisor, role model, and friend. Since our first meeting at HPLA in 2016, Patrick has provided a constant source of excitement and scientific curiosity in every project and research direction that I have worked on, which has been one of the greatest experiences as a graduate student - I am still convinced that we will one day turn lead into gold...even if only for a picosecond.

Next, I would like to sincerely thank my committee members, Prof. Mona Zebarjadi, Dean Pamela Norris, Prof. Liheng Cai, and Dr. Scott Walton, for their continued support and guidance. The insight you have all provided has not only helped guide this dissertation, but has helped craft all aspects of my research endeavors. In particular, I would like to especially thank Scott for not only introducing me to the world of atmospheric plasma physics, but also for those especially late nights in the lab, as they were certainly a highlight of my time in graduate school.

I have absolutely loved graduate school, and that is heavily due to everyone in the ExSiTE lab - I consider you all nothing short of family. The guidance and patience exhibited by former members, particularly Dr. Jeff Braun, Prof. Ashutosh Giri, Prof. Brian Donovan, and Prof. Brian Foley, in my first year was invaluable. Not only in my first year, but literally every day since, I have been grateful for both the mentorship and my friendship with Dr. John Gaskins; allowing me to interrupt you on a daily basis for random research conversations during my first year, up to playing video games during the COVID quarantine, has been critical throughout the last few years. I would also like to specifically thank

Hans and Ethan - despite someone's annual summer boat trip, starting graduate school with the two of you was a fantastic experience. From our first days of learning TDTR together to surfing in Maui, I am incredibly appreciative of my friendship with both of you. Finally, I would like to thank Kiumars, Shafkat, and Yee for the last couple of years; although I 'never invite you to lunch,' I greatly appreciate all of your collaborations and friendships.

As the ExSiTE lab is heavily focused on thermal characterization of materials, it is not only a research necessity, but certainly one of the greatest benefits, to collaborate with such a wide range of researchers. While I am forever grateful to the internal collaborations within the ExSiTE lab, I am exceptionally fortunate to have had the opportunity to work with some of the greatest scientists, including my committee themselves. While a complete list would likely exceed the length of my current dissertation, I would like to especially note my collaborations with: Prof. Melik Demirel, Prof. Jon-Paul Maria, Prof. Joshua Caldwell, Prof. Sean O'Malley, Prof. Oleg Prezhdo, Dr. Evan Runnerstrom, Dr. Bryan Kaehr, Dr. Stanley Chou, as well as the innumerable students and post-docs from your respective groups; these collaborations have greatly advanced my scientific breadth.

I have also been incredibly fortunate to have the support of my friends and family. In particular, I would like to thank my parents for the constant encouragement and support; despite how insignificant it may appear, these factors have been extremely motivating throughout my educational and scientific career. Additionally, thank you Katie and Russell simply for being great siblings - I genuinely miss hanging out with you both every day and always appreciate our time together.

Finally, yet most importantly, I am incredibly thankful for my wife, Kate; I am forever grateful for your love and support over the last few years. Thank you for your constant patience in every aspect of life - I am incredibly lucky to come home to you every day and love you very much.

Contents

List of Figures

List of Tables

Chapter 1

Introduction

1.1 Background

Energy transfer between two materials or media is the underlying mechanism behind nearly every major modern technology. In the solid state, this is realized in examples such as computers, electronic devices, and photovoltaic cells, where electron transfer across an interface determines function. Of course, this transport of charge dictates conversion into thermal energy through electron-phonon interactions (or Joule heating on the macroscale) [10, 11]. The following heat transfer mechanisms that allow for dissipation of the the thermal load across these solid-solid interfaces remains to be an intense area of research, particularly in nanoscale systems [12]. As an example, a select number of the various energy transfer pathways and fundamental carriers that arise in at exemplary metal-semiconductor interface are shown in Fig. 1.1. Although much less investigated, similar phenomena and physical processes arise at interfaces composed of varying phases of matter (e.g., the interface of a solid-liquid junction). For example, a pre-requisite of material corrosion is ion transport across the interface of two media, typically at a solid-liquid interface. This transfer of charge leads to the same processes as discussed above for solid-state electronic devices. Likewise, photo-catalysis and the associated electron/hole exchange between the excited solid and its surrounding medium (typically liquid) can be considered as almost the

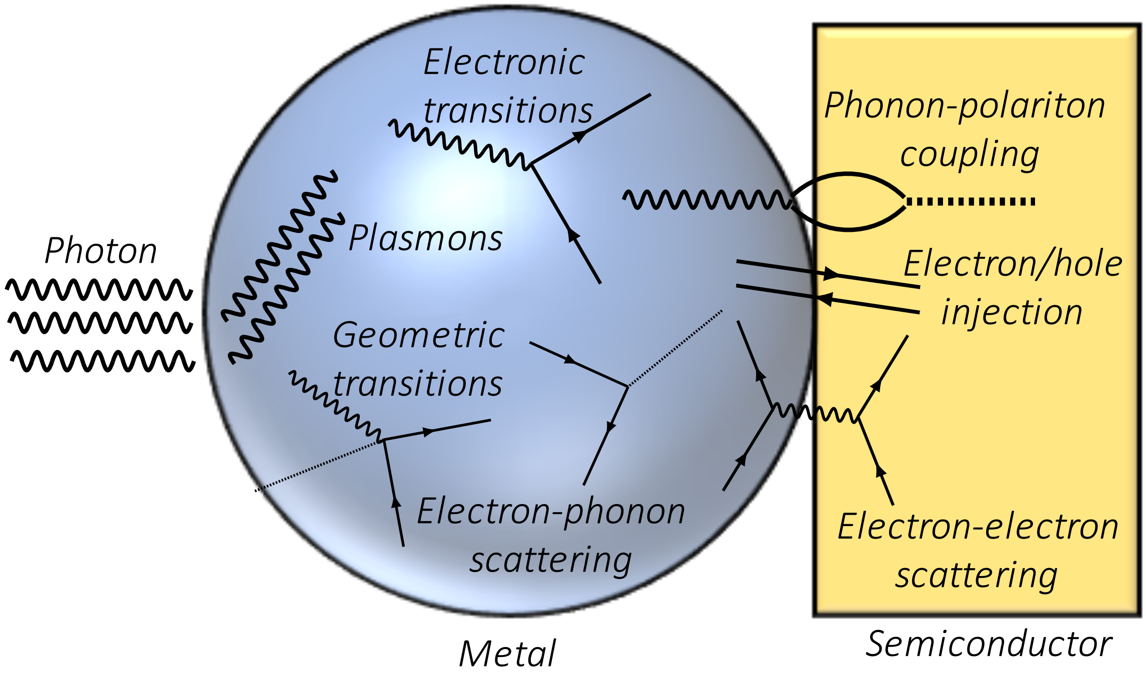

Figure 1.1: A brief summary of some of the energy transfer processes and fundamental carriers that occur in standard metal-semiconductor systems.

inverse of this corrosive process. Ultimately, these nanoscale interactions and dynamics between solids and liquids are the defining factors in a range of applications including, but not limited to, microfluidics, chemical catalysis, and microelectronic thermal management.

The field of nanoscale heat transfer primarily focuses on addressing specifically the transport of thermal energy in these nanoscale systems and their respective interfaces. This explicit separation from the field of 'traditional' heat transfer is due to the variety of physical processes and carrier dynamics that arise in these geometrically-reduced systems; a continuum-based interpretation of energy flow and thermophysical material properties breaks down, requiring a quantum mechanical-based formalism for understanding and manipulating heat transfer in nanoscale systems. A particular focus of this community is on the measure and interpretation of interfacial thermal resistances; as thermal conductivity defines the ratio of heat flux to the temperature drop in a single material system, the thermal boundary conductance of an interface defines the ratio of the heat flux to the temperature drop *across the interface*. Despite this simple relationship, at the nanoscale this thermal boundary conductance defines the net power carried per unit area per unit temperature that an ensemble of individual particles (or waves) carry across an interface. In other words: this thermal boundary conductance is a summary value that is dictated by the quantum-mechanical carriers and the amount of energy they transmit across an interface. In addition to its relationship to the nanoscale nature of energy transfer, this thermal boundary resistance is also a strong indicator or metric of other parameters of interest, such as the relative strength of interfacial bonding, and thus extends its use to fields outside the realm of purely heat transfer.

From the perspective of thermal transport, there are few techniques capable of rigorously measuring these interfacial resistances, even for solid-solid interfaces. The most versatile methods lie in the category of thermoreflectance metrologies, namely time-domain thermoreflectance (TDTR) and frequency-domain thermoreflectance (FDTR) [13]. In the time domain variation, this high repetition rate, ultrafast pump-probe technique paired with a multi-layer solution to the heat equation [14] provides an experimental measure of all the aforementioned processes: photon-electron excitations, electron-phonon scattering, and phonon-mediated thermal transport. Despite being one of the more versatile methods for studying and measuring energy transfer at interfaces, TDTR still remains highly limited in its capabilities. First, this technique requires a thin metal film as a thermal-to-optical transducer for measurements, immediately limiting measurements to optically-polished *solid* samples. Second, the aforementioned multi-layer solution to the heat equation used in TDTR dictates the ability to separate interfacial thermal resistances from the thermal resistance associated with particular 'layers.' This convolution inherently limits the ability to precisely measure a thermal boundary conductance for interfaces where one material composing the interface has low thermal conductivity (e.g., the resistance of the interface is of similar order of the resistance of the material). While these two factors can hinder the measurement of thermal resistances at interfaces composed of two solids, they play a more drastic role at interfaces composed of other phases of matter, due to the inherently low thermal effusivity associated with decreased atomic densities of liquids and gases.

1.2 Statement of Objectives and Scope

The overarching objective of this work is to overcome these limitations in traditional measurements of energy transfer through the development of novel experimental methods. These experimental metrologies will not only quantify the interfacial resistances present at boundaries composed of various phases of matter, but provide fundamental insight to the physical mechanisms underlying energy transfer at these interfaces. Furthermore, a number of these techniques and findings are utilized for engineering material systems with adaptive properties. Each chapter of this dissertation is intended to be relatively ‘self-supporting,’ such that readers interested solely in specific aspects of interfacial energy transport (e.g., only personally concerned with say, plasma-solid interactions) can jump directly to that chapter without major reliance on hundreds of pages of background and theory, though such background and theory is certainly presented within for those interested. Therefore, the remainder of this dissertation is organized as follows:

- **Chapter 2: Theory of energy transfer and thermal transport**: Background on phononic heat conduction in both crystalline and amorphous materials. This chapter provides the necessary framework and terminology presented in the remainder of the dissertation, beginning with the phonon gas model for prediction of thermal conductivity in crystalline solids, which then extends to the Allen-Feldman ‘diffuson’ formalism for vibrational heat transfer in amorphous solids. The chapter is then finalized with a description of common models and interpretations of thermal boundary conductances in phononic material systems.

- **Chapter 3: Experimental measurements of energy transfer**: Despite the presentation of numerous metrology advancements throughout this work, a large fraction of the measurements presented in this dissertation can be easily understood by those familiar with transient thermoreflectance methods. As such, this chapter focuses solely on a detailed description of the most common variation, time-domain thermoreflectance (TDTR), to provide those less familiar with such techniques the baseline knowledge necessary for interpreting such results. This includes a description of the experimental system, the background theory and signal analysis, as well as TDTR's sensitivity to thermophysical parameters of interest. Additionally, the latter half of the chapter provides an interlude on the necessity for advances in thermal metrologies, namely wavelength-tunable approaches to transient thermoreflectance measurements.

- **Chapter 4: Solid-solid interfaces**: This chapter introduces work on two alternate metrics toward analysis of thermal boundary conductance, namely laser ablation thresholds and picosecond acoustic measurements, which will be commonly referred to throughout the remainder of the dissertation. Additionally, I present a novel energy transduction mechanism that arises at metal-semiconductor interfaces, which relied on the aforementioned wavelength-tunable approach to transient thermoreflectance measurements to elucidate upon.
- **Chapter 5: Solid-liquid interfaces**: The first half of this chapter experimentally applies the metrology techniques developed in Chapter 4 toward the measurement of nanoscale energy transfer across solid-liquid interfaces. In particular, I investigate the relationship between macroscale models of heat transfer to the measure of thermal transmission at the nanoscale. The second half of this chapter manipulates such nanoscale solid-liquid interactions for the development of a record-setting tunable thermal conductivity switch, which is enabled through the infiltration of water to a squid ring teeth (SRT)-based biopolymer.
- **Chapter 6: Solid-gas interfaces**: Picosecond acoustic measurements are extended to solid-gas interfaces for the measurement of energy transmission across interfaces composed of non-condensed phases of matter. These results are interpreted within a newly-developed framework of the acoustic mismatch and diffuse mismatch models (AMM and DMM, respectively), derived specifically for the transmission of acoustic waves generated during a picosecond acoustic experiment and transmitted from a

solid surface to the adjacent gaseous phase.

- **Chapter 7: Solid-plasma interfaces**: This chapter demonstrates a time-resolved advance on our prior ‘steady-state’ thermoreflectance measurements of plasma-solid interactions [15]. Through the development of a transient plasma-pump laser-probe measurement technique, we provide the first nanosecond-resolved measurement of energy transduction during plasma-surface interactions. Further, we experimentally demonstrate the ability of an incident pulsed plasma jet to cool the surface of a material.

- **Chapter 8: Summary and future projects**: The major conclusions of this dissertation are summarized to reveal the connection between each study and the overarching goals of this research. Further, a description of several projects are proposed that could expand upon the results of this work.

Chapter 2

Theory of Energy Transfer and Thermal Transport

It is important to consider the basic concepts and methods that are involved in this thesis. This background begins with a summary of heat conduction in phonon-dominated systems, including both crystalline materials and amorphous solids. These concepts will then be extended to a brief review on the concept of energy transfer and interfacial thermal resistances in solid-solid interfaces, the current state of thermal transport at interfaces composed of varying phases of matter, and the techniques therein.

2.1 Homogeneous Media

In this section, we will only consider heat transfer in single-phase, homogeneous media. These concepts will generate the terminology and framework necessary for understanding energy transport at interfaces.

2.1.1 Thermal Transport in Crystals

The concept of energy transfer and thermal transport is most easily understood in the framework of steady-state temperature gradients and invocation of Fourier's Law in one-dimension. The rate of thermal transport, or the heat flux, Q, through a single material is proportional to the steady-state temperature gradient, $\Delta T/\Delta x$, across the length of the material; the ratio these quantities, $\frac{Q}{(\Delta T/\Delta x)}$, is defined as the negative of the material's thermal conductivity, κ [16]. In transient conditions, this rate of thermal transport is described by the heat diffusion equation,

$$C_v \frac{\delta T}{\delta t} = \nabla \cdot (\kappa \nabla T) + Q_{source}, \tag{2.1}$$

where C_v is the volumetric heat capacity, t is time, and Q_{source} is a volumetric heat source term that accounts for energy being added to the system. Thus, transient heat flow within a material is now dictated by both i) the amount of energy required to heat the system by a finite temperature (volumetric heat capacity) and ii) the rate of which this heat can be dissipated within the material (thermal conductivity).

This macroscale perspective of heat conduction remains valid so long as the energy carriers of the system can be described by an equilibrium energy distribution. At the microscale, this criterion is rarely met, as energy is fluctuating among different carriers at all times - various carriers undergo scattering events within their own sub-populations as well as inter-carrier scattering as a means of transferring energy. In the solid-state, a wide-range of energy carriers can co-exist, including: electrons and holes (electronic carriers), phonons (atomic vibrations), magnons (spin waves), and plasmons (plasma waves). As a first-approximation, we can relate these various scattering events to the thermal conductivity of a material through a kinetic theory description [17], referred to as the phonon gas model (PGM), by,

$$\kappa = \frac{1}{3} C_c v^2 \tau, \tag{2.2}$$

where C_c is the volumetric heat capacity of a given energy carrier, v is the carrier velocity, and τ is the average time between scattering events (e.g., relaxation time of a given carrier). This first 'grey' approximation assumes that the all heat carriers maintain equivalent velocities, heat capacities, and relaxation times. In reality, there is a distribution of these quantities, even among the same carrier population. Thus, the thermal conductivity becomes a summation of these individual particle states calculated at each available energy state, ε:

$$\kappa = \sum_{\varepsilon} \frac{1}{3} C_{c,\varepsilon} v_{\varepsilon}^{2} \tau_{\varepsilon}. \tag{2.3}$$

Different materials will typically transfer thermal energy via different primary carrier populations. For example, in free-electron metals, the high electron density leads to an electron-mediated thermal conductivity. In contrast, in insulators, the lack of electrons makes the electronic contribution to thermal conductivity negligible; thermal conductivity is dictated by lattice vibrations (phonons). Regardless, one can apply Eq. 2.3 to the respective carrier of interest, and, in theory, predict the thermal conductivity contributed by that carrier population.

To calculate the thermal conductivity in Eq. 2.3, we require intimate knowledge of the carrier population, velocity, and interaction rates. We will focus the following discussion on derivation of these terms for phonons, though many of the formalisms can be easily extended to other energy carriers with some modifications (e.g., the next section will discuss phonon dispersions, but those interested in electronic carriers are likely familiarized with band diagrams which would provide analogous information).

Phonon Dispersion

In a crystalline solid, the highly ordered, periodic nature of atomic arrangement gives rise to collective, wave-like vibrations of the atoms. These lattice waves carry the majority of the energy in insulating crystals and are termed ‘phonons.’ As with other waves, we can prescribe a dispersion to phonons, which establishes the vibrational frequency’s (ω) dependence on wavevector (k).

To generalize this relationship, we will first consider a one-dimensional chain of atoms. In this approximation, we treat the system as a simple harmonic oscillator such that we

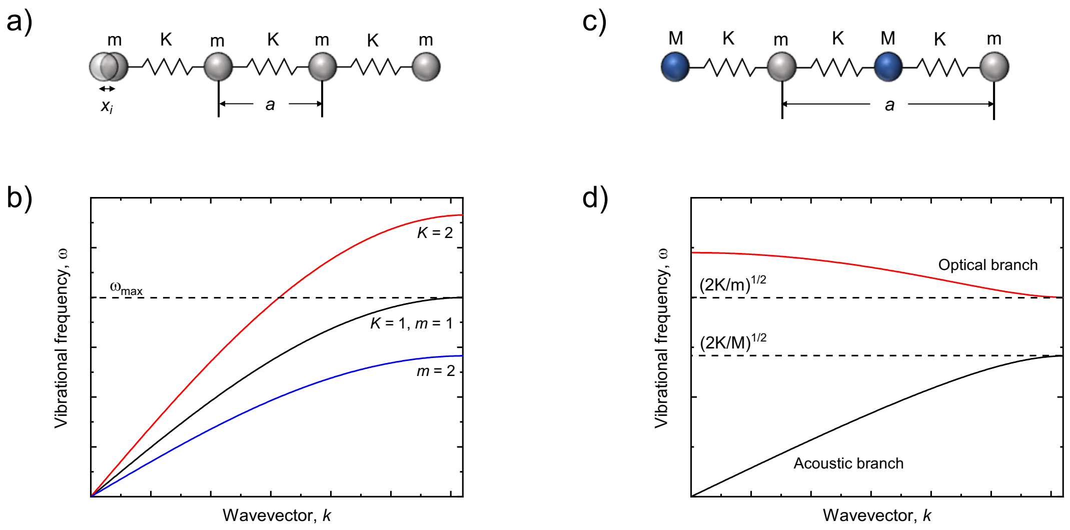

Figure 2.1: a) 1-D mass-on-spring approximation of a periodic array of atoms bonded by an interatomic potential b) Dispersion relation for the single element array of a); the red line is associated with the dispersion with double the spring constant (interatomic potential) of the black line, while the blue line doubles the mass of the atoms. c) 1-D mass-on-spring approximation for a basis consisting of atoms with two different masses. d) Dispersion relation for the above spring model, where $M = 2m$.

approximate the interatomic potential as a spring, with spring constant K, which holds together adjacent atoms of mass m at an equilibrium distance, a; a cartoon schematic of this representation is shown in Fig. 2.1.1a. This simplification allows us to invoke Hooke's Law ($m\frac{d^2x_i}{dt^2} = -Kx_i$, where x is the displacement of atom i about its equilibrium position) and obtain a dispersion relation [18]:

$$\omega(k) = (\frac{4K}{m})^{1/2}|\sin(\frac{ka}{2})|. \tag{2.4}$$

This simple analytical function of a 1-D chain provides insight to a few key aspects of the dispersion relation. First, the solution only exists for k between $[-\pi/a, \pi/a]$; this wavevector range is defined as our first Brillouin zone. Second, the periodicity of the system indicates that $\omega(k) = \omega(\pi/a + k)$; an aspect we will rely on later when considering scattering events and wavevector summations. The dispersion relation for this simple mass-on-spring model is shown in Fig. 2.1.1b.

As with other wave dispersions, this relation provides us a means of calculating the group velocity of the phonon for calculation of thermal conductivity via Eq. 2.3. The phonon group velocity, v_g, is defined as

$$v_g(k) = \frac{\delta\omega}{\delta k}. \tag{2.5}$$

Recall: as the wavevector approaches zero, we are approaching infinite distances in real-space. Thus, in the limit of $k \to 0$, where we are considering the frequency of long wavelength phonons, $v_g \to v_s$, where v_s is the sound velocity of the crystal.

In Fig. 2.1.1b, the dispersion relation is calculated for two potential scenarios: increased spring constant (e.g., an increase in our 'interatomic bonding' potential) and an increased atomic mass. These cases can be directly related to real crystals: materials with heavier masses tend to have reduced group velocities, whereas materials with strong bonds tend to have high group velocities, e.g., sound velocities. Thus, to maximize κ from Eq. 2.3, we would seek crystals with strongly bonded, light atoms; this can be conceptualized most easily by considering the thermal conductivity of silicon relative to that of diamond. In these phonon-dominated systems, the relative light carbon atom capable of forming strong sp^3 bonds lends itself to over an order of magnitude larger thermal conductivity than that of the much heavier Si atoms.

For many real crystals, the basis consists of more than one atom. In this case, our approximation of a single atomic mass in a chain is no longer sufficient; we can gain insight to this effect of varying atomic masses on the phonon dispersion by replacing every other atom in the 1-D chain with a ball of mass M; as shown in the cartoon schematic of Fig. 2.1.1c. This new basis leads to a phonon dispersion given by

$$\omega^2(k) = K(\frac{1}{m}+\frac{1}{M}) \pm K[(\frac{1}{m}+\frac{1}{M})^2 - \frac{4}{mM}\sin^2(\frac{ka}{2})]^{1/2}. \tag{2.6}$$

This solution to the equation of motion gives rise to a second branch in the dispersion: optical phonon modes are now present, as shown in the dispersion of Fig. 2.1.1d. These out-of-phase vibrations are unique in that they have a non-zero frequency in the limit $k \rightarrow 0$. In addition to this new vibrational mode, the presence of this heavier mass leads to a reduction in the group velocity and maximum frequency of the acoustic phonon branch. It should thus not be surprising that crystals consisting of heavy-mass elements typically have lower sound velocities as well as reduced thermal conductivities (as $\kappa \propto \nu$ in our PGM approximation above).

Phonon Heat Capacity and Density of States

Heat capacity is defined as the amount of energy required to heat a substance by a unit of temperature; this can be conceptualized as the amount of energy that can be 'stored' by a material. Mathematically, we can define this for a material at constant volume,

$$C_V = (\frac{\delta U}{\delta T})_V, \tag{2.7}$$

where U is the internal energy of the material, and T is the temperature. The internal energy of phonons at a given frequency can be calculated from the amount of energy carried by the phonon ($\hbar\omega$) multiplied by the phonon occupation at that frequency.

To determine this phonon occupation, we consider two functions: the phonon density of states and the Bose-Einstein distribution. The phonon density of states provides us the number of phonon energy states per unit volume per unit energy. For a given phonon branch, j, the density of states, $DOS_j(\omega)$ in an isotropic crystal is given as

$$DOS_j(\omega) = \frac{\omega^2}{2\pi^2 v_j^3(\omega)}. \tag{2.8}$$

The $DOS(\omega)$ only describes the number of *available* states that phonons can occupy. To determine the number of *occupied* states, we must invoke a distribution function; as phonons are bosons, their equilibrium occupation function is described by the Bose-Einstein distribution,

$$f_{BE}(\omega,T)=\frac{1}{\exp\left(\frac{\hbar\omega}{k_BT-1}\right)}, \tag{2.9}$$

where $\hbar$ is the reduced Planck constant and k_B is Boltzmann's constant. Thus, the *occupied* density of states becomes $DOS(\omega)f_{BE}(\omega,T)$.

Now, with a formalism for the occupation density, we can now return to our calculation of internal energy; the internal energy of a given phonon frequency can thus described simply as $\hbar\omega\cdot DOS(\omega)f_{BE}(\omega,T)$. Then, the *total* internal energy is this internal energy of each phonon, summed over all phonon modes. This can be written as

$$U=\sum_j\int_0^{\omega_{max,j}}\hbar\omega f_{BE}(\omega,T)DOS_j(\omega)d\omega, \tag{2.10}$$

where the summation accounts for each branch, j, of the phonon dispersion, and $\omega_{max,j}$ is the maximum angular frequency of occupied phonons in the branch (for example, see Fig. 2.1.1b). To obtain the lattice heat capacity, we take the derivative of U with respect to temperature:

$$C_V=\frac{\delta U}{\delta T}=\sum_j\int_0^{\omega_{max,j}}\hbar\omega\frac{\delta f_{BE}(\omega,T)}{\delta T}DOS_j(\omega)d\omega=\sum_j\frac{\hbar^2}{2\pi^2k_BT^2v_j^3}\int_0^{\omega_{max,j}}\frac{\omega^4\exp\left(\frac{\hbar\omega}{k_BT}\right)}{\left(\exp\left(\frac{\hbar\omega}{k_BT}-1\right)\right)^2}d\omega. \tag{2.11}$$

Scattering Rates

The last term in our phonon gas model calculation of the thermal conductivity of crystals is the scattering rate of phonons, τ, or the frequency of which phonons undergo collisions with *something* and changes either its momentum or energy (note, prior to a scattering event, we deem the carrier to be propagating 'ballistically'). In most materials at finite temperatures, this *something* that the phonon scatters with can be a range of inclusions, including but certainly not limited to: electronic carriers (electrons/holes), lattice defects (point defects, dislocations, and even the material surface/boundary), as well as other phonons.

As such, there is not a single collision frequency, but typically a number of types of collisions that must be accounted for. As such, when more than one source of scattering is present, we can invoke 'Matthiessen's Rule' where the scattering time of a given phonon branch, j, is simply the summation of all possible scattering processes, i:

$$\tau_j^{-1} = \sum_i \tau_{i,j}^{-1}. \tag{2.12}$$

While a number of additional scattering processes can occur, the primary phonon scattering processes that affect thermal conductivity in most materials are: phonon-phonon scattering, geometric scattering, and point defect scattering. In an ideal (defect-free) crystal of infinite dimensions, intrinsic phonon-phonon scattering mechanisms are the only processes that affect thermal conductivity. These are primarily three-phonon scattering events that can either conserve the phonon wavevector (normal processes) or through resistive, momentum-destroying processes (Umklapp scattering) [19, 20]. Normal scattering is a process that conserves momentum: two phonon wavevectors ($k_1 + k_2$) are summed to produce a third phonon with equivalent momentum ($k_3 = k_1 + k_2$). Importantly, this process lies within the first Brillouin zone such that k_3 lies within $[0, \pi/a]$. On the other hand, Umklapp scattering results in a wavevector k_3 that requires translation to a point outside the first Brillouin zone (recall: $\omega(k) = \omega(\pi/a + k)$); this transformation relies on the addition of a reciprocal lattice vector, G, such that $k_1 + k_2 + G = k_3$, leading to a loss in phonon momentum. While only Umklapp processes are resistive, and thus limit the thermal conductivity of crystals, normal processes are lead to a re-distribution of the phonon population, which in turn leads to an increased probability of Umklapp processes, and thus acts as an in-direct contribution to thermal resistance. Normal processes vary linearly with phonon frequency, ω, whereas Umklapp processes vary with ω^2, causing Umklapp scattering to be the dominant scattering mechanism for high frequency phonons. Given this, the scattering time for intrinsic scattering mechanisms (both normal and Umklapp combined) commonly takes the form [20]

$$\tau_{ph}^{-1} = B\omega^2 T \exp\left(\frac{-C}{T}\right), \tag{2.13}$$

where B and C are constants.

The next scattering mechanism, geometric scattering, is dominant in materials at low temperature and in nanostructures. This occurs when phonons scatter at boundaries such as surfaces, interfaces, and grain boundaries of crystalline systems. As such, it becomes a major scattering mechanism when the material dimension approaches the scattering length of phonons, with a scattering time given by [21]

$$\tau_b^{-1} = (1-p)\frac{v}{d} \tag{2.14}$$

where d is the characteristic length of the geometry and p is a specularity parameter that accounts for roughness of the interface and thus varies between 0 and 1.

The final scattering rate we will consider is phonon-defect scattering processes. In general, 1-D defects (e.g., dislocations) do not induce significant thermal resistance, 2-D defects are accounted for via the description of geometric/boundary scattering, and 3-D defects typically do not affect the *intrinsic* thermal conductivity of a material, but are instead accounted for with effective medium approximations. Given this, our primary consideration here will be on point defects; the scattering time here will account for both ‘traditional’ defects such as vacancies and interstitials, but also applies to isotope atoms as well as alloy atoms. This scattering time follows a Rayleigh scattering form, given by [20],

$$\tau_d^{-1} = A\omega^4, \tag{2.15}$$

where A is a constant.

Thus, when considering these dominant scattering mechanisms, the relaxation time for calculation of thermal conductivity is given by

$$\tau^{-1} = \tau_d^{-1} + \tau_{ph}^{-1} + \tau_b^{-1} = A\omega^4 + B\omega^2 T \exp\left(\frac{-C}{T}\right) + (1-p)\frac{v}{d}. \tag{2.16}$$

It is important to note that this semi-classical description of relaxation time is simply a phenomenological formalism, and the constants A, B, and C are determined by fitting the PGM (Eq. 2.3) with the above scattering rate to experimental data. Nonetheless, these descriptors provide valuable insight to the various mechanisms that induce thermal resistances in perfect crystals; we now have a basis for the roles of temperature, interatomic bonding, and crystalline quality on the resultant thermal conductivity of a material through the above relationships.

2.1.2 Formalism for Thermal Transport in Amorphous Media

In amorphous solids and low-density phases (liquids, gases, plasma), there is no long-range atomic order and we can not prescribe a periodicity to the structure. Thus, we can no longer describe vibrational modes as phonons, since the vibrational wavevectors are poorly defined. Similarly, we can not describe group velocities or scattering rates due to this lack of formalism. Thus, it becomes incredibly difficult to describe thermal transport in amorphous media. While there have been fairly successful frameworks to which we can model the thermal conductivity of amorphous solids, such as the 'model of the minimum thermal conductivity of solids,' [22–24] in which the relaxation time in the PGM is taken to be half a period of vibrational oscillation (e.g., the carrier mean free path is limited to the distance of adjacent atoms, due to the lack of long-range order), there have been an equivalent number of works showing the failure of such formalisms and approximations [25–28].

Rather than attempting to understand energy transfer in amorphous media through approximations on transport theories used in crystalline systems (e.g., PGM), it is far more appropriate to instead turn to alternative descriptions of vibrational modes. One means of doing this is to describe the rate of heat transfer by the diffusivity of vibrational modes. This generalization to diffusivity has no need for a well-defined wavevector and can thus be applied to any vibrational mode (e.g., we can theoretically apply this to crystalline systems with similar accuracy) [26]. Under this formalism, the quantized quasi-particle of atomic

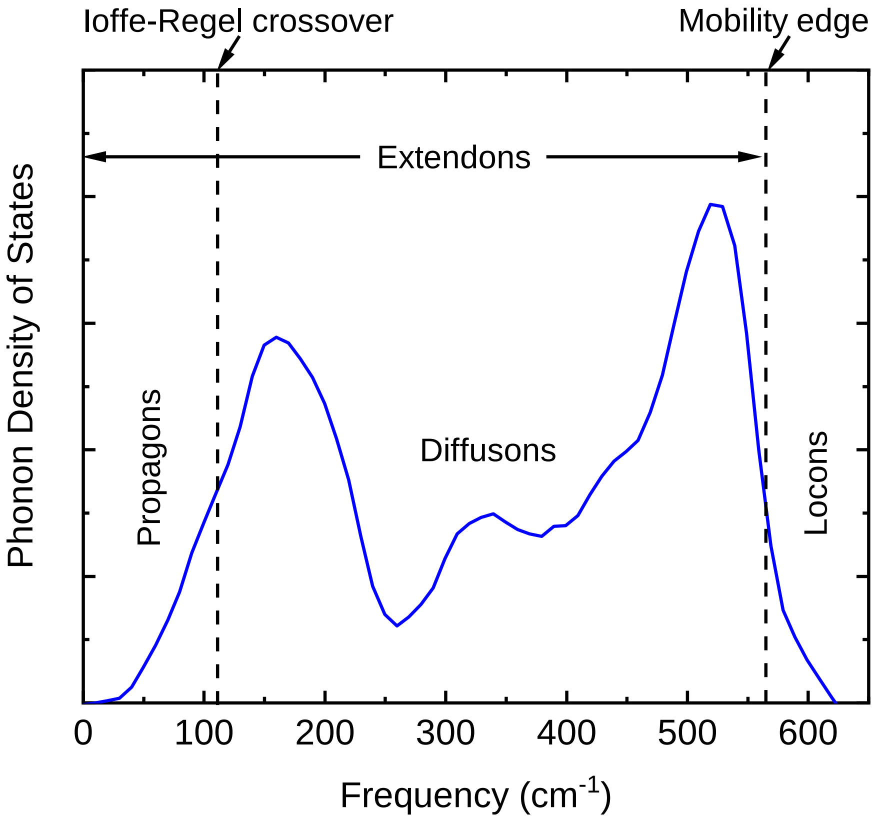

Figure 2.2: Phonon density of states for amorphous silicon calculated via lattice dynamics, with the spectral region associated with each character of vibron being labeled accordingly.

vibrations is termed a ‘vibron’ [29].

Similar to our description of phonons, in which we have non-propagating, high frequency oscillations (optical phonons) and typically propagating, but at lower frequencies, there are acoustic phonons, vibrons can be either localized (locons) or extended (extendons) harmonic normal modes. In three dimensions, the vibrational DOS typically exhibits sharp changes in the number of available states at high frequencies (see Fig. 2.1.2 for an example of the phonon DOS calculated via lattice dynamics using GULP [30]); this boundary in the DOS is defined as the ‘mobility edge’ that separates these two kinds of modes. However, at lower frequencies (encompassed entirely by extendons), a second, less-pronounced boundary, defined by Allen *et al.* as the ‘Ioffe-Regal crossover;’ this crossover separates the spectrum in which ballistic propagation of modes occurs and wavevectors are reasonable defined and the frequency of which wavevectors are less-well-defined and diffusion occurs [29]. In the low-frequency, ballistic regime, the extendons are termed ‘propagons,’ while extendons at in the diffusive regime are deemed ‘diffusons.’ These new definitions of vibrational modes for amorphous media allow us to properly describe the characteristics of vibrational thermal transport in terms of mode diffusivity.

Despite our new vocabulary, it is important to note that there remains much to be found on the individual contributions of each mode to the thermal conductivity of various materials. For example, in Allen *et al.*’s simulations [29], it was shown that propagons and locons only make up 4% and 3% of the vibrational modes in amorphous silicon, respectively, indicating that the thermal conductivity is heavily dictated by diffusons. Indeed, this is expected when considering the relative success of the aforementioned model of the minimum limit to thermal conductivity, which approximates heat transfer rates through a diffusive, random walk of vibrational modes. However, a number of works have demonstrated significant contributions to thermal conductivity from propagons, including experiments in amorphous silicon [31, 32].

2.2 Interfaces

Within the framework of steady-state temperature gradients and invocation of Fourier’s Law in one-dimension as we performed for a single crystal, we define the heat flux, Q, across an interface composed of two materials relative to the temperature difference across the interface, $\Delta T = T_1 - T_2$, through the thermal boundary conductance (TBC, h_k) associated with that interface via $Q = h_k(T_1 - T_2)$. Similar to the factors that affect heat conduction in solids, this TBC is related to numerous factors, including the vibrational density of states of the two media, defects, changes in bonding, and temperature [33, 34]. While these factors can manifest themselves at any length scale, intimate knowledge of the atomic and nanoscale features composing the media is necessary to truly understand conduction and energy transfer.

2.2.1 Thermal Boundary Conductance at Solid-Solid Interfaces

In the same way that carrier scattering leads to thermal resistance in a single material, a thermal resistance arises at the interface due to carrier scattering at the interface. This thermal boundary resistance at the interface of two solids that have phonon-mediated heat conduction has historically been described through two predictive models: the acoustic and diffuse mismatch models (AMM and DMM, respectively) [35]. These models calculate the TBC based on the flux of phonons across an interface, where energy from the hotter side is carried by the phonons across the interface into the cooler material.

As phonon transmission across the interface is binary, either the phonon transmits across the interface or it does not, we will concern ourselves with the probability of this phonon transmission, ζ. This transmission probability is dependent upon a number of factors such as the wavevector and frequency of a given phonon incident upon the interface, the temperature of the system under consideration, and upon extrinsic factors such as the 'quality' of the interface. Under the assumption that the materials comprising the interface are isotropic, we can describe ζ as a function of the phonon frequency, ω, the angle of phonon incidence upon the interface relative to the interface normal, θ, and the phonon mode, j. Further, if we approximate ζ as being temperature-independent, we do not require consideration of anharmonic interactions; this allows us to only require calculation of the transmission probability in one direction. For the consideration of a thermal boundary conductance, we will relate this transmission to the heat current across the interface. The heat current density *incident* upon the interface is the number of phonons with a given frequency and incident angle that are incident upon a unit area per unit time, times the phonon energy ($\hbar\omega$); this is summed over all frequencies and incident angles. Then, the gross heat current density across an interface is this incident heat current times the transmission probability of each phonon, $\zeta(\theta, j, \omega)$. This number of phonons incident from one side on unit area per unit time is given by

$$\frac{N_j(\omega,T)}{4\pi} d\Omega c_j \cos(\theta), \tag{2.17}$$

where c_j is the phonon propagation velocity of mode j, and $d\Omega = d\phi \sin(\theta) d\theta$, where ϕ is the azimuthal angle of incidence of the phonon. Additionally, $N_j(\omega, T)$ is the product of the phonon density of states at the given angles and the Bose-Einstein distribution function. Integrated over all angles, this simplifies to $c_j N_j(\omega, T)$. Thus, the interfacial heat current becomes

$$Q_{int} = \frac{1}{2}\sum_j \int_0^{\pi/2} \int_0^{\omega^{max}} N_1(\omega, T)\hbar\omega c_j \times \zeta(\theta, j, \omega) \times cos\theta sin\theta d\theta d\omega. \tag{2.18}$$

For small temperature differentials across the interface ($T_2 - T_1$), the thermal boundary conductance is then given as

$$h_k = \frac{Q_{int}(T_2) - Q_{int}(T_1)}{(T_2 - T_1)}. \tag{2.19}$$

In principle, we can now calculate/predict the TBC of a given interface if we know the transmission probability function, ζ. One of the primary factors in determining ζ for a given interface is consideration of the overlap in the phonon density of states between the two materials comprising the interface. In contrast to optically-induced transitions, where electrons can only move from a filled to an empty state, phonons propagate across an interface when there is an overlap in the relative states between the two materials. For example, if one side of an interface has a low population of phonons at a given wavevector, k, then there are few carriers of that wavevector to carry energy to the opposing side. As we assume detailed balance at the interface, this also indicates that an equivalent number of phonons will be capable of transmitting in the opposite direction, even if a large phonon population exists at that wavevector in the second material (e.g., the thermal boundary conductance is a constant number, regardless of what direction heat is moving). Thus, the TBC tends to be larger for materials with strong overlap in the phonon density of states between the materials comprising the interface due to an increased ζ.

While both the AMM and DMM reflect the relative overlap in the phonon density of

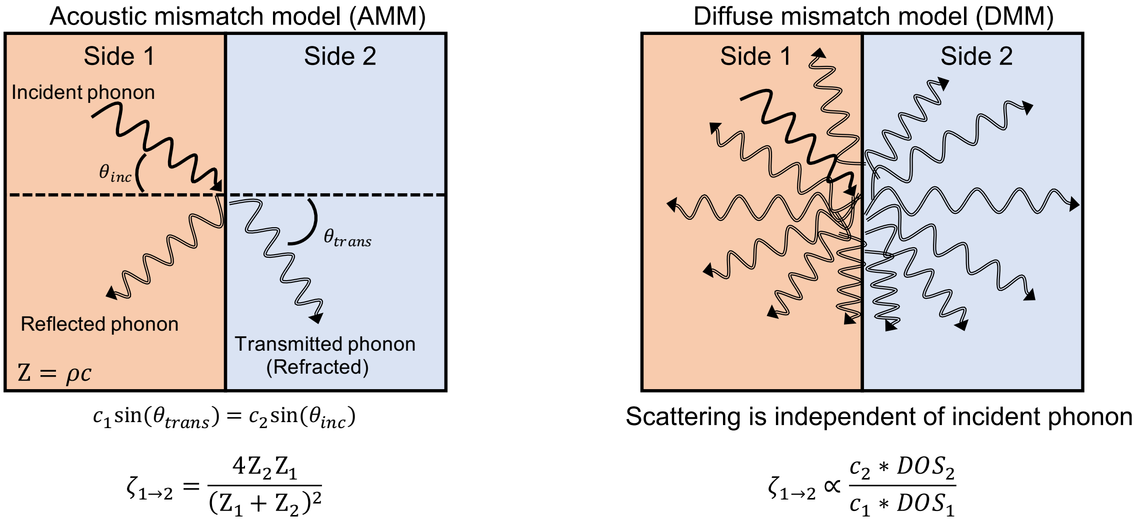

Figure 2.3: Cartoon schematic on the type of phonon interactions with an interface of two materials assumed in the acoustic mismatch model (AMM, left) and diffuse mismatch model (DMM, right).

states between the two materials comprising the interface, the pre-requisites for which a phonon of a given wavevector will transmit across the interface are quite different. More specifically, the scattering processes assumed in the AMM and DMM are polar opposites. On one end of the scattering spectrum is the AMM, where it is assumed that the interface is 'perfect' with no defects or crystalline imperfections and that phonons only undergo elastic interactions at the interface; this is akin to treating the lattice vibrations as a wave in a continuum. As such, the AMM assumes there is no scattering at the interface; upon reaching the interface, phonons can either undergo specular reflection, reflect and mode convert, refract, or refract and mode convert (see Fig. 2.2.1a). Despite this simplification, the AMM has found relative success in the describing interfacial thermal transport at low temperatures (i.e., below the Debye temperature of either material comprising the interface) [36, 37]. To describe the phonon interaction with the interface, we can calculate the angles of reflection or refraction, as well as their respective probabilities, through an acoustic analog to Snell's law for light. Consider a phonon propagating from side 1 towards the interface on side 2 at an angle of θ_{inc} from the interface normal. If the phonon were to transmit, we can calculate the transmission angle, θ_{trans}, through Snell's law:

$$\sin(\theta_{trans}) = \frac{c^2}{c^1}\sin(\theta_{inc}) \tag{2.20}$$

This relationship applies to any mode phonon; the phonon group velocity, c, must simply be accounted for accordingly. For example, if the incident mode is a longitudinal phonon, but is converted to a transverse phonon after transmission, the fraction in Eq. 2.20 would simply be written as c_t^2/c_l^1. It is also important to recognize that the transmitted angle cannot exceed 90°, and thus ζ vanishes for cases where $\sin(\theta_{inc})$ is equal to c^1/c^2; therefore we must only consider angles below this critical angle. Returning to our discussion on density of states overlap, we can note that when considering phonons incident upon the interface from the side with greater phonon velocities, there is no critical angle, and phonons with any incident angle have some finite probability of transmitting; if a phonon transmits across the interface from a high velocity side to a low velocity medium, with probability ζ, then a phonon from the other (low velocity) side will transmit with equivalent ζ back to the high velocity side at equivalent angles.

From continuum acoustics, ζ can be derived at a fundamental level [38] for any incident angle and mode. Most simply, we can consider phonons at normal incidence, where the transmission probability takes the form [39]

$$\zeta = \frac{4Z_2Z_1}{(Z_1+Z_2)^2}, \tag{2.21}$$

where the acoustic impedance, Z_i, is equal to the product of the mass density and sound velocity, $\rho_i c_i$. Most critically, we recognize that AMM relies on the bulk, continuum properties of the two materials comprising the interface for calculation of the phonon transmission function; there is no scattering of phonons at the interface and phonon dispersions are not considered. Despite these extreme simplifications and assumptions, the AMM has found relative success in modeling interfacial thermal resistances at low temperatures (e.g., solids interfaced with cryogenic helium) [36, 37].

As experimental measurements of TBC begin to strongly deviate from AMM predictions at increased temperatures, we must turn to somewhat more rigorous predictive models. Namely, we would like to relax our assumption on interfacial phonon scattering from the AMM; phonon scattering is the origin of thermal resistances in bulk materials, and thus should be expected to play a large role for interfacial thermal conductivities. As such, we will consider the opposite extreme, in which we will model the transmission function under the assumption that *all* phonons will be diffusely scattered at the interface. This diffuse mismatch model, originally proposed by Swartz [37], assumes that any acoustic correlations are ‘destroyed’ upon scattering with the interface, such that ζ becomes dependent only upon the phonon density of states and the principle of detailed balance; the ‘mismatch’ in phonon density of states thus determines the phonon transmission probability. This description can be conceptually related to Fermi’s golden rule: when a phonon reaches the interface, it can either forward scatter or backscatter, and the scattering direction is determined by the relative number of states accessible by the phonon on each side of the interface. In other words, a phonon incident upon the interface of two materials will propagate (scatter) to the side with the larger number of states at the same frequency. This is in strong contrast to the AMM, where a phonon density of states that is favorable to forward scattering in DMM would be indicative of a large contrast in acoustic impedances between the two media, and thus the same phonon would be reflected in the AMM formalism. Furthering our conceptual picture of phonon scattering at interfaces, we should note that in the AMM, $\zeta = 1$ when two materials with identical acoustic properties comprise the interface, as there is no impedance mismatch between the two media. However, the transmission probability is reduced to 50% in the DMM for this scenario.

Quantitatively, we must only modify our transmission probability, ζ, when moving from the acoustic to diffuse mismatch model. In the DMM, ζ can be calculated from the principle of detailed balance and the consideration of diffuse scattering at the interface. Following Swartz and Pohl [35], we define a diffuse scattering as an event in which a scattered phonon’s wavevector and mode are fully independent of the pre-scattered phonon’s wavevector and mode. In other words, diffuse scattering is when a phonon loses ‘memory’ of its initial conditions upon scattering. From this definition, the transmission probability of a given phonon is independent of the phonon's wavevector and mode, and thus the transmission probability for phonons incident from side 1 is simply

$$\zeta_1(\omega) = 1 - \zeta_2(\omega), \tag{2.22}$$

as, since the phonon forgets all details of its origin (the phonon does not know whether it was incident from side 1 or side 2 upon scattering), the probability of reflection from one side must equal the transmission probability of the opposite side.

We can calculate this transmission probability by consider the number of phonons per unit area per unit time that leave side 1, given by

$$\frac{1}{4\pi}\sum_j \int_0^{2\pi} \int_0^{\pi/2} d\theta \cos(\theta)\sin(\theta) d\phi c_{1,j} N_{1,j}(\omega,T)\zeta_1(\omega), \tag{2.23}$$

where $N_{1,j}(\omega,T)$ takes the form of Eq. 2.17. Our definition of diffuse scattering indicates that ζ is independent of the incident angle, which greatly simplifies Eq. 2.23, reducing to:

$$\frac{1}{4}(\sum_j c_{1,j} N_{1,j}(\omega,T))\zeta_i(\omega). \tag{2.24}$$

Invoking the principle of detailed balance, we recognize that this flux must be equal to the number of phonons that are leaving side 2 per unit area per unit time:

$$\sum_j c_{1,j} N_{1,j}(\omega,T)\zeta_1(\omega) = \sum_j c_{2,j} N_{2,j}(\omega,T)[1-\zeta_1(\omega)]. \tag{2.25}$$

And thus the transmission function can be obtained:

$$\zeta_1(\omega) = \frac{\sum_j c_{2,j} N_{2,j}(\omega,T)}{\sum_{1,j} c_{1,j} N_{1,j}(\omega,T)}. \tag{2.26}$$

More advanced theories that are rigorous to an atomistic level, such as the atomistic Green's function method [40, 41], have more recently been implemented for gaining a fundamental understanding TBCs at solid-solid interfaces. Additionally, *ab initio* calculations have gained traction as a means to calculating thermal conductivity and TBC [42, 43]. Nonetheless, these formulations tend to provide poor agreement to experimental data, with first-principles calculations providing a modest improvement, indicating more complex processes than considered in the models are at play [33, 44, 45]. Furthermore, the above discussion solely applies to phonon-dominated conduction, and typically neglects any role of electron-mediated energy transfer. While select works have shown that electron-dominated conduction can play a major role in interfacial heat transfer [46, 47], it has been traditionally neglected.

2.2.2 Energy Transfer Across Phases Composed of Varying Phases of Matter

Energy transfer and TBC across solid/non-solid interfaces display a larger knowledge gap when compared to the vastly-studied case of solid-solid interfaces. This knowledge gap arises due to experimental measurement limitations, and only very recent developments of the necessary models to provide insight to the fundamental mechanisms arising at the nanoscale of solid-liquid interfaces. Nonetheless, these nanoscale interactions and dynamics across various phases of matter are critical to an array of technologies and phenomena. For example, these interactions at solid-liquid interfaces are ultimately the defining factors in a range of applications including, but not limited to, microfluidics [48–50], chemical catalysis [51–53], and microelectronic management [54, 55]. An increased understanding of such nanoscale dynamics provides insight into the mechanisms of various interfacial phenomena, such as protein folding and adsorption [56–58], cell formation [59, 60], and other self-assembly processes [61–63]. While countless studies have focused on attempting to understand these solid-liquid interactions at the macroscale, common metrics such as contact angle become over-simplistic and fail to realize the complex phenomena occurring on the nanoscale. For example, works alluding to nanoscale effects at interfaces attempt to relate measurements of the contact angle to chemical composition and molecular-scale thermodynamic effects at the solid-liquid interface [64, 65]. Additionally, other works have gone in the opposite direction: manipulating the molecular order at a solid-liquid interface, such as structure and composition, to control macroscale wetting [63, 66]. While general empirical trends have been observed that relate macroscopic measurements of solid-liquid interactions to nanoscale interfacial properties, these trends assume that macroscopically observable interactions scale to the nanoscale interfacial region.

To further complicate the picture, the aforementioned models used to predict and understand heat transfer at solid-solid interfaces, outside of the AMM at cryogenic temperatures [67], which have been formulated over a number of decades, can not be readily applied to thermal transport at a solid/non-solid interface above $\sim$ 10 K. The lack of periodicity and inability to define group velocities in disordered phases, such as in liquids and gases, renders these predicative models invalid. Only recently have the necessary models and theories been developed to enable a more fundamental understanding of solid-liquid interactions at the nanoscale [68]. Furthermore, as the density of the second phase decreases, there arises a larger gap in previous literature and thus the fundamental understanding of energy transfer across the two interfaces, further limiting the application of prior formalisms. In the cases of energy transfer from a solid to a gaseous medium, only convective heat transfer has been widely investigated as a means of energy transfer. Even so, experimental reports on the heat transfer coefficients at these solid-gas interfaces remain sparse and highly limited. The ability to measure the TBC across such interfaces not only provides a critical value necessary for engineering applications, but also elucidates the mechanisms that drive energy transfer between the two phases of matter.

The fourth phase of matter, plasma, has been strongly neglected from a fundamental heat transfer perspective. The select works investigating energy transfer from a plasma to a solid have relied on macroscale measurements, typically operated in a steady-state regime [69, 70]. In doing so, the micro- and nanoscale mechanisms that drive such energy transfer cannot be well-understood.

Chapter 3

Experimental Measurements of Energy Transfer

Thermoreflectance spectroscopy is a robust technique that has been used to interrogate the band structure and optical transitions in metals for decades [71–75]. In recent years, these thermoreflectance methods have been extended to the field of nanoscale thermal transport, and have become ubiquitous in their use for thermophysical characterization of thin films and their associated interfaces. Namely, time-domain thermoreflectance (TDTR) and frequency-domain thermoreflectance (FDTR) have gained traction as the principle methods for measurement of thermal boundary conductance of interfaces in nanosystems. Given such, the framework of TDTR/FDTR has been extensively discussed in a number of seminal works, reviews, and prior dissertations. Thus, only a brief scope of TDTR that is directly pertinent to the remainder of the document is included in the following section; this includes a description of the experimental build, the multi-layer heat equation that is solved for thermophysical characterization, and background on the sensitivity of this thermal model to the experimentally-acquired data..

In addition to TDTR/FDTR, which rely on solution of a multi-layered heat equation for extraction of thermal boundary conductance, a description of wavelength-tunable pump-probe approaches to interrogation of energy transfer in nanosystems is included in this chapter; these methods will provide direct insight to non-equilibrium processes such as electron-phonon coupling and energy transduction occurring on < 500 ps timescales.

3.1 Time-Domain Thermoreflectance

3.1.1 Experimental System

The TDTR systems used in this work are both based on high-repetition rate, femtosecond pulse duration Ti:sapphire oscillators (Spectra Physics Tsunami). This oscillator emanates a train of $\sim$90 fs pulses centered at a wavelength of 800 nm every 12.5 ns (e.g., 80 MHz repetition rate). These pulses are split into a 'pump' and a 'probe' path via polarization optics. The pump pulses are electro-optically modulated at a given frequency, f, (8.8 MHz unless noted otherwise) and focused to the sample surface. The probe pulses are sent to a mechanical translation stage in order to create a temporal delay between the pump and probe. These pulses are then aligned to be collinear with the pump pulse and focused to the sample surface with a microscope objective; the focused beam has a Gaussian intensity profile (e.g., fundamental transverse mode, TEM_{00}). The thermoreflectance of the probe (change in reflectivity due to a temperature change) is measured with a photodiode and sent to a lock-in amplifier, where the EOM modulation is used as the reference signal for lock-in detection, as a function of pump-probe delay time to obtain the thermal decay from the metal transducer into the surrounding films. A cartoon schematic of TDTR is shown in Fig. 3.1

We use two TDTR systems in this work: a 'two-tint' and a 'two-color' variation. Following frequency modulation, the two-color system uses a BiBO crystal to frequency double the pump beam to a wavelength of 400 nm; the two-tint system keeps both the pump and probe at $\sim$800 nm. The two-color system allows for a wider range of metal transducers to be used for measurements and simplifies spectral filtering of the pump and probe beam. Otherwise, the systems are nearly identical. Standard metal film transducers are 80 nm of aluminum or gold, which are typically electron-beam evaporated onto the sample of

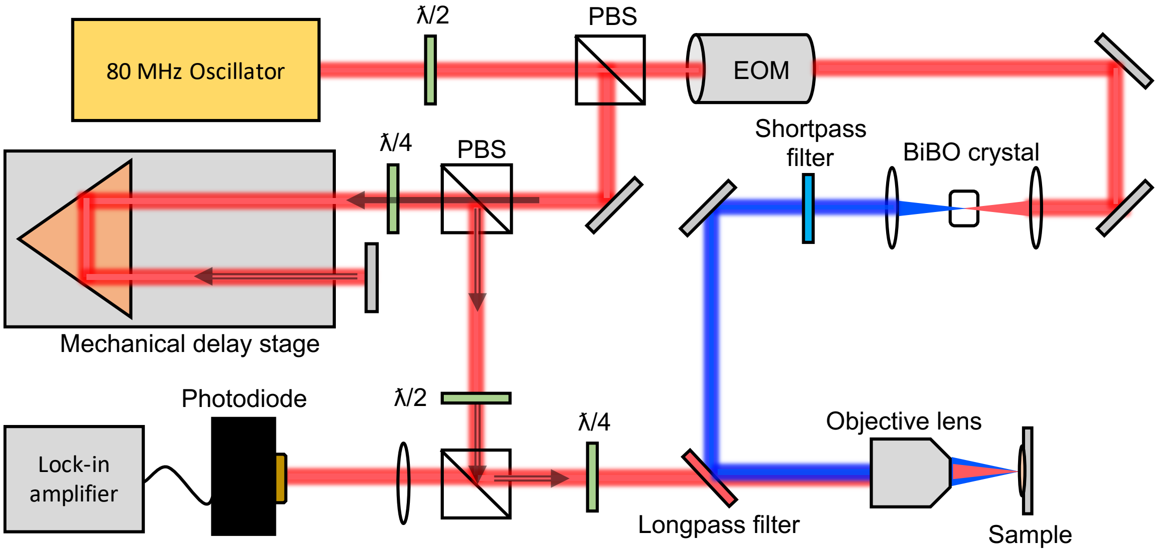

Figure 3.1: Schematic of our two-color TDTR system.

interest.

3.1.2 Theory and Signal Analysis

The thermal analysis for TDTR given below will rely on two critical aspects of our experiment: the known intensity profile of the pump pulse, TEM_{00}, and the use of a metal transducer/wavelength combination where the pump and probe interact with the surface of the film. These factors ensure a well-described heat input on the transducer surface, given by,

$$p(r) = A\frac{2}{\pi r_0^2}\exp\left(\frac{-2r^2}{r_0^2}\right), \tag{3.1}$$

where r_0 is the $1/e^2$ beam radius and A is a constant that accounts for the power absorbed at the metal surface (e.g., laser power and reflectance). Given the cylindrical symmetry of the pump and probe beams, we can use Hankel transforms to simplify the solution. The Hankel transform of $p(r)$ is

$$P(k) = A\exp\left(-\pi^2 k^2 r_0^2/2\right). \tag{3.2}$$

As we are considering a periodic point source as the heating event (high repetition, modulated focused laser), we can apply the frequency-domain solution of the heat equation for a semi-infinite solid:

$$g(r) = \frac{\exp(-qr)}{2\pi\Lambda r}, \tag{3.3}$$

and

$$q^2 = (i\omega/D), \tag{3.4}$$

where ω is the angular frequency of the periodic heating source, Λ is the thermal conductivity of the material, and D is the thermal diffusivity. The Hankel transform of this solution, $g(r)$, is

$$G(k) = 2\pi \int_0^\infty g(r) J_0(2\pi kr) r dr \tag{3.5}$$

$$G(k) = (\frac{1}{\Lambda(4\pi^2 k^2 + q^2)})^{1/2}. \tag{3.6}$$

From this, the distribution of the temperature oscillations on the surface, $\Theta(r)$ can be determined via the inverse transform of the product of $G(k)$ and $P(k)$,

$$\Theta(r) = 2\pi \int_0^\infty P(k) G(k) J_0(2\pi kr) k dk. \tag{3.7}$$

These temperature oscillations, induced by the pump beam, are measured via the change in reflectivity with the probe beam (e.g., thermoreflectance measurement). As the probe laser also has a Gaussian intensity profile, with its own $1/e^2$ radius, r_1, the thermoreflectance response is a weighted average of the temperature distribution $\Theta(r)$ and the probe's spatial profile. This response is given by,

$$\Delta T = \frac{4}{r_1^2} \int_0^\infty \Theta(r) \exp(-2r^2/r_1^2) r dr, \tag{3.8}$$

and

$$\Delta T = 2\pi A \int_0^\infty G(k) \exp\left(-\pi^2 k^2 (r_0^2 + r_1^2/2)\right) k dk. \tag{3.9}$$

3.9 can be generalized to a layered geometry, rather than our initial solution of a semi-infinite solid; the iterative approach has been outlined in a number of works in greater detail [14, 76]. In considering a layered structure, we replace $G(k)$ from 3.6 with a thermophysical property matrix:

$$G(k) = \left(\frac{B_1^+ + B_1^-}{B_1^- - B_1^+}\right)\frac{1}{\gamma_1}. \tag{3.10}$$

For a number of layers, n, where $n = 1$ is the surface layer, each layer is described by three parameters; the thermal conductivity, Λ_n, thermal diffusivity, D_n, and its thickness, L_n. In this approach, the thermal boundary conductance between two layers is simply modeled as a layer with zero thickness and zero heat capacity. With this in mind, the matrix takes the form:

$$\begin{pmatrix} B^+ \\ B^- \end{pmatrix}_n = \frac{1}{2\gamma_n} \begin{pmatrix} \exp(-u_n L_n) & 0 \\ 0 & \exp(u_n L_n) \end{pmatrix} \times \begin{pmatrix} \gamma_n + \gamma_{n+1} & \gamma_n - \gamma_{n+1} \\ \gamma_n - \gamma_{n+1} & \gamma_n + \gamma_{n+1} \end{pmatrix} \begin{pmatrix} B^+ \\ B^- \end{pmatrix}_{n+1}, \tag{3.11}$$

$$u_n = (4\pi^2 k^2 + q_n^2)^{1/2}, \tag{3.12}$$

$$q_n^2 = i\omega/D_n, \tag{3.13}$$

$$\gamma_n = \Lambda_n u_n. \tag{3.14}$$

For extraction of thermophysical properties, namely thermal conductivity and thermal boundary conductance, we are interested in analysis of TDTR data on time-scales associated with thermal diffusion, e.g., $t >\sim 100$ ps. As the pulse duration of our experiment is nearly three orders of magnitude lower than this time scale, we can approximate the laser output simply as a series of delta functions, separated by the repetition rate of the laser, and modulated at frequency, f. The lock-in amplifier evaluates frequency components of the temperature change and probe intensity (3.8) at both f and $-f$. Additionally, the time delay between the pump and probe, t, shifts the relative phase of the probe frequency spectrum. Thus, the lock-in response takes the form,

$$Re[\Delta R_M(t)] = C \sum_{M}^{m=-M} (\Delta T(m/\tau + f) + \Delta T(m/\tau - f)) \exp(i2\pi mt/\tau), \tag{3.15}$$

$$Im[\Delta R_M(t)] = -iC \sum_{M}^{m=-M} (\Delta T(m/\tau + f) - \Delta T(m/\tau - f)) \exp(i2\pi mt/\tau), \tag{3.16}$$

where C is a constant that accounts for the thermoreflectance coefficient of the material and absorbed power of the pump beam. The limit of the sum is set as $M = 10\tau/t$. As noted by Ref. [14], the real part of $\Delta R_M(t)$ converges slowly, so an additional Gaussian factor, $\exp(-\pi(f/f_{max}))$ where f_{max} is the maximum frequency considered in the calculation, is multiplied to each term. Typically, choosing an $f_{max} \approx 10/t_{min}$, where t_{min} is the first pump-probe delay time considered in the analysis, achieves accurate results. Note, for pump-advanced TDTR systems (as used in the wavelength-variable systems described in the following section), an additional phase shift must be accounted for: $\Delta R(t) = \Delta R_M(t) \exp(i2\pi ft)$.

To measure and extract a thermophysical parameter of interest, we model this response function and use a least-squares fitting routine to vary terms in the property matrix until a ‘best-fit’ to our experimental data is obtained. In the next section, I discuss the sensitivity of TDTR measurements to these thermophysical properties and the ability to reliably obtain accurate values.

3.1.3 Sensitivity to Parameters of Interest

In contrast to the vast amount of literature on the TDTR/FDTR thermal models, the discussion of sensitivity in prior works is quite brief and difficult for one to intuitively extend to their own measurements. Thus, in this section, I aim to provide a more rigorous description of standard sensitivity analysis and its associated effects on the uncertainty/error bars for various thermophysical parameters.

In order to measure a thermal parameter of interest when fitting the above multi-layer heat equation to experimental data, the modeled curve should be dynamic with respect to the thermal variable. In other words, if I vary the thermal variable from the best-fit value by 10%, then the model should no longer match the experimental data if we are *sensitive* to the parameter. In contrast, if my arbitrary 10% change in the thermal property produces the exact same model as the pre-altered solution, then we are clearly unable to accurately measure this property.

The sensitivity of the thermal model, V, to a physical parameter, x, is defined as [77],

$$S_x = \frac{\delta V}{\delta ln(x)}. \tag{3.17}$$

This sensitivity allows us to directly quantify the extent of which a change in the thermophysical parameter of interest alters the thermal model used to fit TDTR data. The magnitude of S_x defines the sensitivity to a given parameter; if a small change in x greatly affects our thermal model, we should be able to accurately fit for the parameter. Note, the sign of S_x is dictated simply by the response of the model to the change in parameter; negative values of S_x indicate that the thermoreflectance will decrease when the thermophysical parameter is increased (or vice-versa). Of course, in TDTR, as we consider the temporal decay of energy, we can plot S_x as a function of pump-probe delay time. In order to extract two separate parameters, we not only want them to have large magnitudes of S_x at *some* time delay, but also want the temporal function of S_x to have greatly different curvatures.

To put this in perspective, let us consider an example 'calibration' sample, where the

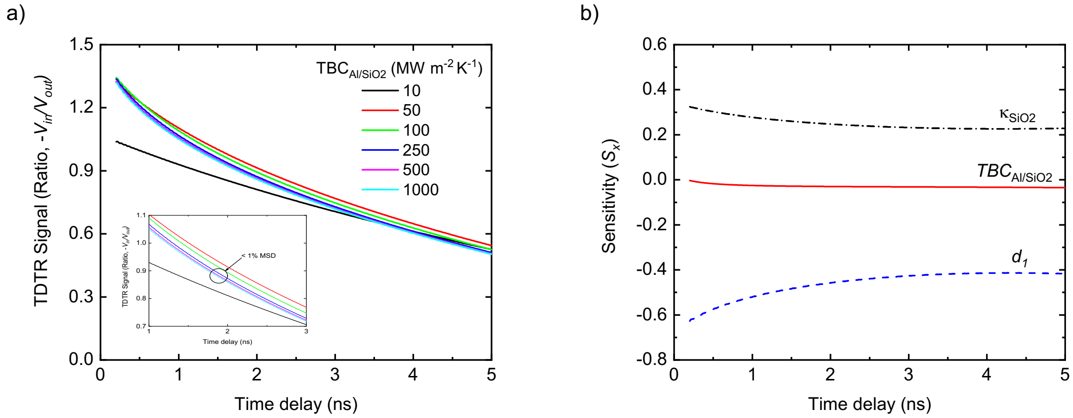

Figure 3.2: a) Calculated thermal model for 80 nm Al/α-SiO$_2$ with varying values for the TBC; aside from the case of an unphysically-low TBC (black line), there is negligible change in the model, indicating a lack of sensitivity to the TBC. b) Sensitivity (Eq. 3.17 of the TDTR signal to various thermophysical parameters for the case of 80 nm Al/α-SiO$_2$.

material constants are well-described in literature: 80 nm Al/$\alpha-$SiO$_2$. In this case, we have *a priori* knowledge of the thermal conductivity for the two layers, as well as their heat capacity, so if the best-fit model to our experimental data measures a thermal conductivity outside of the known value for SiO$_2$, then usually it is a signature that our alignment is incorrect in some capacity. But what if I want to measure the less-studied thermal boundary conductance of the Al/SiO$_2$ interface? In theory, I can vary the TBC until the model matches the experimental data.

In Fig. 3.2b, I have plotted the sensitivity, S_x, for three parameters in this simple sample geometry, the thermal conductivity of the SiO$_2$ (κ_{SiO_2}), the thickness of the aluminum layer (d_1), and the thermal boundary conductance of the Al/SiO$_2$ interface (TBC_{Al/SiO_2}). Even in this simple geometry, we see that we are highly *insensitive* to the TBC of interest; we can not accurately measure the TBC of an Aluminum/Silica interface. Though, this does indicate that any assumption for TBC will not greatly affect the measurement of κ_{SiO_2}.

We can now think of this lack of sensitivity in terms of our best-fit model and quantify our uncertainty of a measured value. In Fig. 3.2a, I have plotted the thermal model for the above geometry using a range of TBC values. We can see that for any TBC value above 50 MW m^{-2} K $^{-1}$, the thermal model only undergoes small changes. So what range of TBC values are considered ‘acceptable’ fits to our data? To accurately quantify the true uncertainty in our TDTR measurements, we consider the mean-square deviation (MSD) of our multi-layer thermal model to the experimental TDTR data. For a single unknown parameter, this simple consideration of the normalized residual, or the model’s MSD, relative to the experimental TDTR data is sufficient (assuming the other parameters are well-known); an increase in the normalized residual is equivalent to a poor fit to the data. In most cases, a normalized residual of < 0.01 is considered a ‘very good’ fit to the experimental data. For the Al/SiO_2 case, accepting only TBC values within this residual range leads to us only being capable of defining a lower bound - above 100 MW m^{-2} K^{-1}, the fits are still statistically representative of the experimental data.

In most cases for TDTR, we can reliably fit a single decay curve for two thermophysical parameters of interest. In these scenarios, the uncertainty is generated through what we colloquially call ‘contour plots.’ To determine the uncertainty/bounds of these parameters, we generate theoretical model curves with varying thermophysical parameters around the best-fit values obtained with least-square minimization of our thermal model to the experimental data. We can then quantify the difference between these curves similar to above, using the normalized residual. Except, in this scenario, we consider MSD for all combinations of the two parameters of interest. For example, in the Al/SiO2 scenario above, the MSD is calculated for all values of TBC. If we want to simultaneously fit for the TBC and κ_{SiO_2}, we now calculate the MSD for all combinations of TBC and κ_{SiO2} (within some physically-meaningful limits). An example contour plot is shown in Fig. 3.3 for this simple calibration scenario. In this case, the error bars of our data must encompass all values within the black circle, which defines the combination of parameters that achieve MSD < 0.01.

Unless otherwise stated, the sensitivity analysis described above is used to calculate the error bars reported in this work; in many cases, the uncertainty associated with the thermal model is overwhelmingly the primary source of error, rather than spot-to-spot deviations or error due to instrument noise.

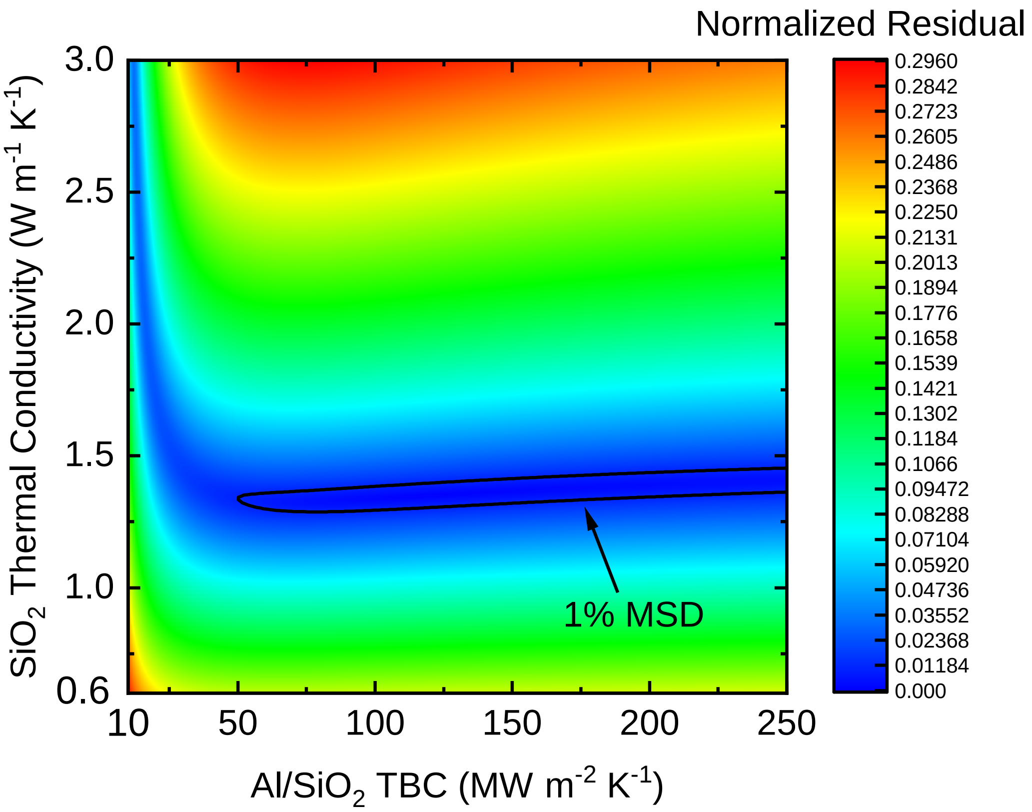

Figure 3.3: The normalized residual (i.e., the accuracy of the model's fit relative to the obtained thermal decay curve) for values of best-fit for our thermal model for 80 nm Al/SiO$_2$. The black line denotes the region of $<1\%$ MSD, which encompasses values that provide acceptable fits to the data.

3.2 Wavelength-Tunable Ultrafast Measurements

Traditional thermoreflectance techniques, described above, rely on a thin metal transducer atop the material of interest; the film is chosen such that it i) has a large absorption coefficient at the pump wavelength, and ii) has a large, but constant, thermoreflectance coefficient at the probe wavelength (dR/dT). These factors ensure that the pump is heating the *surface* of the film (one of the criterion for the solution to the heat equation provided above), and that the probe response is indicative of the sample temperature. While this can be achieved with many noble metals, it certainly limits the applications of TDTR/FDTR. For example, the requisite transducer inherently limits the interfaces available for study: TDTR is primarily sensitive to the metal/substrate interface, not ‘buried’ interfaces that are critical for understanding multilayer heat transfer. Further, investigation of non-equilibrium processes, even in these noble metals, is extremely difficult to perform correctly: when electrons and phonons are out-of-equilibrium, the thermoreflectance coefficient is ill-defined, requiring *apriori* knowledge of dR/dT_e and dR/dT_p for accurate interpretation of pump-probe data [78]. To overcome these limitations, a number of the works described in this thesis rely on a wavelength-tunable pump-probe system that I have developed. The ability to tune wavelengths allows for direct relationship between the optical response and carrier sub-populations, allowing one to eliminate obscurities associated with thermoreflectance coefficients. Moreso, they allow for ‘direct-probing’ of non-metals, which provides insight to sub-layer energy transfer processes that are inaccessible via TDTR. An introduction to these concepts and an example of the necessity for such systems is described below for the measurement of the electron-phonon coupling factor in the prototypical material system, Au.

Advantages to Single-Wavelength Approaches

Energy transfer among out-of-equilibrium particle populations is the fundamental basis for a number of applications where temporally-short excitation sources are utilized. Examples range from high-frequency, high-power electronics where electronic relaxation defines the rate of charge transport [79, 80] and, at sufficiently high fields, induces dielectric breakdown [81–83], to photothermal therapies [84, 85] and material processing [86, 87] with ultrafast sources, where the heat-affected zone is heavily dictated by the rate of which electrons couple to vibrational states. The majority of understanding of these non-equilibrium processes is rooted on interpretation of ultrafast pump-probe reflectivity measurements. In metals, the relation between non-equilibrium energy transfer and optical response is most commonly understood within the framework of the two-temperature model (TTM) [88]. In a typical experiment, a sub-picosecond laser pulse excites the electron subsystem to very large temperatures, while the lattice remains cold. Following a time determined by the material's electron-phonon coupling constant, G, these electrons gradually transfer their energy to the material's lattice; the two systems eventually reach equilibrium and diffusive heat transfer processes ensue. The most common method in which to interrogate these electron and phonon dynamics during and after sub-picosecond laser heating is through monitoring the reflectivity of a time-shifted probe pulse. The transient change in reflectivity of the probe pulse due to the heating from the sub-picosecond heating event is then assumed to be a measure of the transient temperature changes in the metal. Without invoking physical models, the probe reflectance change due to these pump-induced temperature excursions is given simply by [89]

$$\frac{\Delta R}{R} = \frac{R(T) - R(T_0)}{R(T_0)} \tag{3.18}$$

where R is the reflectivity prior to excitation at an initial temperature of T_0, and $R(T)$ is the probe reflectivity at the excited temperature, T. Inclusion of the TTM simply re-states this relationship as a function of the individual temperatures of the electron and phonon subsystems, e.g., $R(T_e, T_p)$. The magnitude of reflectivity change due to these temperature excursions is thus defined by the thermo-reflectance coefficients, dR/dT_e and dR/dT_p. Through these relations, one can, in theory, directly relate the measured reflectivity to the temperature transients of the two subsystems.

While the basis of this approach is straight-forward, knowledge of these thermo-optic coefficients is crucial towards accurately understanding the non-equilibrium energy transfer dynamics and measuring thermophysical properties such as G. Without *a priori* knowledge of dR/dT_e and dR/dT_p, which are also both wavelength and temperature dependent, it is difficult, if not nearly impossible, to accurately separate these optical coefficients from the thermophysical properties of interest. This issue has lead to a large discrepancy in reported values of the electron-phonon coupling factor, G, via pump-probe measurements. In the case of gold, due to its relatively flat density of states around the Fermi energy and its high Debye temperature, one should expect a constant G at elevated temperatures above the Debye temperature, given by [90, 91]

$$G = \frac{\pi^2 m_e^* C_s^2 n_e}{6\tau(T_e)T_e} \tag{3.19}$$

where m_e^* is the effective mass of the electrons, C_s is the speed of sound, n_e is the electron number density, and $\tau(T_e)$ is the electron relaxation time. In many cases, $\tau(T_e) \sim 1/T_e$, leading to the expectation of a constant G [92]. Regardless of analytical derivations and theoretical/computational studies, many experiments report a G that is not constant as a function of fluence/electron temperature. Likewise, experiments performed under nearly identical conditions, such as similar electronic temperature excursions, report differing values for G [1, 47, 93–98]. These differences have been hypothesized to be driven by fluence-dependent electron scattering processes in parallel to the electron-phonon interaction, non-thermal relaxation of the excited electron system, or steady-state heating that would occur due to pulse accumulation from high repetition rate laser pulses but not in lower repetition rate amplified systems (i.e., measurement artifacts). Clearly, a self-consistent experimental understanding of the role of electron temperature on the electron-phonon coupling factor in gold is missing, leaving theories of electron-phonon coupling in metals during non-equilibrium conditions unverified.

Thus, the questions that we seek to answer in this work are: i) what is the cause of the wide range of values and dsicrepencies reported for G of gold? and ii) how does the electron-phonon coupling factor of gold vary with electron temperature during non-equilibrium conditions when $T_e \neq T_p$?

Most pump-probe systems are based on a visible-to-near infrared lasers, commonly centered at a wavelength of 800 nm. The *static* optical properties of Au at these wavelengths, and most metals, are in-fact dominated by free electrons and are well described by the Drude model [99]. Given this, it is commonly, albeit potentially incorrectly, assumed that the *change* in optical properties due to temperature excursions lie within this Drude regime. For a given temperature excursion, there are two physical considerations. The first temperature-dependent term is the plasma frequency, defined as

$$\omega_p = \sqrt{\frac{n_e e^2}{m_e^* \varepsilon_0}}, \tag{3.20}$$

While the effective mass, m_e^* can have a temperature dependence, it is typically negligible for free, intraband electrons. Rather, the number density, n_e, has the most prominent temperature dependence, as it is directly related to the thermal expansion coefficient of the lattice. The second temperature dependence arises in the scattering rate of the free electrons, which is commonly estimated through Matthiessen's rule, $\tau_f^{-1} = A_{ee}T_{ee}^2 + B_{ep}T_p$, where A_{ee} and B_{ep} are constants related to the temperature dependencies electron-electron and electron-phonon scattering rates, respectively.

There are a number of intrinsic flaws associated with this approach. First, while the Drude model applies to NIR wavelengths under static conditions (e.g., 800 nm), the optical response following short-pulse excitation is strongly dependent on interband transitions under conditions of strong electron-phonon non-equilibrium due to smearing of the Fermi-Dirac distribution at elevated electron temperatures [100–102]. Thus, the Drude model is not expected to be applicable. Further, the temperature coefficients lack a wavelength dependence, indicating the perturbation of the optical response due to a temperature excursion lacks a wavelength dependence, which is well-known to not be the case. Finally, these scattering coefficients are derived from low-temperature resistivity methods [103]; in the original work where A_{ee} is defined, the coefficient is explicitly defined as not being

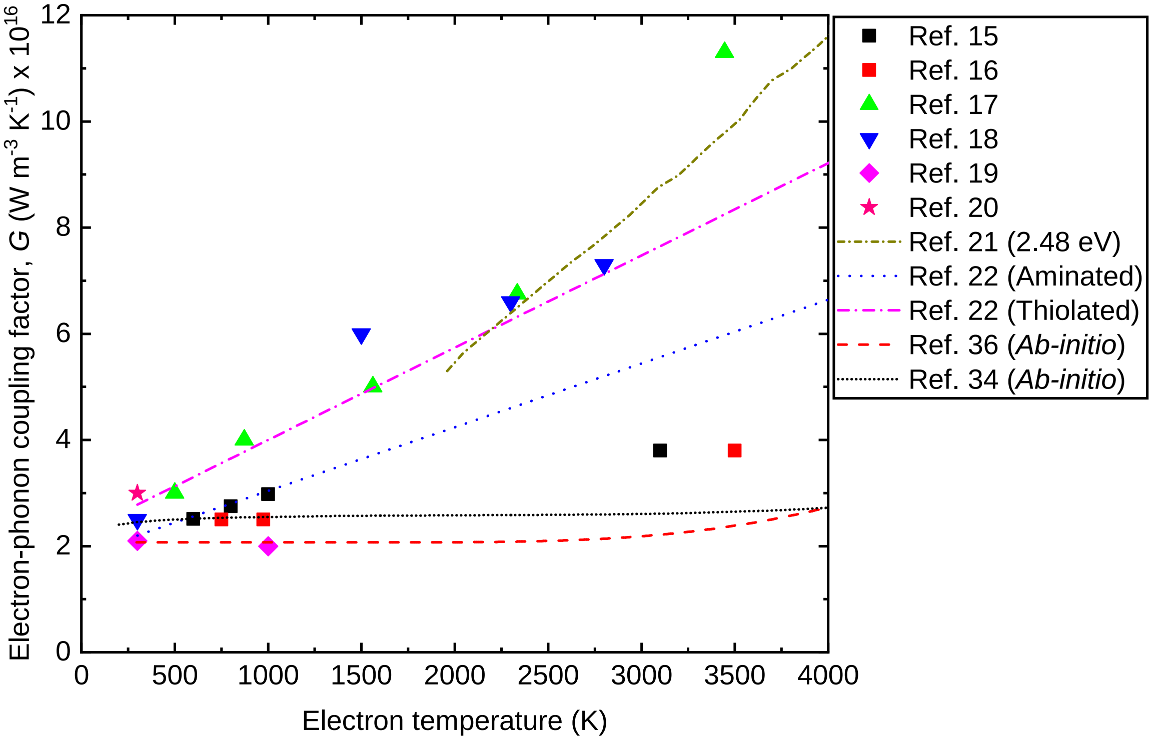

Figure 3.4: Compilation of previous literature values for the measured electron-phonon coupling factor of thin Au films as a function of excited electron temperature are shown as solid symbols, models and DFT calculations are shown as lines. The experimental results are based on ultrafast pump-probe experiments with probe wavelengths in the visible, typically <800 nm.

applicable to radiation frequencies corresponding to visible light [104].

Recent works have avoided these models, and instead rely on perturbation theory to relate the electron temperature to interpret transient reflectivity data at visible wavelengths [102]; this approach provides one of the more accurate determinations of the electron-phonon coupling factor [105]. In fact, Hohlfeld *et al.* directly monitored the temporal evolution of the Fermi-Dirac distribution in Au following short-pulse excitation, providing a direct measure of the electron temperature. In doing so, they provide a commonly-referenced value for the electron-phonon coupling factor ($G = 2.1 \times 10^{16}$ W m^{-3} K^{-1}) [1]. While this approach is highly accurate, it is far from straight-forward; this approach requires pump-probe data to be acquired at a large number of wavelengths centered about the interband transition of the metal of interest to directly measure the electron temperature. Furthermore, in metals with more complex band structures than that of Au, where multiple electron transitions occur in a small energy range, the ability to directly relate reflectance to the change in electron distribution can be extremely difficult [102].

Nonetheless, these inadequacies provide crucial information towards measurement of electron-phonon interactions via ultrafast pump-probe measurements. As referenced above, the temperature of the phonon subsystem contributes significantly to the transient reflectivity signal, and is weakly dependent on wavelength. In the regime of which reflectivity is considered to be intraband in nature, and thus the Drude model is applicable, one obtains a nearly constant thermoreflectance coefficient, which is dominated by the temperature rise of the phonon subsystem. Conversely, the temperature of the electron subsystem and its associated thermo-optic coefficient is strongly dependent on wavelength, due to its strong dependence on interband transitions, but trends toward zero at photon energies far from interband transition threshold [101, 102]. Given such, we expect that for probe wavelengths far from the interband electronic transitions in a metal, that the thermoreflectance is dominated, if not solely proportional to, the lattice temperature of the metal.

In this work, we investigate the role of interband contributions applied to transient optical responses in ultra-fast pump-probe experiments using both experiments and first principle calculations. We interrogate the temporal dynamics of $\sim$20 nm Au on insulating substrates following excitation with a 400 fs, 520 nm pulse using probe wavelengths spanning from 0.85 eV to 4.35 eV (1500 nm - 285 nm) as a means of separating the contributions of the electron and phonon subsystems to the perturbed optical response. Furthermore, we perform *ab initio* calculations to understand the role of intra- and interband contributions to the modulated optical response. In doing so, we find that the electron-phonon coupling factor of Au is in-fact constant at least up to electron temperatures of $\sim$2,000 K, consistent with Eq. 2 and free electron theory. In doing so, we posit that the variations in the reported values of G in Au from prior literature could be obfuscated from interband transitions leading to inaccuracies in the thermo-optical model. We summarize an array of literature values for the electron-phonon coupling factor of Au in Fig. 17.1.

In excellent agreement with a wealth of literature, we find the ultrafast transient dynamics to be strongly dependent on the probe wavelength in the visible; an example is demonstrated in Fig. 4.12. Even in cases of constant pump fluence, ensuring a constant electron-phonon coupling factor, and thus constant temperature transients for the two subsystems, for each probe wavelength, the signals are vastly different. This observation is traditionally attributed to a variation in thermo-optic coefficients for each wavelength; as the wavelength approaches resonance with an electronic transition, dR/dT_e increases. Indeed, a least-squares minimization of the TTM to our experimental data demonstrates that dR/dT_e is strongly dependent on the wavelength of the probe, at least for visible wavelengths. Conversely, the phonon-contribution to modulated reflectance, dR/dT_p, is weakly coupled to wavelength. Additionally, at most visible wavelengths, dR/dT_p is found to be orders of magnitude greater in magnitude than dR/dT_e, in agreement with prior works [78].

We perform a least-squares minimization routine to fit the TTM to our experimental data as a function of wavelengths and fluences, with three variations of free-variables. In one case, as done in most prior works, we use literature values for the thermo-optic coefficients, and solely fit for the electron-phonon coupling factor. Additionally, we perform these calculations with a constant electron-phonon coupling factor, but instead fit for the

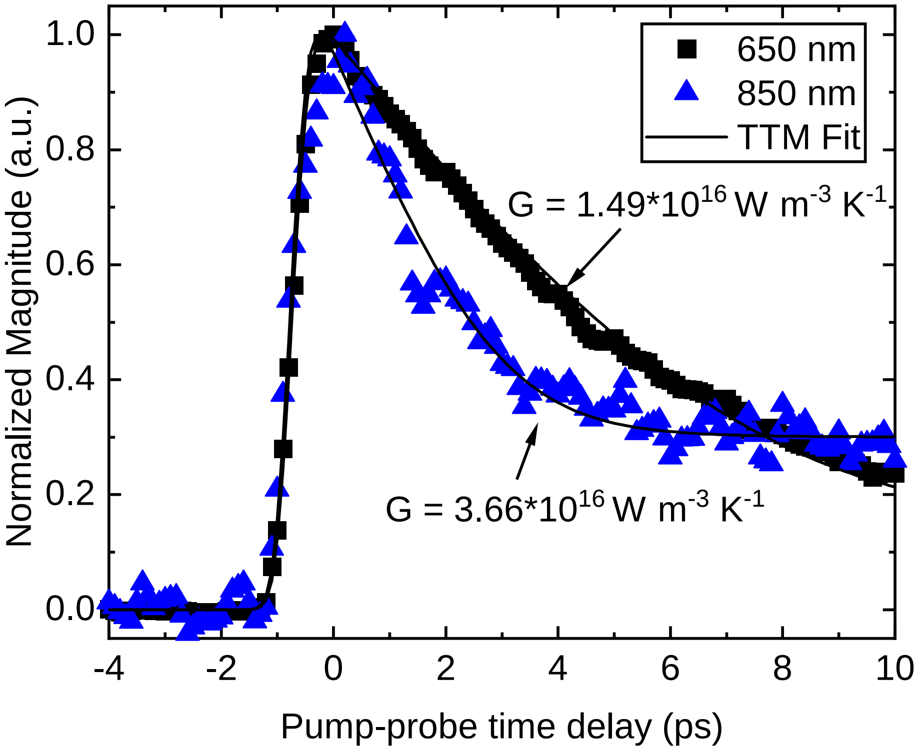

Figure 3.5: Experimental data for 20 nm Au films on sapphire substrates at probe wavelengths of 650 nm (black squares) and 850 nm (blue triangles). Using a perturbed Drude model to relate the electron/phonon subsystems to their respective temperatures yields over a factor of two difference in the calculated electron-phonon coupling factor, even with a constant excitation fluence.

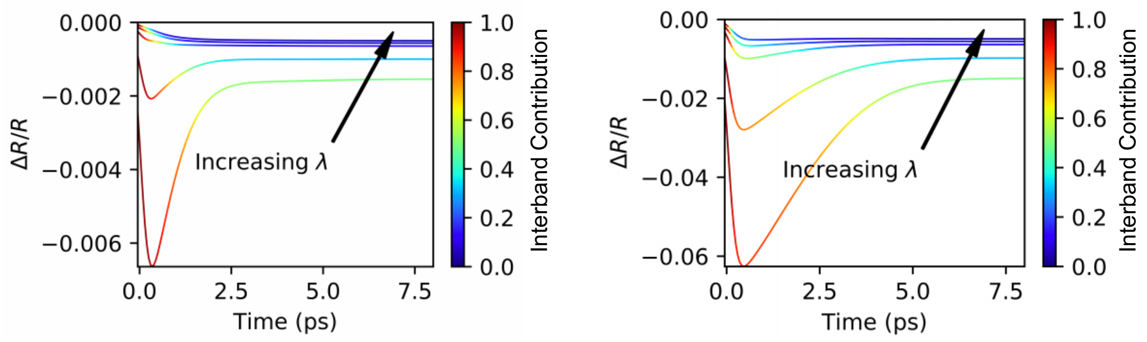

Figure 3.6: Relative contribution of direct interband transitions to the probe response of Au at an absorbed fluence of 1 J m^{-2} (left) and 10 J m^{-2} (right) for wavelengths of 600, 700, 900, 1100, and 1300 nm.

thermo-optic coefficients. Finally, we repeat these calculations with both the thermo-optic coefficents and electron-phonon coupling factor as free variables. These results are summarized in the following discussion.

As expected, fitting for both the thermo-optic coefficents as well as the electron-phonon coupling factor shows perfect agreement with our experimental data, however un-physical as this approach may be. Conversely, a constant electron-phonon coupling factor, while fitting for the thermo-optic coefficients or application of the perturbed Drude model, fails to capture the experimental data at wavelengths close to the interband transition; this approach is found to show good agreement only for wavelengths above $\sim$700 nm for the fluences used in this work. Similarly, fitting for G while using the Drude approach causes the TTM calculations to deviate greatly from the experimental data as the interband transition is approached.

To understand the origin of this deviation, we perform *ab initio* calculations of the excitation, relaxation and time-dependent optical response using the approach detailed in Ref. 106. Briefly, we combine density-functional theory and maximally localized Wannier functions[107] to evaluate contributions of direct interband and phonon-assisted intraband transitions to the carrier distributions (pump excitation) and time-dependent complex dielectric function (probe response) of the metal.[108, 109] The hot carrier energy distribution is evolved using the Boltzmann Transport Equation (BTE) with an *ab initio* collision integral including electron-electron and electron-phonon scattering. This parameter-free approach predicts the time-dependent optical response of the metal after pump excitation in quantitative agreement with ultrafast experiments on different plasmonic geometries and materials.[106, 110]

The computational framework described above provides the temporal evolution of the complex dielectric function, separated into direct and indirect contributions as

$$\varepsilon(\omega,t) = \varepsilon_{direct}(\omega,t) + \varepsilon_{indirect}(\omega,t), \tag{3.21}$$

where ω is the frequency of the probe beam. Implementing this dielectric function into the Fresnel equations provides a modulated response given by

$$\frac{dR(\omega,t)}{R(\omega,t)} = \frac{g'(\omega,0)}{g(\omega,t)}(d\varepsilon_{direct}(\omega,t) + d\varepsilon_{indirect}(\omega,t)). \tag{3.22}$$

As shown in Fig. 7.2, we find that interband contributions to the modulated response dominate the optical response at ultrafast time-scales for wavelengths less than ~700 nm, invalidating the application of the Drude model to pump-probe data. Furthermore, with increasing fluence, smearing of the Fermi-Dirac distribution leads to a large interband contribution to the modulated response, even for wavelengths initially far from the d-to-s-band transition in Au. Attempting to fit these first principle results with a TTM leads to similar issues as found in our experimental data; when the interband contribution to the modulated response becomes significant, the perturbed Drude model and/or fitting with a constant G fails.

These first-principle calculations, as well as extrapolation of the wavelength dependence in the thermo-optic coefficients for visible wavelengths elucidates a means to avoid thermo-optical models that are not widely applicable; for probe wavelengths sufficiently far from electronic transitions, the optical response becomes truly free-electron-like. This Drude-like response ultimately lacks sensitivity to the electron temperature, and is instead indicative of solely the temperature of the phonon subsystem. Additionally, this free-electron response is linearly proportional to the lattice temperature. This has the advantage of the changes in reflectivity being driven by relatively smaller temperature rises, since the heat capacity of the lattice is orders of magnitude lower than the heat capacity of the electrons. Thus, the nonequilibrium dynamics due to large excursions can be monitored through the much smaller temperature rises of the lattice. In most pump-probe experiments that interrogate these nonequilibrium dynamics of materials in the reversible, non-damage fluence/temperature regime, these lattice temperature rises can be minor, and less than a few hundred Kelvin. This greatly simplifies the thermo-optic analysis used in relating the electron and phonon temperature rises to the measured changes in probe reflectivity, in that in this limit of perturbatively-small temperature changes, a linear relationship can be assumed between the changes in reflectivity and change in temperature. This linear relationship will remain true for relating $dR(T_p)$ to the lattice temperature rises even during large electron temperature changes where $dR(T_e)$ is a more complex, nonlinear function of T_e [78].

Therefore, assuming the transient probe thermoreflectivity response is in the pure Drude, free-electron regime, the measured change in reflectivity is directly proportional to the temperature evolution of the phonon subsystem, given by

$$C_p \frac{\delta T_p}{\delta t} = \nabla(\kappa_p \nabla T_p) + G(T_e - T_p) \tag{3.23}$$

where C_p and κ_p are the heat capacity and lattice thermal conductivity of the lattice, respectively. For sufficiently thin films, the thermal conductivity term can be neglected, as the film is homogeneously heated at time-scales corresponding to electron-phonon coupling. Thus, in directly monitoring the temperature evolution of *only* the lattice, the exponential rise time in the modulated signal is equivalent to C_p/G.

We experimentally demonstrate this hypothesis at wavelengths far from the interband transition, even following ultrafast excitation, using probe wavelengths in the UV and NIR, corresponding to photon energies of 4.35 eV and 0.85 eV, respectively. At these wavelengths, the electronic temperature must be in excess of 5000 K to allow interband transitions to affect the optical response of the probe. As shown in Fig. 7.3a and Fig. 7.2 the transient response is vastly different from the typical response at visible wavelengths; there is no presence of a ‘hot-electron’ peak, followed by a decay over a few picoseconds. Rather, there is a clear exponential rise in the signal, qualitatively similar to the expected increase in lattice temperature following pulsed excitation. Indeed, using the same least-squares minimization routine as performed for probe wavelengths in the visible, we find a constant electron-phonon coupling factor for both UV and NIR probes, regardless of fluence. Additionally, the rise-time is in excellent agreement with our first principle calculations. This finding of a constant G is in contrast to a number of experimental works, including our own data at visible wavelengths. Nonetheless, the finding of constant electron-phonon coupling factor is in excellent agreement with computational and theoretical approaches for the electron temperatures observed in this work, as well as works that directly monitor the decay of the Fermi-Dirac distribution [1]. We attribute the discrepency between our data far from interband transitions and previous experimental works/our visible data to the assumed relations defining the thermo-optic coefficients at visible wavelengths. We compare our data to an array of literature values for the electron-phonon coupling factor of thin Au films and nanoparticles, and show excellent agreement with works that *directly* monitor the electron temperature evolution of Au [1]. Additionally, G measured via probe wavelengths far from the smeared Fermi-Dirac distribution is relatively constant, in agreement with both recent *ab initio* [111], one of which relies on the same computational metholodologies described within this work [109] and analytical calculations (Eq. 2); these data are summarized in Fig. 7.3b.

Conclusion

We demonstrate through a combination of pump-probe measurements with wavelengths spanning UV (285 nm) through the NIR (1500 nm) paired with *ab initio* calculations that the electron-phonon coupling factor of Au is constant up to electron temperatures of at least 2000 K. At wavelengths far from the interband transition of Au, the modulated probe

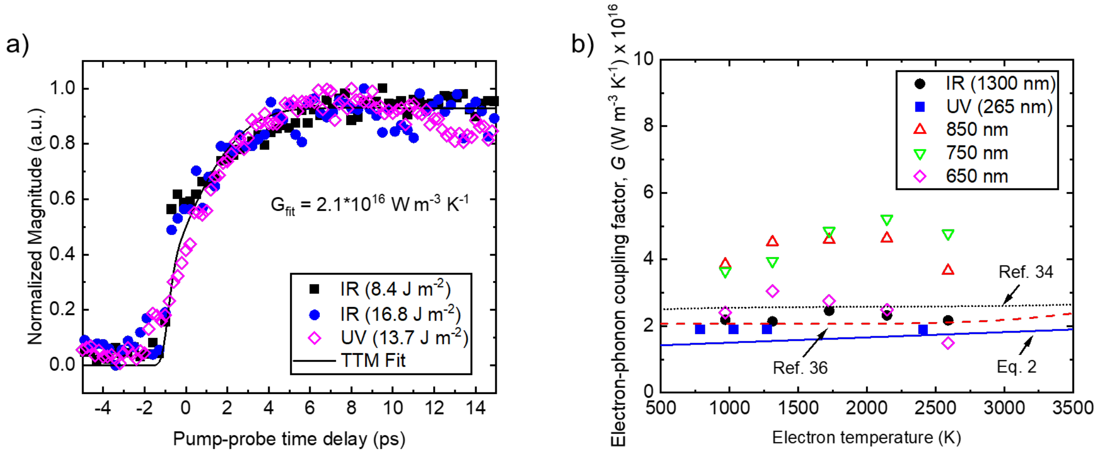

Figure 3.7: a) Experimental pump-probe data at a wavelength of 1300 nm for fluences corresponding to electron temperature rises of ∼1100 K (black squares) and ∼2200 K (blue circles and magenta diamonds). demonstrate the transient reflectivity is dominated by the lattice temperature of the Au, thus eliminating interband contributions. b) Measured electron-phonon coupling factor from this work's ultrafast pump-probe experiments (symbols), *ab initio* calculations (dashed red and dotted black lines), and calculated from Eq. 2 (solid blue line). At visible probe wavelengths, the measured G displays anomalous nonlinearities due to an incorrect application of the Drude model, whereas probe wavelengths that measure far from perturbations of the Fermi-Dirac distribution (e.g., probe via intraband excitations) is relatively constant as a function of electron temperature, up to electron temperatures of ∼2500 K. We find a constant electron-phonon coupling factor that is in excellent agreement with previous works that directly monitor the electron temperature distribution [1].

response is dominated by the lattice temperature and allows one to avoid convoluted optical models to interpret the transient response. Additionally, although the *static* optical response of Au can be described through the Drude model, Fermi-smearing invalidates the use of a perturbed Drude model to describe the modulated response for most visible wavelengths.

Chapter 4

Solid-Solid Interfaces

In this chapter, I will introduce two alternative approaches towards the analysis of thermal boundary conductance, namely the utilization of the laser ablation threshold and transmission of acoustic waves as metrics of relative changes in TBC. Additionally, through the implementation of a mid-infrared pump-probe method, I demonstrate a novel energy transduction mechanism that can arise at metal-semiconductor interfaces during cases of strong electron-phonon non-equilibrium. The work presented in this chapter has been published in peer-reviewed journals, namely *Physical Review B*[7], *Applied Physics Letters*[112], and *Nature Nanotechnology*[113].

4.1 Background

Thermal transport at solid-solid interfaces remains to be a highly-studied research topic due to the technological necessity for engineering specific interfacial resistances paired with the complex underlying physics driving thermal conductance at interfaces. The most widely used and most versatile method for measuring the TBC at solid-solid interfaces remains to be transient and frequency-domain thermoreflectance techniques (TDTR and FDTR, respectively). While TDTR lends itself toward the *measurement* of TBC and energy transfer across interfaces, it relies on a multi-layer solution to the heat equation for analysis of pump-probe data. While additional drawbacks to this method will be presented through this dissertation, one of the more obvious issues is the lack of physics elucidated upon simply from extraction of a TBC.

4.2 Role of Interfacial Thermal Resistances During Laser-Processing of Thin Films

4.2.1 Introduction

Ablation, from a thermodynamic standpoint, is the process of evaporative material removal when a critical temperature is reached. However, laser-induced ablation has become a general term referencing any laser-induced mass removal, with expected ejection mechanisms ranging from non-thermal, photomechanical spallation [3, 114, 115] to a thermally-driven vaporization process [116, 117]. This mixture of mechanisms and definitions has clouded the current understanding of the basic heat transport processes that drive material ablation [3, 115, 118], especially when considering thin films and nanocomposites. On the nanoscale, the high densities of inclusions, defects and interfaces can lead to thermal transport properties in materials that can be drastically varying from those intrinsic to their respective bulk phases [12, 119]. Thus, an understanding of the heat transport processes that drive material ablation in nanosystems is lacking; this lack of understanding is amplified by the aforementioned ambiguities in the role of diffusive thermal transport and thermal resistance in bulk materials during laser ablation.

Diffusive heat transport generally drives ablation processes in materials when the characteristic energy deposition time (i.e., pulse width, t_p) is much greater than the electron-phonon equilibration time (τ_{ep}) [3]. In this temporal regime, the electrons and lattice are in equilibrium during the majority of the laser pulse absorption; thus, the assumption of $T_e \sim T_i$ is valid, where T_e is the electron temperature and T_i is the ion temperature. In this “thermal ablation” regime [3], thermal expansion limits the ablation threshold, hence defining the condition that the absorbed laser energy must be fully converted into the energy of the broken bonds in some thickness defined by a thermal penetration depth of the pulse ($\delta_T = (\alpha t_p)^{1/2}$, where α is the thermal diffusivity). In this regime, the thermal ablation threshold, which determines the onset of the material removal process, follows the well known $\sqrt{t_p}$ pulse width dependence [114, 120], given by [3]

$$F_T \approx \frac{(\alpha t_p)^{1/2} \varepsilon_b n_a}{A}, \tag{4.1}$$

where ε_b is the atomic binding energy, n_a is the number density of atoms in the target, and A is the absorptivity of the material.

The threshold fluence given in Eq. 4.1 is derived by performing a basic energy balance with the absorbed laser pulse and the heat equation used to describe diffusive thermal transport in a homogeneous material [3]. This threshold applied to thin films and nanosystems is thus questionable, as previously mentioned, the heterogeneity induced from interfaces and inclusions can lead to thermal transport properties to be vastly different from that of the homogeneous bulk phase [12, 119]. For example, when film thickness approaches δ_T, interfaces and boundaries adjacent to these thin films can pose significant thermal resistance that impede heat flow out of locally heated volumes in thin films. Indeed, this finite thermal boundary conductance, h_K, can represent a limiting thermal resistance in a wide array of thin films and nanosystems [33, 35, 121, 122]. Furthermore, for thermal ablation conditions (i.e., when $t_p >> \tau_{ep}$, as previously mentioned), thermal diffusion could be dominated by the thermal boundary conductance as opposed to the thermal properties of the film or substrate. For example, characteristic time scales associated with the interfacial temperature drop [67] driven by h_K are estimated as $\tau_\mathrm{int} = Cd/h_\mathrm{K}$, where C and d are the heat capacity and film thickness of the thin film material [123]. For a homogeneously heated Au film where $d \approx 100$ nm (the ballistic penetration depth of electrons after laser irradiation in Au is $\sim$100 nm) [1], the time scale necessary for complete diffusion of energy across an Au film on a substrate is $\sim$5 ns, assuming h_K is $\sim$50 MW m^{-2} K^{-1} [124–126]. Thus in the regime where this timescale is two orders of magnitude greater than laser deposition time (e.g., when using picosecond pulses), the thermal energy deposited by the laser pulse would be initially confined in the volume of the film. As thermal ablation processes occur up to nanosecond times scales [127] and are greatly affected by the ablated material's temperature [118], energy diffusion, limited by the interfacial thermal resistance, would be expected to play a role in such processes in thin films.

To the best of our knowledge, this effect of thermal confinement during thermal ablation conditions has never been experimentally and systematically investigated, leaving a large void in the understanding of how Eq. 4.1 applies to thin film systems for predicting ablation thresholds. Qualitatively, in this temporal regime where the deposited laser energy is confined in the thin films due to a thermal boundary resistance at the film/substrate interface, it would be expected that lower applied fluences would be necessary for ablation to occur, as less energy from the absorbed laser pulse is necessary for equivalent power densities in a thin films compared to its bulk counterpart. Thus, in this regime with increasing interface conductances, thermal energy is better coupled to the substrate, and the ablation threshold should correspondingly increase.

An additional consideration in applying Eq. 4.1 to thin films lies in the binding energy terms, ε_b, as the interatomic cohesion forces of a pure material are not the only forces present in the thin film on substrate system. This is evident throughout literature [2, 128, 129] for laser ablation in liquids; the overlying liquid layer mechanically confines the system and becomes an additional force that the spalled material must overcome, thus leading to an increase in the relative ablation threshold for that material. In this context, for thin films, the binding energy term must also be related to the interfacial bonding environment between the film and the substrate as the film must overcome the work of adhesion at this interface. Note, this interfacial bond strength can be intimately related to the thermal boundary conductance across solid/solid interfaces [121, 130–135].

This work seeks to elucidate the role of diffusive thermal transport mechanisms during short-pulse laser ablation of thin films. When the film thickness approaches the length and time scales associated with energy diffusion, thermal boundary resistances are expected to

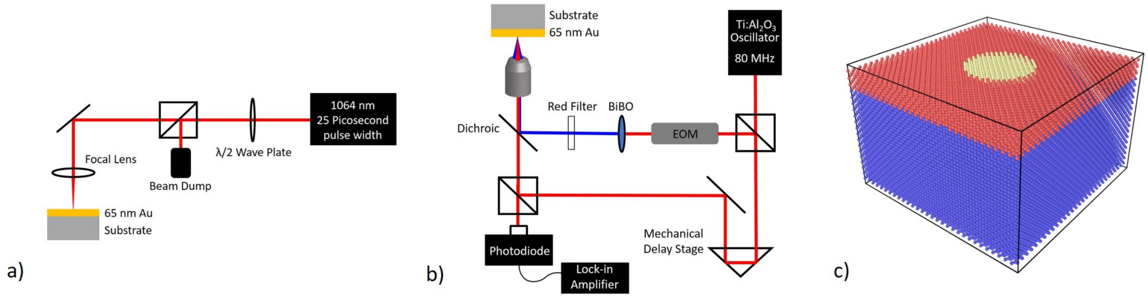

Figure 4.1: a) A schematic of the experimental set-up for the ablation threshold experiments. The Au/substrate sample is placed in a liquid cell for threshold measurements in water. b) A schematic of the experimental set-up for our TDTR measurements. c) A schematic of the computational domain representing a thin film (red and yellow atoms) on a substrate (blue atoms) described by the Lennard-Jones potential.

influence the ablation threshold of a material. In this work, we experimentally demonstrate the failure of Eq. 4.1 for predicting the ablation threshold for thin films. By obtaining the ablation threshold of gold thin films deposited on various substrates with varying thermal boundary conductances across the Au/substrate interfaces, we find that the thermal confinement within the film controls both the damage threshold and the heat-affected zone.

4.2.2 Methods

Sample Fabrication

We conducted the thermal ablation threshold and thermal boundary conductance measurements on 65 nm Au films on different substrates with varying interfacial resistances. The Au films were electron-beam deposited on fused silica (SiO_2), silicon, nickel, titanium, sapphire (Al_2O_3, and copper substrates; all substrates were purchased from MTI corporation. Prior to deposition, the substrates are rinsed with acetone, ethanol, and methanol then subsequently dried with nitrogen gas. Note, no efforts to remove native oxides on certain substrates were undertaken.

Picosecond Laser Ablation

The single-pulse ablation threshold experiments utilized a 25 picosecond Nd:YAG laser operating at its fundamental wavelength of 1064 nm as shown in Fig. 4.1a. The beam size is experimentally determined with the knife-edge method for both air and liquid environments. We also use the beam waist, ω_0, as a fitting parameter during threshold measurements for confirmation of the spot size at the target surface; the two methods are in good agreement for bulk targets. In the case of our thin films, as discussed in detail later, we find that the best-fit value for the beam-waist increases with increasing thermal boundary conductance. This phenomenon is attributed to in-plane thermal diffusion during the ablation process. The thermal ablation threshold for these 25 picosecond pulses is determined in each Au/substrate system by measuring the induced damage area as a function of incident laser fluence. The results are then fit to [4]

$$D^2 = 2\omega_0^2 ln(\frac{F}{F_{\mathrm{th}}}) \tag{4.2}$$

where both ω_0, the beam waist, and F_{th}, the ablation threshold are used as free parameters to the best-fit, while D is the diameter of the ablation area and F is the applied fluence and are experimentally measured. The ablation measurements were performed in both air and water environments; in the liquid environment, the target was submerged in 15 mm of pure DDI water utilizing a flow cell, as described in [2, 136], to avoid scattering with pre-existing nanoparticles. The subsequent damage area was measured using dark-field optical microscopy which matches the damage areas measured via scanning electron microscopy. This method of measuring damage areas has been shown to provide similar and accurate results to other methods of determining damage and ablation thresholds [137]. It should be noted that our ablation 'crater' depth is limited to the thickness of our films and there is no visible damage to the substrates in values used for the threshold measurements; we emphasize the lack of *visible* damage to the substrate in our measurements, as there may be underlying microstructure alteration and formation of defects not observable in our microscopy characterization. Further, we find redeposition of ablated material on the substrate surface, indicative of droplet formation. This finding implies that at least one mechanism leading to thermal ablation in this work is phase explosion; the possibility of this phase-transformation occurring simultaneous to other ejection processes is discussed later.

Time-Domain Thermoreflectance

For measurement of the interfacial thermal resistance, we utilize a two-color TDTR scheme, as described in more detail elsewhere [93, 138, 139] and graphically depicted in Fig. 4.1b.Our TDTR system is centered around a Spectra Physics Tsunami Ti:Sapphire oscillator, emanating $\sim$90 fs, 800 nm (center wavelength with 10.5 nm bandwidth) pulses at an 80 MHz repetition rate. The output of the oscillator is split into pump and probe paths. The pump, after passing through an electro-optical modulator and a second-harmonic generation crystal, is converted to a modulated pulse train of 400 nm pulses; in this work, we modulate the pump train at 8.8 MHz. The probe pulses are mechanically delayed to known time intervals relative to the pump pulse. We monitor the in-phase and out-of-phase voltages from the reflected probe pulses at the frequency of the pump modulation frequency with a lock-in-amplifier. These lock-in signals are related to the surface temperature of the Au film, and are related to the thermal properties of the samples, including the Au/substrate thermal boundary conductance [77, 123, 140, 141]. The in-phase data is fit to a thermal model where the thermal boundary conductance is our free parameter [14, 93, 142]; the thermal conductivity of the film and substrate are obtained from literature values [143–145] and the film thicknesses are determined from profilometry measurements. The measured thermal boundary conductance and associated error is obtained from measuring five spots on the film.

Molecular Dynamics Simulations

To explore the nanoscopic mechanisms responsible for dictating thin film damage, we perform molecular dynamics (MD) simulations on representative thin films with varying boundary conditions with the region defined by substrate atoms. For our MD simulations, we employ the widely used 6-12 Lennard Jones (LJ) potential, $U(r) = 4\varepsilon[(\sigma/r)^{12} - (\sigma/r)^{6}]$, where U is the interatomic potential, r is the interatomic separation, and σ and ε are the LJ length and energy parameters, respectively. The cutoff distance is set to 2.5σ (for computational efficiency) with the time step for all simulations set to 0.1 fs. As we are interested in understanding the effects of TBC on the damage area in thin films in general, the use of LJ potential is sufficient to provide qualitative insight. For the thin films, the length and energy parameters are modeled for argon with σ_s=3.405 $\AA$ and ε_s=10.3 meV and the atoms are placed in an fcc structure with a lattice constant of a_0=1.56σ. The substrate atoms are also placed in an fcc lattice with the same lattice constant, and the energy and length parameters are set to σ_s=3.405 $\AA$ and ε_s=10.3 meV, respectively. To mimic a weakly bonded interface, the film-substrate energy parameter is set to ε_{f-s}=2.6 meV, whereas, for the strongly bonded interface, ε_{f-s}=10.3 meV. The sizes of the computational domains are $30a_0 \times 30a_0 \times 20a_0$ with periodic boundary conditions applied in all directions. The mass for all atoms is set to 40 g mol^{-1}.

Initially the computational domains are equilibrated under the Nose-Hoover thermostat [146], and the number of atoms, volume and temperature of the simulation are held constant followed by the NPT integration, which is the isothermal-isobaric ensemble with the number of particles, pressure and temperature of the system held constant for a total of 1.5 ns at 0 bar pressure and 70 K temperature. To melt a region of the thin film, we heat the atoms contained in a cylindrical area in the center of the thin film at a temperature of 300 K (under the NVT ensemble, with the number of particles, volume and temperature held constant) for a total of 1 ns after equilibration, while the NVT integration at a temperature of 70 K is simultaneously applied to the rest of the computational domain; note, the melting temperature of LJ argon is 87 K [147]. A schematic of the computational domain is shown in Fig. 4.1c, where the red atoms represent the thin film, the yellow atoms represent the melted region in the thin film and the blue atoms represent the substrate.

After we melt the cylindrical region in the thin film, the atoms in the thin film region are allowed to equilibrate under the NVE integration, which is the microcanonical ensemble with the number of atoms, volume and the energy held constant, while the substrate atoms are simulated under the NVT integration. We monitor the melted regions of the computational domains with the varying boundary conditions between the film and the substrate atoms to shine more light on the influence of the different mechanisms that dictate diffusive damage of thin films. The results of these simulations are discussed in detail in the following section.

4.2.3 Results and Discussion

Figure 4.2.3a shows the measured thermal ablation threshold values for the various Au films as a function of substrate thermal conductivity. The lack of substrate dependence suggests that the thermal properties of the substrate are not primary factors dictating the different ablation thresholds in the thin Au films; note, we find a similar lack-of-trend is found in the thermal ablation threshold as a function of substrate effusivity. Furthermore, even if a general monotonic decrease trend could be gleaned from Fig. 4.2.3a, these data would suggest that the faster in which heat is being transferred away from the heat-affected zone and into the bulk of the substrate heat sink, the lower the ablation threshold, which is counterintuitive from a simple energy balance argument. This suggests another energy diffusion mechanism must be limiting the ablation threshold in these films on substrate systems.

As we discussed previously, due to the typical times scales of thermal diffusion, we hypothesize that the thermal boundary conductance, h_{K}, at the Au/substrate interface imposes the limiting resistance that will dictate thermal ablation of the Au films under these conditions. We plot the thermal ablation threshold in ambient conditions as a function of measured h_{K} for the various Au/substrate interfaces in Fig. 4.2.3b. We find that the ablation

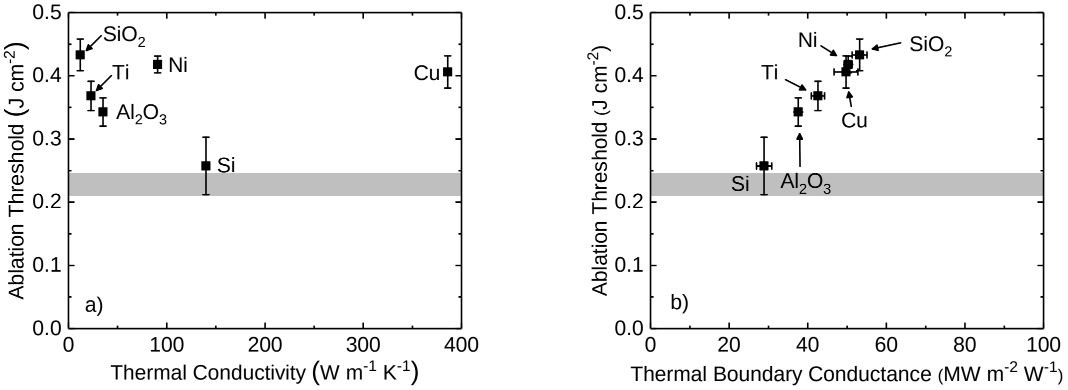

Figure 4.2: a) Measured ablation thresholds of Au films as a function of the associated substrate's thermal conductivity. b) The thermal ablation thresholds as a function of the measured thermal boundary conductance between Au films and the labeled substrates. The gray bar represents range of previously reported values for the 'bulk' ablation threshold of Au in air [2, 3].

threshold of these systems scales linearly with their respective thermal boundary conductances as shown in Fig. 4.2.3b, supporting our hypothesis that h_K at the film/substrate interface can influence the thermal ablation threshold more directly than the substrate thermal properties. The measured thermal boundary conductances agree well with previously reported values for various Au/substrate interfaces [124–126, 133, 139]. The thermal boundary conductance is a diffusive thermal resistance that is well known to impact the overall heat transport in thin films and nanosystems. Thus, our data suggest that thermal ablation thresholds in this picosecond regime are related to the heat transport mechanisms that underpin the diffusive thermal resistance at the film/substrate interface.

In the "bulk" limit of ablation thresholds, previous experimental [2] and computational [3] works have determined threshold values for bulk Au targets through numerous methods, with reasonable agreement at 0.210 J cm^{-2} and 0.245 J cm^{-2}, respectively, in ambient conditions; the experimental value was reported as slightly lower than theory due to a roughened surface, leading to an enhancement in photon absorption [2, 148]. Under these circumstances, Eq. 4.1 is valid as only the properties of a pure substance must be considered (in particular, a constant thermal diffusivity and cohesion energy can be assumed). Thus, in the limit where interfacial resistances are large and thus confine thermal energy to the volume of the thin film, the ablation threshold approaches the previously measured bulk damage threshold.

The primary mechanisms driving laser ablation of thin films is typically discussed in terms of delamination and ejection of condensed material due to thermo-mechanical effects at the interface [149, 150]. Though, even in the case of laser-induced forward transfer (LIFT), previous experimental works using picosecond pulses have shown the process to follow melting dynamics in fashion similar to that of nanosecond melting of thin films [151]. Furthermore, as shown by numerous computational works, at higher fluences, phase explosion (or an analogous phase-transformation such as explosive boiling, whereby the material is transformed into a metastable liquid state) occurs and is the primary mechanism for material ejection [129, 152, 153]; a mechanism occurring independent of the ablated material's thickness. As our threshold measurements are derived from a fit to Liu's equation over a large span of applied fluences, it is likely that a complex mix of these dynamics occurs within the heated volume simultaneously, potentially dependent on fluence. This is further supported by two observations of the damaged region: Redeposition of ablated material and delamination of the surrounding film. Droplet formation during ablation, a consequence of explosive boiling or phase explosion, is known to lead to redeposition of such droplets on the target surface, which we observe in our microscopy images. Furthermore, we find delamination outside the area in which material is ejected, indicating that a thermomechanical mechanism occurs simultaneous to phase explosion. Nonetheless, regardless of mechanism, as Eq. 4.1 is derived from a basic energy balance, the binding term, ε_b, references the energy necessary to overcome some adhesive force. Typically, this term implicitly references the binding energy between two atoms within a material (i.e., atomic disintegration). In a thin film system, the interfacial atoms have some adhesive force between the film and substrate, which can be overcome. During a gas-phase transformation, these interfacial atoms would play less of a role, making the binding energy a more negligible term, as the disintegration energy in the bulk of the film would be the dominant adhesive force to be overcome for the material's ablation threshold. This does not imply the interface is to be neglected; should heat be efficiently dissipated into the substrate, the Au film could rapidly drop below the temperature necessary for the phase-transformation, and remain adhered in condensed phase. On the contrary, should mechanical spallation be the primary ejection mechanism, one would expect the interfacial adhesion to be the dominating term, as it is the weakest energy to overcome, and the bulk of the film would spall once reached. As discussed later, the measured value of thermal boundary conductance is known to be related to both phonon mismatch at the interface as well as interfacial bonding. Thus, the TBC reflects both dissipation rate and adhesion of the film.

To study this hypothesis in more detail, we repeat the ablation threshold experiments on the same Au/substrate systems while submerged in 15 mm of DI water, as depicted by the open circles in Fig. 4.2.3. The thermal ablation thresholds are higher for the Au films when submerged in liquid as compared to the air experiments, but only for the Au/substrate systems with the highest h_K's; in other words, as the thermal boundary conductance is lowered (resistance is increased), the presence of the liquid on the Au has a reduced effect. In the limit of Au/Si (lowest h_K), the liquid layer does not affect the ablation threshold. This further supports our discussion regarding diffusive heat transport across the nanoscale interfaces as the underlying mechanisms affecting thermal ablation. The addition of the liquid layer, and resulting Au/water interface conductance, creates an additional parallel path for thermal transport out of the Au film. In Fig. 4.2.3, an additional thermal boundary conductance of 50 ± 30 MW m^{-2} K^{-1} is assumed for the Au/liquid interface [142, 154, 155]. As can be seen, the lower values for h_K (higher resistances at the Au/substrate interface), such as Au/Si, the additional thermal pathway is not large enough to drastically affect this threshold, and it does not deviate far from the theoretical minimum value found in previous literature [2]. Though the nominal value of ablation threshold for Au on Si substrates appears independent of environment, the large error associated with both the measured threshold and previous measurements of thermal boundary conductance at a solid/water interface leaves the possibility of it being within the linear range found in the solid/solid

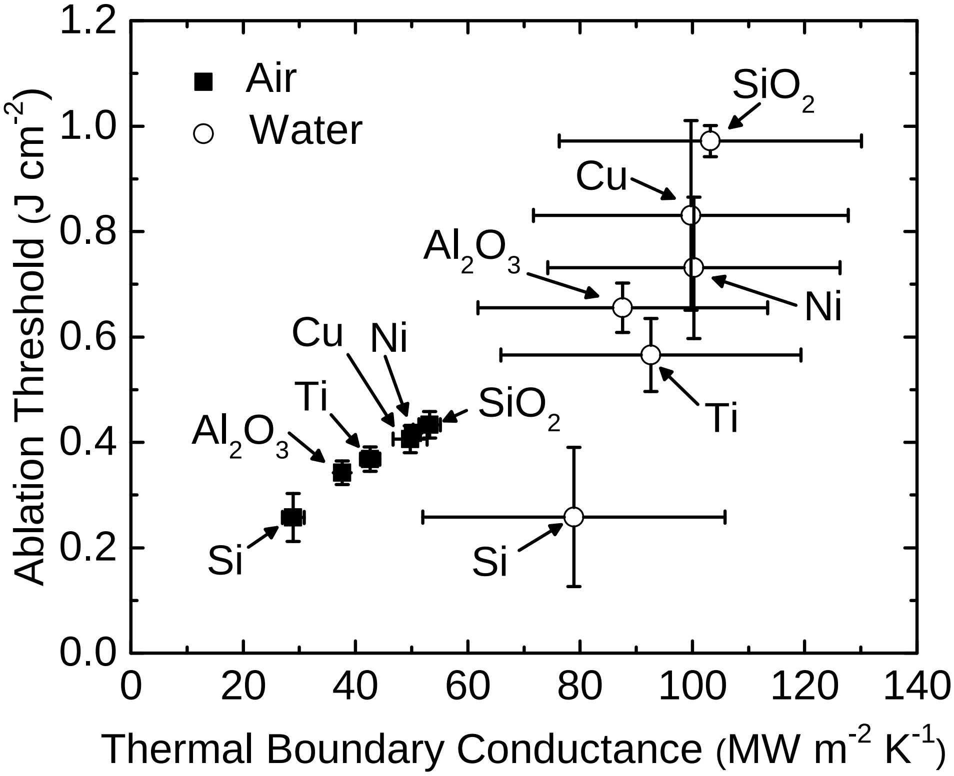

Figure 4.3: Ablation thresholds against the thermal boundary conductance in air (black squares) and liquid (open circles) environments, where the Au/liquid interface is assumed to have a thermal boundary conductance of 50 ± 30 MW m^{-2} K^{-1}; as the liquid provides a parallel path for thermal transport, the Au/water interfacial conductance can be summed with the measured Au/substrate interface.

interfacial conductances. Additionally, although they can not be accounted for in error bars, phenomena leading to damage outside of thermal effects should be considered during ablation in a liquid environment. For example, cavitation and plasma confinement are hypothesized to lead to secondary erosion effects during laser ablation in liquids [2].

Furthermore, given the relatively modest increase in pressure with the addition of water on the Au surface (∼150 Pa), we do not believe this change in thermal ablation threshold upon liquid submersion is due to an increase in mechanical confinement from the additional pressure. While an increase in ablation threshold has been observed during laser ablation in liquids [2, 152] due to mechanical confinement of the spalled material, previous work by Losego *et al.* [133] has shown that pressures on the order of MPa are necessary for spallation to occur for 80 nm Au films. This suggests orders of magnitude more pressure from the liquid addition would be necessary to impact the thermal ablation threshold if the liquid was mechanically confining the thermally excited Au.

As an additional experiment to support our assertion that the thermal boundary conductance at the Au/substrate interface is the limiting factor impacting thermal ablation thresholds, we considered the measured damage area of the Au films on the different substrates, as shown in Fig. 4.2.3. The damage area trends inversely to thermal boundary conductance (i.e., higher damage areas for the Au/substrate samples with lower h_K at a set fluence). In the time scale of the diffusive damage (i.e., nanoseconds [156]), competing thermal diffusion processes are occurring, namely, diffusion across the Au/substrate interface and in-plane thermal diffusion in the Au film. A reduction in thermal boundary conductance promotes increased in-plane diffusion of the deposited energy, which leads to an increase in damaged area. This hypothesis is further supported by the increasing best-fit value of the beam waist, ω_0, with increasing thermal boundary conductance as shown in Fig. 4.2.3. As Eq. 4.2 is derived for one-dimensional transport, a fitted value larger than the experimental beam-waist would be expected should lateral transport begin to play a substantial role in the ablation process. In the original derivation of Eq. 4.2, Liu found sound agreement between the measured area of a laser-induced amorphous region and the incident laser-energy profile, indicating negligible lateral thermal transport during picosecond-laser-induced phase transformations [4]. As we find the beam waist in his interpolation model to deviate from the experimentally-measured beam waist, which is held constant during the ablation experiments, this further supports our posit regarding a thermal boundary conductance-limiting thermal ablation threshold in these films. For example, at a set fluence, one would expect that a larger beam waist results in a lower *effective* fluence, thus decreasing the damage area at a constant incident power; this is equivalent to a constant beam waist with power dissipated from the thin film to a supporting substrate due to enhanced cross-plane thermal transport.

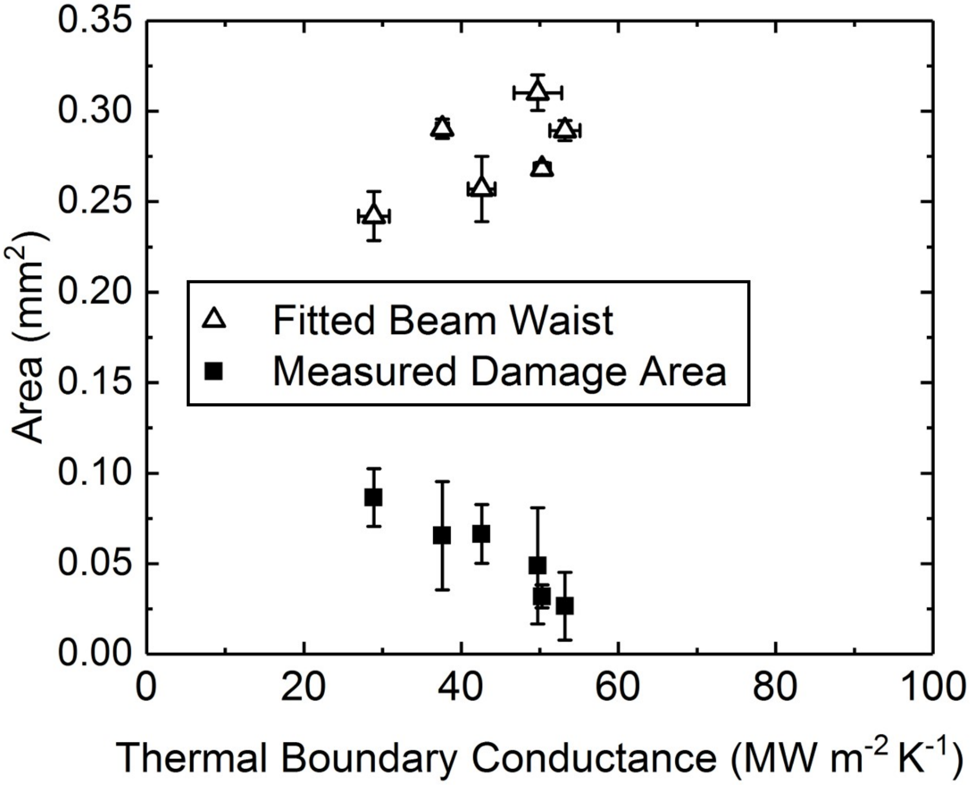

Figure 4.4: Observed damage areas of each Au/substrate system at a fluence of ∼0.94 J cm^{-2} and the beam-waist value obtained from fitting to Eq. 2. With increasing thermal resistance at the interface, there is an increase in in-plane thermal diffusion, leading to larger damage areas and deviation of Liu's interpolation model [4].

Given this, it is evident that Eq. 4.1 cannot accurately be applied to nanosystems and thin films without modification of various terms; the threshold is very clearly dependent on the thermal boundary conductance present at the film interface. Thus, we turn our discussion now to the underlying nanoscale heat transport mechanisms that are impacting thermal ablation of thin films, which will lead to the necessary understanding required for future studies to derive thin film equivalents of Eq. 4.1. Thermal transport across a thin film and its underlying substrate, and hence the measured h_{K}, can be influenced by numerous factors, which has been reviewed in detail in previous works [33, 121]. Most notably in relation to our thermal ablation data, we focus on the following three factors that can drive changes in thermal boundary conductance: i) lattice temperature, ii) phonon spectrum mismatch and iii) interfacial bonding.

i) Temperature: Assuming elastic phonon scattering at the Au/substrate interface [157–161], the phonon thermal boundary conductance from the Au film to the substrate will follow temperature trends similar to that of the lattice heat capacity of Au. In other words, the thermal boundary conductance will be relatively constant above the Debye temperature of Au ($\sim$165 K). Due to the relatively weak mechanical bond at the Au/substrate interface (especially given the fact that we make no effort to remove native oxides on some of the substrates) [125, 133, 139], we do not expect inelastic processes to dominate the measured h_{K} across these interfaces [132, 162]. Furthermore, on these thermal ablation time scales, we do not expect hot electron-interface or substrate coupling to play a role, as the time scale for this excited electron-phonon processes has been shown to only influence heat transport within a few picoseconds after laser heating [95, 96, 139, 163]. Along these lines, previous works have shown that after electron-phonon equilibration following pulse excitation, which takes place within a few picoseconds in Au, the thermal boundary conductance is dominated solely by phonon interaction between the film and substrate [139, 161, 164]. Thus, even though these thermal boundary conductance measurements have not been extended to the high-temperature regime representative of when thermal ablation occurs, it is unlikely the trend in h_{K} vs. substrate would shift. Therefore, we surmise that the trends

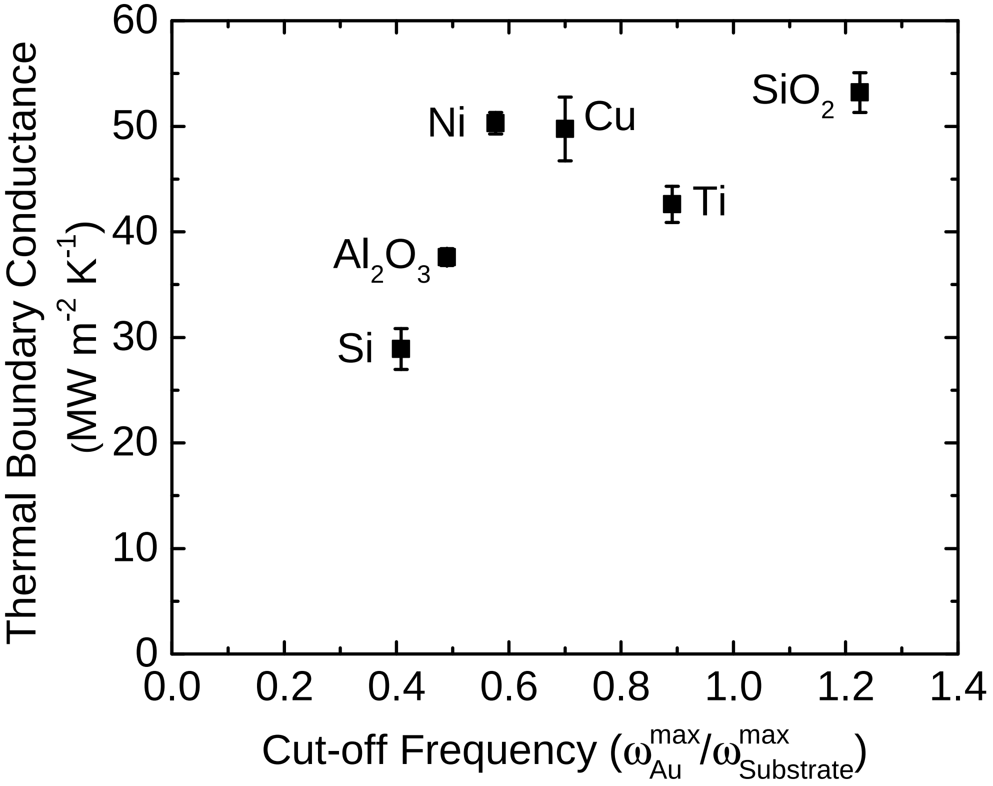

Figure 4.5: Thermal boundary conductance plotted as a function of the Au/substrate cutoff frequency ratios determined by phonon dispersion plots obtained in literature.

in h_K shown in Fig. 4.2.3 to be representative of the phonon resistance mechanisms influencing thermal ablation. To understand the underlying phonon coupling that influences our measured thermal ablation thresholds, we now focus our discussion on the role of phonon spectrum mismatch and interfacial bonding effects.

ii) Phonon spectrum mismatch: To a decent first approximation, the phonon energy transmission across solid interfaces can be related to the spectral overlap of the phonon densities of states between the film and substrate [35, 124, 165]. This could indeed be the limiting factor in our thermal ablation measurements, which is apparent in the trends in Fig. 4.2.3, which plots the thermal boundary conductance across the various Au/substrate interfaces vs. ratio of phonon cutoff frequencies between Au and the substrate ($\omega_\mathrm{Au}^\mathrm{max}/\omega_\mathrm{Substrate}^\mathrm{max}$). In general, h_K scales as the phonon spectra between the Au and substrate become better

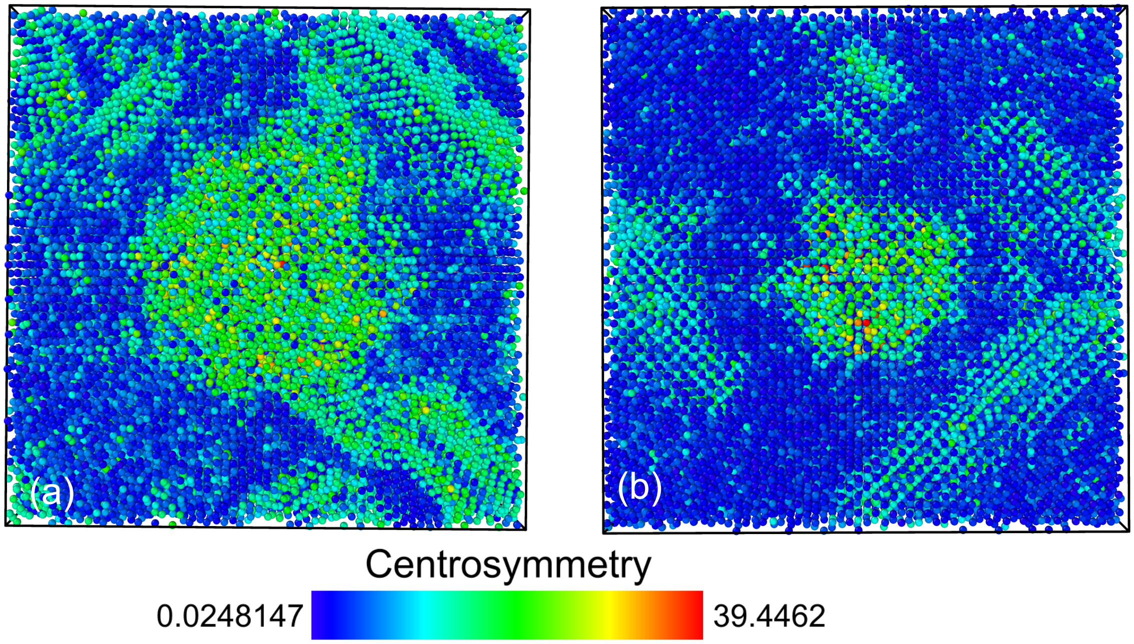

Figure 4.6: Top view of the computational domains with atoms colored according to their centrosymmetry parameter for the (a) weakly bonded and (b) strongly bonded interfaces.

overlapped, which his consistent with several prior works [166, 167]. However, as we discuss below with regards to the mechanical coupling at the Au/substrate interface, we can not rule out changes in the bonding environment.

iii) Interfacial bonding: The influence of interfacial bonding on thermal boundary conductance has been well studied [33, 121, 130, 134, 168–171], and previous works have reported on bonding effects at Au/substrate interfaces [125, 126, 133]. In general, the thermal boundary conductance across interfaces can be influenced by both the phonon spectrum overlap (discussed above) and the interfacial bonding. Most notably, Losego et al. [133] demonstrated a direct relationship between the thermal boundary conductances across Au/self assembled monolayer/quartz interfaces and interfacial pressure determined via laser spallation experiments. This would suggest that the thermal ablation threshold in our measurements are a measure of interfacial bonding, which directly impacts the measured thermal boundary conductance.

Clearly, based on our discussion of ii and iii above, we can not distinguish between the roles of interfacial bonding and phonon spectrum overlap on the origin of the substrate dependence of thermal ablation thresholds in the thin Au films. Thus, to gain more insight into the nanoscopic mechanisms driving thermal ablation in these thin films, we conduct molecule dynamics simulations. The parameters of these simulations are discussed in detail in Section II.D. These simulations are utilized as toy models to explore the individual roles of the previously mentioned factors involved in the role of interfacial thermal transport on diffusive damage of thin films. To visualize the defected region in the computational domain after melting the region in the thin film and allowing the structure to evolve under the various ensembles, we make use of the centrosymmetry parameter, which is a measure of the local lattice disorder around an atom [172]. For an atom on an fcc lattice site, surrounded by the 12 nearest neighbor atoms on a perfect lattice, the centro-symmtry parameter will be zero, while for defects and dislocations, the centro-symmetry parameter will be high. We color the atoms based on this criteria (where the most blue atoms are described by a centro-symmetry parameter that is for a perfect lattice position and the red atoms represent a highly defected atom). Figure 4.2.3 shows the top surface of the thin film for a weakly bonded (Fig. 4.2.3a) and the strongly bonded (Fig. 4.2.3b) interfaces at 150 ps after melting. As is clear, for the weakly bonded case, the defected region is larger compared to the strongly bonded case, which is qualitatively in line with our experimental results on the measured damage area of Au films on different substrates. This suggests that the interfacial bonding (and therefore, the h_{K}) can influence the damaged area in thin films.

To understand the relative effect of increasing h_{K} on the defected area, while the interfacial bonding is set to that of the strongly bonded case, we increase the mass of the substrate atoms to 280 g mol^{-1}. This effectively shifts the spectrum of the phonon density of states (DOS) of the substrate atoms to lower frequencies and increases the overlap between the DOS of the thin film (as shown in Fig. 4.2.3a). Note, increasing the mass of the atoms from 40 g mol^{-1} to 280 g mol^{-1} reduces the thermal conductivity. However, the better spectral overlap between the thin film and the substrate region for the case where the substrate atoms have a prescribed mass of 280 g mol^{-1} ensures that h_{K} is increased [132]. Figure 4.2.3b shows the top view of the computational domain with the atoms colored according

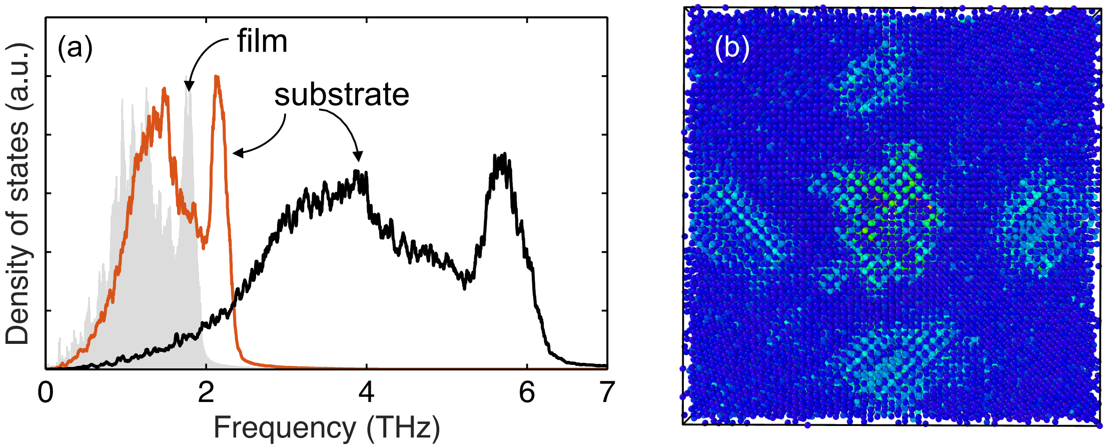

Figure 4.7: (a) Phonon density of states for atoms representing the thin film system and the atoms representing the substrates with 40 (black) and 280 (red) g mol^{-1}. (b) Top view of the computational domains with atoms colored according to their centrosymmetry parameter for the case where the substrate atoms have a prescribed mass of 280 g mol^{-1}. The better spectral overlap between the thin film region and the substrate atoms with a mass of 280 g mol^{-1} ensures that h_K is higher compared to the case where the substrate atoms have a lower mass.

to their centrosymmetry parameter. The defected area for the computational domain with the better spectral overlap is greatly reduced compared to the case with the lower h_K in Fig. 4.2.3a and Fig. 4.2.3b.

4.2.4 Conclusion

In conclusion, the thermal ablation threshold in metal thin films is found to be dependent on the interfacial thermal resistance of the system. While our results suggest thermal confinement in the thin film is the primary ablation mechanism for picosecond laser pulses of thin films, it is likely that changes in interfacial bonding are also playing a role in the obtained threshold values. For weakly bonded systems in our simulations, the defected area surrounding the melted region is larger compared to that of a strongly bonded system, which is qualitatively in line with our experimental results on the measured damage area of Au films on different substrates. This suggests that the interfacial bonding (and therefore the h_K) can influence the damaged area in thin films. Furthermore, when the interfacial bond strength is set to that of the strongly bonded case, we increased h_{K} by shifting the phonon density of states (DOS) of the substrate to better overlap the DOS of the thin films. The defected area for the computational domain with better spectral overlap (and therefore larger h_{K}) is greatly reduced compared to the case with the lower h_{K}. While this model finds excellent agreement with our experimental results, where lower thermal boundary conductances ultimately lead to increased defected regions, ii and iii above can not be separated; both interfacial bonding and spectral overlap lead to similar results while the opposite term is held constant. Additionally, although typically applied for in-situ measurement of beam-waist where systems are dominated by 1-D transport, we find variation in the waist-parameter in Eq. 4.2 of Liu's model to provide a relative measure of transverse thermal transport for thin-film systems.

4.3 Thermal Conductance and Picosecond Acoustics in Plasma-Processed Layers

4.3.1 Introduction

The predominant failure mechanisms in thin film optical devices/materials arises from thermomechanical effects within the lens, mirror, etc[173, 174]. For example, a typical mirror is comprised of a thin aluminum film on a given substrate; upon reflection of light, a portion of the photon energy is absorbed by the metal film, which creates a temperature rise on the surface[175]. To avoid the aforementioned thermomechanical failure, it is common to utilize a high thermal conductivity substrate to dissipate heat from the film surface into the bulk of the substrate[176], and thus avoid damaging effects. While this works in certain regimes, a large number of works have shown that the damage threshold from high-power laser interactions[177], flip-chip photodiodes[178], and other electronic devices does not necessarily scale with the thermal conductivity of the underlying substrate. Rather, the thermal resistance of the interface[33, 35] between the thin film and its supporting substrate becomes a limiting factor and defines the threshold of which these devices or material systems undergo thermal failure.

Aluminum is a good choice of material for UV optics due to its excellent reflectivity to wavelengths as short as 90nm. Unfortunately, the native oxide layer that readily forms on aluminum severely degrades the performance of aluminum reflectors. A promising solution is the use of fluorine-containing layers that protect the aluminum from oxidation and provide high transmission[179–181]. Further, aluminum fluoride layers are useful as barrier coatings in advanced Li-ion battery architectures, where localization of large temperature rises and thermal runaway are predominant failure mechanisms[182]. To-date, the thermal properties of aluminum fluoride thin films have yet to be reported, leaving the potential for unknown thermal degradation of these materials. In this work, we measure the thermal properties of thin aluminum oxyfluoride (AlO_xF_y) layers on the surface of aluminum films on glass substrates using time-domain thermoreflectance (TDTR); this optical pump-probe technique measures both the thermal resistance of the AlO_xF_y layer, as well as the thermal boundary conductance (TBC) associated with the interface composing the AlO_xF_y and its underlying aluminum substrate[14, 183]. Furthermore, this method allows for measurement of picosecond ultrasonics, providing additional insight to the mechanical and adhesive properties of the AlO_xF_y film[133, 184, 185].

4.3.2 Methods

AlOxFy layers were prepared by plasma treatment of bare Al coatings on glass in the U. S. Naval Research Laboratory's (NRL) Large Area Plasma Processing System (LAPPS)[186, 187]. The system makes use of linear hollow cathode electron sources to generate sheet-like electron beams with typical current densities of 1-5 mA cm^{-2}, and beam energies between 1-5 keV. Co-axial magnetic fields of 100-300 Gauss are used to collimate the electron beam and thus improve uniformity along its length[188]. These parameters are sufficient to produce uniform plasma sheets compatible with typical wafer-scale systems (diameter $>$ 300 mm). LAPPS is able to generate uniform, very low electron temperature, T_e, ($<$ 1 eV), plasmas with densities in the range of 1010-1012 cm^{-3}, thus providing the ability to deliver a well-controlled flux of ions characterized by very low energies (< 5 eV) to material surfaces located adjacent to plasma sheet[189]. The low ion energies serve to preserve surface morphology and practically eliminate ion-induced damage during processing. For this work, LAPPS was combined with an auxiliary discharge, which serves to dissociate the working gas as it enters the reactor and provides additional control over the ratio of ions to reactive neutrals incident on the surface[190].

Gas mixtures of argon (Ar), sulfur-hexafluoride (SF_6), and ammonia (NH_3) were used to treat aluminum thin films deposited on glass. This gas mixture was passed through an inductively couple plasma (ICP) discharge source operating at 350 W, which significantly increases the relative concentration of F radicals in the reactor[190] compared to the use of the electron beam alone[191, 192]. This mixture was chosen to provide both a large flux of F atoms and HF radicals to the surface. The latter is likely formed through hydrogen abstraction from the NH_3 molecule by F atoms. Evidence for the production of gas-phase HF, known to be highly effective at removing oxygen from surfaces and fluorinating Al_2O_3[193, 194], is shown in Fig. 4.3.2.

The material systems studied in this work is 80 nm thick aluminum electron-beam evaporated on quartz substrates at a chamber pressure of 10^{-6} Torr; the quartz substrate is alcohol cleaned followed by an O_2 plasma treatment prior to deposition. The native oxide layer developed on the surface due to exposure to the ambient prior to plasma treatment. Pre and Post-treatment X-Ray Photo-electron Spectroscopy (XPS) measurements, shown in Table 1, indicate a plasma exposure of 240 sec. transforms the native oxide layer (Al_2O_3) into a Fluorine-rich (AlO_xF_y) layer at the surface. From analysis of the high-resolution spectra (not shown), we estimate the AlO_xF_y layer to be less than 5 nm in thickness. That is to say, the plasma treatment involves the conversion of the native oxide layer, Al_2O_3, into an AlO_xF_y layer of comparable thickness. As was the case for a variety of material systems in previous works[195, 196], F concentration scales with dose and so, it is reasonable to expect that F concentration increases with plasma exposure times.

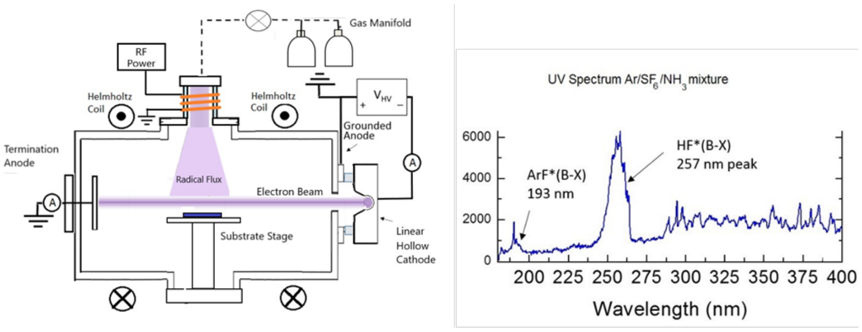

Figure 4.8: (left) Schematic of LAPPS configuration with auxiliary inductively coupled plasma radical source. (right) UV spectrum of Ar/SF_6/NH_3 plasma showing the presence of excited HF molecules.

To enhance the sensitivity in our thermal model used in TDTR, we electron-beam evaporate an additional 80 $+/-$ 4 nm Al film on to the AlO_xF_y layer. This additional film thus acts as our optical transducer during the thermal measurements and provides symmetry about the AlO_xF_y layer, as equivalent TBCs on both Al/AlO_xF_y interfaces can be assumed. To assure sample-to-sample consistency, both the initial Al film and final Al transducer for all samples are created in a single deposition. The remaining $\sim 5\%$ deviation in film thickness across the sample surface is the primary source of uncertainty in our TDTR measurements and obtained values of thermal conductance through the oxyfluoride layer and its respective interfaces.

4.3.3 Results and Discussion

As shown in Fig. 4.3.3, we find over a two-fold decrease in the measured thermal conductance after 240 seconds of plasma treatment; this thermal conductance is comprised of the thermal resistance of the interface layer itself (Al_2O_3 or AlO_xF_y) as well as the TBC between the top and underlying Al films. In other words, assuming no change in the thermal conductivity of the passivation layer relative to the native oxide, the thermal conductance of an Al/Al_2O_3 interface is found to be approximately two times greater than the thermal conductance across an Al/AlO_xF_y interface; more on this TBC reduction is discussed below. More rigorously for this experimental geometry, the measured thermal conductance, G, can be represented as a series thermal resistance, given by,

$$G_{measured} = (\frac{2}{TBC} + \frac{d}{\kappa})^{-1} \tag{4.3}$$

where TBC is simply the thermal boundary conductance between the Al films and the AlO_xF_y layer, while κ and $d$are the thermal conductivity and thickness of the AlO_xF_y layer, respectively. Note, the factor of two arises from the assumption of interfacial symmetry about the intermediate layer.

We begin by considering the case of the native oxide, Al2O3, at zero processing times.

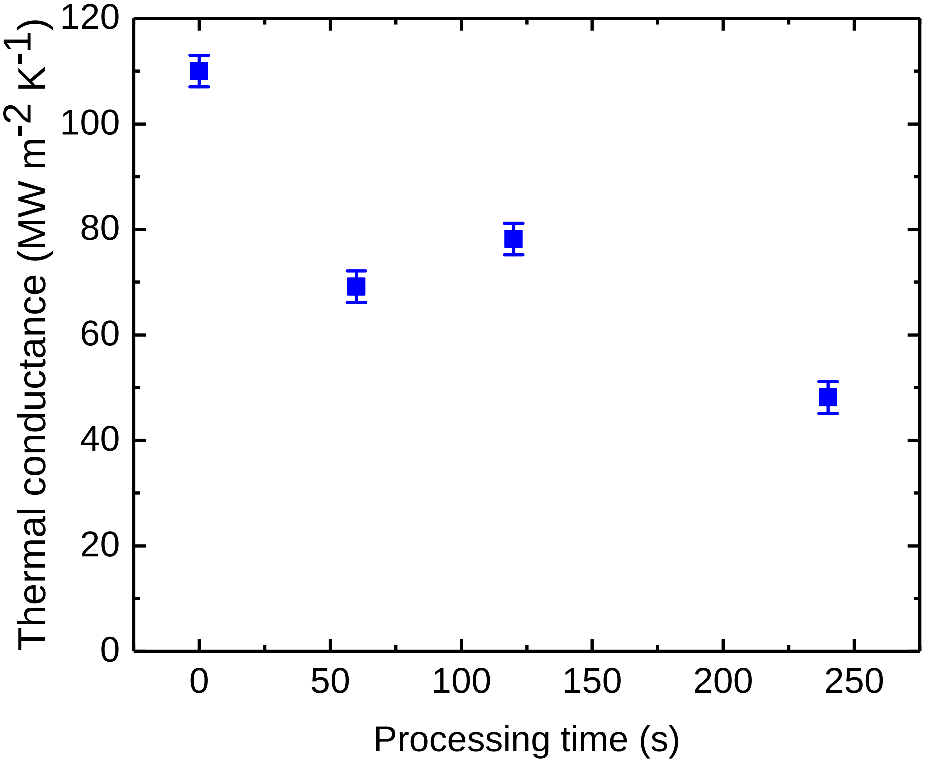

Figure 4.9: a) Measured ratio of in-phase to out-of-phase signal at early pump-probe time delays for an 80 nm Al/native oxide/80 nm Al film (dashed blue line) and 80 nm Al/AlO$_x$F$_y$/80 nm Al film (straight red line) on a SiO$_2$ substrate; an acoustic echo can be observed every 22 picoseconds on the surface of the top Al film. The intensity of this acoustic pulse over time is related to its transmission at the Al/oxide interface, which is proportional to bonding between the two layers. b) Acoustic transmission as a function of measured thermal conductance across the Al/AlO$_x$F$_y$ and Al/native oxide interface; a general monotonic increase is observed, implying interfacial bond strength is a dominant factor for the change in TBC observed in the various layers.

There are two limiting cases regarding the thermal conductivity in this equation: pure, crystalline Al_2O_3 with a thermal conductivity of 35 W m^{-1} $K^{-1}$and fully-amorphous Al2O3 at no less than $\sim$ 1 W m^{-1} K^{-1} 29. With these limits, we find that the measured TBC at the Al/Al_2O_3 interface is 220-330 W m^{-1} K^{-1}. These values are within the limits of previously measured Al/Al_2O_3 TBCs and are on par with DMM calculations in prior works8.

In the case of Al/AlO_xF_y interfaces, there are no previous values from 'bulk' thermal conductivity measurements. Furthermore, the assumption of a crystalline-like thermal conductivity for these plasma-processed layers is most likely not applicable; numerous works have shown that AlF_3 and AlO_xF_y layers and coatings are amorphous and lacking long-range symmetry[197–200]. While the degree of crystallinity of these oxyfluoride layers is unknown, we can determine realistic bounds for the thermal boundary conductance of the Al/AlO_xF_y interface. Based on the minimum limit to thermal conductivity of amorphous solids34, a fully amorphous AlO_xF_y layer has a thermal conductivity of likely no less than 1 W m^{-1} K^{-1}, whereas a fully crystalline structure would not exceed that of its crystalline oxide counterpart (35 W m^{-1} K^{-1}). In repeating the same series thermal resistor approach for the plasma-processed AlO_xF_y layer with this assumed thermal conductivity range of 1 to 35 W m^{-1} K^{-1} yields an Al/AlO_xF_y TBC between 98 and 112 MW m^{-2} K^{-1} for the longest-processed sample. While the aforementioned assumption of asymmetry may not be strictly valid, as plasma processing may produce a slight depth-dependent change in composition, it would not drastically affect this extracted TBC for Al/AlO_xF_y interfaces. If one were to assume a completely un-modified lower boundary, such that one interface is Al/AlO_xF_y and the second remains an Al/Al_2O_3 interface, the TBC for these Al/AlO_xF_y interfaces at the longest processing time ranges from 58 to 95 MW m^{-2} K^{-1} and thus remains over a factor of two lower than that of an Al/Al_2O_3 interface. Similarly, potential variations in the thickness of the oxyfluoride layer due to plasma processing do not significantly vary the calculated TBC for an Al/AlO_xF_y interface. To understand this drastic reduction in TBC when comparing an oxide to fluoride layer, we consider one of the primary factors leading to changes in interfacial heat transfer at the nanoscale: bonding. The role of bonding has been well studied, with a large number of previous works reporting the effect of bonding on thermal boundary conductance[93, 133, 168, 201, 202] specifically at aluminum/substrate interfaces[35, 130, 164]. To gain experimental insight to the bond strength between the Al transducer and the passivation layer, we perform picosecond acoustic measurements for the four samples; this method has been described in-depth in numerous works[133, 185, 203]. In short, this method allows for direct measure of zone-center acoustic phonon propagation in the metal transducer and its dissipation across the substrate interface. Experimentally, an acoustic strain pulse is launched from the Al surface towards the passivation layer. Upon interaction with this interface, the strain pulse partially reflects toward the surface of the film and partially transmits towards the substrate. As the measured reflectivity is sensitive to changes in strain at the surface of the Al film, a 'blip' can be observed in the transient reflectance data as this strain pulse reaches the surface (see Fig. 4.3.3a). This acoustic wave will then undergo another reflection at the Al/air interface, thus rebounding towards the passivation layer a second time; this process will repeat until the acoustic wave has fully dissipated. Each interaction with the film/substrate interface leads to an exponential decay in the magnitude of this acoustic pulse due to energy transmission across the interface, where the time-dependent intensity of the measured reflectance can be described by the following equation[125, 185],

$$I(t,T) = A * \exp(\Gamma t) cos((\frac{2\pi}{T}t - \delta) - B * \exp(-\frac{t}{\tau})), \tag{4.4}$$

where A, B, and δ can be are scaling factors, Γ is the damping factor of the measured acoustic intensity due to interfacial energy transfer, T is the period of which this acoustic wave reaches the sample surface, and the exponential function accounts for thermal decay through the metal film. The acoustic energy transmission associated with this process can be quantified through this damping factor, Γ, and the periodicity of the observed acoustic 'blip,' T, each obtained from fitting Eq. 4.4 to the experimental pump-probe data, via,

$$Acoustic transmission = 1 - \exp(-\Gamma T). \tag{4.5}$$

For example, in a well-bonded interface, typically associated with high TBCs, more acoustic energy can be transmitted across the interface, leading to an increase in this acoustic transmission factor[201]. Conversely, in cases where the transducer is poorly bonded to the substrate, one would expect a reduced damping factor and thus acoustic transmission across the interface. Indeed, in comparing the measured acoustic transmission of our Al/AlO$_x$F$_y$ films to the measured thermal conductance across the passivation layer, we find there is a nearly-linear, monotonic trend between the two parameters, as shown in Fig. 4.3.3b. This agreement implies that the passivation layer is weakly bonded to the metal Al film. Through simple inspection of Ellingham diagram for oxides and fluorides, one can see that the Gibbs' free energy associated with aluminum oxide formation is nearly 25 percent lower (greater magnitude) than that of aluminum fluoride[204]. From this perspective alone, it is unsurprising that Al-F bonds would be weaker than that of Al-O bonds, and thus lead to a reduction in metallic film adhesion to the oxyfluoride layer compared to that of the oxide layer alone, ultimately reducing the thermal conductance across the processed layer. We further note that the observed periodicity of the acoustic signal remains unchanged for various processing conditions, indicating there is no measurable change in thickness of the plasma-processed oxyfluoride layer. Finally, given the low ion energies associated with the plasma, roughness or defect formation is not likely to play a meaningful role in the reduction in thermal conductance or acoustic transmission with increased plasma processing times. The ability of the LAPPS system to chemically modify materials without plasma induced damage is well documented[205–207].

4.3.4 Conclusion

In summary, we have experimentally measured the interfacial thermal conductance between an Al film and an AlO$_x$F$_y$, layer grown via plasma-processing. These values were compared to the TBC of aluminum and its native oxide, which was shown to be in excellent agreement with previous experiments and theory; the TBC of Al/AlO$_x$F$_y$ interfaces are found to be 2-to-3 times lower than that of the Al/native oxide interface. Through pi-

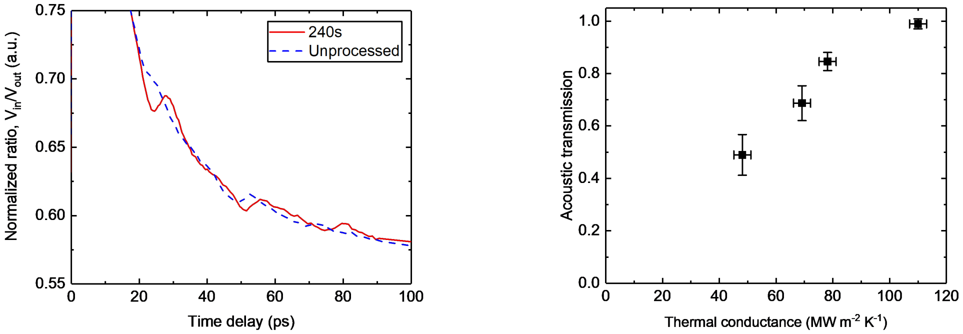

Figure 4.10: a) Measured ratio of in-phase to out-of-phase signal at early pump-probe time delays for an 80 nm Al/native oxide/80 nm Al film (dashed blue line) and 80 nm Al/AlO_xF_y/80 nm Al film (straight red line) on a SiO_2 substrate; an acoustic echo can be observed every 22 picoseconds on the surface of the top Al film. The intensity of this acoustic pulse over time is related to its transmission at the Al/oxide interface, which is proportional to bonding between the two layers. b) Acoustic transmission as a function of measured thermal conductance across the Al/AlO_xF_y and Al/native oxide interface; a general monotonic increase is observed, implying interfacial bond strength is a dominant factor for the change in TBC observed in the various layers.

cosecond acoustic measurements, it was determined that changes in interfacial bonding are the predominant mechanism for changes in TBC between the layers. These findings have important implications for the use of AlO_xF_y layers as optical films and barrier coatings in battery architectures, as it becomes more necessary to account for thermal accumulation due to the lesser conductance of these layers.

4.4 Ballistic Thermal Injection

4.4.1 Introduction

Light-matter interactions that induce charge and energy transfer across interfaces form the foundation for multiple technological phenomena including photocatalysis [208, 209], energy harvesting [210], and photodetection [211]. One of the most common mechanisms associated with these processes relies on injection of the carrier itself; this electron injection is one of the most common mechanisms associated with these processes and is considered to be a relatively well-understood phenomenon that can be manipulated at nearly all length (nm to bulk) and time (sub-ps to steady-state) scales [212, 213]. However, the exact role of electron injection in these applications remains unclear. Plasmon-assisted photocatalytic efficiencies can improve when intermediate insulation layers are used to inhibit charge transfer [214, 215] or when off-resonance excitation is used [216], yet the typical assumption is that charge injection is responsible for the catalytic enhancement [217, 218]. While considerable effort has been paid to characterizing novel plasmon-induced behavior and transport mechanisms [219, 220], current understanding still relies on a charge injection motif that has been established through long-time, quasi-steady state experiments. This is despite the fact that photothermal effects play an explicit role in such experiments when charge transfer is inhibited, and can further behave in a synergistic manner even when electron injection is ‘allowed’ to occur [221].

We hypothesize a novel energy transduction mechanism that arises from the non-equilibrium dynamics of excited charges at metal-semiconductor interfaces, without charge injection.

Such an energy transduction mechanism has yet to be demonstrated. These non-equilibrium dynamics exist when electron temperatures are highly elevated relative to the crystal lattice temperature and can only occur at ultra-fast timescales. In this regime, interfacial energy injection (without concomitant charge injection) from an excited metal to a non-metal offers the possibility of remotely manipulating the photonic and electronic properties of non-metals without relying on specific photonic or electronic excitations in the non-metal or metal contact. This would enable remote control of the non-metal's functional properties via injected heat, a mechanism of modulation that relies only on the 2nd Law of Thermodynamics.

To test this hypothesis, we must identify a system that lacks facile charge injection across a metal-semiconductor interface when in an excited state. Electron injection and/or interfacial electronic thermal diffusion can only occur in response to a gradient in the electronic chemical potential or Fermi level induced by an extrinsic perturbation (e.g., photonic excitation, temperature differences, or applied bias). Additionally, the excited carriers must have enough energy to traverse or tunnel through any Schottky barrier that exists at the interface. But what happens when the excited carriers are not accompanied by a change in electronic chemical potential? What if a Schottky barrier does not exist at the interface? We address the first question by using a noble metal, gold, with a nearly temperature-independent electronic chemical potential. We address the second question by using a degenerate semiconductor, yttrium-doped cadmium oxide (Y:CdO), which forms a barrier-free ohmic contact with gold. In concert, these two effects should eliminate the ability for light-induced charge transfer to occur at this metal-semiconductor interface. This opens the path to an entirely new means of interfacial energy transduction: excited electrons in the metal ballistically couple their energy, rather than charge, to the pre-existing electrons of the semiconductor (i.e., Au electrons have not yet scattered with phonons in the Au and are 'hot' upon reaching the Au/CdO interface). This ballistic thermal injection (BTI) process has yet to be recognized as a means of energy transfer as it is very elusive to observation: the process is contingent on non-equilibrium conditions to facilitate energy injection across an interface, yet simultaneously requires the absence of a potential gradient to limit charge injection. In the case of continuous wave, constant irradiation experiments, where the electrons and lattice are approximately in thermal equilibrium, this BTI process would be indistinguishable from charge injection. This can be alleviated by using ultra-fast, spectrally resolved optical pump-probe experiments to look for spectroscopic signatures that would indicate alternative relaxation pathways [222]. In this work, we investigate the non-equilibrium energy transfer across a metal/semiconductor interface with a novel ultrafast metrology that temporally and spectrally resolves changes in the optical properties of the semiconductor at and around the epsilon-near-zero (ENZ) condition. Because the optical properties of an ENZ medium are highly sensitive to spatial variations in electron density and energy [223–225], this technique provides unique insight into the energy transduction and relaxation mechanisms within the semiconductor. Furthermore, as we optically excite the metal contact from the air/metal interface with a pump pulse, the possibility for plasmonic resonance conditions to induce energy transfer is eliminated. Rather, we monitor the ENZ condition of the doped cadmium oxide semiconductor with a sub-picosecond probe pulse following excitation; this ENZ mode is a bulk plasmon, and functions as a sensor of charge and energy transfer from the metal into the CdO.

4.4.2 Methods

Gold in contact with Y:CdO is an ideal metal-semiconductor heterostructure to understand and manipulate our proposed non-equilibrium driven energy transfer pathway. Due to its large electron affinity (5.9 eV), CdO (Y:CdO) is intrinsically (extrinsically) an n-type degenerate semiconductor with a Fermi level residing deep within the conduction band. Y:CdO is thus expected to always form an ohmic contact with gold (work function $\sim$5.4 eV). Simultaneously, below an electron temperature of $\sim$3000 K, the Fermi level or electronic chemical potential of gold remains relatively constant, which limits thermally driven electronic diffusion [92].

With these two factors in mind, charge carriers are not expected to flow between two materials following pulsed excitation of conduction electrons in gold. Importantly, the weak electron-phonon coupling factor of Au allows its excited electrons to stay at highly elevated temperatures for prolonged times relative to other metals. Thus, following ultrafast excitation of Au, energy can ballistically traverse the Au film through the electron subsystem to reach the Au/CdO interface, and this can occur before the electron subsystem thermalizes and loses its excess energy to the Au phonon subsystem/lattice. As this energy front in Au reaches the Au/CdO interface, the hot electron subsystem in Au can then directly couple excess energy into CdO's electron subsystem due to the strong overlap of electronic wavefunctions between the two materials. This results in ballistic energy transduction across the interface without charge transfer. A schematic of the typically-assumed charge injection process and our proposed BTI process are shown in Fig. 4.4.2a and 4.4.2b, respectively. We note that the scattering processes following either charge injection or the proposed BTI energy transfer mechanism, such as hot electron-electron scattering, are excluded for clarity.

In addition to the unique ability to separate energy and charge transfer processes, doped CdO is a model mid-infrared plasmonic material that supports free electron densities on the order of 10^{19}-10^{21} cm^{-3} while maintaining high electron mobilities of 300-500 cm^{-2} V^{-1} s^{-1} [226–228]. These electronic properties enable strong, sharp, and resonant light-matter interactions at mid- to near-infrared frequencies. As in other plasmonic materials, these resonances are highly sensitive to local changes in the electronic environment, including electron density, effective mass, and dielectric constant. A key difference here is that, rather than probing surface and environment-sensitive surface plasmon polaritons as is common in thin-film metallic plasmonics, we optically monitor the resonant radiative bulk ENZ mode (also known as the Brewster mode) of the CdO following optical excitation of the Au film. Our sample geometry is especially convenient for this experiment, as the Au film also acts as a mirror that enhances the free-space coupling of the ENZ/Brewster mode, which allows us to monitor the reflectivity of the CdO/Au heterostructure from the backside through a transparent substrate. Thanks to the high electronic mobility, the ENZ/Brewster

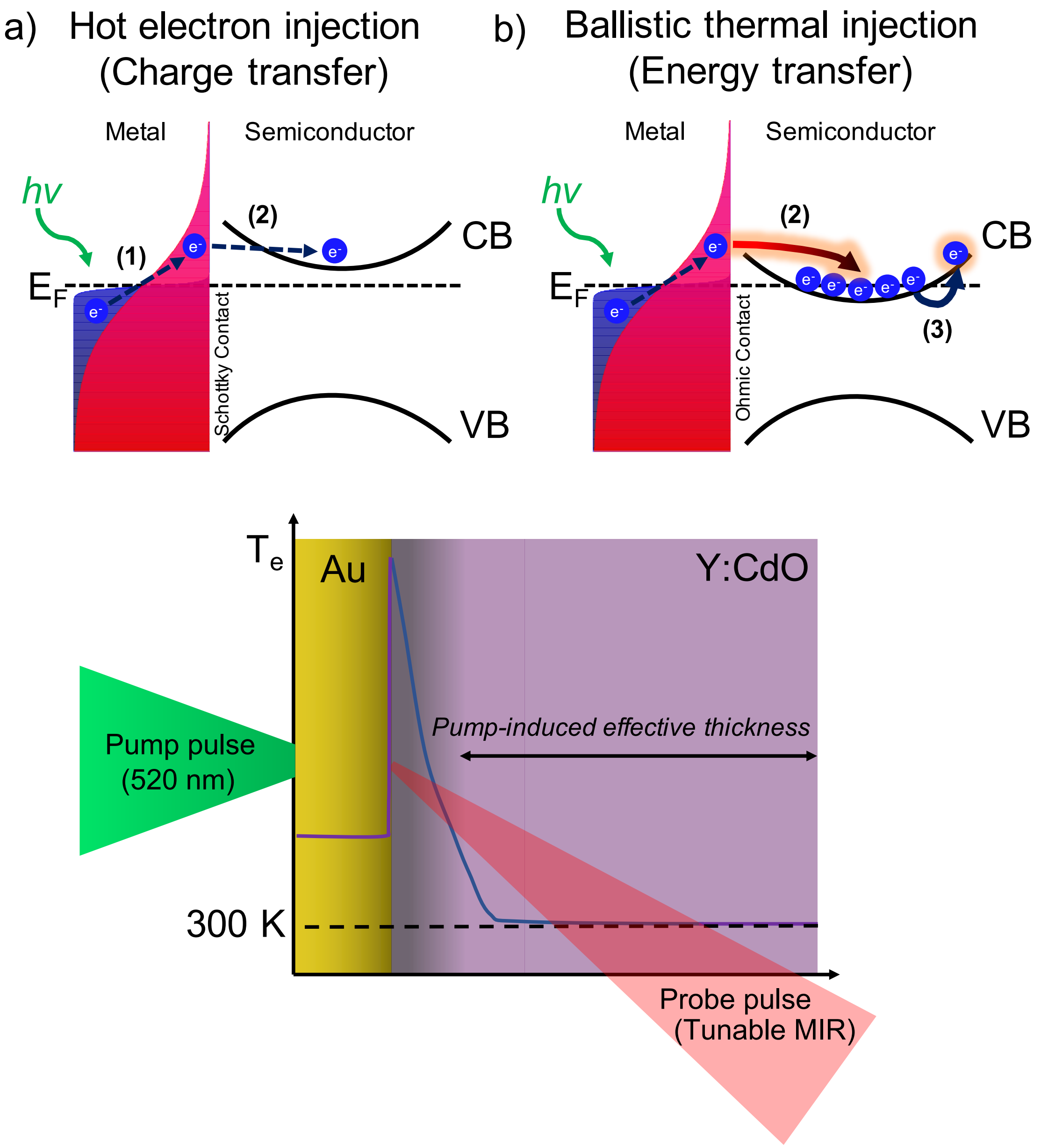

Figure 4.11: a) The typically-assumed process occurring at metal/semiconductor interfaces following photo-excitation of the metallic contact. In this case, (1) hot-electrons are first generated in the gold. At sufficiently high electron temperatures, (2) the electrons traverse the interface and add charge to the conduction band of the semiconductor. b) Our proposed process for metal/semiconductor interfaces following ultrafast excitation of the metal contact. This mechanism relies on hot-electron generation in the metal (1); prior to electron-phonon coupling (less than a couple picoseconds), energy propagates ballistically towards the metal/semiconductor interface. (2) The electron energy front reaches the interface, whereby the electrons transfer their *energy*, rather than charge, to the pre-existing free electrons in the semiconductor's conduction band. (3) The pre-existing semiconductor's electrons are now at an elevated temperature and are promoted to elevated states in the conduction band (e.g., intraband excitations). c) Schematic of our ultrafast ENZ experiment to spatially resolve the electron energy distribution following potential injection processes. The 520 nm pump beam excites the Au surface at the Au/air interface, while a sub-picosecond probe pulse monitors the ENZ mode of a thin Y:CdO film.

mode manifests as a sharp resonant dip in the reflectivity (i.e., an absorption peak), making it straightforward to resolve changes in optical behavior. This scheme provides high sensitivity to the spatial distribution of electronic energy in the semiconductor as well as its temporal evolution following energy transfer from the metallic film; a schematic of this measurement technique and the sample configuration is shown in Fig. 4.4.2c. In the following, we demonstrate long-lived modulation of the CdO ENZ mode following Au excitation, and show that this modulation can be explained only by the BTI process and not by a charge transfer mechanism.

4.4.3 TDTR Measurements

To gain initial insight into the hot-electron dynamics at the Au/CdO interface, and ensure our hypothesis of ballistic thermal injection can occur in these systems, we first perform time-domain thermoreflectance (TDTR) measurements [78, 229] on the Au/CdO samples supported by a sapphire (Al_2O_3) substrate, where both the pump and probe are focused on top Au film/air interface. These measurements allow us to quantify ultra-fast energy flow across the Au/CdO and CdO/substrate interfaces and asseess time scales of thermal transport at each interface. Our TDTR experiment can be conceptually summarized as follows. First, the sub-ps pulse excites electronic carriers in the metal, which quickly (10's of fs) scatter and decay into a 'hot' Fermi-Dirac distribution. At this stage, the electronic subsystem is at a greatly elevated temperature, while the phononic subsystem remains cold (i.e., approximately at its initial temperature). In the case of metals in contact with dielectrics (e.g., Al_2O_3), these hot carriers are spatially confined to the metal and can neither traverse the metal/dielectric interface nor directly couple their energy to electrons or phonons in the insulator. Instead, they couple to and lose energy to the phononic subsystem (i.e., the lattice) of the metal film. Following this electron-phonon coupling, phonon-based thermal conduction out of the metal and into the insulator over hundreds of picoseconds to nanoseconds. The entire process is monitored via temporal changes in the metal's thermoreflectance: the reflectance signal decays with time as the surface of the metal film loses energy to the underlying substrate via phonon interactions at the metal/non-metal interface [161, 183, 230, 231].

Conversely, when Au is in direct contact with a different metal (e.g., Au/Ti or Au/Pt interfaces [139, 229, 232, 233], the excited electrons are no longer confined and can directly couple energy across the metal/metal interface, leading to an 'instantaneous' (sub-picosecond) temperature rise of electrons in the underlying metal. These hot-electrons in the underlying metal can subsequently lose energy to the phononic subsystem more quickly than those in the Au, which creates a sub-surface temperature rise. This sub-surface heating leads to a bi-directional heat flux originating from some depth under the Au/air surface, and manifests as a temporally delayed rise in the thermoreflectance signal as heat is conducted back into the Au through the lattice (e.g., 'back-heating'). This back-heating signature is thus a strong indication of electron energy transfer from the Au film into the underlying metal film [229]. This phenomenon acts as a transient thermal diode: the injection of energy from Au to the buried metal substrate occurs on sub-picosecond time-scales, whereas the lattice-mediated 'back-heating' occurs on hundreds of picoseconds to nanoseconds.

Indeed, TDTR measurements (Fig. 4.4.3a) on 15 nm Au/100 nm CdO films display the back-heating and the transient thermal diode effects, indicating that hot electrons in the Au are transferring their energy to free electrons in the CdO at ultra-fast time scales. Conversely, when a thin 15 nm dielectric HfO_2 layer is placed between the Au and CdO, this energy transfer process is inhibited and no sign of back-heating is observed. This observation rules out any possibility that the pump beam is directly exciting the CdO film and is the cause for subsurface heating, as the HfO_2 is optically transparent to the pump wavelength. It also confirms our posit that a dielectric barrier, which limits the electron wavefunction overlap between Au and CdO, will inhibit thermal energy transduction across the Au/CdO interface.

As mentioned, interpreting of spectroscopic characteristics in typical pump-probe experiments such as TDTR can be quite difficult, as several mechanisms can lead to nearly identical signatures. In both metal/metal and Au/CdO heterostructures, there are two potential mechanisms for subsurface heating at ultra-fast time scales: charge injection and our proposed BTI process. In both situations, ohmic contact between two materials with high carrier density may lead one to expect facile charge injection into the underlying metal or CdO. In that case, the injected electron would eventually decay within the underlying metal or CdO via electron-phonon coupling and induce a sub-surface temperature rise. Contrarily, the back-heating signatures could result from BTI without any concomitant charge flow: optically deposited energy ballistically traverses Au's electronic subsystem to reach the interface, where it couples directly to the electronic subsystem of the underlying metal or CdO. Following this BTI process, the now-excited electrons in the underlying metal/CdO would couple to the lattice and lead to sub-surface heating.

4.4.4 *Ab Initio* Time-Dependent Density Functional Theory

To distinguish these processes, we simulate the electronic interactions involved in the nonequilbrium photo-induced dynamics via *ab initio* real-time time-dependent density functional theory (TDDFT) for electrons coupled to nonadiabatic molecular dynamics (NAMD) for atomic motions (Fig. 4.4.3c). The calculations reveal that following photo-excitation of the Au, the hot electron remains within Au, with the tail of its wavefunction extending into the CdO layer. This tail directly couples energy to electrons in the CdO within picoseconds, followed by electron-phonon relaxation through high-frequency phonon modes [234]. Concurrently, (Fig. 4.4.3b and 4.4.3c) the hot electron's wavefunction quickly ($\sim$6 ps) re-localizes within the Au, which quenches BTI. Additional calculations performed with thicker Au and CdO slabs demonstrate similar shift of wavefunction localization from Au to CdO, and then back to Au. The localization shift requires longer time in thicker slabs, slowly approaching the experimental result (Fig. 4.4.3a). The electron-phonon relaxation becomes slightly slower in thicker slabs at early time, because Au atoms are heavier than CdO atoms. The calculations show that energy transfer from Au to CdO is mediated by hot electron energy coupling and not a phononic or charge-injection process. This result, obtained with small representations of the Au/CdO interface, agrees well with our observed

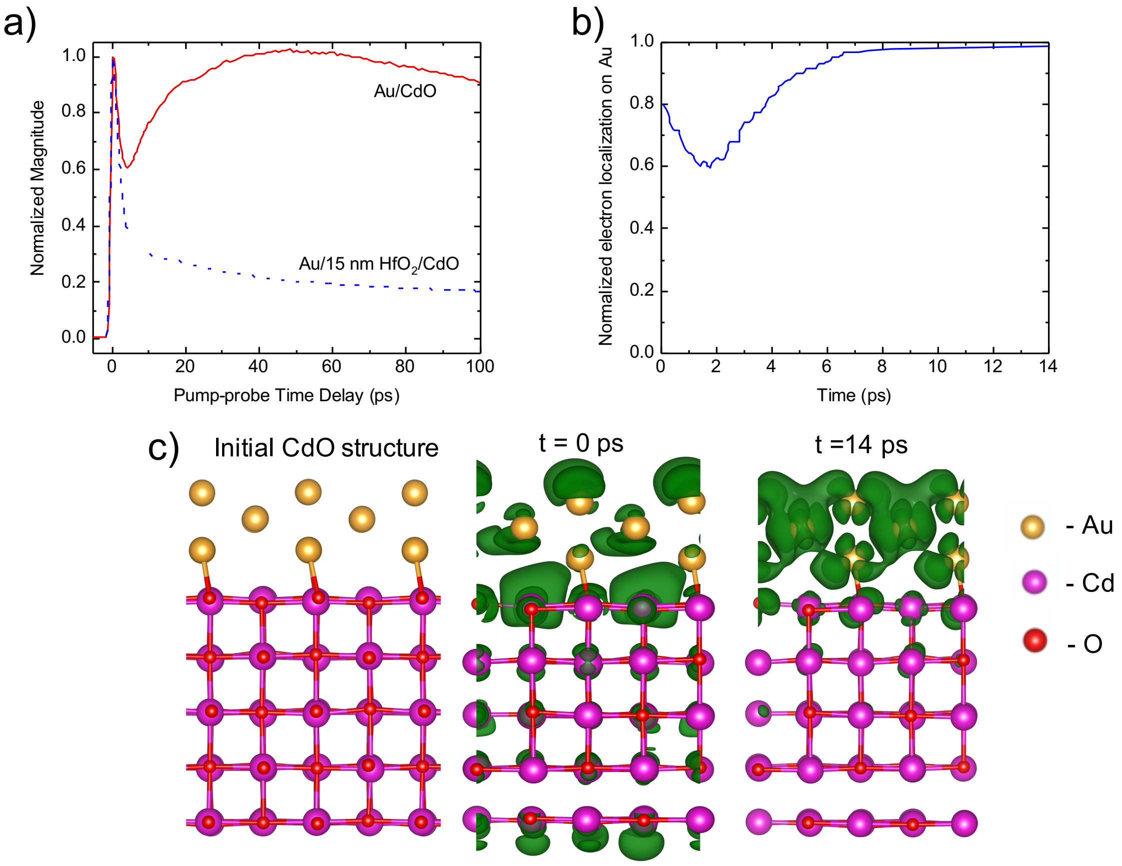

Figure 4.12: a) TDTR curves for 15 nm Au on 100 nm CdO, with a carrier concentration of 7.7×10^{19} cm^{-3}. In the case where the two are in direct contact (straight red line), back-heating is clearly observed, indicative of electron injection. Conversely, the addition of a thin dielectric layer between the two media (dashed blue line) inhibits this injection effect and leads to electron thermalization only within the Au film. b) Evolution of electron localization on Au atoms; zero-time corresponds to the initially-excited state. While the electron remains primarily localized within the Au slab, its wavefunction extends into the CdO, which allows for a greatly-increased energy transfer rate due to the high frequency modes available within the CdO. After a few picoseconds, as the structure relaxes, the electron re-localizes solely within the Au layer, thus ending the BTI process. c) Left: Optimized structure of the Au/CdO simulation cell. Yellow, large purple and small red balls represent Au, Cd and O atoms respectively. The CdO slab is about twice thicker than the Au slab, mimicking experiments. Middle and Right: Charge densities of the initial pumped and final states, respectively. The excited hot electron localized on Au has a tail into CdO. The relaxed electron is localized nearly fully on Au, because the Au Fermi level is inside CdO bandgap.

experimental trends and supports the two-temperature interpretation of our results.

4.4.5 Ultrafast Infrared Measurements

This novel BTI mechanism offers a unique opportunity to manipulate the electrons in an optically active material without relying on direct photonic or electronic perturbations, as is commonly done. Instead, the BTI process remotely manipulates the photonic or electronic response of a non-metal through optical excitation of the metal transducer. To demonstrate this, we perform additional pump-probe experiments on the heterostructure, where a tunable wavelength probe monitors the ENZ behavior of the CdO, following visible (520 nm) excitation of the Au film, at picosecond time scales. This ENZ mode is highly sensitive to the electronic environment and free carrier dynamics within the CdO. By monitoring CdO's optical behavior, we gain direct knowledge of how the electronic environment changes with time during the BTI process.

Following the pump excitation of gold, the ENZ absorption peak of CdO at $\sim$3800 nm red-shifts, which increases absorption (decreases reflectivity) at longer wavelengths. Concurrently, absorption (reflectivity) decreases (increases) at shorter wavelengths, though to a lesser extent. This asymmetric red-shift persists for hundreds of picoseconds following thermal excitation of the gold film.

Our observation of a red-shift immediately negates the possibility of electron injection from the Au into the CdO layer. Based on the Drude model, the ENZ mode of a conducting thin film is centered at the screened plasma frequency, $\omega_{ENZ} = \omega_p/\sqrt{\varepsilon_\infty}$, where ε_∞ is the high-frequency dielectric constant, $\omega_p = \sqrt{n_e e^2/m^* \varepsilon_0}$, and where n_e is the free electron density and m^* is the effective mass of the electrons. Therefore, any electron injection would increase n_e and result in a blue-shift of the ENZ absorption peak, in direct contrast to our experimental results.

While one could argue that hole injection or heating of the CdO layer may be occurring, which would result in a decrease in n_e and an increase in m^*, respectively, both would lead to a symmetric red-shift. As indicated prior and shown in Fig. 4.4.5a and Fig. 4.4.5c, we clearly observe an *asymmetric* red-shift. To understand the origin of this asymmetry, we perform optical transfer matrix method (TMM, Fig. 4.4.5b,c) calculations to model how the electron distribution changes in the CdO layer following Au excitation. (A more detailed description can be found in the Appendix.)

Our TMM calculations reveal that n_e remains unchanged in the CdO, regardless of pump fluence or relative pump-probe time-delay indicating that neither electron nor hole injection occurs. Rather, in accordance with our BTI hypothesis, the energy distribution of these charges changes based on the following physical processes. First, the Au couples its electronic energy to the CdO, thus heating free electrons within a thin ($<$5 nm) CdO layer near the Au/CdO interface. This energy heats the electrons, which leads to a local increase in m^* within this layer [235]. Additionally, because scattering rate is inversely proportional to the effective mass, our model also captures a local decrease in the damping frequency of the free electrons. As this heated layer is now out-of-equilibrium relative to the remainder of the CdO, electrons from the bulk of the film diffuse towards the hot CdO layer, which temporarily forms an accumulation layer near the Au/CdO interface and slightly decreases n_e throughout the remainder of the CdO film. This increase in the local number density leads to a corresponding decrease in the high frequency permittivity, ε_∞ [236, 237]. As shown in Fig. 4.4.5c, the TMM calculations only re-produce our experimental results, with excellent agreement, when our proposed BTI energy transfer mechanism is invoked. TMM-simulated electron or hole injection cannot explain the observed asymmetric red-shift in ENZ absorption, regardless of whether the charge is injected into the full CdO layer or a thin slab near the interface. These TMM simulations incorporate rigorous relationships between the optical parameters (plasma frequency, scattering rate, high-frequency dielectric constant) and electronic parameters (electron number density, mobility, and effective mass), consistent with previous observations [236, 237]. We also note that a lack of 'net' charge transfer, as observed in these ultrafast experiments, exists through pre-existing theories, namely via non-equilibrium electronic thermal diffusion. While we cannot fully rule out the effects of this mechanism, we believe it may be playing a supporting role and

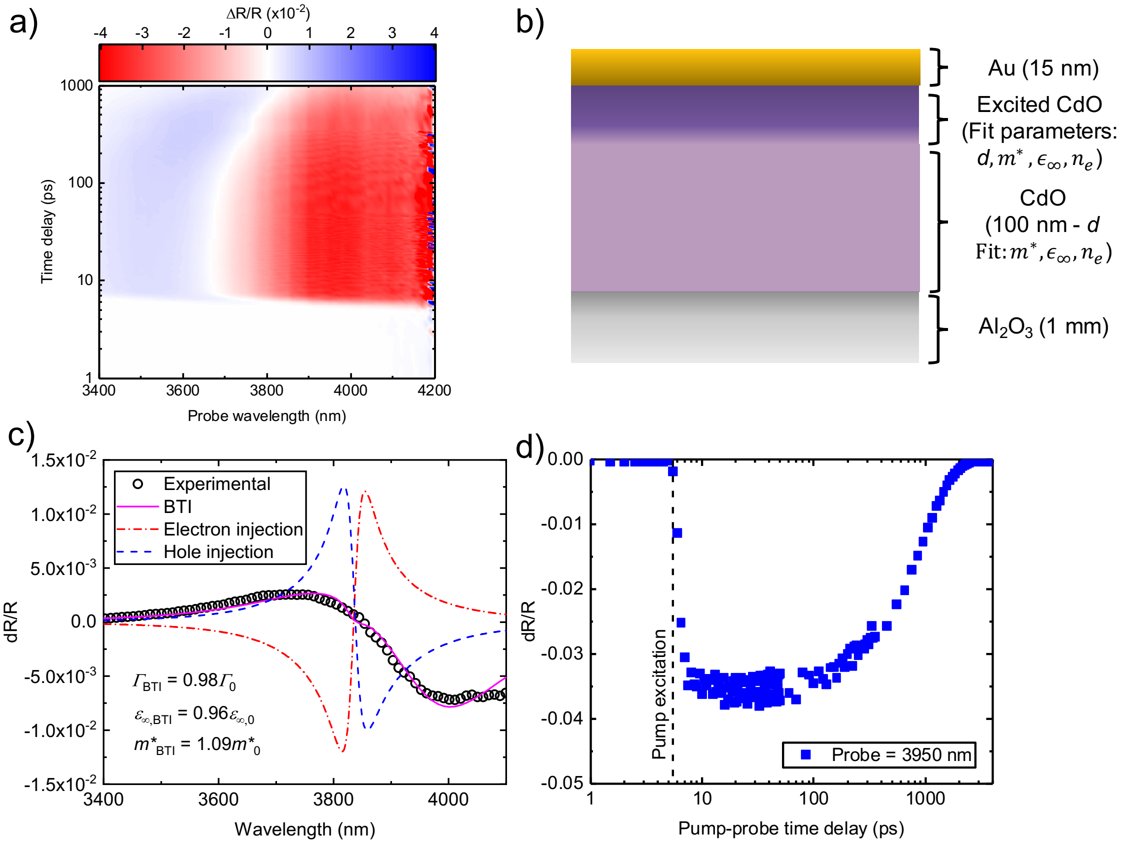

Figure 4.13: a) Transient reflectivity measurements at a fluence of ∼0.5 J m^{-2}. The x-axis denote the wavelength of the probe beam, while the y-axis represents the time delay between the 520 nm pump pulse and the tunable IR probe beam; the spectral resolution of these data is 10 nanometers. Note, the pump pulse arrives at ∼6 picoseconds. Additionally, red represents a *decrease* in probe reflectance, while the blue represents an increased reflectance. b) Schematic of the TMM simulation along with the various fit parameters. c) Change in reflectivity for the Au/CdO heterostructure immediately following pump excitation and the simulated reflectance curves calculated via transfer matrix method for various injection mechanisms. Clearly, neither hole or electron injection are able to capture the observed trend. The inset values are the TMM best-fit values, which determined a 5 nm perturbation layer in agreement with our two-temperature model calculations. d) Transient reflectivity of the Au/CdO heterostructure probed at 3950 nm following visible excitation of the Au film; the 1/e decay time of this curve is approximately 700 picoseconds.

operating in-tandem with the proposed BTI mechanism.

Finally, we note that electronic non-equilibrium within the CdO, and thus associated remote modulation of the ENZ mode, is altered for prolonged times with a 1/e decay time of approximately 700 ps (Fig. 4.4.5d). This length of modulation is orders of magnitude greater than previous works investigating light-induced changes in plasmonic absorption of the CdO film. This long-lived modulation is ultimately enabled by the aforementioned 'transient thermal diode' effect that is enabled by the BTI process across the Au/CdO interface.

4.4.6 Conclusion

We find that under non-equilibrium conditions, photo-excited metals can undergo an electron-mediated ballistic energy transfer process that can remotely modulate the electronic environment of an underlying degenerate semiconductor. We term this effect 'ballistic thermal injection' (BTI) to distinguish it from the well-studied charge injection effects caused by hot electrons traversing an energy barrier. Our results are explained through transient reflectivity (TDTR) measurements to understand the fundamental carrier dynamics at the Au/CdO interface. Additionally, we perform mid-infrared, ultra-fast pump-probe experiments to obtain spectral, temporal, and ultimately spatial resolution of the electronic environment within the CdO layer following excitation of the Au film. Ultimately, the carrier dynamics derived from the transient spectra fully agree with our TDTR results, and can only be accurately modeled by the BTI process rather than by charge injection. While we describe the first observation of this unique energy transduction mechanism, future work into both theory and application could provide benefit to both increasing understanding and manipulation of BTI. First, while computationally expensive, particularly for the larger unit cells considered in this work, extending the computations to include both electrons and holes would certainly be of interest. Second, directly calculating the optical response of the heterostructure in systems exhibiting BTI with TDDFT could provide fundamental benefit to further understanding this mechanism and extending the application space, though may rely on non-linear responses that are currently difficult to accurately implement, particularly for structures containing ‘bulk’ semiconductor/insulator layers. From an application perspective, although BTI does not directly lend itself to ultra-fast switching, one could easily conceive of several applications where longer modulation lifetimes are more beneficial, such as catalysis, sensing, or energy harvesting, through an increased interaction time. The long-lived modulation of epsilon-near-zero media such, in particular, can be utilized as a selective emitter for thermophotovoltaic (TPV) conversion, as BTI can prolong the desired state of emissivity, or nonlinear phenomena such as four-wave mixing and high harmonic generation. Furthermore, the proposed BTI energy transduction mechanism could provide explanation for discrepancies between current theory and experimental results in light-matter interactions, such as photocatalysis, that rely on either the framework of a charge transfer motif or solely phononic heat conduction.

Chapter 5

Solid-Liquid Interfaces

In the first half of this chapter, I apply the metrology techniques developed in Chapter 4 toward the measurement of nanoscale energy transfer across solid-liquid interfaces. In particular, I investigate the relationship between macroscale models of heat transfer to the measurement of thermal transmission at the nanoscale. The second half of this chapter demonstrates the manipulation of these nanoscale solid-liquid interactions for the development of a record-setting tunable thermal conductivity switch, which is enabled through the infiltration of water to a squid ring teeth (SRT)-based biopolymer. The work presented in this chapter has been published in peer-reviewed journals, namely *Langmuir*[185] and *Nature Nanotechnology*[238]

5.1 Nanoscale Wetting and Energy Transmission at Solid-Liquid Interfaces

5.1.1 Introduction

Nanoscale interactions and dynamics between solids and liquids are ultimately the defining factor in a range of applications, including, but not limited to, microfluidics [48–50], chemical catalysis [51–53], and microelectronic thermal management [54, 55]. An increased understanding of such nanoscale dynamics provides insight into the mechanisms of various interfacial phenomena, such as protein folding and adsorption [56–58], cell formation [59, 60], and other self-assembly processes [61–63]. While countless studies have focused on attempting to understand these solid/liquid interactions at the macroscale, common metrics such as contact angle become oversimplistic and fail to realize the complex phenomena occuring on the nanoscale. For example, works alluding to nanoscale effects at interfaces attempt to relate measurements of contact angle to chemical composition and molecular scale thermodynamic effects at the solid/liquid interface [64, 65]. Additionally, other works have gone in the opposite direction: manipulating the molecular order at a solid/liquid interface, such as structure and composition, to control macroscale wetting [63, 66]. While general empirical trends have been observed that relate macroscopic measurements of solid/liquid interactions to nanoscale interfacial properties, these trends assume that macroscopically observable interactions scale to the nanoscale interfacial region. However, only recently have the necessary models and theories been developed to enable a more fundamental understanding of solid/liquid interactions at the nanoscale [68]. Thus, it is critical to develop novel and feasible experimental probes that can interrogate these nanoscale solid/liquid dynamics to validate these theories. This will facilitate experimental insight into the true nature of the wetting of a liquid on a solid surface at length scales much smaller than typical contact angle measurements.

The majority of these recent experimental advances have investigated the structural component of a liquid interacting with a solid. Work studying the atomic arrangement of liquids at an interface [239–241], as well as the movement [242–244], or “flow”, of such atoms has provided much of the framework for understanding of solid/liquid interfaces. Though the structural and mechanical nature of these interfaces are an undeniably important first-step in understanding phenomena driven by these interactions, insight into the exchange of energy across solid/liquid interfaces would be expected to provide complementary and novel information regarding the nature of wetting of surfaces at the nanoscale. As referenced prior, many of the macroscale phenomena driven by these nanoscale interactions are ultimately dependent on the ability for energy to couple from one phase to the next.

With respect to thermal transport, recent work has pushed the theoretical understanding of vibrational scattering and energy exchange across solid/liquid interfaces [155, 245–248]. In addition to this, fundamental theory, modeling, and simulations have helped frame a basis to suggest that the strength of the bond at the solid/liquid interface, which can determine the equilibirum contact angle, can be correlated to the efficacy of thermal transport [249–258]. Limited experimental results involving liquids other than water are available to validate and shape these works. In general, various experimental works have shown that greater hydrophobicity at solid/water interfaces, determined via contact angle experiments, leads to a decrease in thermal boundary conductance (TBC), a measure of nanoscale energy transport across the interface [154, 202, 259]. In general, these results imply that a smaller contact angle, and hence better "wetting", leads to greater thermal boundary conductance. However, experimental works studying energy coupling across planar solid/liquid interfaces in which the liquid is not water, and relating this energy coupling to wetting, are scarce. The strengths of the intermolecular forces in a liquid relative to the interfacial bonding environment are the underlying mechanism that drives the manifestation of contact angles and wettability [260]. In the extreme case of weak intermolecular interactions in a liquid (e.g., fluorinatied fluids such as 3M© Fluorinert©), comparable liquid-liquid and solid/liquid interaction energies can lead to macroscopic observables and uncertainties (e.g., contact angle measurements) that are not indicative of the true nanoscale interactions and resulting dynamics at the solid/liquid interface. This leads to the following major question regarding solid/liquid energy coupling on the nanoscale: How valid is the use of macroscale wettability (e.g., contact angles) in describing the nanoscale solid/liquid interactions that drive energy transport across solid/liquid interfaces? We seek to answer this question in our work.

Thus far, the limited experimental studies probing the nanoscale thermal transport interactions at solid/liquid interfaces have shown that optical pump-probe techniques are

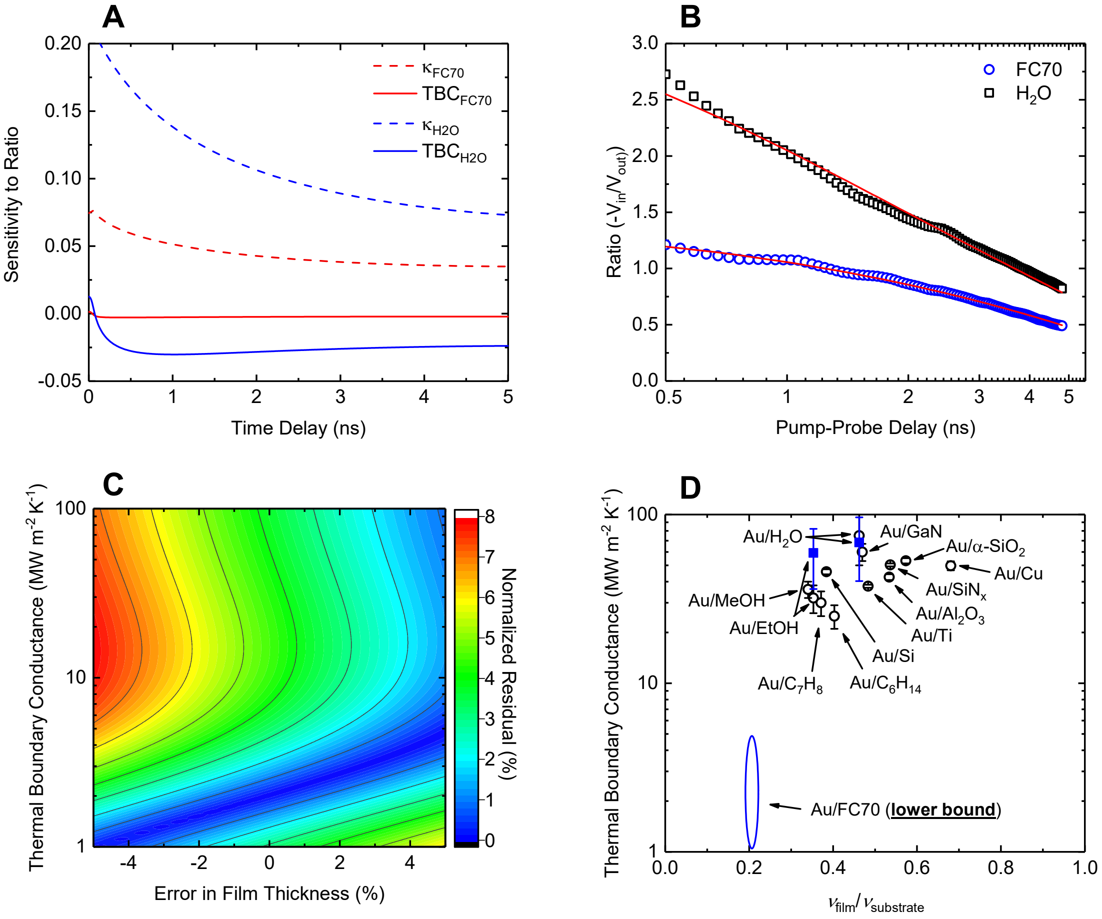

Figure 5.1: a) Sensitivity plot of the ratio of in-phase to out-of-phase signal in time-domain thermoreflectance (TDTR) at 8.8 MHz for a Au/water (blue) and Au/FC70 (red) interface when fitting for thermal conductivity (κ) and thermal boundary conductance (TBC). b) Experimental TDTR data with the line of best fit for SiO_2/Au/FC70 and Au/H_2O stacks. Note, a bidirectional model is used as we probe through the transparent SiO_2 slide. c) Normalized residuals (i.e., the model's fit relative to the best-fit thermal decay curve) for a single TDTR scan with an SiO_2/75 nm Au/FC70 stack. Assuming a 5% error in the Au metal transducer thickness, the minimum possible thermal boundary conductance for Au/FC70 varies from roughly 1 to 5 MW m^{-2} K^{-1}. d) Measured thermal boundary conductance for various Au/solid (Au/GaN [5], Au/SiN_x [6], Au/SiO_2, Au/Cu, Au/Al_2O_3, Au/Ti, and Au/Si [7]), Au/liquid (Au/Methanol, Au/Ethanol, Au/Toluene, Au/Hexane [8], Au/H_2O [9]) from literature (open circles), and Au/liquid (Au/H_2O, Au/Ethanol and Au/FC70), from this work, interfaces as a function of the ratio of the longitudinal sound speeds of the two media. The blue circle denotes the bounds of the lower limit of thermal boundary conductance for Au/FC70 interfaces assuming a 5% error in metal transducer thickness.

particularly well-suited for this application [154, 202, 261–264]. Traditional thermoreflectance techniques, the current standard for measurement of interfacial energy transport, lack sufficient sensitivity to energy transport across solid/liquid interfaces as discussed further below. Thus, in this work, we develop an altered pump-probe schematic that provides enhanced sensitivity to the measurement of acoustic phonon propagation (i.e., picosecond acoustics) in a solid metal film in contact with a liquid. As acoustic phonons are the primary thermal carrier in metals that drive the thermal boundary conductance (TBC) across metal/non-metal interfaces [124, 165, 265], the damping of such modes upon interaction with the solid/liquid interface provides a metric describing energy transport across this interface [125, 133, 184, 262]. We perform these measurements on an array of gold-liquid interfaces; the results are compared to macroscale wettability determined via contact-angle measurements. In addition, we measure the thermal ablation threshold, a separate metric of interfacial energy transport [7], of Au thin films submerged in these various liquids; the two methods are found to be in good agreement. In both cases, we find a deviation from our metric describing nanoscale energy transport from that suggested by macroscale wettability.

5.1.2 Failure of Thermoreflectance Techniques to Measure TBC

From the perspective of macroscale equilibrium thermodynamics, the interface between two media are described by the Dupré equation,

$$\gamma_{SL} = \gamma_S + \gamma_L - W_{SL}, \tag{5.1}$$

where γ represents the surface energies of the solid/liquid interface (γ_{SL}) between the solid medium (γ_S) and the liquid medium (γ_L), and W_{SL} represents the work of adhesion between the two media [266, 267]. These surface energies are defined as the energy per area required to form the surface of a given material. As interfaces form, the energy required to form these surfaces is reduced as the two media begin to form bonds; this is the work of adhesion.

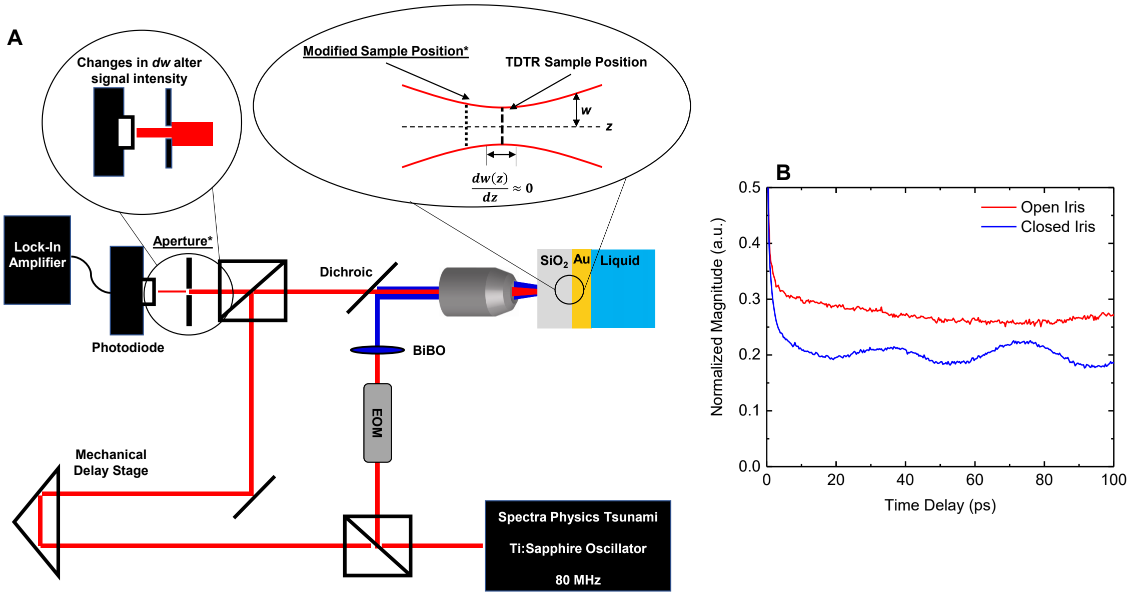

Figure 5.2: a) Schematic of our pump-probe setup. The modifications that vary from a typical TDTR setup to enhance picosecond acoustic and brillouin scattering signals are underlined and starred. b) Normalized magnitude of the detected signal before and after our alterations to a typical TDTR apparatus as a function of pump-probe delay time. By moving our sample out of the Rayleigh length and adding an iris prior to the photodiode greatly enhances the signal produced from picosecond acoustics.

Many works determine this adhesive energy at the solid/liquid interface, quantified by W_{SL}, through the Young-Dupré equation,

$$W_{SL} \approx \gamma_L (1 + \cos(\theta)), \tag{5.2}$$

where θ is the measured contact angle of the wetting liquid [267]. This formulation has held remarkably true down to atomic scales as demonstrated by Shenogina *et al.* [252] via molecular dynamics simulations. However, in situations where contact angles are hard to define, such as those at interfaces between solids and so-called ‘highly-wetting fluids,’ as determined via macroscopic techniques, this relationship is difficult to experimentally realize.

Attempts to move beyond the use of Eq. 2 to quantify solid/liquid interaction strength and resulting energy transport have been made through methods such as liquid density depleted boundary layers and depletion lengths near solid/liquid interfaces. These quantities have been described in computational studies as fundamental parameters of interfacial thermal transport [268]. However, the experimental measurement of density depletion is non-trivial, requiring advanced methods such as neutron reflectivity measurements [269], and has not been applied extensively to many interfaces [269, 270], creating a lack of validation between these computational studies and experimental works investigating energy transport at solid/liquid interfaces. More readily accessible thermoreflectance techniques, namely time-domain and frequency-domain thermoreflectance (TDTR and FDTR, respectively), have been used to measure interfacial energy transport in planar geometries, providing unique insight to nanoscale energy exchange in many material systems [33, 93], including select solid-liquid interfaces [8, 35, 154, 202]. While this method would be optimal for probing the solid-liquid interactions on the nanoscale due to its routine use in measurements of TBC, as thermal boundary conductance is intimately related to the interfacial bonding environment [93, 125, 130, 133, 162, 168–170, 195], the experimental insensitivity to the interfacial resistance posed by a solid-liquid interface, due to the large thermal resistance of liquids relative to that of the interface, make this approach prone to large uncertianites or, in some cases, unmeasurable at interfaces involving low thermal effusivity fluids. We quantify this lack of sensitivity and resulting uncertainty in measuring solid-liquid thermal boundary conductance via TDTR measurements in Fig. 5.1.1. The relative sensitivity of the interfacial resistance is significantly lower compared to that of the liquid thermal conductivity, as shown in Fig. 5.1.1a for both water and the fluorocarbon-based liquid, FC70. Note, we calculate this measurement sensitivity based on the TDTR sensitivity analysis presented in Ref. [77].

We experimentally confirm this predicted lack of sensitivity with TDTR measurements of 75 nm Au films on amorphous SiO_2 substrates submerged in the respective liquids; the experimental data and thermal model fit are shown in Fig. 5.1.1b. For fitted values of both liquids, we find that only a lower limit to thermal boundary conductance can be obtained; this lower limit is found to be as low as $\sim$1.9 MW m^{-2} K^{-1} for an FC70/Au interface and

$\sim$40 MW m^{-2} K^{-1} for H_2O/Au interfaces. To determine these bounds, we generate theoretical model curves with varying thermophysical parameters, namely the thickness of the metal transducer, around the best fit values obtained with least-square minimization of our thermal model to the measured data. We quantify the difference between the theoretical and experimental curves using a normalized residual. An example contour, where we consider 5% error in the Au thickness, shows the minimum range for which the Au/FC70 thermal boundary conductance allows no more than 1% error in the minimum value. As seen, a 1% residual encompasses TBC values no less than $\sim$1 to $\sim$5 MW m^{-2} K^{-1} over this possible range of film thicknesses, yet the contour diverges and allows for infinitely high TBC values within the 1% residual bound for only slightly greater film thicknesses. Note, the best-fit value ($\sim$68 MW m^{-2} K^{-1}), as well as the bounds from error analysis, for the H_2O/Au interface remains within the range of previously reported measurements [9, 154, 155]. It is also worth noting that the TBC at the FC70/Au interface is the lowest value for TBC ever measured at room temperature. This result is rather counter intuitive given that FC70 is considered a "highly wetting fluid", and traditionally highly wetted interfaces are thought to imply higher TBCs than non-wetted interfaces. However, the ability to only measure a lower bound to TBC with correspondingly large uncertainty restricts a more conclusive finding using TDTR. Note, this large uncertainty is due to the inherent limits of the thermal model used in TDTR; as the liquid thermal conductivity reduces, the uncertainty associated with the thermal boundary conductance at the solid/liquid interface increases. Thus, for low thermal conductivity materials or liquids, in a bi-directional heat transfer model, the uncertainty in TBC will be inherently large.

In considering this TBC associated with Au/fluorocarbon solutions, it is useful to compare the measured value to the interfacial thermal resistances associated with other Au interfaces. Assuming a simple acoustic mismatch model (AMM) for interfacial resistances [35], one would predict an increase in TBC with increasing overlap of the sound velocities, v, of the two media, as the phonon density of states are proportional to these velocities from the perspective of the Debye model (i.e., as $v_{\mathrm{film}}/v_{\mathrm{substrate}}$ approaches 1, TBC is expected to increase). As shown in Fig. 5.1.1d, the experimentally-measured thermal boundary conductances for various Au/solid and Au/liquid interfaces are plotted as a function of the ratio of the longitudinal sound velocities for the two media comprising the interface; we only consider Au interfaces as their TBCs are considerably lower than most metal/dielectric interfaces when no adhesion layer is utilized [124, 166, 271]. As expected, one can observe a general increase in TBC for liquids that have greater overlap in their vibrational density of states relative to the Au film. In the case of Au/FC70, the blue circle denotes the limits of the possible lower bounds in the thermal model. As the value of best fit in the model depends on the thermophysical parameters of the substrate and metal film, we consider a potential of 5% error in the film thickness, one of the model's most sensitive parameters. As seen, the obtained lower bound for Au/FC70 interfaces is anomolously low compared to previously measured Au interfaces.

While this lower bound is within the sensitivity/experimental limitations of TDTR, the ability to obtain a nominal value, or even meaningful upper bound, for TBC with various Au/liquid interfaces, that are poorly wetted as the nanoscale, is not plausible. The inability to define an upper bound is supported through consideration of the mean square deviation of the thermal model applied to the experimental TDTR data obtained for the two liquids. As shown in the contour plot in Fig. 5.1.1c, which represents this mean square deviation when fitting for various combinations of thermal boundary conductance of the solid/liquid interface and thermal conductivity of the liquid layer, any value greater than this lower limit associated with the TBC leads to the same quality of fit to our data [272, 273].

5.1.3 Picosecond Acoustics to Quantify Phonon Transmission

To overcome this lack of sensitivity, we seek alternative pump-probe experiments to quantify nanoscale energy transport at solid-liquid interfaces. Namely, we probe the damping of acoustic phonon modes (e.g., picosecond acoustics) in the solid layer upon interaction with the solid-liquid interface. This measurement allows for optical detection of the propagation of acoustic modes through the piezo-optic effect of energy coupling between

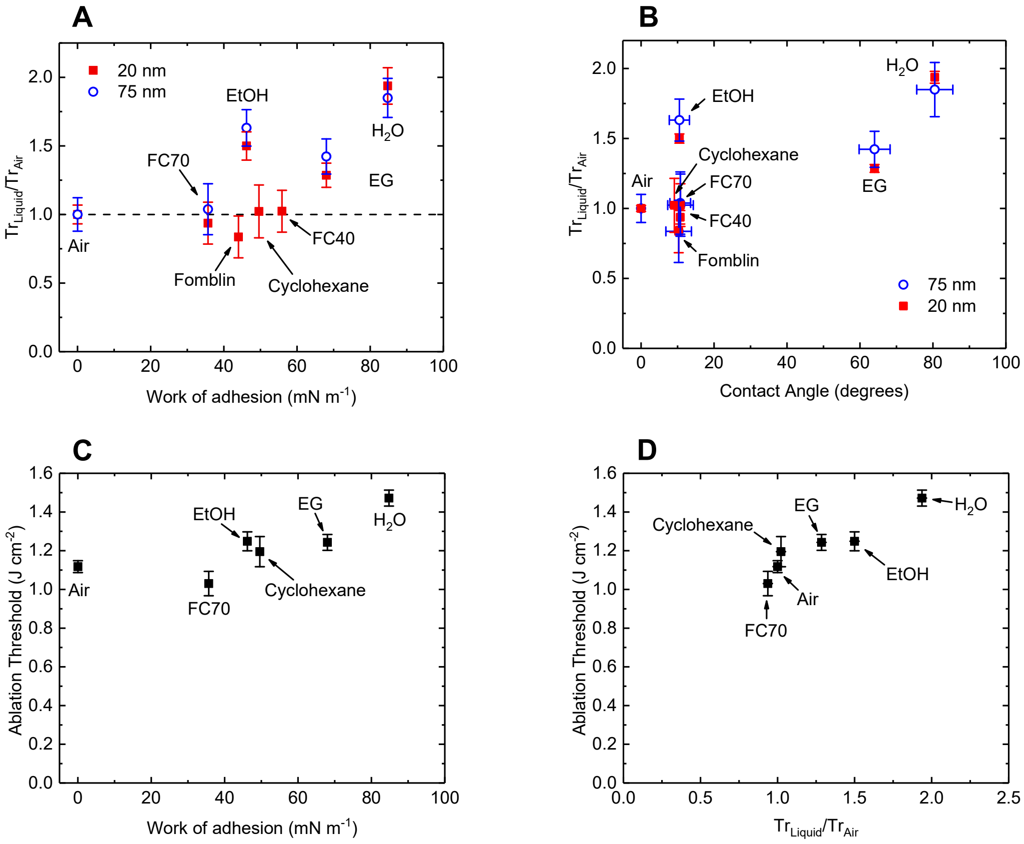

Figure 5.3: a) Measured transmission of acoustic phonon modes at the solid-liquid interface as a function of the work of adhesion calculated via Young-Dupré equation for various liquids on 75 nm Au films. Note, the values are normalized by the nominal value of air for 75 nm Au films and the dashed line is a guide to the eye for an acoustic transmission value equivalent to the value of an Au/air interface. In these experiments, the nominal transmission coefficient can only be considered a qualitative measure due to the brillioun scattering/interference induced by a pressure-front in the underlying substrate leads to an inability to quantify the transmissivity of acoustic modes. b) Measured transmission of acoustic phonon modes as a function of the measured contact angle. As seen, there remains a deviation between the measure of nanoscale energy transport and macroscale metrics for solid/liquid wetting. c) Measured ablation threshold of 200 nm Au films as a function of the work of adhesion calculated via Young-Dupré equation for various liquids on Au surfaces. d) Measured ablation threshold as a function of the measured transmission coefficient in various media; the two measures of nanoscale energy transport show great agreement.

the solid film and contacting layers [201, 262, 274], and can be applied outside of thin Au films, as demonstrated in various material systems including polymers and other amorphous materials [274–277], semiconductors [278–280], superlattices [281, 282], etc. The time-dependent intensity of these picosecond acoustic signals can be described via [125]

$$I(t,T) = A * \exp(-\Gamma t) * \cos((2\pi/T)t - \delta) - B * \exp(-t/\tau), \tag{5.3}$$

where A, B, and δ are scaling factors, Γ is the damping due to interfacial energy transfer, T is the period of the pressure front, and the second term, $\exp(-t/\tau)$, accounts for the thermal decay rather than the signal associated with the acoustics. Fitting this equation to the picosecond acoustic signal over the first nanosecond provides us with two important variables: the period, T, and damping, Γ, of the acoustic modes. After obtaining these values, the transmission of these acoustic modes across the solid-liquid interface can be determined as

$$Transmission = 1 - \exp(-\Gamma T), \tag{5.4}$$

Although these signals inherently exist in TDTR, as the pump *always* creates an acoustic wave propagating through the metal film, its detection is non-trivial, moreso when using an Au transducer due to its low piezoreflectance response at the commonly used TDTR probe wavelength of 800 nm [203, 283]. Typically, this can be overcome by performing transient transmission experiments with the use of thin (i.e., partially transparent) metal films, which produce much larger responses. These gains in signal from testing in a transmission configuration can potentially be obscured by non-linear interactions between the beam and liquid as the beam passes through the liquid. Thus, we alter our typical TDTR layout to enhance the picosecond acoustic signal in a reflection geometry with optically opaque films, allowing for quantitative analysis of acoustic wave transmissivity across Au/liquid interfaces.

To enhance the picosecond acoustic signal, we make two major adjustments: the film is moved out of the Rayleigh length of the focused probe beam waist and a partially-closed iris is implemented just before the photodiode. In moving the sample to the linear regime of a focusing beam, as the strain wave propagates to the surface of the transducer, a larger change in spot-size occurs at the sample surface. This deviation in spot-size is more easily detected with the addition of an iris prior to the photodiode; as the back-reflected probe beam is focused to the photodiode surface, the iris partially clips the edges of the beam. With changing spot size, the spatial variation leads to increased (or decreased) portions of the beam being cut-off by the iris [133]. This deviation is then translated to a change in signal at the photodiode. These modifications are depicted in Fig. 5.1.2a. This alteration leads to a drastic increase in sensitivity to picosecond acoustic signals during TDTR measurements on 75 nm Au films supported by amorphous SiO_2 substrates. The signals before and after these adjustments are demonstrated. It should be noted that this technique simultaneously enhances the change in signal produced from brillouin scattering within the substrate as shown in Fig. 5.1.2b. At our probe wavelength of 800 nm, Brillouin scattering leads to optical interference between the partial reflection of the beam with the pressure front propagating through the substrate and the primary reflection at the Au/SiO_2 interface with an oscillation frequency of $\sim$21.19 GHz [284]. To avoid the creation of beat frequencies and distorted signals, our choice of a 75 nm Au film ensures the picosecond acoustic signal of the film is in resonance with this interference frequency; the resonance of the two effects allows us to determine relative decay between the varying media. Thus, all transmission coefficients are normalized to that of the 75 nm Au film in air, as we can not decouple the two phenomena.

As can be seen in Fig. 5.1.2a, the measured acoustic transmission at across various solid/liquid interfaces shows no discernible trend. For example, Fomblin provides the same acoustic attenuation as that of air, whereas Ethanol exhibits nearly a 60% increase, despite the two liquids having nearly the exact same value for their work of adhesion. Additionally, we repeat these acoustic-damping experiments in a transmission geometry with thin, 20 nm Au films submerged in the varying media; As the optical response associated with the acoustic mode propagation is much greater in this thickness regime, we do not require the use of an iris or operating off-focus to enhance our signal, and thus are able to eliminate the contribution of interference due to reflection in both the Au film and the pressure-front in the underlying SiO_2 substrate [203, 284] within our scans. We find the two methods, and thus two film thicknesses, are in excellent agreement, as shown in Fig. 5.1.2a. Furthermore, as shown in Fig. 5.1.2b, in considering only the contact-angle associated with the interface, rather than accounting for the liquid's inherent interaction energy (γ_L), there is a distinct lack of trend with energy transport at the interface. This clearly demonstrates that macroscopic wetting metrics are not sufficient to describe nanoscale dynamics in many fluids, particularly those with low contact angles. Given the agreement between methods, with both finding the Au/air and Au/fluorocarbon interfaces to have similar transmission coefficients, we consider other measurements at solid-liquid interfaces to further explore the differences between contact angle measurements and nanoscale energy transport.

5.1.4 Ablation Threshold as Metric for TBC

As shown in our previous work, the thermal ablation threshold associated with short-pulse, single-shot measurements provides an accurate metric for changes in thermal transport at interfaces, and correlates well with TDTR measurements of thermal boundary conductance [7]. This threshold quantifies the minimum laser fluence, or energy density, required to remove mass from a material's surface; the nominal value for this threshold is dependent on the laser pulse duration and thermal properties of the material system. In our previous work, we found that the ablation threshold for 25 picosecond pulses, where the electrons and lattice reach equilibrium during the pulse and diffusive heat transfer is the characteristic process, the assumption of homogeneous thermal properties of a bulk target break down in thin film systems. Instead, the thermal boundary conductance between the Au film and substrate becomes a limiting factor. In fact, there is a monotonic, linear increase in ablation threshold with increasing TBC [7]; the nominal value for the ablation threshold was measured to increase 6.46 J m^{-2} per MW m^{-2} K^{-1} increase in thermal boundary conductance. Thus, as a probe of energy transport at solid-liquid interfaces and means of quantifying the thermal boundary conductance for interfaces with large uncertainties, we measure the ablation threshold for 200 nm Au films with an overlying liquid layer; these results are depicted in Fig. 5.1.2c. Given the aforementioned change in laser fluence necessary to induce ablation for a given increase in thermal boundary conductance (6.45 J m^{-2} per MW m^{-2} K^{-1}) and the measured TBC for a Au/water interface ($\sim$68 MW m^{-2} K^{-1}), one would predict a TBC for the Au/FC70 interface to be $\sim$1-3 MW m^{-2} K^{-1}; this prediction is in good agreement with the range of lower bound from uncertainty analysis on our TDTR measurements which spans $\sim$1-5 MW m^{-2} K^{-1}.

Although the ablation threshold for the thin Au films follow a nearly linear trend with the bulk wetting and thermophysical properties associated with the overlying liquid, where the threshold is plotted as a function of the liquid's measured work of adhesion, a clear deviation from any such trend is again observed in the fluorocarbon-based liquids, similar to our picosecond acoustic measurements of transmissivity, where fluorocarbon liquids have nearly the same ablation threshold as that found in air. In comparing these ablation threshold values to the picosecond ultrasonic measurements of acoustic transmissivity, as shown in Fig. 5.1.2d, we find that the two methods are in excellent agreement, where an increase in phonon transmission corresponds to a nearly monotonic increase in fluence necessary to induce ablation of thin Au films. This agreement between ablation threshold and phonon transmission further indicates that acoustic phonons are indeed the primary thermal carriers contributing to thermal boundary conductance at Au/liquid interfaces and electronic transport does not play a significant role of interfacial heat transfer in these systems. Our posit regarding a phonon-dominated TBC is further supported by a two-temperature model [90, 285] and thermoreflectance coefficient analysis [78] of the pump-probe reflectivity signals, which shows no change in the electron-phonon coupling factor of Au, regardless of the liquid layer, and thus indicates a lack of interfacial electron-phonon coupling or charge transfer [139].

Clearly, both the picosecond acoustic transmission measurements and ablation threshold measurements show that the Au/fluorocarbon interactions do not follow similar trends as the other liquids with respect to the Young-Dupré equation. In fact, the experiments suggest that the interaction energy between Au and these fluorocarbon liquids are similar to that as Au and air (based on the acoustic phonon transmission and ablation thresholds being similar for both Au/air and Au/fluorocarbon liquid). Indeed, the bounds of our analysis for the TBC of Au/fluorocarbon interfaces of $\sim$1-5 MW m^{-2} K^{-1} from our various experiments is on par with the previously measured TBC of Au/air interfaces by Park *et al.,* where a value of 4 ± 4 MW m^{-2} K^{-1} was obtained. This defies the macroscopic observation that FC70, and other fluorinated fluids, are "highly wetting," since a highly wetting fluid would imply relatively strong solid/liquid interaction energies. Considering the relatively weak intermolecular bonds of fluorocabon fluids relative to other fluids, it is not surprising that molecules in a fluid that have inherently weak intermolecular interactions with each other will also not want to interact with a surface.

Although on the macroscale, fluorinert and other fluorocarbons are known, and measured here, to have both low surface energy and a correspondingly low work of adhesion, our metrics display a clear discrepency relative to the macroscopic definitions of wetting. The comparatively large hydrophobicity, for example, of fluorocarbons is attributed to their 'fatness,' or large molecular cross-sectional area, leading to their reduced surface energy [286], and their previously measured hindrance to thermal conductance when measured as self-assembeled monolayers [287]. Furthermore, the low polarizability of both fluorine and carbon bonds leads to reduced London dispersion forces, which only exist due to momentary dipoles, leading to their inherent, repulsive nature [288]. Such features may lead to a greatly reduced, if even existant, stern layer at the solid-liquid interface compared to the case of other liquids, such as water. Finally, given the high solubility of gases in fluorocarbons due to these weak intermolecular forces [289, 290], it is possible that a vapor layer of such gases forms at the solid-liquid interface, greatly inhibiting the energy transport across the interface; as determined by Takata *et al.* [291], these vapor layers are not found to exist in solid-liquid interfaces involving water, including under super-hydrophobic conditions. This vapor layer could explain the similarity in thermal boundary conductance between Au-fluorocarbon interfaces and Au-air interfaces. As density-depletion is known to occur at solid-water interfaces, yet the macro- and nanoscale metrics for wetting provide similar results in such cases, this effect is not a likely explanation for disparities in thermal transport at the fluorocarbon-solid interface. These microscopic features lead to deviations in energy transport on the nanoscale, but similar macroscopic properties to other solvents. Interfacial electronic transport,

5.1.5 Summary

These results show a clear deviation between macro- and nanoscale measures of liquid wetting a solid surface based on energy transport mechanisms at the interface of the two phases, as the relative acoustic impedance, contact angle, and work of adhesion between of the solid/liquid interface fail to agree with various measurements of nanoscale thermal transport. Thus, these results raise the question: what metrics should be used to quantify solid/liquid interaction energies on the nanoscale that are universal to all solid/liquid interfaces? Comparing the transmission of acoustic phonon modes across this interface to our ablation threshold experiments, we find excellent agreement (Fig. 5.1.2d), not only reinforcing the notion that macroscale observables are poor indicators of nanoscale energy transport at an interface composed of varying phases, but also that these experimental methods provide a means to individually, yet accurately, probe such energy transfer. With the improved detection outlined in this work and the non-destructive nature of the measurement, picosecond acoustics is thus shown to be a versatile method for insight towards energy transport at interfaces. This clear discrepency between macro- and nanoscale phenomenon at solid-liquid interfaces provides insight to the need for better metrics of interactions between various phases of matter at the nanoscale.

5.2 Dynamic Thermal Switching Enabled via Solid-Liquid Interactions in Squid-Ring Teeth Proteins

The ability to actively manipulate the vibrational energy exchange and thermal conductivity of materials would enable novel directions in a wide range of nanoscale science and technology. For example, a new class of thermally driven devices, such as thermal rectifiers, logic gates, and transistors could be realized with the ability to actively modulate the thermal conductivity [292]. While the efficiency of these devices would not rival their electrical analogs, these devices could in-principle be powered "for free" if the source of the "power" is from wasted heat. Similarly, the ability to actively modulate the temperature of a device has been shown to create massive gains in thermoelectric efficiency, which would enable a new and resurgent direction to the decades-old thermoelectric problem [293, 294]. Modulation of temperature gradients in materials could also lead to advances in all-solid state electrocaloric or magnetic refrigeration [292, 295, 296].

Numerous examples of variable, yet reversible, thermal conductivities in materials have been realized, albeit, with only small modulations in their phonon or vibrational thermal conductivity. Prominent examples of such vibrational thermal switches that include: liquid crystal networks that can be oriented with external magnetic field, thus increasing their thermal conductivity from $\sim$0.20 to $\sim$0.35 W m^{-1} K^{-1} (Ref. 297), reversible delithiation of $LiCoO_2$ cathode materials under electrochemical tuning leading to reductions in the thermal conductivity from 5.4 to 3.7 W m^{-1} K^{-1} (Ref. 298), and an 11% increase in thermal conductivity in lead zirconate titanate thin films through manipulation of their nanoscale ferroelastic domains when subjected to external electric fields [299]. In these aforementioned studies of thermal conductivity switches, the underlying mechanisms driving the switching phenomena have been based on manipulating the thermal carrier populations or scattering rates. This approach of actively manipulating the lattice or vibrational thermal conductivity, κ, will be inherently limited to relatively small $\Delta\kappa$ since, under typical conditions (i.e., not extreme pressures or temperatures), the scattering of only a relatively small window of the vibrational spectrum will be impacted. Here, we seek to not only enhance the ability to modulate thermal conductivity to enable on/off ratios much larger than the current state-of-the-art, but also extend this dynamic control of thermal transport to biological, soft materials. We achieve this by moving beyond traditionally-used approaches of actively impacting the vibrational scattering rates; instead, we utilize the unique nanocrystalline structures of networked proteins inspired from squid ring teeth, a unique structural protein, and actively manipulate the displacement amplitude of the vibrations in these cross-linked networks.

Indeed, precedent for actively tuning the thermal conductivity in soft materials is established in the orders of magnitude changes in thermal conductivity that have been predicted in polymeric systems based on strain, chain alignment, and crystallinity. For example, record tunability, with a factor of 12 change in thermal conductivity, has been calculated for polyethylene by combining effects of strain and phase changes [300]. Experimentally, the recent discovery of high thermal conductivity in ordered or aligned polymers departs significantly from our conventional wisdom about relatively low thermal conductivities in polymeric systems [301–304]. This suggests the possibility for a large span in variability of thermal conductivity when the system is altered from disordered to ordered, aligned, or crystalline phases. Thus, actively, rapidly, and reversibly modulating degree of order in a soft material could in principle lead to these large changes in thermal conduction using these same concepts.

5.2.1 Squid Ring Teeth Proteins

Based on this conjecture, we have identified a class of tandem-repeat (TR) protein that enables just this: namely, rapid and reversible changes in the dynamics of the protein chains via hydration. Our protein design relies on synthetic tandem repeat polypeptides based on squid proteins. Squid proteins have inspired the design and development of various technologies including invisibility cloaking [305], self-healing materials [306], synthetic nacre [307], and renewable bioplastics [308]. Particularly, squid ring teeth (SRT) proteins are high strength hydrogen-bonded thermoplastic polymers that can be extracted from the tentacles of the squid suction cups or expressed recombinantly in bacteria [309]. We adapted a known molecular biology technique, rolling-circle amplification, to create a tandem repeat DNA assembly strategy enabling production of SRT-mimic, tandem repeat genes with different lengths from a repetitive building block in a single cloning step [310]. We used this rolling-circuit amplification method to prepare a library of TR sequences with a controlled distribution of lengths. We designed four repetitive TR polypeptides (i.e., TR-n4, TR-n7, TR-n11, and TR-n25, where n denotes the repeat number) based on the crystal-forming polypeptide sequence of PAAASVSTVHHP and the amorphous polypeptide sequence of YGYGGLYGGLYGGLGY. These repetitive polypeptides form hydrogen-bonded crystalline physical crosslinks and amorphous disordered segments, which are reminiscent of semicrystalline polymers, illustrated in Fig. 5.4a.

5.2.2 Thermal Conductivity of SRT Proteins

As these proteinaceous materials can simply be solvent casted to planar geometries, transient thermoreflectance techniques are ideal for measurement of the protein's thermal properties. Hence, we use time-domain thermoreflectance (TDTR) to measure the thermal conductivity of these protein films. The sample geometry of our TDTR measurements of these TR samples are shown in Fig. 5.4a, with a two-dimensional cartoon view of the protein's structure, as determined by XRD and FTIR studies described in previous work [310], shown in Fig. 5.4b. The thermal conductivity of the TR films are shown in Fig. 5.4c. As expected, under ambient conditions ($<$ 35% relative humidity; see Appendix details), the thermal conductivity of these proteinaceous films do not depend on repeat units or molecular weight and demonstrate similar thermal conductivities to disordered polymers and water insoluble proteins [311–314]. The physics of the vibrational thermal conductivity of disordered soft materials, such as polymers or TR films in ambient conditions, has been studied for quite some time and is well understood to be driven by a random walk of vibrational energy interacting at length scales on the order of the interatomic spacings, akin to Einstein's

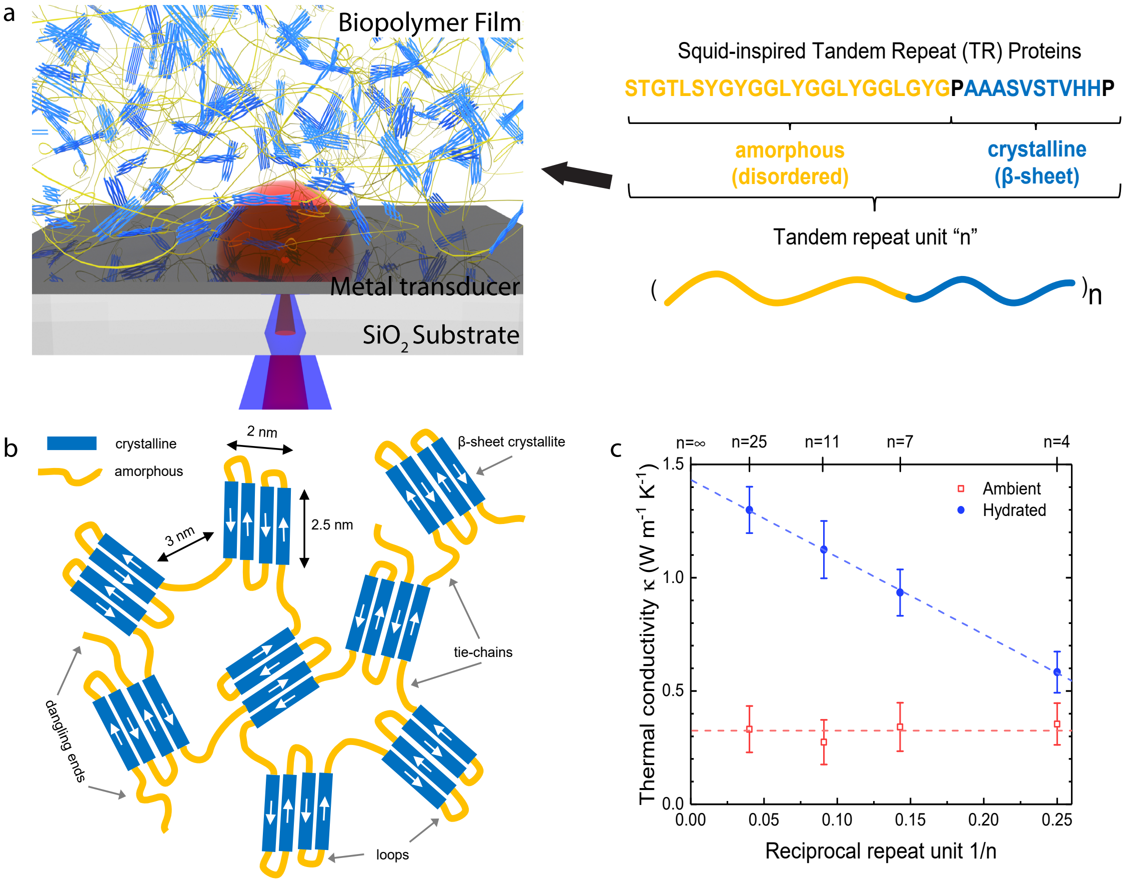

Figure 5.4: Structure and thermal conductivity of tandem-repeat protein-based materials: a) Schematic of the TDTR measurements; the pump and probe beams pass through the transparent glass substrate and interact with an 80 nm Al transducer; thermal diffusion from the Al film into the overlying TR film allows for thermal conductivity measurements of the proteinaceous material. The blue squares and yellow lines are indicative of the β-sheets and amorphous tie-chains that compose the film. b) Two-dimensional cartoon view of TR proteins, composed of crystalline (blue) and amorphous (yellow) strands. c) The measured thermal conductivity as a function of reciprocal repeat units for the four TR protein films. In ambient conditions (open red squares), there is no material dependence. Upon hydration (closed blue circles), a linear increase with increasing n is found.

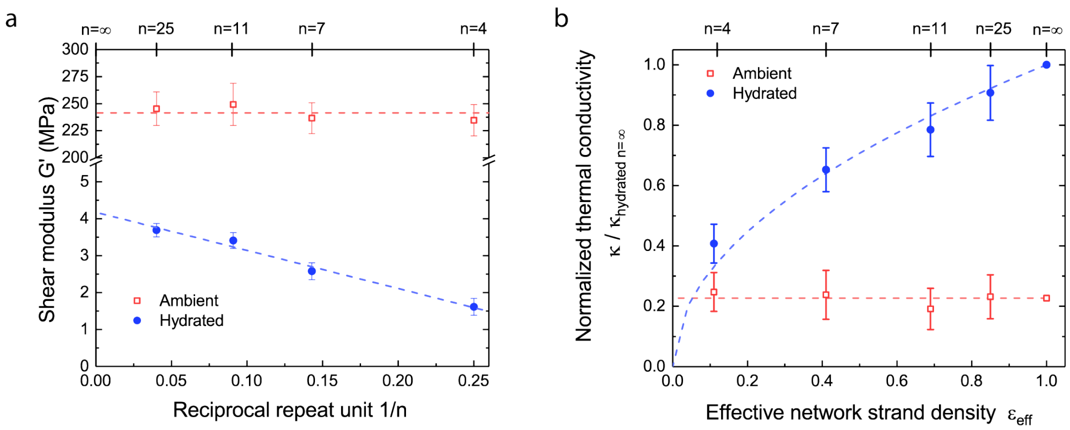

Figure 5.5: Thermo-mechanical properties in varying states: a) Measured shear modulus, G, as a function of $1/n$. In the highly-bonded, dense network associated with the proteins in ambient conditions, no n dependence is found. Conversely, there is a linear increase in G with increasing n upon hydration. Error bars represent one standard deviation. b) Measured thermal conductivity, normalized by the predicted thermal conductivity for the case when $n = \infty$, as a function of the effective network strand density, ε_{eff}, of the TR films.

original picture of vibrational heat transport and the so-called minimum limit to thermal conductivity [23, 24]. In terms of the TR films in this ambient state, this finding suggests that the thermal conductivity is limited by the amorphous regions, and any potential benefit of higher thermal conductivity in the nanocrystalline β-sheet ordered regions is lost from scattering in the amorphous domains. When these TR films are hydrated, the thermal conductivity not only increases as compared to the ambient state, but also a nearly linear dependency on $1/n$ emerges, as shown in Fig. 5.4c. In the TR sample with the highest number of repeat units, n (or low $1/n$), we observe a nearly factor of 4 increase in the thermal conductivity. The increase in thermal conductivity suggests that the amorphous chain conformation and overall network morphology, which are dependent on tandem repetition [303, 315], are impacting the overall thermal conductivity.

The role of the amorphous domains on thermal conductivity is elucidated via measurements of the shear modulus, G, using oscillatory rheology and dynamic mechanical analysis (Fig. 5.6a). The modulus of polypeptides in ambient conditions is constant at an average G = 241 ± 13 MPa, which agrees with previous reports [309, 310, 316] on the mechanical properties of SRT. This ambient modulus is independent from tandem repetition

n, suggesting that the amorphous chains are heavily constrained by hydrogen bonding and weak interactions, and chains are in a glassy state. On the other hand, hydrated TR proteins exhibit a modulus, G, ranging from 1.5 to 4 MPa with a linear dependence on reciprocal repeat units $1/n$.

In proteinaceous materials, the modulus is directly related to the network morphology; this network is composed of β-sheets, which act as physical cross-links, and amorphous segments which are the network strands. The effective strand density (or tie-chain density), ε_{eff}, was calculated from structural characterization, mechanical analysis, and entropic elasticity theory [317–319]. Based on entropic elasticity theory [320], the tie-chain density is given by $\varepsilon_{\text{eff}} = 1 - (\beta_c/n)$, where β_c is the β-sheet crystallite size (≈ 4 β strands for TR proteins), and n is the number of repeats in the polypeptide chain ($n \approx \text{MW}/3.46$ kDa for the TR proteins with MW being the molecular weight of the proteins). The tie-chain density varies between zero (i.e., highly defective, $\beta_c = n$) and unity (i.e., perfect network, $n \to \infty$). The dependence with n indicates an increase in tie-chain density with tandem repetition and a decrease in defective chain conformations such as loops and dangling ends. Given the thermal conductivity of materials is generally related to their stiffness, where stiffer materials generally exhibit higher thermal conductivities than softer materials, the increase in thermal conductivity with tie-chain density is consistent with $\kappa \sim \sqrt{\varepsilon_{\text{eff}}}$ in hydrated polypeptides (Fig. 5.6b).

5.2.3 Quasi-Elastic Neutron Scattering

However, a seemingly puzzling aspect of this aforementioned conclusion regarding $\Delta\kappa$'s dependence on $1/n$ and modulus is that the magnitude of the modulus of the TR samples decreases when hydrated as compared to its state in ambient conditions, which is not consistent with the observed increase in κ when hydrated. Our aforementioned posit was that the increase in κ with hydration was due to an increased contribution of the chain transport dynamics to the overall thermal conductivity. To investigate these vibrational dynamics, we turn to elastic and quasielastic neutron scattering (QENS). QENS can measure

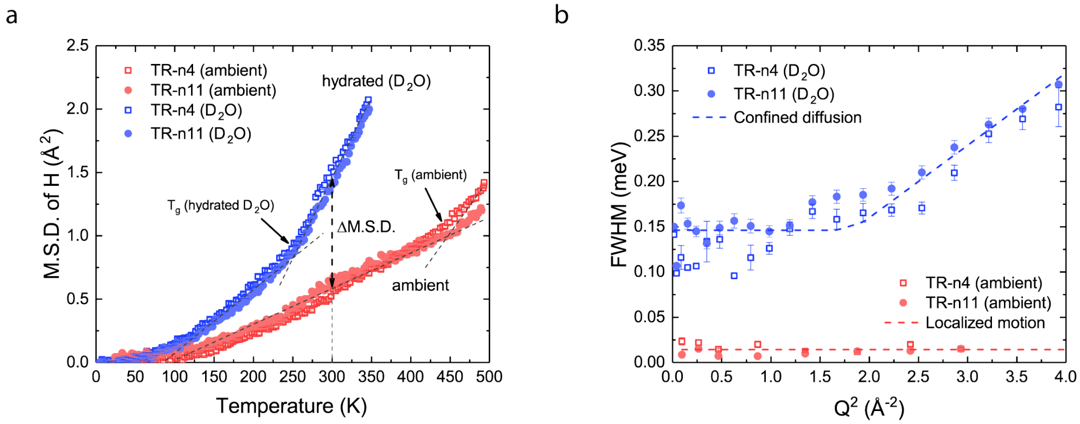

Figure 5.6: Quasielastic neautron scattering: a) The measured mean-square displacement, or vibrational amplitude, of hydrogen atoms in the TR films as a function of sample temperature. As seen, the dense, hydrogen-bonded network opens up and allows for increased movement upon hydration. b) The full-width half-maximum of the quaselastic peaks of the ambient and hydrated proteins as a function of the square of the scattering wave vector, Q^2. Error bars represent one standard deviation.

molecular dynamic processes such as rotations, relaxations, and diffusive motions with 1 - 30 Å and pico- to nanosecond resolution by directly probing the self-diffusion of hydrogen atoms [321]. The hydration dynamics were measured using deuterated water (D_2O) to differentiate water and protein dynamics since deuterium is invisible to neutron scattering due to its negligible scattering cross-section yet can still plasticize the TR proteins as H_2O does. The mean square displacement (MSD, Figure 5.6a) of hydrogen atoms in the protein were calculated from the elastic scattering intensity as a function of the scattering wave vector, Q, and temperature, T, through the Debye-Waller factor [322].

TR polypeptides in ambient conditions show very localized motions at $T > 70$ K, which is common for proteins and is typically originated by methyl group rotations [323], and exhibit a glass transition around 450 K. Therefore, neutron spectroscopy does not show any segmental or backbone motion at room temperature (300 K). Thus, the disordered chains are constrained in a dense hydrogen bonding network with minimal vibrational freedom. Conversely, in the hydrated state, the MSD increases and we observe much larger vibrational amplitudes, as well as a decrease in the glass transition temperature (250 K) [324]. In this case, the water molecules break the hydrogen bonding between the disordered chains, allowing for more delocalization of the hydrogen motion. Protein chain dynamics were further investigated by quasielastic measurements. Figure 5.6b shows the full width half maximum, Γ(Q), of the quasielastic peaks of ambient and D_2O-hydrated TR-n4 and TR-n11 proteins, plotted as function of Q^2. In ambient conditions ($<$ 1% relative humidity during our QENS measurements), TR proteins show a Q-independent behavior (15 μeV) characteristic of localized motions (i.e., methyl group rotations [323]). On the other hand, D_2O-hydrated TR proteins show a Q-independent plateau at low Q values (0.15 meV), while a linear scaling with Q^2 is observed at higher Q. This two-regime Q-dependence is characteristic of diffusion in a confined space and can be described by the Volino and Dianoux (VD) model for bounded diffusion in a potential of spherical symmetry [325], which corresponds to confined diffusive motions of the amorphous segments within the β-sheet nanocrystals.

5.2.4 Nanoscale Heat Transport Mechanisms

Our results can be conceptually interpreted under previous formalisms for vibrational heat transport in disordered systems [326], where the thermal conductivity is driven by the mode diffusivity [31, 326, 327]. In disordered systems, under the taxonomy developed in Ref. 29, heat transport is driven through interactions of quasi-localized diffuson modes, and the mode diffusivity of these diffusons are directly related to the MSD. Thus, the increase in MSD of the TR proteins upon hydration, which we attribute to increased motion of the amorphous strands, is the origin of the increase in κ from ambient to hydrated states shown in Fig. 5.4b. However, this increase in MSD is found to be independent of the number of repeat units, n, and thus it cannot explain the monotonic increase in thermal conductivity with increasing tandem repetition measured upon hydration of the TR films. The linear dependence on $1/n$, however, is driven by the change in modulus of the samples, and indeed, is a competing factor that is decreasing the thermal conductivity, consistent with theory[326] in that the mode diffusivity is directly related to the force constants. However, the increase in κ due to the increase in MSD outweighs the decrease due to modulus changes, and thus a net increase in $\Delta\kappa$ is realized upon hydration.

As a first approximation for the accuracy of this qualitative picture, we further consider these data from the framework of the changes in heat capacity and mode diffusivity of the diffusons upon hydration. The thermal conductivity of the diffusons are given by [76, 328] $\kappa_{\text{diffuson}} = \Sigma_{\omega} C_{\omega} D_{\omega}$, where C_{ω} is the diffuson heat capacity of a given mode with frequency ω per volume and D_{ω} is the diffuson diffusivity per mode. As detailed in Ref. 326, the diffuson diffusivities are proportional to the square of the heat current operator, $|S_{ij}|^2$, which measures the thermal coupling between vibrational modes i and j based on their frequencies and spatial overlap [31]. Mathematically, S_{ij} is directly proportional to $(\mathbf{R}_i - \mathbf{R}_j) = \Delta\mathbf{R}$, or the change in the average positions of atoms i and j. Thus, summed over all modes, the measured MSD from our neutron scattering experiments is proportional to $|S_{ij}|^2 \sim \Delta\mathbf{R}^2 \sim$ MSD. Furthermore, S_{ij} of the diffusons is also related to the interatomic spring constants of the system, K. Given the group velocity of a material is a measure of its relative stiffness and displacement changes in the continuum limit, we assume that the group velocity is proportional to the spring constant ($K \sim v^2$). Thus, we approximate the square of the heat current operator as $|S_{ij}|^2 \sim (MSD)v^4$. While the aforementioned trends in elastic moduli provide a qualitative understanding of the change in stiffness in this thermal switch, the complex, highly anisotropic nature and viscoelasticity of the bio-polymer films leads to issues in attempting to relate the measured modulus to a nominal sound speed of the material in the two states (i.e., the group velocity of coherent thermal carriers). To overcome this difficulty, we perform time-domain Brillouin scattering measurements on the TR films in ambient and hydrated conditions. This spectroscopy technique provides a direct measurement of longitudinal acoustic waves, i.e., long wavelength vibrational modes, traversing the viscoelastic TR films, as described in the Appendix. With this and the measured heat capacities, we can approximate the change in thermal conductivity of our samples upon hydration by examining the ratio of

$$\frac{\kappa_{hydrated}}{\kappa_{ambient}} = \frac{\Sigma_{\omega} C_{\omega,h} D_{\omega,h}}{\Sigma_{\omega} C_{\omega,a} D_{\omega,a}} \approx \frac{C_h |S_{ij}|_h^2}{C_a |S_{ij}|_a^2} = \frac{C_h (MSD)_h v_h^4}{C_a (MSD)_a v_a^4} \tag{5.5}$$

The respective values for the volumetric heat capacity, speed of sound, and MSD for TR-n4 and -n11 are tabulated in Table III of the Appendix; given such, we predict switching ratios of $\sim$3.70 and $\sim$4.90, respectively.

It should be noted that the switching mechanism cannot be explained with an effective medium approximation. In typical composite materials, hydrating the host system would not allow for a thermal conductivity greater than that of water; the thermal conductivity can only scale between, or be less than, that of either the host material (which, in this case, would be the TR films) and/or the 'inclusions' (i.e., the added water). In the TR films, the change in thermal conductivity is not due to a composite effect between the protein and the added water; the change in thermal conductivity is associated with a change in protein dynamics upon hydration, whereby the material is physically, yet reversibly, altered to a state that allows for increased anharmonicity and thus increased thermal conductivity.

These large and reversible changes in κ of the TR samples upon hydration present a unique opportunity to design thermal conductivity switches. Figure 9.6a shows the thermal conductivity of TR-n25 with repeated hydration and water removal. These data demonstrate the relative measurement speed of this switch, which is on the order of seconds. We note that the change in thermal conductivity of hydrated to ambient states is reversible over several switching cycles, as shown in the data in Fig. 9.6b for thermal conductivity as a function of cycle number for TR-n11. We note that the nearly factor of 4 change in κ is the largest reported in any solid system at room temperature, offering a unique material platform to realize robust thermal conductivity switches. To quantify the dynamic control of thermal conductivity, we consider the ratio associated thermal switching, i.e., $\kappa_{max}/\kappa_{min}$; in the case of our TR protein films, this ratio is $\kappa_{hydrated}/\kappa_{ambient}$. We plot this ratio as a function of temperature for wide-range of thermal switches within a biologically-relevant temperature window ($\sim$260 K - $\sim$380 K), including our TR material studied in this work, in Fig. 9.6c. We find our SRT-based TR proteins provide one of the largest figure-of-merits associated with thermal switching within this range compared to inorganic materials that show phase transitions. Looking ahead, by extrapolating the linear trend with $1/n$, we hypothesize this switching ratio can achieve values as large as $\sim$4.5 for TR films as the repeating units approaches infinity and a perfect network is formed.

5.2.5 Conclusions

In summary, we find that tandem repetition of DNA sequencing provides a means of programming thermophysical properties of the synthesized material. Furthermore, due to the physical topological network associated with our synthetic, SRT-mimic films, rapid and reversible ‘switching’ is enabled through hydration of the material. These results can be conceptually understood from the perspective of previous formalisms of heat transport in disordered systems; quantifying the ratio of thermal conductivities for the hydrated and ambient states with a simplified diffuson model finds good agreement with experimental results. In considering the figure-of-merit associated with the variable thermal conductivity between the pristine and hydrated state of the TR films, we find these bio-inspired materials exceed that of previous counterparts. Projecting these findings to a perfect network (i.e., when n approaches infinity), the thermal switching ratio is predicted to reach $\sim$4.5.

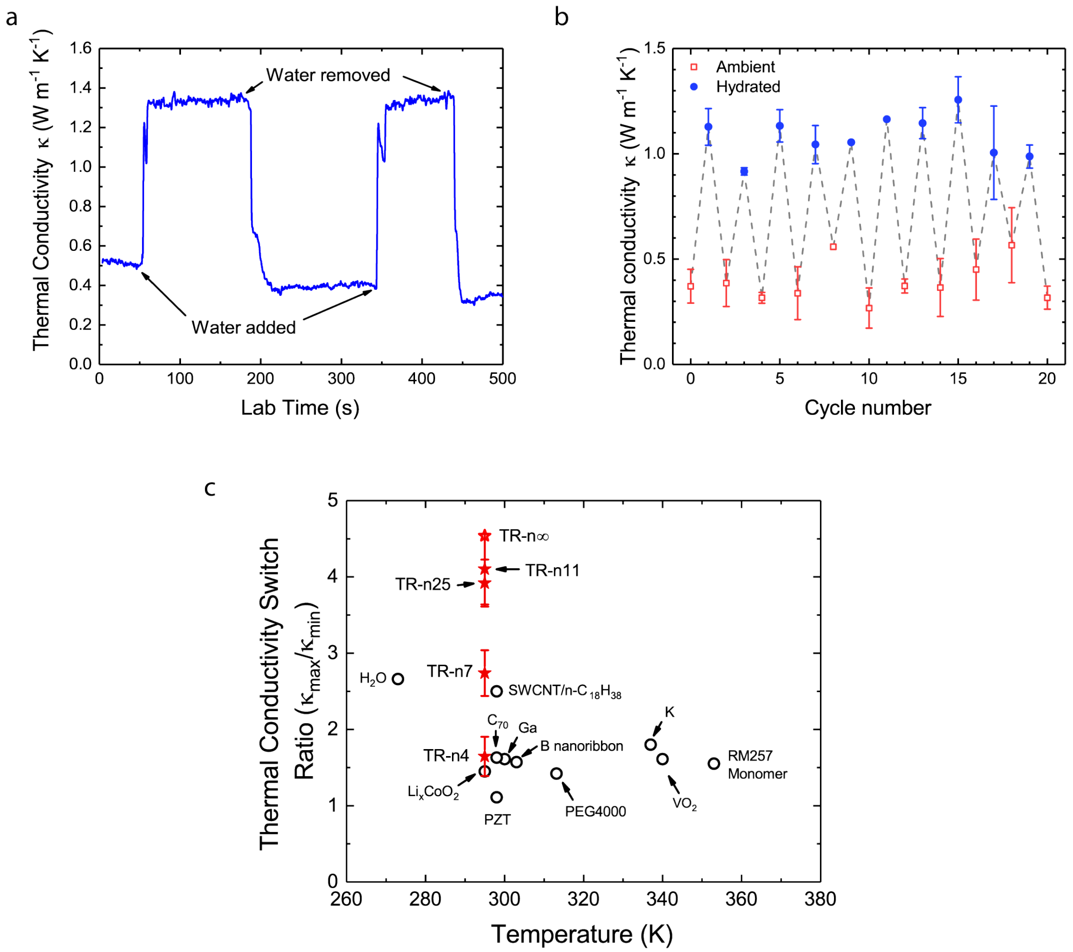

Figure 5.7: Metrics of thermal conductivity switching: a) The measured thermal conductivity as a function of real time, providing insight to the time-scale associated with switching for hydrated and ambient states for TR-n25. b) Measured thermal conductivity of TR-n11 over 20 hydration cycles shows high repeatability in switching capabilities. Error bars represent the standard deviation of three TDTR scans. c) The ratio associated with thermal switching ($\kappa_{max}/\kappa_{min}$) within a biologically-relevant temperature range; as seen, the TR films provide one of the largest switching ratios.

Chapter 6

Solid-Gas Interfaces

In this chapter, I extend the application of picosecond acoustic measurements to solid-gas interfaces as a measurement of the energy transmission/thermal boundary conductance between gold and Argon. These results are interpreted within a newly-developed framework of the acoustic mismatch and diffuse mismatch (AMM and DMM, respectively), derived specifically for the transmission of acoustic waves generated during a picosecond acoustic experiment and transmitted from a solid into an adjacent gaseous phase. This work is in preparation for submission to the *Journal of Physical Chemistry Letters*.

6.1 Background

The exchange of energy between a solid surface and adjacent gas molecules is a prerequisite for a range of fundamental processes and applications, including: thermal mitigation of electronic devices and nanostructures via convection, deposition methods accessed with vapor adsorption (both chemical and physical techniques), and even for consideration of drag coefficients in moving bodies [329]. At a continuum level, this interfacial heat transfer is understood through convection, as the coupled heat-mass transfer of a moving fluid is the dominant heat transfer process; this is similar to our case of solids, where the interfacial thermal resistance plays a negligible role until the dimensions of the system are greatly reduced. Indeed, non-continuum heat transfer effects arise when the characteristic length scale of the system become comparable to the mean free path of the gas. Thus, a detailed description of the nanoscopic energy transfer mechanisms across a solid-gas interface are necessary in not only systems with reduced dimensionality (e.g., nanostructures), but also systems immersed in low pressure gases due to the inverse relationship of gas pressure and the molecular mean free path.

To gain insight to the rate of energy transfer across a solid-gas interface, we can consider a flux of gas molecules impinging upon a solid surface. If the incident gas molecules were to 'stick' to the surface without any reflections, the entirety of the molecule's momentum, and thus energy, would have been transferred to the solid body. In this simple scenario, the rate of energy transfer is nothing more than the incident energy flux (e.g., the average energy per gas molecule times the particle flux). In a more physically-relevant scenario, where the molecules only transfer a fraction of their energy and reflect upon interaction with a solid surface, it should not be surprising that the primary descriptor for this non-continuum rate of energy transfer at a solid-gas interface is given by [330],

$$\alpha = \frac{\langle E_f - E_i \rangle}{\langle E_s - E_i \rangle}, \tag{6.1}$$

where E_i and E_f are the average molecular energies of the incident and scattered gas particles, respectively, and E_s is the energy flux that would be achieved if the reflected molecules were in thermal equilibrium with the solid surface post-scattering. The descriptor, α, varies from zero (adiabatic, specular reflection) and unity (perfect accommodation), and is termed the *accommodation coefficient*. Not only is this formalism reliant upon the flux of gas molecules being well-described by a single-temperature (or average energy), but it should be noted that it typically does not provide *apriori* prediction of heat fluxes unless a pre-existing, detailed knowledge of solid-gas interactions are already known.

It is important to note the extensive volume of literature that has investigated this exchange of kinetic energy at the solid-gas interface via beam scattering experiments [331–335]. These ultra-high vacuum studies are typically performed on 'clean' metal surface, where the greatly reduced pressures facilitate ballistic propagation of gas molecules from a source to the sample as well as sample to the detector. These studies have provided valuable insight to gas-surface interactions; for example, these studies have demonstrated that kinetic energy is more readily transferred when the mass of the incident atom is similar to the mass of the atoms comprising the solid surface [336, 337]. Despite such insight, it is critical that similar understanding of gas-solid dynamics is achieved at near-atmospheric pressures, due to both technological relevance and the transfer to a diffusive nature of the interactions.

To this end, there is an intrinsic difficulty in experimentally-resolving the energy transfer rates at solid-gas interfaces in ambient conditions. First, the measurement must have spatial resolution on the order of the characteristic length scale of energy transport ($\sim$sub-micron for atmospheric conditions); the experimental method must be capable of resolving both flux and temperature distributions at this scale without altering heat flow. Similarly, the temporal resolution must be adequate for resolving the proper mechanisms of heat transfer at the solid-gas interface; at ultrafast (TDTR) timescales, there is insufficient time for mass transport to occur, and the technique is only capable of resolving conductive heat transfer mechanisms. On the contrary, steady-state methods can measure a heat transfer coefficient that is dominated by convection, as it is the primary heat transfer pathway in gases due to the phase's intrinsically-low thermal conductivity. Lastly, due to the comparatively low heat transfer coefficients associated with solid-gas interfaces (< 1 MW m^{-2} K^{-1}) relative to those at solid-solid interfaces (typically > 25 MW m^{-2} K^{-1}), or conduction in bulk solids, it is difficult to decouple the weak heat loss to the gas relative to that of the supporting substrate.

While traditional TDTR/FDTR and related thermoreflectance metrologies are encumbered by these considerations, there are certainly aspects of these methods that are well-suited for measurements of energy transfer at solid-gas interfaces. For example, the use of focused laser pulses allows for highly localized measurements of energy transfer, allowing for resolution of flux and temperature measurements on the order of the length scale of interest. Rather, primary limitation in these methods is in analysis of the heat transfer coefficient with the multilayer thermal model prescribed in Chapter 2, and the associated sensitivity analysis outlined in Chapter 3; heat conduction into the solid substrate in TDTR measurements dominates the thermal decay curve, leading to negligible experimental sensitivity to the TBC of the solid-gas interface. Thus, in this chapter, we apply an altered pump-probe schematic that provides enhanced sensitivity to the measurement of acoustic phonon propagation (i.e., picosecond acoustics) in a solid metal film in contact with a gas. Because acoustic phonons are the primary thermal carrier in metals that drive the TBC across metal/nonmetal interfaces, the damping of such modes upon interactions with the solid/gas interface provides a metric describing energy transport across this interface. Here, we perform these picosecond ultrasonic measurements on Au/Ar interfaces at a range of pressures and temperatures to investigate the nature of heat transfer across solid-gas interfaces. Our choice of an Au transducer is due to both its large piezo-optic coefficient, thus enhancing the signal associated with acoustic wave propagation in the film, as well as the inert nature of Au. Similarly, the use of a noble gas mitigates chemical interactions/bonding and allows for invocation of the ideal gas law. For interpretation of our experimental results, we consider the scattering limits of heat transfer across a solid-gas interface by deriving the energy generated and transmitted during a picosecond acoustic experiment when specifically considering the energy flux at a solid-gas interface.

6.2 Picosecond Acoustics

To overcome the lack of sensitivity of TDTR's thermal model to the TBC of an interface composed of materials with high thermal resistances, we instead perform picosecond acoustic measurements in which we probe the damping of acoustic phonon modes in the solid layer upon their interaction with the solid-gas interface. This measurement allows for optical detection of acoustic modes through the piezo-optic effect of energy coupling between the solid film and contacting layers [201, 262, 274], and can be applied outside of thin films, as demonstrated in various material systems including polymers and other amorphous materials [274–277], semiconductors [278–280], and superlattices [281, 282]. The time-dependent intensity of these picosecond acoustic signals can be described via[125]

$$I(t,T) = A\exp(-\Gamma t)\cos((2\pi/T)t - \delta) - B\exp(-t/\tau) \tag{6.2}$$

where A, B, and δ are scaling factors, Γ is the damping due to interfacial energy transfer, T is the period of the pressure front, and the second term, $\exp(-t/\tau)$, accounts for the thermal decay rather than the signal associated with the acoustics. Fitting this equation to the picosecond acoustic signal over the first nanosecond of pump-probe delay time provides us with two important variables: the period, T, and damping, Γ, of the acoustic modes. After these values are obtained, the transmission of these acoustic modes across the solid-gas interface can be determined as

$$transmission = 1 - \exp(-\Gamma t) \tag{6.3}$$

Although these acoustic signals inherently exist in TDTR, as the pump *always* creates an acoustic wave propagating through the metal film due to the rapid heating/cooling of the metal layer, its detection is sometimes non-trivial due to low piezo-reflectance coefficients or in cases of highly damped interfaces. To enhance the picosecond acoustic signal, we make two major adjustments to our standard TDTR detection scheme: the film is moved out of the Rayleigh length of the focused probe beam waist and a partially-closed iris is implemented just before the photodiode. In moving the sample to the linear regime of a focusing beam, as the strain wave propagates to the surface of the transducer, a larger change in spot-size occurs at the sample surface. This deviation in spot-size is more easily detected with the addition of an iris prior to the photodiode; as the back-reflected probe beam is focused to the photodiode surface, the iris partially clips the edges of the beam. With changing spot size, the spatial variation leads to increased (or decreased) portions of the beam being cut-off by the iris [133]. This deviation is then translated to a change in signal at the photodiode.

6.3 Results and Discussion

We perform these picosecond acoustic measurements on 20 nm Au films deposited on crystalline Al_2O_3 substrates in varying Argon gas environments to investigate the mechanism of solid-gas interfacial thermal transport. An example of these experimental data is shown in Fig. 6.3a and Fig. 6.3b, including a best-fit curve of Eq. 6.2. From these best-fit of Eq. 6.2 under varying experimental conditions, we can calculate the interfacial acoustic transmission coefficient via Eq. 6.3. At a given temperature, we find the acoustic transmission generally increases with both the pressure and temperature of the Ar gas (see example in Fig. 6.3b). Conceptually, this may be understood simply as the fact that there is an increase in the number of molecules impinging upon the solid surface with increasing pressure, thus increasing the number of ‘carriers’ capable of transferring heat from the solid to the gaseous environment (recall: $n \propto P$). However, at constant pressure, the molecular density decreases with increasing temperature, invalidating this simple approximation. To gain a more robust understanding of the fundamental mechanisms of acoustic energy transfer from the solid surface to the surrounding gas environment, we turn to models capable of accounting vibrational states of both species.

Similar to the limits of the thermal accommodation coefficients, there are two primary models used for the understanding of heat transfer across an interface. While both rely on a description of the primary heat carriers in most solids, acoustic phonons, the underlying physics are drastically different. On one end is the acoustic mismatch model (AMM), where only the acoustic impedances of the two medium comprising the interface are considered; this explicitly describes the transmission of acoustic waves with only consideration of the sound velocity and density of the medium ($Z = \rho c$). The extension of this model to a solid/gas interface is rather straightforward and based on nothing more than classical acoustics. For dispersionless phonon energies in a solid, the AMM-predicted transmission

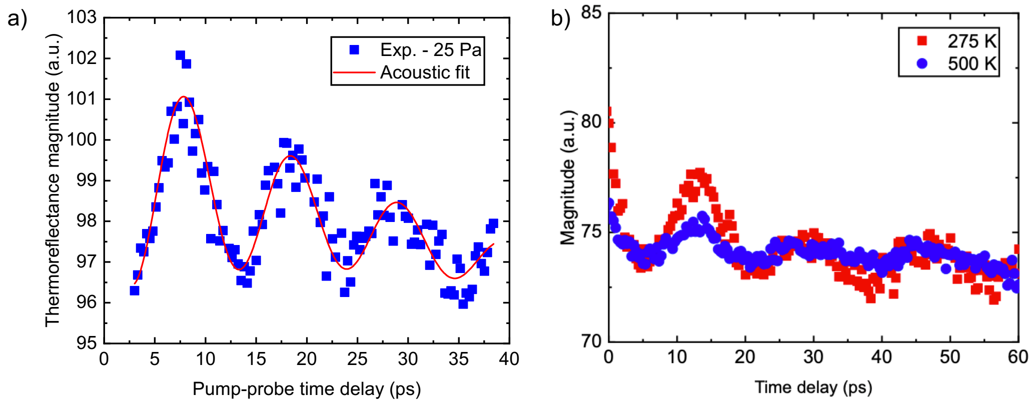

Figure 6.1: a) Example data of our experimental picosecond acoustic data (blue squares) for a 20 nm Au film on a sapphire substrate in a 25 Pa, 300 K Ar environment, including the line of best fit of Eq. 6.2 (red line). b) Comparison of experimental picosecond acoustic data at 275 K (red squares) and 500 K (blue circles); note, the pressure is constant for the two cases.

from the solid to the gas is given by

$$\zeta_{s\to g,AMM} = \frac{4Z_sZ_g}{(Z_s+Z_g)^2} = \frac{4\rho_sc_s\rho_gc_g}{(\rho_sc_s+\rho_gc_g)^2} \tag{6.4}$$

where ‘s’ and ‘g’ refer to the properties of the solid and gas, respectively. While the acoustic impedance of solids is relatively constant over a range of moderate environmental conditions, this is the not the case for Z_g. For a given volume of gas, the mean particle velocity and density will vary with both pressure and temperature. For the case of an ideal gas, the pressure, P, and temperature, T, dependence of ρ_g and c_g can be obtained from Kinetic theory, providing the acoustic impedance in terms of its pressure and temperature as

$$Z_g = 2P\sqrt{\frac{2m_g}{\pi k_BT}}. \tag{6.5}$$

As we are specifically interested in the energy flux of acoustic carriers generated in a picosecond acoustic experiment, we want to investigate the impedance specifically associated with these excited carriers. In our picosecond acoustic experiment, we excite a bandwidth of phonon frequencies that are centered around a specific phonon frequency, ω_{ps}, based on the thickness of the thin metal film transducer ($\omega_{ps} = 2\pi c_L/d$, where c_L and d are the longitudinal speed of sound and the thickness of the thin metal film, respectively. Thus, we define a frequency dependent acoustic impedance of the solid as

$$Z_{s,\omega} = \frac{\hbar\omega}{c_L} f_{BE} \frac{\omega^2}{2\pi^2 c_L^3} \tag{6.6}$$

where the denominator of the rightmost expression is simply the Debye density of states of the Brillouin zone center longitudinal acoustic modes and f_{BE} is the Bose-Einstein distribution function. Thus, in a picosecond acoustics experiment, the acoustic impedance of the mode excited in the thin film transducer is

$$Z_{s,\omega_{ps}} = \frac{2h}{d^3 c_L(\exp(\frac{hc_L}{k_B T d}) - 1)} \tag{6.7}$$

where h is Planck's constant and k_B is Boltzmann's constant. Thus, the energy transmission of acoustic waves from the film transducer to a gas during a picosecond acoustic experiment is given by

$$\zeta_{\mathrm{s}\rightarrow\mathrm{g},\omega_{\mathrm{ps}}} = 16 \frac{\dfrac{hP}{d^3 c_{\mathrm{L}}\left(\exp\left[\dfrac{hc_{\mathrm{L}}}{k_{\mathrm{B}}Td}\right] - 1\right)}\sqrt{\dfrac{2m_{\mathrm{g}}}{\pi k_{\mathrm{B}}T}}}{\left(\dfrac{2h}{d^3 c_{\mathrm{L}}\left(\exp\left[\dfrac{hc_{\mathrm{L}}}{k_{\mathrm{B}}Td}\right] - 1\right)} + 2P\sqrt{\dfrac{2m_{\mathrm{g}}}{\pi k_{\mathrm{B}}T}}\right)^2}. \tag{6.8}$$

Note, as the AMM is derived under the assumption of specular interactions of acoustic waves, these functions inherently assume specular transmission. However, on the other end of the scattering extreme lies diffusive scattering of energy. The energy transmission in this diffusive regime is commonly described via the aforementioned diffuse mismatch model (DMM).

The DMM predicts the transmission of energy across an interface based on the ratios of the vibrational densities of states of the materials adjacent to the interface. From the principle of detailed balanced, combined with the definition of diffusive scattering applied to the power fluxes of the solid and gas at the interface, the transmission of energy from the solid into some thermal bath of gas molecules at the interface is given by

$$\zeta_{s\rightarrow g,DMM} = \frac{q_g}{q_s + q_g} \tag{6.9}$$

where q is the power flux spectrally integrated over all energies. In a picosecond acoustic experiment, the spectral energy flux is centered around the acoustic frequency, ω_{ps}, thus, we define the spectral power flux at this frequency, $q_{s,\omega_{ps}}$, as

$$q_{\mathrm{s},\omega_{\mathrm{ps}}} = \hbar\omega_{\mathrm{ps}} \frac{\omega_{\mathrm{ps}}^2}{2\pi^2 c_{\mathrm{L}}^3} \frac{1}{\left(\exp\left[\frac{\hbar\omega_{\mathrm{ps}}}{k_{\mathrm{B}}T}\right] - 1\right)} c_{\mathrm{L}} = \frac{2hc_{\mathrm{L}}}{d^3\left(\exp\left[\frac{hc_{\mathrm{L}}}{k_{\mathrm{B}}Td}\right] - 1\right)}. \tag{6.10}$$

The power density of the monoatomic molecular gas impinging the solid interface is derived in a previous work [273] and is given by

$$q_g = \frac{4P}{m_g k_B T} \int_0^\infty \varepsilon(\frac{\varepsilon}{k_B T})^2 (\frac{2\varepsilon}{m_g})^{-\frac{1}{2}} \exp[-\frac{\varepsilon}{k_B T}] d\varepsilon. \tag{6.11}$$

Simply by inspection of these AMM and DMM transmission functions derived for solid-gas interfacial energy transfer during a picosecond acoustic experiment, one can see the two have inverse dependencies with increasing temperature; the AMM predicts an increasing energy flux with increasing temperature, whereas the DMM predicts an inverse relationship between TBC and environmental temperature such that flux decreases with increasing temperature. Interestingly, this DMM result is in contrast to the DMM-predicted TBC at solid-solid interfaces, where both experiments and theory display a clear increase in TBC with increasing temperature.

As we cannot directly deconvolve the transmission of acoustic waves into the sap-

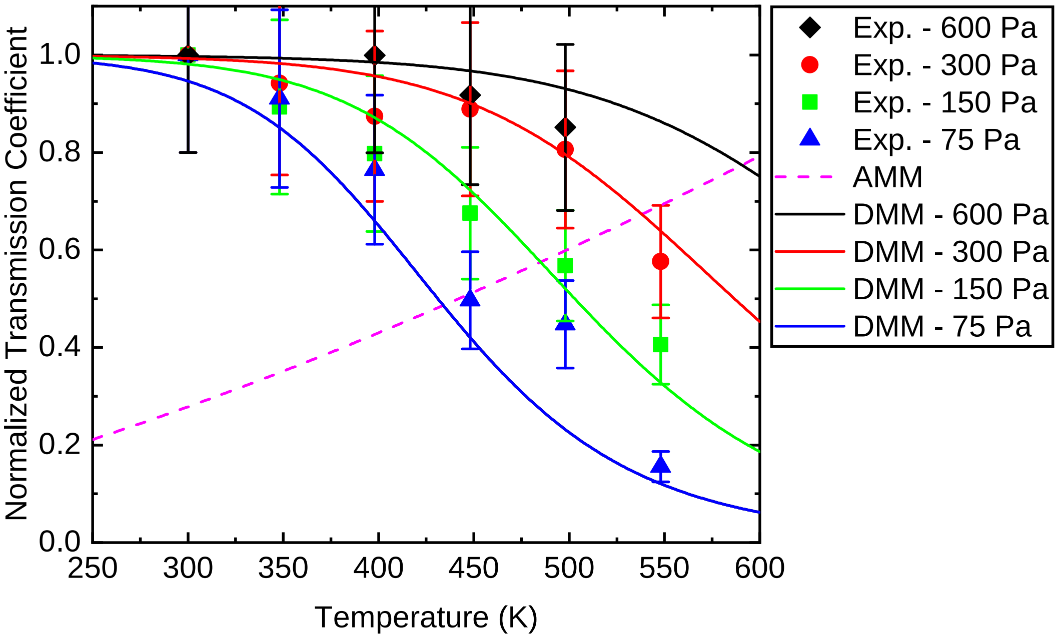

Figure 6.2: Measured acoustic transmission, normalized to the Ar/20 nm Au/sapphire net acoustic transmission measured at 300 K, as a function of both temperature and pressure. These experimental data are compared to the transmission function derived for the AMM (dashed line) and DMM (solid lines) to understand the nature of heat transfer at solid-gas interfaces.

phire substrate from their transmission to the gaseous medium, we normalize the measured acoustic transmission, calculated via Eq. 6.3, to the transmission measured at 300 K. We compare these normalized data to the models derived above in Fig. 6.3. Given the inverse trends in temperature for the AMM and DMM, there is little requirement for interpretation of these results: the measured acoustic transmission for Au/Argon interfaces is found to be in strong agreement with the DMM transmission function derived above. This result indicates that energy transmission for this relatively inert, ideal gas scenario is primarily diffusive in nature; vibrational carriers are scattering non-specularly at the solid-gas interface.

In addition to the mechanisms of heat transfer at the solid-gas interface, the use of picosecond acoustics appears to be a means of quantifying gas adsorption upon a solid surface. To recognize this, we can consider the behavior of an ideal gas adsorbate under isothermal conditions. Namely, we consider the empirical Freundlich equation with relation to our experimental picosecond acoustic data. This adsorption isotherm takes the form

$$\theta_{occupied} = kP^{1/n} \tag{6.12}$$

where k and n are constants the describe the system, both adsorbate and adsorbent, at a given temperature, P is the pressure of the gas, and $\theta_{occupied}$ is the number of 'sites' occupied by adsorbates on the solid surface. As a first approximation, we consider an assumption in which the acoustic transmission is linearly proportional to the number of occupied sites. A comparison between our experimental data and Eq. 6.12 is shown in Fig. 6.3, where reasonable agreement between the two is observed. This finding is critical for two reasons. First, this result indicates that the acoustic energy transmitted from a solid surface to an adjacent gaseous environment is directly related to the adsorption of the species upon the surface; with an increasing number of occupied sites, there is an increase in energy transmitted. Second, from an application perspective, these results show that the measure of interfacial energy transfer provides direct insight to the adsorption kinetics and

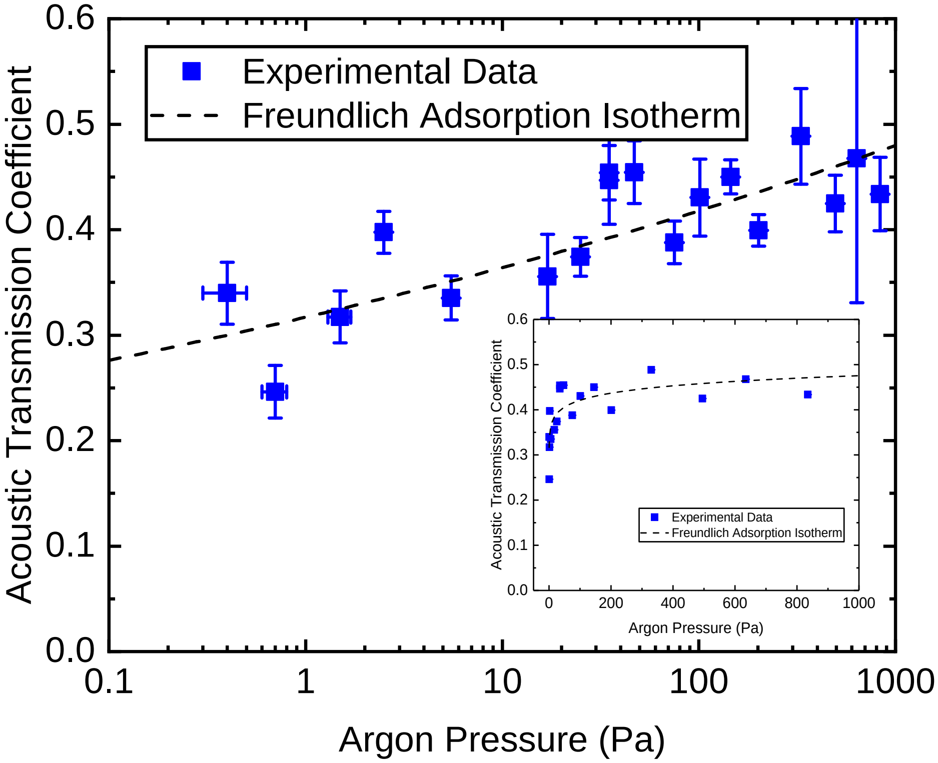

Figure 6.3: Measured acoustic transmission at 300 K as a function of Argon pressure (blue squares) in comparison to the Freundlich adsorption isotherm (Eq. 6.12, dashed line).

can be used as a means of both quantifying and monitoring adsorption.

Chapter 7

Solid-Plasma Interfaces

In this chapter, I present a time-resolved thermoreflectance study of plasma-surface interactions; this study is enabled by the development of a transient plasma-pump, laser-probe measurement technique and provides the first nanosecond-resolved measurement of energy transduction during plasma-surface interactions. Specifically, I elucidate upon the first experimental observation of plasma-induced cooling of a target surface. This work is an extension of our initial work on plasma-surface interactions in which we monitor the ‘steady-state’ energy transfer from a plasma to a Au surface using time-domain thermoreflectance [15], and is in preparation for submission to *Science*.

7.1 Introduction

Plasmas have long been used for the synthesis [338] and manipulation [339–341] of materials because of their unique ability to deliver both energy and chemically-active species to the surface of plasma exposed materials - an attribute that separates them from other approaches to materials processing. Indeed, the energy flux serves to drive the surfaces out of thermal equilibrium with the bulk material, thus enabling local physicochemical processes that can be harnessed to remove (etch) substrate material, deposit different material, or chemically modify the surface. Aside from intentional material modifications, understanding energy delivery at the plasma-surface interface is critical for an array of technologies such as nuclear fusion, where plasma-facing materials must meet complex, yet strict, requirements to avoid degradation from the aforementioned energetic processes [342]. While the benefits or detriments of energy delivery is commonly associated with an increase in temperature, the temperature, is in fact, the net result of the difference between energy delivered to and released from the surface. This can be understood by considering the power balance at the surface [343],

$$P_{in} - P_{out} = P_{absorbed} \tag{7.1}$$

where the power delivered to (P_{in}) and released from (P_{out}) the surface is determined by the flux of energetic particles and radiation arriving at and leaving the surface, along with endothermic and exothermic reactions occurring at the plasma-surface interface. The difference between P_{in} and P_{out} is absorbed by the material (P_{heat}), with a temperature determined by the heat capacity of the material. Of course, the power balance does not dictate the energy delievered that the energy delievered to the surface must exceed that released from the surface. Indeed, the complex array of incident plasma species and chemical reactions at the surface could, in theory, enable local temperatures to both increase or decrease during plasma irradiation. This potential for *plasma cooling*, or the decrease in the temperature of a surface during plasma irradiation, would lead to novel avenues for microelectronic cooling, refrigeration, and temperature-controlled material processing.

Our current understanding of energy delivery from a plasma to a material surface is guided using a variety of ancillary plasma diagnostics [344], steady-state temperature measurements [345, 346], models [347, 348], and post-treatment, *ex-situ* surface characterization to 're-construct' energy deposition and absorption [343, 349, 350]. More recently, *in-situ* materials characterization techniques have been developed that allow for real time or quasi-real time analysis [15, 351]. While certainly of value, none of these approaches provide a direct measure of the localized, transient response associated with the energy flux at the surface. To observe plasma cooling, the transient thermal response of a material must be monitored to separate the localized and transient energy transport mechanisms from the

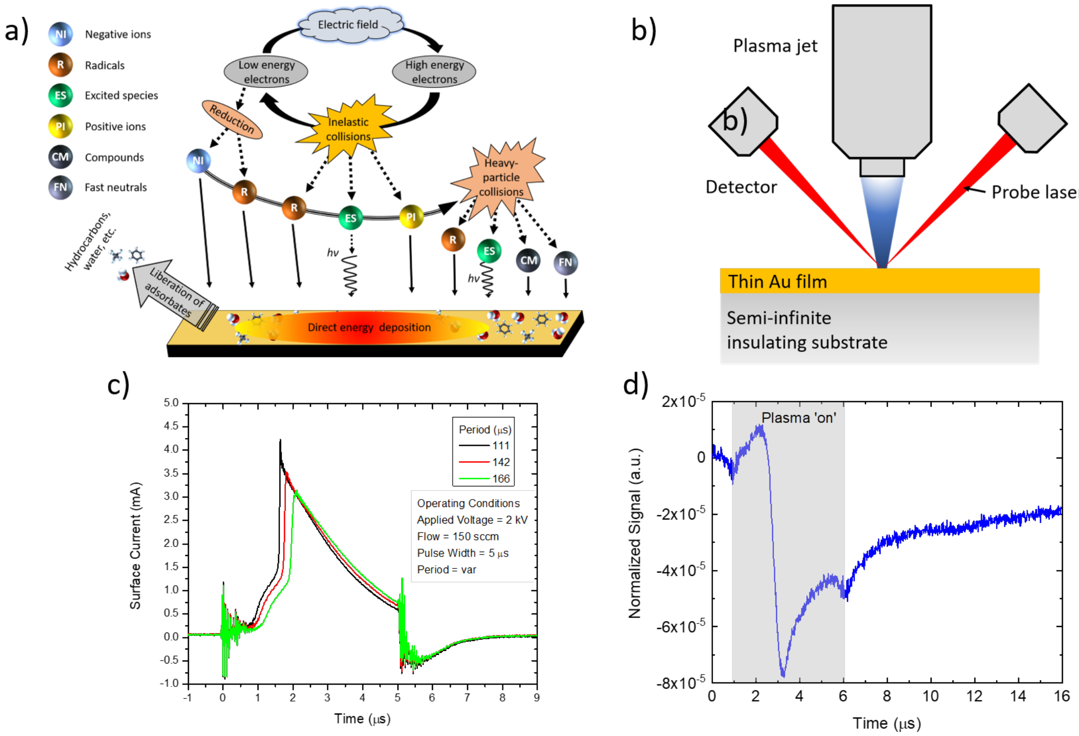

Figure 7.1: a) Experimental schematic. A pulsed atmospheric plasma jet bombards an Au surface, while a continuous wave laser monitors the thermoreflectance of the Au surface to gain insight to the plasma-surface energy transfer mechanisms. c) Measured thermoreflectance as a function of time for a 5 μs plasma pulse and d) the measured surface current at the Au film.

spatially and temporally averaged net power transfer and temperature rise.

In this work, we experimentally demonstrate the ability of an incident plasma to cool the surface of a material. While seemingly counterintuitive that an incident flux of energy would lead to a decrease in surface temperature, this plasma cooling is enabled by exposing a surface to a pulsed plasma, which allows the spectrum of different energetic processes associated with plasma exposure (Fig. 7.1 a) to be parsed in time and measured through time resolving the relative temperature changes occurring in a material exposed to a directed plasma with nanosecond resolution. Our experiment relies on a pulsed atmospheric pressure plasma jet incident upon an 80 nm Au film supported by a sapphire substrate. We simultaneously measure the reflectance of a continuous wave laser from the Au surface following the plasma-surface interaction (e.g., plasma pump - laser probe measurements);

a simplified schematic of our experimental configuration is shown in Fig. 7.1b. For the operating conditions in this work, there are negligible laser-plasma interactions, and the reflected beam is not affected by any direct interactions. Rather, we rely on the strong thermoreflectance coefficient of Au at visible wavelengths to directly measure the plasma-induced temperature change on the Au surface by means of lock-in detection at the plasma jet repetition frequency, with the use of a periodic waveform analyzer to obtain nanosecond time resolution during the plasma-surface energy transfer process. Furthermore, we note that we do not observe any changes in the *static* reflectivity of the Au surface; the reflectivity signals presented in this work are, in all cases, the differential reflectivity, which is the change in reflectivity of the Au surface relative to the un-perturbed reflectance (e.g., the reflectivity when no plasma is present).

The use of a thin Au film supported by an insulting substrate achieves two factors that are critical to understanding energy transfer at the plasma-surface interface. First, as Au is a noble metal and chemically-inert. Thus, there are minimal surface reactions (e.g., surface oxidation) that would alter the surface and distort the interpretation of energy deposition mechanisms. Second, as charge transfer and hot-electron effects occur on much faster time scales than investigated in this work, the insulating substrate ensures that charged species and electronically-driven energy transfer from the plasma to the metal surface remain localized to the surface of the Au film. This critical aspect ensures that the measured surface temperature is indicative of only plasma-Au energy transfer and subsequent thermal diffusion rather than ballistic mechanisms that traverse deep into the substrate [113, 352].

7.2 Results

In considering plasma interactions, there is incident flux of various species including charged particles, photons, as well as excited and reactive neutrals (Fig.7.1 a), which provides energy to the plasma-exposed material [343]. The flux of charged particles can be measured as a net surface current, as shown in Fig.7.1 c for our experimental system. In these example data, the plasma jet is produced by applying a high voltage for a duration of 5 μs; this voltage width will henceforth be considered the plasma ‘pulse-width.’ The delay in rise in current is due to the standoff between the biased electrode and the surface, as shown in Fig.7.1 b. Likewise, as the reflectance of Au is linearly proportional to temperature (e.g., $\Delta R = \beta \Delta T$, where β is the thermoreflectance coefficient of Au), we can directly measure the temperature rise induced by the flux of these various species; an example of our measured thermoreflectance data is shown in Fig.7.1 d. Note, the thermoreflectance coefficient for this laser wavelength (637 nm) is negative, and thus surface heating corresponds to a decrease in measured reflectance [78, 353].

A few salient features can be noted in each of these curves. First, at the beginning and end of the plasma pulse, an anomalous decrease in signal magnitude can be observed. We note that this is an artifact in our periodic waveform analyzer and *not* a true change in optical reflectance due to the plasma pulse; these features are present even when the laser is turned off and the photodetector is blocked. Second, a peak in reflectivity is observed at 2 μs. As the thermoreflectance coefficient at this laser wavelength (637 nm) is negative, this observation suggests a *reduction* in surface temperature at this time-frame. While a more in-depth discussion can be found below, it is important to note that the transfer of energy to a surface is expected to lead to an *increase* in surface temperature, as the flux of all species is directed into the surface. Third, there is a simultaneous, rapid increase of both the measured thermoreflectivity and surface current, around 3 μs followed by a transient decay.

As discussed above, the flux of various charged species incident upon the metal film results in a net current, which leads one to invoke Joule’s first law where there the power dissipated is proportional to the product of the resistance and the squared current (e.g., $P \propto I^2 R$). As with other current sources, this relationship explicitly leads to an increase in temperature, even without consideration of nanoscale effects and interactions. As the measured thermoreflectance is indicative of a change in the gold’s temperature, one should expect that the temporal derivative of this reflectivity trends with the current, since temperature is directly related to particle number density/charge, which is the temporal integrand of current (e.g., $R \propto T \propto Q = \int i \cdot dt$). Indeed, as shown in Fig.7.2 a, the temporal derivative of our thermoreflectance data is in excellent agreement with the measured current, and thus heating is primarily driven by simple inductive heating. We note the appearance of a periodic modulation in the reflectance derivative that is the result of numerical differentiation. In stark contrast is the strong deviation between current and derivative associated with the observed reduction in temperature around 1 μs. This leads to the obvious question: What could be the mechanism for this plasma-induced cooling?

7.3 Discussion

Although the notion of cooling resulting from an energy flux is seemingly counter-intuitive, there are a number of physical processes arising at the plasma-surface interface that are known to lead to a reduction in temperature. Thermionic emission, for example, has been theoretically devised as a refrigeration method, with potential efficiencies on par with Carnot cycles [354], it is nearly impossible to experimentally achieve at or near room temperature, with the exception of limited cases in select material systems such as superlattices [355] and 2-D heterostructures [356]. In the case of thermally-driven electron emission, the current emitted from a metal surface with work function ϕ at a temperature T is given by,

$$J(\phi, T) = AT^2 e^{-\phi/k_B T} \tag{7.2}$$

where $A = m_e k_B^2 / 2\pi^2 \hbar^3 \approx 120$ A cm^{-2} K^{-2} and k_B is Boltzmann's constant. In the case of Au, with a work function of over 5.25 eV, this leads to an exceptionally small current density, certainly impractical for effective cooling at operational temperatures; for a temperature rise of 1337 K (the melting temperature of Au), one would expect a current density of $\sim$ 34 nA m^{-2}. In the area probed in our experiments, approximately $\sim$150 μm^3, and the observed time of cooling (800 ns, see discussion of two-temperature model calculations below), there would be less than 2×10^{-20} electrons emitted from the surface; this corresponds to temperature reduction on the order of pico-Kelvins. Given such, we certainly would expect no cooling-effect from an atmospheric plasma jet due to thermal excitations.

Alternatively, there are two potential effects that could be leading to the observed cooling phenomenon. First, which has been recently shown to lead to a temperature decrease in high-repetition laser ablation[357], would be material ejection from the surface. It is well-known that plasma jets lead to modification of a material surface. In fact, when the jet used in this work is operated at higher power (much greater than reported here), we do see erosion of the Au film. In addition to potential sublimation of the Au surface itself, adsorbate desorption could be the underlying mechanism for observed cooling. It is well known, for example, that water will adsorb on Au surfaces even under UHV conditions [358], albeit in weakly bound physisorbed states ($<<$ 1 eV). In such a case, many species emanating from the plasma jet would deliver enough energy to liberate water molecules. This process is effectively plasma-induced evaporative cooling of the surface.

The second potential mechanism driving the observed cooling is in line with thermionic emission; the Nottingham effect, whereby electrons undergo field emission due large values of charge separation and is well-known to cool material surfaces could be playing a role [359]. Given the plasma induces a large flux of charged species toward the Au surface, it is possible that when these species are in close proximity to the metal, the potential exceeds the work function/Schottky barrier, and electrons are removed from the gold film.

During the observed cooling, the peak differential reflectivity is measured to be $\Delta R/R \approx 3\times10^{-5}$. Based on an array of previous works [78, 353], the thermoreflectance coefficients of thin Au films are of similar order, $\Delta R/\Delta T \approx 2-4\times10^{-5}$, indicating the observed cooling is on the order of approximately 1 K.

In the case of material removal for evaporative cooling, the process of atomic desorption from the target surface must occur prior to energy deposition into the bulk of the material. Based on the spot size ($\approx 55\mu$m) and skin depth ($\approx$ 15 nm) of our laser in Au, the probed

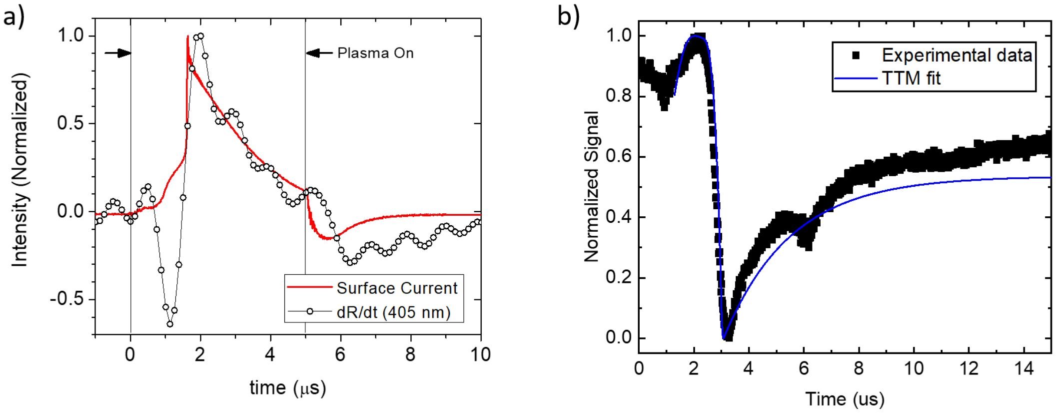

Figure 7.2: a) Measured surface current (solid red line) overlaid with the temporal derivative of the measured changed in reflectivity due to the plasma pulse. The two are in reasonable agreement, aside from the reduction in surface temperature around 1 μs, indicating Joule heating to be the primary mechanism of energy transfer from the plasma to the Au surface. b) Measured thermoreflectance data due to the plasma pulse (black dots) and two-temperature model calculations for the sample system (solid blue line). The observed cooling can be attributed to either removal of surface atoms of the Au or electron ejection from probed Au volume.

volume is $\approx$150 μm^3. Pairing this volume with the volumetric heat capacity of Au, $\approx$2.49 MJ m^{-3} K^{-1}, a local 1 K temperature reduction would require 0.37 nJ to be removed from the probed volume. At room temperature, a reasonable approximation to the average thermal energy of each particle in a solid is simply $3k_BT$, or $\approx 1.24\times10^{-20}$ J. With these values in mind, it would require 3×10^{10} atoms to be removed from the probed volume. If a uniform ‘sheet’ of atoms were removed across the probed area, this number of atoms corresponds to a single monolayer of material removed. With a heat capacity of $\approx$4.2 MJ m^{-3} K^{-1}, a similar temperature decrease requires sub-monolayer thicknesses, or non-uniform distributions, of water to be removed from the surface. This is certainly plausible given our measurements are conducted at STP [358] and so adsorption occurs at much faster time scales than the separation time between subsequent plasma pulses (tens of nanoseconds-to-microseconds for contaminant adsorption, compared to tens-to-hundreds of microseconds between each measured plasma pulse). Likewise, a mixture of adsorbed hydrocarbons (e.g., adventitious carbon) and water would be expected under these conditions.

We can repeat a similar analysis for the number of electrons that would need to be emitted for a 1 K temperature reduction within the probed volume of the Au; at the time-scales measured here, the electron and phonon temperatures can be considered in equilibrium, and thus the energy requirement for a temperature decrease remains dominated by the phononic heat capacity of Au, as used above. Nonetheless, one must consider the energy lost per electron; the average energy of an electron in a metallic system is approximately 3/5 of the Fermi energy ($\sim$5.5 eV for Au). Thus, to reach the 0.37 nJ necessary for a 1 K temperature decrease at room temperature, approximately 7×10^8 electrons would need to be emitted from the Au surface.

To gain insight into which of these mechanisms, if not some combination of the two, is driving the observed cooling process, we perform two-temperature model (TTM) calculations [285] for our experimental geometry; this method allows us to explicitly calculate energy losses/gains to the electron and lattice subsystems. While additional details can be found in the Supporting Information, we use the measured surface current as the heating source for the electronic subsystem, and the thermal properties (e.g., thermal conductivity and interfacial thermal resistances) of our 80 nm Au/Al_2O_3 are determined from time-domain thermoreflectance (TDTR) measurements. To simulate the atomic or electronic ejection, we supply a 'cooling' source that removes energy from either the phononic or electronic subsystem, respectively. While we ultimately find that atom or electron ejections can re-produce our experimentally-measured data with high accuracy (see Fig.7.2 b), these calculations provide insight into the time-scale of this cooling process; the best TTM fit to our data requires that the cooling occurs over 800 nanoseconds.

We must now consider the temporal flux of various species incident upon the Au surface (Fig.7.1 a) within these 800 nanoseconds. To properly understand this, we perform a series of time-resolved plasma diagnostic measurements; notably, our time-resolved photoemission experiments elucidate upon the only species present at the time-scales corresponding to the observed cooling: high energy photons. In other words, we find overwhelming evidence of sufficiently-high fluence of photons impinging upon the Au surface at the time scales corresponding to the observed cooling (Fig.7.3 a) and importantly, they are present prior to the dramatic rise in measured current. The difference is characteristic of a pulsed plasma jet, produced with a remotely located active electrode. While the excited species that relax via photon emission and the charged particles are simultaneously produced near the electrode when the high voltage is applied, the photons arrive at the surface well before the comparatively low-velocity charged species. The range of photons in a typical plasma produced in mixture of air and helium extend from IR to extreme UV, with energies that range from below one eV to above 20 eV. As some of these energies greatly exceed the work function of Au, photo-emitted electrons are certainly being ejected from the surface of the Au film. Likewise, photon-driven desorption is possible and has been shown in the water/Pd(111) system for much lower photon energies than observed in this work (6.4 and 5 eV) [360].

This observation of a photon-driven cooling mechanism is further supported by spatially-resolved thermoreflectance measurements. As shown in Fig.7.3b, we raster the plasma jet with respect to the position of the laser probe, allowing us to extract a spatio-temporal temperature profile. In agreement with our previous work [15], we observe a heating profile of ≈ 0.5 mm; this is approximately $1/3$ of the tube diameter of which the jet emanates from. More importantly, in this work, we observe cooling of the Au surface in regions extending beyond this heated width. This can be understood by recognizing the plasma is 'guided' by the helium flow leaving the tube, such that the majority of the plasma-produced particles arrive at the surface over an area dictated by the diameter of the gas flow/surface intersection. Conversely, the photons formed via spontaneous emission from excited species fromed as the plasma propagates toward the surface (Fig.7.1 a) have both random phase and direction, thus interacting with a much larger surface area. Hence, it is reasonable to see heating at the center of the impact point where charged particle interactions dominate and the photon-driven cooling at extended widths.

While a photon-driven process seems likely, both liberation of surface adsorbates and electronic emission can be supported by our experimental measurements, two-temperature

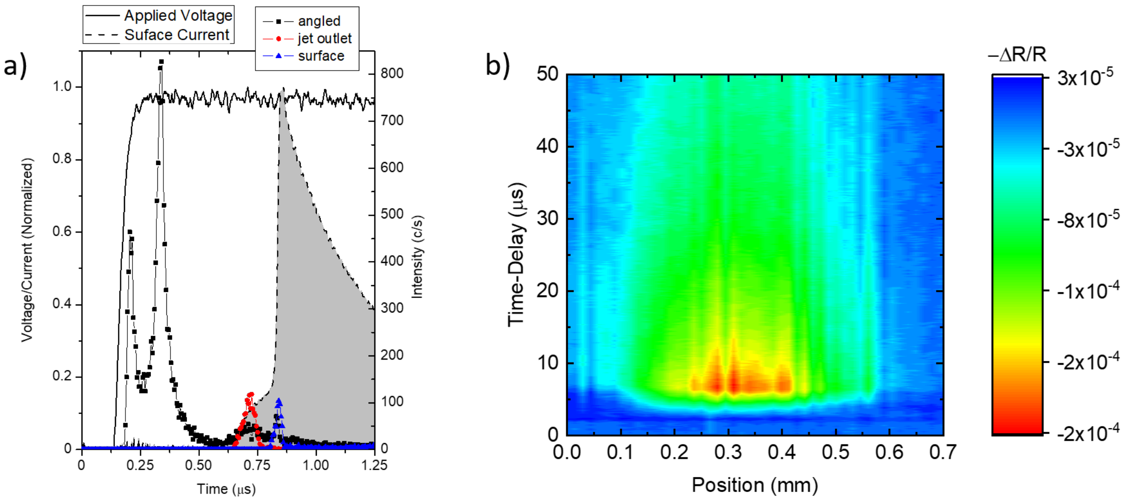

Figure 7.3: a) Angle-dependent, time-resolved emission measurements of He jet interacting with gold surface. The emission line is from He at 667 nm (3d to 3p transition). This line emanates due to a transition to an optically allowed state that produces a 58 nm photon. Thus, the 667 nm line becomes a proxy for the 58 nm line. b) Spatially-resolved thermoreflectance measurements of an Au surface. A width of 0.5 mm is heated from the flux of plasma species, while the observed photon-induced cooling extends to a much larger region.

analysis, and prior TDTR measurements. Discerning the potential contribution of the two processes requires additional considerations.

As the emitted photon wavelength greatly exceeds the work function of Au, it will certainly eject electrons from the surface of the Au film, and the small number of electrons necessary for a 1 K reduction in surface temperature is easily achievable even if only a small fraction of optically-excited electrons escape the surface. Likewise, photon-driven desorption is possible and has been shown in the water/Pd(111) system for much lower photon energies than observed in this work (6.4 and 5 eV) [360]. Thus, it is critical to consider the time of which these photons are present: both during the observed cooling at the beginning of the plasma pulse, as well as at the *end* of the pulse duration. If the cooling were dominated by electron emission, one should expect cooling to occur in both circumstances due to the large electron density of Au - yet cooling is only observed in the former situation. On the other hand, desorption would only occur during the first ‘pulse’ of photons, as the adsorbates will already have been liberated from the surface during the arrival of the second pulse occurring at the end of the plasma jet. Thus, evaporative cooling is the most likely mechanism of the demonstrated process of plasma cooling.

To further reinforce this plasma-induced evaporative cooling of a metal surface, we consider the relative heating and cooling contributions with varying plasma-jet parameters. For example, as the applied voltage of the electrodes is increased, we observe a corresponding increase in the measured surface current, as well as an increase in the peak temperature of our thermoreflectance measurements (Fig. 7.4a); these observations can be attributed to an increase in the flux of charged species formed during the jet formation with increasing voltage. However, the minimum temperature achieved during cooling is negligibly affected by these changes, at least within the regimes considered in this work. In other words, an increase in charged species incident upon the surface does not appear to affect the cooling profile. Yet, the flux high energy photons responsible for either desorption or electronic emission will be increasing under this change in plasma parameter - the cooling effect has become saturated (e.g., the population of electrons or adsorbates responsible for cooling has been entirely evacuated in the probed region) and the additional flux does not play a role. A similar observation is observed with varying widths of the plasma pulse, whereby the net cooling magnitude is relatively constant above some voltage width, but is then relatively constant; this is in contrast to the peak temperature rise induced by the other plasma species. Interestingly, as shown in Fig. 7.4b, below some critical pulse width ($\approx 2\ \mu$s), this cooling process can occur without plasma-induced heating of the Au surface; a sufficient number of high energy photons are produced at the nozzle for desorption to occur, while the flux of other species is too low for heating. Just above this threshold, a spike in both the heating and cooling profile is observed due to an avalanche effect of both energetic particles as well as the high energy radiation associated with their production. These observations not only reinforce the notion of desorption-induced cooling of the Au surface, but also indicate potential regimes of which the relative heating and cooling of the target surface can be manipulated through various plasma parameters.

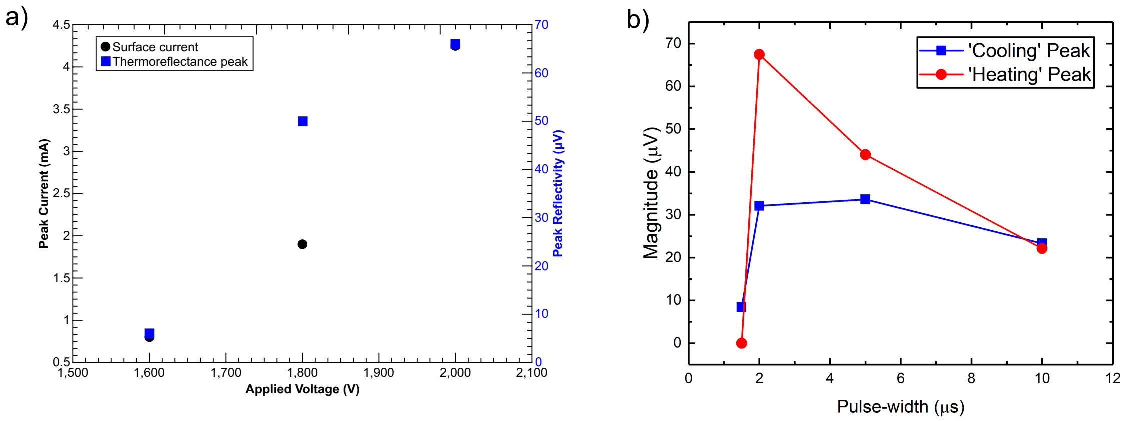

Figure 7.4: a) Peak of the measured surface current (black circles) and peak thermorflectance signal associated with plasma-induced heating of the Au surface (blue squares). b) Relative thermoreflectance magnitude of the heating (red circles) and cooling (blue squares) peak during plasma-Au interactions as a function of the pulse-width of the incident plasma jet. Below a threshold pulse width, there is only net cooling of the sample.

7.4 Summary

In summary, we have provided the first nanosecond-resolved measurement of energy transduction during plasma-surface interactions with a transient thermoreflectance method. Simple inductive heating of the metal Au surface through a flux of charge species is the predominant mechanism of energy transfer, which cools primarily through conduction into the material; this process is in excellent agreement with our two-temperature model calculations. Furthermore, we find that the plasma jet induces transient cooling of the Au surface prior to Joule heating. Over the course of approximately 800 nanoseconds, the plasma jet liberates either electrons or surface species from the Au film, thus temporarily cooling the metal surface. This unique process, previously overwhelmed by the resistive heating of material surface during steady-state temperature and flux measurements, opens the door to a new means of surface cooling and provides critical insight to the plasma-material interactions that drive material modification and processing.

Chapter 8

Summary and Future Projects

8.1 Summary

In Chapter 2, the basic theory of thermal transport, within the framework of both macroscale and nanoscale heat transfer concepts, was introduced. In particular, a basic derivation of the kinetic theory model for understanding thermal conductivity in phononic materials was discussed. This framework was then extended to the terminology necessary for understanding thermal transport in amorphous materials, a necessary discussion for understanding the results presented in Chapter 5. Finally, we derived the basic formalisms for interfacial heat transfer, namely the acoustic mismatch and diffuse mismatch models (AMM and DMM, respectively); this terminology is a requisite for the majority of the following chapters, and the derivation is greatly expanded upon for Chapter 6 and the AMM/DMM framework derived specifically for understanding heat transfer across solid-gas interfaces.

Chapter 3 provided an introduction to thermoreflectance methods, namely time-domain thermoreflectance (TDTR), which is critical for the remaining chapters of this dissertation. In particular, we derived the multilayer heat equation used for modeling and extracting thermophysical parameters from experimental data. An emphasis was placed on the sensitivity analysis used for calculation of uncertainty and error bars in TDTR; these concepts are critical for understanding the need for alternate metrologies for measuring the thermal boundary conductance across low thermal conductivity phases of matter. Finally, this Chapter introduces the necessity for tunable-wavelength approaches to measuring energy transport by demonstrating the inaccuracy and failures of single-wavelength techniques in interpreting the electron-phonon coupling factor of the prototypical material system, Au.

In Chapter 4, I present works that demonstrate the applicability of two unique metrics for interpreting the thermal boundary conductance of a given interface: the ablation threshold of thin films and dampening of acoustic waves across an interface. These metrics are presented in material systems that are highly accessible with standard TDTR analysis as a means of demonstrating the accuracy and future applicability of these measurements; these metrics are then applied for TDTR-inaccessible interfaces, namely solid-liquid and solid-gas interfaces, in Chapters 5 and 6, respectively. Finally, this chapter elucidates upon a novel energy transduction mechanism, Ballistic Thermal Injection (BTI), that can arise at metal-semiconductor interfaces. This unique mechanism is demonstrated through the application mid-infrared, tunable pump-probe measurements.

Chapter 5 applies the experimental metrology techniques developed in the prior chapter for measurement of nanoscale energy transfer across solid-liquid interfaces. In particular, we consider these nanoscale metrics of energy transfer with respect to the macroscale observables, such as contact angle and adhesion energy, of a given interface. I demonstrate that these macroscale observables are not applicable for estimation of the energy transfer rates of a given solid-liquid interface, particularly at the ‘extremes’ of such metrics (e.g., extremely high or low contact angles present strong disagreement between nanoscale measurements and the macroscale metric). In the second half of this chapter, these nanoscale solid-liquid interactions are manipulated for a record-setting tunable thermal conductivity switch, which is enabled through the infiltration of water to a squid ring teeth (SRT)-based biopolymer.

Chapter 6 extends the application of acoustic metrologies to the case of solid-gas interfaces as a means of interpreting the otherwise-immeasurable thermal boundary conductance associated with this pairing. These results are interpreted within a newly-developed framework of the acoustic mismatch and diffuse mismatch models (AMM and DMM, respectively), derived specifically for the transmission of acoustic waves generated during these picosecond acoustic measurements. We find that the continuum-like approximation of energy transfer, the AMM, is a poor descriptor of the nanoscale mechanisms of diffusive heat transfer from a solid surface to an adjacent gas. Rather, the experimental data is well-described by the energy flux calculated from the diffuse mismatch model, indicating that vibrational carriers are scattered at the interface with no 'memory' of their pre-scattering conditions (e.g., wavevector or mode). Additionally, it is demonstrated that these picosecond acoustic measurements provide a metric of gas adsorption density on the solid surface.

Chapter 7 considers the measurement of energy flux from the fourth phase of matter, plasma, upon a solid surface. Specifically, this chapter presents the development of a transient plasma-pump, laser-probe measurement techniques, providing the first nanosecond-resolved measurement of energy transduction during plasma-surface interactions with an atmospheric plasma jet. In particular, these measurements elucidate upon an otherwise-unconsidered process during these interactions: Plasma cooling. Through a detailed analysis of these measurements, we find that the solid metal surface is primarily heated through inductive heating due to a flux of charged species; this imparted energy is then dissipated through conduction. Prior to this heating event, the formation of high energy photons (58 nm) in the plasma jet are found to interact and liberate surface adsorbates, thus inducing a rapid *decrease* in the surface temperature of the solid. Through manipulation of various plasma parameters, the relative contributions of these heating and cooling profiles can be tuned.

8.2 Future Work

- **Ballistic thermal injection in functional devices** - In Chapter 4, I demonstrate a novel energy transduction pathway that can arise at metal-semiconductor interfaces during cases of strong non-equilibrium. Given the ever increasing necessity for higher frequency and higher power electronic devices, such states of non-equilibrium can frequently arise, making thermal mitigation even more difficult. It would thus be of great technological relevance to study the bounds of this process for implementation to these functional device architectures. For example, one may expect a large contribution from BTI in high-electron mobility transistors, where metal electrodes are coupled to highly doped semiconductors.

- **Mode-resolved thermoreflectance** - In Chapter 5, we investigated the interfacial energy transfer of coherent acoustic phonons (CAPs) from a solid surface to a liquid layer. Though in most cases, there is a large range of vibrational frequencies and carriers that contribute to this interfacial heat transfer in addition to these CAPs. To-date, the majority of our understanding of these spectral heat fluxes arises from theory and computational results; an experimental counterpart capable of directly resolving the energy transfer of specific vibrational modes has yet to be developed. It would thus be of great interest to tune the wavelength of a probe laser in thermoreflectance measurements to specific vibrational modes and directly resonate with them, similar to the means of which we tune to the plasmonic resonance of CdO to resolve BTI in Chapter 4. Such an advance would provide direct interrogation of the mode-specific temperature, and thus potentially provide experimental measure of spectral energy fluxes.

- **Biopolymers for novel energy storage** - Thermal energy storage is a large focal point of research due to its promise in greatly improving upon building and energy efficiencies. Currently, near-room-temperature materials capable of storing large volumes of energy are lacking; the majority of modern technologies rely on either high operating temperatures or low efficiencies. While chapter 5 of this dissertation provided a detailed study on the unique thermal conductivity properties of squid ring teeth (SRT) proteins, an extension to the thermal *storage* properties (e.g., heat capacity and thermal effusivity/diffusivity) of SRT would be of great interest for potential applications in room temperature energy storage.

- **Tunable-wavelength plasma spectroscopy** - In Chapter 7, we provide a *nanosecond* time-resolved study of plasma-surface energy transfer by monitoring changes in the surface temperature during the flux of an atmospheric plasma jet. While certainly a massive advance in plasma diagnostics, it would be of fundamental interest to push these limits further to *picosecond* time-resolved studies. In doing so, one would gain insight to an array of processes, such as non-equilibrium mechanisms (i.e., electron-phonon coupling) as, say, high energy charged species transfer their energy to the solid surface. This would allow one to gain direct insight to the fundamental inter-carrier scattering processes that arise.

  Additionally, in line with moving to higher time resolution, it would be of great scientific interest to move to wavelength-resolved thermoreflectance measurements during plasma-surface interactions. For example, atmospheric plasma jets are frequently used for the modification of 'soft' materials, such as tissue and polymers; by directly interrogating the resonances of vibrational carriers in these polymers, one could gain insight to which mode the plasma carriers couple energy. Similarly, one could imagine a study in which the band gap of a material is monitored on the picosecond time scale during the plasma interaction; this would allow one to separate changes in carrier density from the temperature of a sample (or, in extreme cases, monitor *in situ* changes in the band structure of a solid state medium during plasma interactions).

8.3 Published Work

As part of my dissertation research, I have published seven first-author journal publications [7, 89, 112, 113, 185, 238, 361] and contributed to sixteen other journal publications [15, 234, 362–375]. Additionally, two first-author manuscripts are submitted or in the final stages of preparation for submission to peer-reviewed journals based on the work in this dissertation. I am also first-author on three additional publications [177, 376, 377] and co-author on three journal publications [136, 378, 379] as a result of research performed during my undergraduate studies; at least two of these were completed during my graduate studies and thus warrant mention here.

Bibliography

[1] J. Hohlfeld, S. Wellershoff, J. Gudde, U. Conrad, V. Jahnke, and E. Matthias, "Electron and lattice dynamics following optical excitation of metals," *Chemical Physics*, vol. 251, pp. 237–258, 2000.

[2] J. Tomko, J. J. Naddeo, R. Jimenez, Y. Tan, M. Steiner, J. M. Fitz-Gerald, D. M. Bubb, and S. M. O'Malley, "Size and polydispersity trends found in gold nanoparticles synthesized by laser ablation in liquids," *Physical Chemistry Chemical Physics*, vol. 17, no. 25, pp. 16327–16333, 2015.

[3] E. G. Gamaly, a. V. Rode, B. Luther-Davies, and V. T. Tikhonchuk, "Ablation of solids by femtosecond lasers: Ablation mechanism and ablation thresholds for metals and dielectrics," *Physics of Plasmas*, vol. 9, p. 949, 2002.

[4] M. J. Liu, "Simple technique for measurements of pulsed Gaussian-beam spot sizes," *Opt. Lett.*, vol. 7, no. 5, pp. 196–198, 1982.

[5] B. F. Donovan, C. J. Szwejkowski, J. C. Duda, R. Cheaito, J. T. Gaskins, C.-Y. P. Yang, C. Constantin, R. E. Jones, and P. E. Hopkins, "Thermal boundary conductance across metal-gallium nitride interfaces from 80 to 450K," *Applied Physics Letters*, vol. 105, p. 203502, 2014.

[6] T. Jeong, J.-g. Zhu, S. Chung, and M. R. Gibbons, "Thermal boundary resistance for gold and CoFe alloy on silicon nitride films," *Journal of Applied Physics*, vol. 111, p. 83510, 2012.

[7] J. A. Tomko, A. Giri, B. F. Donovan, D. M. Bubb, S. M. O'Malley, and P. E. Hopkins, "Energy confinement and thermal boundary conductance effects on short-pulsed thermal ablation thresholds in thin films," *Physical Review B*, vol. 96, p. 14108, 2017.

[8] J. Park, J. Huang, W. Wang, C. J. Murphy, and D. G. Cahill, "Heat transport between Au nanorods, surrounding liquids, and solid supports," *Journal of Physical Chemistry C*, vol. 116, no. 50, pp. 26335–26341, 2012.

[9] A. Schmidt, M. Chiesa, X. Chen, and G. Chen, "An optical pump-probe technique for measuring the thermal conductivity of liquids," *Review of Scientific Instruments*, vol. 79, no. 6, 2008.

[10] E. Pop, “Energy dissipation and transport in nanoscale devices,” *Nano Research*, vol. 3, no. 3, pp. 147–169, 2010.

[11] K. L. Grosse, M.-H. Bae, F. Lian, E. Pop, and W. P. King, “Nanoscale Joule heating, Peltier cooling and current crowding at graphene-metal contacts.,” *Nature Nanotechnology*, vol. 6, no. 5, pp. 287–290, 2011.

[12] D. G. Cahill, P. V. Braun, G. Chen, D. R. Clarke, S. Fan, K. E. Goodson, P. Keblinski, W. P. King, G. D. Mahan, A. Majumdar, H. J. Maris, S. R. Phillpot, E. Pop, and L. Shi, “Nanoscale thermal transport. II. 2003-2012,” *Applied Physics Reviews*, vol. 1, p. 011305, 2014.

[13] P. Jiang, X. Qian, and R. Yang, “Tutorial: Time-domain thermoreflectance (TDTR) for thermal property characterization of bulk and thin film materials,” *Journal of Applied Physics*, vol. 124, no. 16, p. 161103, 2018.

[14] D. G. Cahill, “Analysis of heat flow in layered structures for time-domain thermoreflectance,” *Review of Scientific Instruments*, vol. 75, no. 12, pp. 5119–5122, 2004.

[15] S. G. Walton, B. M. Foley, J. Tomko, D. R. Boris, E. D. Gillman, S. C. Hernández, A. Giri, T. B. Petrova, and P. E. Hopkins, “Plasma-surface interactions in atmospheric pressure plasmas: In situ measurements of electron heating in materials,” *Journal of Applied Physics*, vol. 124, no. 4, p. 43301, 2018.

[16] J. B. J. Fourier, *Theorie Analytique de la Chaeleur*. Cambridge University press, 2009.

[17] W. G. Vincenti and C. H. Kruger, *Introduction to physical gas dynamics*. Wiley New York, 1965.

[18] C. Kittel and P. McEuen, *Introduction to Solid State Physics*. Wiley New York, vol. 8 ed., 1996.

[19] P. Klemens, “The thermal conductivity of dielectric solids at low temperatures (theoretical),” *Proceedings of the Royal Society of London A: Mathematical, Physical and Engineering Sciences*, vol. 208, pp. 108–133, 1951.

[20] J. Callaway, “Model for lattice thermal conductivity at low temperatures,” *Physical Review*, vol. 113, pp. 1046–1051, 1959.

[21] G. Chen, *Nanoscale Energy Transport and Conversion: A Parallel Treatment of Electrons, Molecules, Phonons, and Photons.* Oxford University Press, USA, 2005.

[22] G. A. Slack, “The thermal conductivity of nonmetallic crystals,” *Solid State Physics*, vol. 34, pp. 1–71, 1979.

[23] A. Einstein, “Elementary observations on thermal molecular motion in solids,” *Annalen der Physik*, vol. 35, pp. 679–694, 1911.

[24] D. G. Cahill, S. K. Watson, and R. O. Pohl, “Lower limit to the thermal conductivity of disordered crystals,” *Physical Review B*, vol. 46, pp. 6131–6140, 1992.

[25] A. Majumdar, “LOWER LIMIT OF THERMAL CONDUCTIVITY : DIFFUSION VERSUS LOCALIZATION,” *Microscale Thermophysical Engineering*, vol. 2, pp. 5–9, 1998.

[26] W. Lv and A. Henry, “Examining the Validity of the Phonon Gas Model in Amorphous Materials,” *Scientific Reports*, vol. 6, p. 37675, 2016.

[27] A. Giri, J. L. Braun, C. M. Rost, and P. E. Hopkins, “Scripta Materialia On the minimum limit to thermal conductivity of multi-atom component crystalline solid solutions based on impurity mass scattering,” *Scripta Materialia*, vol. 138, pp. 134–138, 2017.

[28] H. Mizuno, S. Mossa, and J.-L. Barrat, “Beating the amorphous limit in thermal conductivity by superlattices design,” *Scientific Reports*, vol. 5, p. 14116, 2015.

[29] P. B. Allen, J. L. Feldman, J. Fabian, and F. Wooten, “Diffusons, locons and propagons: character of atomic vibrations in amorphous Si,” *Philosophical Magazine B*, vol. 79, pp. 1715–1731, 1999.

[30] J. D. Gale and A. L. Rohl, “The General Utility Lattice Program (GULP),” *Mol. Simul.*, vol. 29, p. 291, 2003.

[31] J. M. Larkin and A. J. H. Mcgaughey, “Thermal conductivity accumulation in amorphous silica and amorphous silicon,” *Physical Review B*, vol. 144303, no. March, pp. 1–12, 2014.

[32] J. Moon, B. Latour, and A. J. Minnich, “Propagating elastic vibrations dominate thermal conduction in amorphous silicon,” *Physical Review B*, vol. 97, no. January, p. 024201, 2018.

[33] C. Monachon, L. Weber, and C. Dames, “Thermal Boundary Conductance: A Materials Science Perspective,” *Annual Review Of Material Research*, vol. 46, no. March, pp. 433–463, 2016.

[34] P. E. Hopkins, “Thermal transport across solid interfaces with nanoscale imperfections: Effects of roughness, disorder, dislocations, and bonding on thermal boundary conductance,” *ISRN Mechanical Engineering*, vol. 2013, no. 1, pp. 1–19, 2013.

[35] E. T. Swartz and R. O. Pohl, “Thermal boundary resistance,” *Reviews of Modern Physics*, vol. 61, no. 3, pp. 605–668, 1989.

[36] R. Peterson and A. Anderson, “Acoustic-mismatch model of the Kaptiza resistance,” *Physics Letters A*, vol. 40, pp. 317–319, 1972.

[37] E. T. Swartz, *Solid-solid thermal boundary resistance*. PhD thesis, Cornell University, 1987.

[38] B. A. Auld, *Acoustic Fields and Waves in Solids*. Wiley, New York, vol. i ed., 1973.

[39] W. A. Little, "The transport of heat between dissimilar solids at low temperatures," *Can. J. Phys.*, vol. 37, p. 334, 1959.

[40] B. Latour, N. Shulumba, and A. J. Minnich, "Ab initio study of mode-resolved phonon transmission at Si/Ge interfaces using atomistic Green's functions," *Physical Review B*, vol. 96, p. 104310, 2017.

[41] P. E. Hopkins, P. M. Norris, M. S. Tsegaye, and A. W. Ghosh, "Extracting phonon thermal conductance across atomic junctions: Nonequilibrium Green's function approach compared to semiclassical methods," *Journal of Applied Physics*, vol. 106, no. 6, p. 063503, 2009.

[42] S. Sadasivam, U. V. Waghmare, and T. S. Fisher, "Electron-phonon coupling and thermal conductance at a metal-semiconductor interface: First-principles analysis," *Journal of Applied Physics*, vol. 117, no. 13, p. 134502, 2015.

[43] S. Sadasivam, N. Ye, J. P. Feser, J. Charles, K. Miao, T. Kubis, and T. S. Fisher, "Thermal transport across metal silicide-silicon interface: First-principles calculations and Green's function transport simulations," *Physical Review B2*, vol. 95, p. 085310, 2017.

[44] J. T. Gaskins, G. Kotsonis, A. Giri, S. Ju, A. Rohskopf, Y. Wang, T. Bai, E. Sachet, C. T. Shelton, Z. Liu, Z. Cheng, B. M. Foley, S. Graham, T. Luo, A. Henry, M. S. Goorsky, J. Shiomi, J. P. Maria, and P. E. Hopkins, "Thermal Boundary Conductance Across Heteroepitaxial ZnO/GaN Interfaces: Assessment of the Phonon Gas Model," *Nano Letters*, vol. 18, no. 12, pp. 7469–7477, 2018.

[45] K. Gordiz and A. Henry, "Phonon Transport at Crystalline Si/Ge Interfaces: The Role of Interfacial Modes of Vibration.," *Scientific reports*, vol. 6, no. February, p. 23139, 2016.

[46] B. C. Gundrum, D. G. Cahill, and R. S. Averback, "Thermal conductance of metal-metal interfaces," *Physical Review B*, vol. 72, no. 24, p. 245426, 2005.

[47] W. Wang and D. G. Cahill, "Limits to Thermal Transport in Nanoscale Metal Bilayers due to Weak Electron-Phonon Coupling in Au and Cu," *Physical Review Letters*, vol. 109, p. 175503, 2012.

[48] J. Atencia and D. J. Beebe, "Controlled microfluidic interfaces," *Nature*, vol. 437, no. 7059, pp. 648–655, 2005.

[49] M. W. J. Prins, "Fluid Control in Multichannel Structures by Electrocapillary Pressure," *Science*, vol. 291, no. 5502, pp. 277–280, 2001.

[50] B. S. Gallardo, "Electrochemical Principles for Active Control of Liquids on Submillimeter Scales," *Science*, vol. 283, no. 5398, pp. 57–60, 1999.

[51] C. Sievers, Y. Noda, L. Qi, E. M. Albuquerque, R. M. Rioux, and S. L. Scott, "Phenomena Affecting Catalytic Reactions at Solid–Liquid Interfaces," *ACS Catalysis*, vol. 6, no. 12, pp. 8286–8307, 2016.

[52] I. I. Nedrygailov, C. Lee, S. Y. Moon, H. Lee, and J. Y. Park, "Hot Electrons at Solid-Liquid Interfaces: A Large Chemoelectric Effect during the Catalytic Decomposition of Hydrogen Peroxide," *Angewandte Chemie - International Edition*, vol. 55, no. 36, pp. 10859–10862, 2016.

[53] H. Söngen, C. Marutschke, P. Spijker, E. Holmgren, I. Hermes, R. Bechstein, S. Klassen, J. Tracey, A. S. Foster, and A. Kühnle, "Chemical Identification at the Solid–Liquid Interface," *Langmuir*, vol. 33, no. 1, pp. 125–129, 2017.

[54] A. Bar-Cohen, M. Arik, and M. Ohadi, "Direct liquid cooling of high flux micro and nano electronic components," *Proceedings of the IEEE*, vol. 94, no. 8, pp. 1549–1570, 2006.

[55] A. C. Kheirabadi and D. Groulx, "Cooling of server electronics: A design review of existing technology," *Applied Thermal Engineering*, vol. 105, pp. 622–638, 2016.

[56] V. Hlady and J. Buijs, "Protein adsorption on solid surfaces.," *Current Opinion in Biotechnology*, vol. 7, no. 1, pp. 72–7, 1996.

[57] J. D. Andrade, V. L. Hlady, and R. a. V. Wagenen, "Effect of plasma protein adsorption on protein conformation and activity," *Pure and Applied Chemistry*, vol. 56, no. 10, pp. 1345–1350, 1984.

[58] A. T. Garland, *The Behavior of Proteins at Solid-Liquid Interfaces*. PhD thesis, The University of Texas at Austin, 2014.

[59] D. Huang, T. Zhao, W. Xu, T. Yang, and P. S. Cremer, "Sensing small molecule interactions with lipid membranes by local pH modulation," *Analytical Chemistry*, vol. 85, no. 21, pp. 10240–10248, 2013.

[60] B. A. Howell and A. Chauhan, "Interaction of cationic drugs with liposomes," *Langmuir*, vol. 25, no. 20, pp. 12056–12065, 2009.

[61] O. J. Rojas, L. Macakova, E. Blomberg, Å. Emmer, and P. M. Claesson, "Fluorosurfactant self-assembly at solid/liquid interfaces," *Langmuir*, vol. 18, no. 21, pp. 8085–8095, 2002.

[62] S. De Feyter and F. C. De Schryver, "Self-assembly at the liquid/solid interface: STM reveals," *Journal of Physical Chemistry B*, vol. 109, no. 10, pp. 4290–4302, 2005.

[63] G. M. Whitesides and P. E. Laibinis, "Wet chemical approaches to the characterization of organic surfaces: self-assembled monolayers, wetting, and the physical-organic chemistry of the solid-liquid interface," *Langmuir*, vol. 6, no. 1, pp. 87–96, 1990.

[64] W. R. Tyson and W. Miller, “Surface free energies of solid metals: Estimation from liquid surface tension measurements,” *Surface Science*, vol. 62, no. 1, pp. 267–276, 1977.

[65] W. Zisman, “Relation of the Equilibrium Contact Angle to Liquid and Solid Constitution,” *Contact Angle, Wettability, and Adhesion*, vol. 43, no. 43, pp. 1–51, 1964.

[66] W. Norde, “Adsorption of proteins from solution at the solid-liquid interface,” *Advances in Colloid and Interface Science*, vol. 4, pp. 267–340, 1986.

[67] P. L. Kapitza, “Research of a mechanism of the heat transmission in Helium-II,” *Zhurnal Eksperimental’noi i Teoreticheskoi Fiziki*, vol. 11, pp. 1–31, 1941.

[68] S. Garde and A. J. Patel, “Unraveling the hydrophobic effect, one molecule at a time,” *Proceedings of the National Academy of Sciences*, vol. 108, no. 40, pp. 16491–16492, 2011.

[69] A. Magunov, “Scanning calorimetry measurements of the energy parameters of a plasmo-chemical polymer oxidation reaction,” *Plasma Physics Reports*, vol. 28, pp. 359–366, 2002.

[70] M. Freed, M. Kruger, K. Poolla, and C. Spanos, “Wafer-grown heat flux sensor arrays for plasma etch proccesses,” *IEEE Transactions on Semiconductor Manufacturing*, vol. 18, pp. 148–162, 2005.

[71] J. H. Weaver, D. W. Lynch, C. H. Culp, and R. Rosei, “Thermoreflectance of V, Nb, and paramagnetic Cr,” *Phys. Rev. B*, vol. 14, pp. 459–463, 1976.

[72] E. Colavita, A. Franciosi, D. W. Lynch, G. Paolucci, and R. Rosei, “Thermoreflectance investigation of the antiferromagnetic and paramagnetic phases of Cr,” *Phys. Rev. B*, vol. 27, pp. 1653–1663, 1983.

[73] D. W. Lynch, R. Rosei, and J. H. Weaver, “Infrared and visible optical properties of single crystal Ni at 4K,” *Solid State Communications*, vol. 9, no. 24, pp. 2195–2199, 1971.

[74] R. Rosei and D. W. Lynch, “Thermomodulation spectra of Al, Au, and Cu,” *Phys. Rev. B*, vol. 5, pp. 3883–3894, 1972.

[75] J. L. Hostetler, A. N. Smith, and P. M. Norris, “Thin-film thermal conductivity and thickness measurements using picosecond ultrasonics,” *Microscale Thermophs. Eng.*, vol. 1, pp. 237–244, 1997.

[76] J. L. Feldman, P. B. Allen, and S. R. Bickham, “Numerical study of low-frequency vibrations in amorphous silicon,” *Physical Review B*, vol. 59, no. 5, p. 3551, 1999.

[77] R. M. Costescu, M. A. Wall, and D. G. Cahill, “Thermal conductance of epitaxial interfaces,” *Physical Review B*, vol. 67, no. 054302, p. 54302, 2003.

[78] E. L. Radue, J. A. Tomko, A. Giri, J. L. Braun, X. Zhou, O. V. Prezhdo, E. L. Runnerstrom, J. P. Maria, and P. E. Hopkins, “Hot Electron Thermoreflectance Coefficient of Gold during Electron-Phonon Nonequilibrium,” *ACS Photonics*, vol. 5, no. 12, pp. 4880–4887, 2018.

[79] V. P. Zhukov, V. G. Tyuterev, E. V. Chulkov, and P. M. Echenique, “Electron-phonon relaxation and excited electron distribution in gallium nitride,” *Journal of Applied Physics*, vol. 120, no. 8, p. 85708, 2016.

[80] B. Gelmont, K. Kim, and M. Shur, “Monte Carlo simulation of electron transport in gallium nitride,” *Journal of Applied Physics*, vol. 74, no. January 1993, p. 1818, 1993.

[81] H. Frohlich, “T heory of Electrical Breakdown in Ionic Crystals,” *Proceedings of the Royal Society A*, vol. 160, pp. 230–241, 1937.

[82] B. C. Stuart, M. D. Feit, S. Herman, a. M. Rubenchik, B. W. Shore, and M. D. Perry, “Optical ablation by high-power short-pulse lasers,” *Journal of the Optical Society of America B*, vol. 13, p. 459, feb 1996.

[83] E. Suzuki, Y. Hayashi, and H. Yanai, “Transport processes of electrons in MNOS structures,” *Journal of Applied Physics*, vol. 50, no. 11, pp. 7001–7006, 1979.

[84] V. K. Pustovalov, “Light-to-heat conversion and heating of single nanoparticles, their assemblies, and the surrounding medium under laser pulses,” *RSC Advances*, vol. 6, no. 84, pp. 81266–81289, 2016.

[85] X. Huang and M. A. El-Sayed, “Gold nanoparticles: Optical properties and implementations in cancer diagnosis and photothermal therapy,” *Journal of Advanced Research*, vol. 1, no. 1, pp. 13–28, 2010.

[86] S. Wellershoff, J. Hohlfeld, J. Güdde, and E. Matthias, “The role of electron-phonon coupling in femtosecond laser damage of metals,” *Applied Physics A: Materials Science & Processing*, vol. 107, pp. 99–107, 1999.

[87] M. D. Perry, B. C. Stuart, P. S. Banks, M. D. Feit, V. Yanovsky, and A. M. Rubenchik, “Ultrashort-pulse laser machining of dielectric materials,” *Journal of Applied Physics*, vol. 85, no. 9, pp. 6803–6810, 1999.

[88] J. K. Chen, D. Y. Tzou, and J. E. Beraun, “A semiclassical two-temperature model for ultrafast laser heating,” *International Journal of Heat and Mass Transfer*, vol. 49, no. 1-2, pp. 307–316, 2006.

[89] E. L. Radue, J. A. Tomko, A. Giri, J. L. Braun, X. Zhou, O. V. Prezhdo, E. L. Runnerstrom, J.-P. Maria, and P. E. Hopkins, “Hot Electron Thermoreflectance Coefficient of Gold during Electron–Phonon Nonequilibrium,” *ACS Photonics*, vol. 5, pp. 4880–4887, dec 2018.

[90] S. I. Anisimov, B. L. Kapeliovich, and T. L. Perel'man, "Electron emission from metal surfaces exposed to ultrashort laser pulses," *Zh. Eksp. Teor. Fiz.*, vol. 66, pp. 776–781, 1974.

[91] M. Kaganov, I. Lifshitz, and L. Tanatarov, "Kaganov, M.I. Lifshitz, I.M. Tanatarov, L.V.," *Sov. Phys. JETP*, vol. 4, p. 163, 1957.

[92] Z. Lin, L. V. Zhigilei, and V. Celli, "Electron-phonon coupling and electron heat capacity of metals under conditions of strong electron-phonon nonequilibrium," *Physical Review B*, vol. 77, no. 7, p. 075133, 2008.

[93] P. E. Hopkins, J. C. Duda, B. Kaehr, X. W. Zhou, C. Y. Peter Yang, and R. E. Jones, "Ultrafast and steady-state laser heating effects on electron relaxation and phonon coupling mechanisms in thin gold films," *Applied Physics Letters*, vol. 103, no. 21, p. 211910, 2013.

[94] A. Giri, J. T. Gaskins, B. F. Donovan, C. Szwejkowski, R. J. Warzoha, M. A. Rodriguez, J. Ihlefeld, and P. E. Hopkins, "Mechanisms of nonequilibrium electron-phonon coupling and thermal conductance at interfaces," *Journal of Applied Physics*, vol. 117, p. 105105, mar 2015.

[95] P. E. Hopkins, J. L. Kassebaum, and P. M. Norris, "Effects of electron scattering at metal-nonmetal interfaces on electron-phonon equilibration in gold films," *Journal of Applied Physics*, vol. 105, no. 2, p. 023710, 2009.

[96] P. E. Hopkins and P. M. Norris, "Substrate influence in electron – phonon coupling measurements in thin Au films," *Applied Surface Science*, vol. 253, pp. 6289–6294, 2007.

[97] B. Mueller and B. Rethfeld, "Nonequilibrium electron-phonon coupling after ultrashort laser excitation of gold," *Applied Surface Science*, vol. 302, pp. 24–28, 2014.

[98] K. O. Aruda, M. Tagliazucchi, C. M. Sweeney, D. C. Hannah, G. C. Schatz, and E. A. Weiss, "Identification of parameters through which surface chemistry determines the lifetimes of hot electrons in small Au nanoparticles," *Proceedings of the National Academy of Science*, vol. 110, no. 11, pp. 4212–4217, 2013.

[99] P. B. Johnson and R. W. Christy, "Optical Constants of the Noble Metals," *Physical Review B*, vol. 6, p. 4370, 1972.

[100] M. Cardona, *Modulation Spectroscopy*. New York: Academic, 1969.

[101] R. W. Schoenlein, W. Z. Lin, J. G. Fujimoto, and G. L. Eesley, "Femtosecond Studies of Nonequilibrium Electronic Processes in Metals," *Physical Review Letters*, vol. 58, pp. 1680–1683, 1987.

[102] T. Heilpern, M. Manjare, A. O. Govorov, G. P. Wiederrecht, S. K. Gray, and H. Harutyunyan, "Determination of hot carrier energy distributions from inversion of ultrafast pump-probe reflectivity measurements," *Nature Communications*, vol. 9, p. 1853, 2018.

[103] A. H. MacDonald, “Electron-Phonon Enhancement of Electron-Electron Scattering in Al,” *Physical Review Letters*, vol. 44, no. 7, p. 489, 1980.

[104] B. M. Kaveh and N. Wiser, “Electron-electron scattering in conducting materials,” *Advances in Physics*, vol. 33, no. 4, pp. 257–372, 1984.

[105] S. D. Brorson, A. Kazeroonian, J. S. Moodera, D. W. Face, T. K. Cheng, E. P. Ippen, M. S. Dresselhaus, and G. Dresselhaus, “Femtosecond room-temperature measurement of the electron-phonon coupling constant in metallic superconductors,” *Physical Review Letters*, vol. 64, no. 18, pp. 2172–2175, 1990.

[106] A. M. Brown, R. Sundararaman, P. Narang, A. M. Schwartzberg, W. A. Goddard, and H. A. Atwater, “Experimental and Ab Initio Ultrafast Carrier Dynamics in Plasmonic Nanoparticles,” *Physical Review Letters*, vol. 118, no. 8, p. 087401, 2017.

[107] I. Souza, N. Marzari, and D. Vanderbilt, “Maximally localized Wannier functions for entangled energy bands,” *Physical Review B*, vol. 65, no. 3, p. 035109, 2001.

[108] A. M. Brown, R. Sundararamen, P. Narang, W. A. Goddard III, and H. A. Atwater, “Nonradiative Plasmon Decay and Hot Carrier Dynamics: Effects of Phonons, Surfaces, and Geometry,” *ACS Nano*, vol. 10, pp. 957–966, 2016.

[109] A. M. Brown, R. Sundararaman, P. Narang, W. A. Goddard III, and H. A. Atwater, “Ab initio phonon coupling and optical response of hot electrons in plasmonic metals,” *Physical Review B*, vol. 94, p. 075120, 2016.

[110] M. N. Su, C. J. Ciccarino, S. Kumar, P. D. Dongare, S. A. Hosseini Jebeli, D. Renard, Y. Zhang, B. Ostovar, W. S. Chang, P. Nordlander, N. J. Halas, R. Sundararaman, P. Narang, and S. Link, “Ultrafast Electron Dynamics in Single Aluminum Nanostructures,” *Nano Letters*, vol. 19, no. 5, pp. 3091–3097, 2019.

[111] A. Giri, M. V. Tokina, O. V. Prezhdo, and P. E. Hopkins, “Electron–phonon coupling and related transport properties of metals and intermetallic alloys from first principles,” *Materials Today Physics*, vol. 12, p. 100175, 2020.

[112] J. A. Tomko, D. R. Boris, S. G. Rosenberg, S. G. Walton, and P. E. Hopkins, “Thermal conductance of aluminum oxy-fluoride passivation layers,” *Applied Physics Letters*, vol. 115, no. 19, p. 191901, 2019.

[113] J. A. Tomko, E. L. Runnerstrom, Y.-S. Wang, J. R. Nolen, D. H. Olson, K. P. Kelley, A. Cleri, J. Nordlander, J. D. Caldwell, O. V. Prezhdo, J.-P. Maria, and P. E. Hopkins, “Long-lived modulation of plasmonic absorption by ballistic thermal injection,” *Nature Nanotechnology*, 2020.

[114] B. N. Chichkov, C. Momma, S. Nolte, F. von Alvensleben, and A. Tunnermann, “Femtosecond, picosecond and nanosecond laser ablation of solids,” *Applied Physics A: Materials Science & Processing*, vol. 63, no. 2, pp. 109–115, 1996.

[115] L. V. Zhigilei, Z. Lin, and D. S. Ivanov, “Atomistic Modeling of Short Pulse Laser Ablation of Metals: Connections between Melting, Spallation, and Phase Explosion,” *The Journal of Physical Chemistry C*, vol. 113, no. 27, pp. 11892–11906, 2009.

[116] J. Yang, Y. Zhao, X. Zhu, J. Yang, Y. Zhao, and X. Zhu, “Transition between nonthermal and thermal ablation of metallic targets under the strike of high-fluence ultrashort laser pulses,” *Applied Physics Letters*, vol. 88, p. 94101, 2006.

[117] P. Lorazo, L. J. Lewis, and M. Meunier, “Thermodynamic pathways to melting, ablation, and solidification in absorbing solids under pulsed laser irradiation,” *Physical Review B*, vol. 73, p. 134108, 2006.

[118] D. Von Der Linde and K. Sokolowski-Tinten, “Physical mechanisms of short-pulse laser ablation,” *Applied Surface Science*, vol. 154, pp. 1–10, 2000.

[119] D. G. Cahill, W. K. Ford, K. E. Goodson, G. D. Mahan, A. Majumdar, H. J. Maris, R. Merlin, and S. R. Phillpot, “Nanoscale thermal transport,” *Journal of Applied Physics*, vol. 93, no. 2, pp. 793–818, 2003.

[120] D. W. Bauerle, *Laser processing and chemistry*. Springer Science & Business Media, 2013.

[121] P. E. Hopkins, “Thermal Transport across Solid Interfaces with Nanoscale Imperfections Effects of Roughness, Disorder, Dislocations, and Bonding on Thermal Boundary Conductance,” *ISRN Mechanical Engineering*, vol. 2013, no. 1, 2013.

[122] P. M. Norris, N. Q. Le, and C. H. Baker, “Tuning Phonon Transport: From Interfaces to Nanostructures,” *Journal of Heat Transfer*, vol. 135, no. 6, p. 061604, 2013.

[123] R. J. Stoner and J. Maris, “Kapitza conductance and heat flow between solids at temperatures from 50 to 300 K,” *Physical Review B*, vol. 48, no. 22, pp. 16373–16387, 1993.

[124] R. Cheaito, J. T. Gaskins, M. E. Caplan, B. F. Donovan, B. M. Foley, A. Giri, J. C. Duda, C. J. Szwejkowski, C. Constantin, H. J. Brown-Shaklee, J. F. Ihlefeld, and P. E. Hopkins, “Thermal boundary conductance accumulation and interfacial phonon transmission: Measurements and theory,” *Physical Review B*, vol. 91, no. 3, pp. 1–12, 2015.

[125] J. C. Duda, C.-Y. P. Yang, B. M. Foley, R. Cheaito, D. L. Medlin, R. E. Jones, and P. E. Hopkins, “Influence of interfacial properties on thermal transport at gold:silicon contacts,” *Applied Physics Letters*, vol. 102, no. 8, p. 81902, 2013.

[126] D.-w. Oh, S. Kim, J. A. Rogers, D. G. Cahill, and S. Sinha, “Interfacial Thermal Conductance of Transfer-Printed Metal Films,” *Advanced Materials*, vol. 23, pp. 5028–5033, 2011.

[127] X. Xu, “Phase explosion and its time lag in nanosecond laser ablation,” *Applied Surface Science*, vol. 197-198, pp. 61–66, 2002.

[128] M. E. Povarnitsyn, T. E. Itina, P. R. Levashov, and K. V. Khishchenko, “Mechanisms of nanoparticle formation by ultra-short laser ablation of metals in liquid environment.,” *Physical Chemistry Chemical Physics*, vol. 15, no. 15, pp. 3108–14, 2013.

[129] M. E. Povarnitsyn, T. E. Itina, M. Sentis, K. V. Khishchenko, and P. R. Levashov, “Material decomposition mechanisms in femtosecond laser interactions with metals,” *Physical Review B - Condensed Matter and Materials Physics*, vol. 75, pp. 1–5, 2007.

[130] P. E. Hopkins, M. Baraket, E. V. Barnat, T. E. Beechem, S. P. Kearney, J. C. Duda, J. T. Robinson, and S. G. Walton, “Manipulating Thermal Conductance at Metal-Graphene Contacts via Chemical Functionalization,” *Nano Letters*, vol. 12, pp. 590–595, 2012.

[131] A. Giri, L. Braun, and P. E. Hopkins, “Implications of Interfacial Bond Strength on the Spectral Contributions to Thermal Boundary Conductance across Solid, Liquid, and Gas Interfaces: A Molecular Dynamics Study,” *Journal of Physical Chemistry C*, vol. 120, pp. 24847–24856, 2016.

[132] J. C. Duda, T. S. English, E. S. Piekos, W. A. Soffa, L. V. Zhigilei, and P. E. Hopkins, “Implications of cross-species interactions on the temperature dependence of Kapitza conductance,” *Physical Review B*, vol. 84, no. 193301, pp. 2–5, 2011.

[133] M. D. Losego, M. E. Grady, N. R. Sottos, D. G. Cahill, and P. V. Braun, “Effects of chemical bonding on heat transport across interfaces,” *Nature Materials*, vol. 11, no. 6, pp. 502–506, 2012.

[134] R. Prasher, “Acoustic mismatch model for thermal contact resistance of van der Waals contacts,” *Applied Physics Letters*, vol. 94, no. 4, pp. 1998–2001, 2009.

[135] J. Yang, Y. Yang, S. W. Waltermire, X. Wu, H. Zhang, T. Gutu, Y. Jiang, Y. Chen, A. A. Zinn, R. Prasher, T. T. Xu, and D. Li, “Enhanced and switchable nanoscale thermal conduction due to van der Waals interfaces,” *Nature Nanotechnology*, vol. 7, no. December 2011, pp. 91–95, 2012.

[136] M. Amin, J. Tomko, J. Naddeo, R. Jimenez, D. Bubb, M. Steiner, J. Fitz-Gerald, and S. O’Malley, “Laser-assisted synthesis of ultra-small anatase TiO2 nanoparticles,” *Applied Surface Science*, vol. 348, pp. 30–37, 2015.

[137] N. Sanner, O. Utéza, B. Bussiere, G. Coustillier, a. Leray, T. Itina, and M. Sentis, “Measurement of femtosecond laser-induced damage and ablation thresholds in dielectrics,” *Applied Physics A: Materials Science and Processing*, vol. 94, pp. 889–897, 2009.

[138] P. E. Hopkins, L. M. Phinney, S. P. Kearney, T. W. Grasser, and C. T. Harris, "Criteria for Cross-Plane Multilayer Thin Film Systems," *International Journal of Heat and Mass Transfer*, vol. 132, no. August 2010, p. 081302, 2010.

[139] A. Giri, J. T. Gaskins, B. F. Donovan, C. Szwejkowski, R. J. Warzoha, M. A. Rodriguez, J. Ihlefeld, and P. E. Hopkins, "Mechanisms of nonequilibrium electron-phonon coupling and thermal conductance at interfaces," *Journal of Applied Physics*, vol. 117, no. 10, p. 105105, 2015.

[140] P. M. Norris, A. P. Caffrey, R. J. Stevens, M. J. Klopf, J. T. McLeskey Jr., and A. N. Smith, "Femtosecond pump – probe nondestructive examination of materials," *Review of Scientific Instruments*, vol. 74, no. 1, 2003.

[141] B. M. Clemens, G. L. Eesley, and C. A. Paddock, "Time-resolved thermal transport in compositionally modulated metal films," *Physical Review B*, vol. 37, no. 3, 1988.

[142] A. J. Schmidt, X. Chen, and G. Chen, "Pulse accumulation, radial heat conduction, and anisotropic thermal conductivity in pump-probe transient thermoreflectance," *Review of Scientific Instruments*, vol. 79, no. 11, p. 114902, 2008.

[143] D. R. Lide, *CRC Handbook of Chemistry and Physics, 74th Edition*. 1994.

[144] E. R. Dobrovinskaya, L. A. Lytvynov, and V. Pishchik, *Sapphire: Material, Manufacturing, Applications*. Springer, 2009.

[145] D. D. L. Chung, "Materials for thermal conduction," *Applied Thermal Engineering*, vol. 21, pp. 1593–1605, 2001.

[146] W. G. Hoover, "Canonical dynamics: Equilibrium phase-space distributions," *Physical Review A*, vol. 31, no. 3, pp. 1695–1697, 1985.

[147] A. J. H. Mcgaughey and M. Kaviany, "Thermal conductivity decomposition and analysis using molecular dynamics simulations. Part I. Lennard-Jones argon," *International Journal of Heat and Mass Transfer*, vol. 47, pp. 1783–1798, 2004.

[148] M. S. Brown and C. B. Arnold, "Laser Precision Microfabrication," in *Springer Series in Materials Science* (K. Sugioka, M. Meunier, and A. Piqué, eds.), vol. 135 of *Springer Series in Materials Science*, ch. 4, pp. 91–120, Berlin, Heidelberg: Springer Berlin Heidelberg, 2010.

[149] D. Wortmann, J. Koch, M. Reininghaus, C. Unger, C. Hulverscheidt, D. Ivanov, and B. N. Chichkov, "Experimental and theoretical investigation on fs-laser-induced nanostructure formation on thin gold films," *Journal of Laser Applications*, vol. 24, no. July, 2012.

[150] P. Delaporte and A.-P. Alloncle, "Laser-induced forward transfer: A high resolution additive manufacturing technology," *Optics & Laser Technology*, vol. 78, pp. 33–41, 2016.

[151] M. Domke, L. Nobile, S. Rapp, S. Eiselen, J. Sotrop, H. P. Huber, and M. Schmidt, “Understanding thin film laser ablation: The role of the effective penetration depth and the film thickness,” *Physics Procedia*, vol. 56, no. C, pp. 1007–1014, 2014.

[152] M. E. Povarnitsyn and T. E. Itina, “Hydrodynamic modeling of femtosecond laser ablation of metals in vacuum and in liquid,” *Applied Physics A: Materials Science and Processing*, vol. 117, pp. 175–178, 2014.

[153] C. Shih, M. V. Shugaev, C. Wu, and L. V. Zhigilei, “Generation of Subsurface Voids , Incubation Effect , and Formation of Nanoparticles in Short Pulse Laser Interactions with Bulk Metal Targets in Liquid : Molecular Dynamics Study,” *Journal of Physical Chemistry C*, vol. Just Accep, 2017.

[154] Z. Ge, D. G. Cahill, and P. V. Braun, “Thermal conductance of hydrophilic and hydrophobic interfaces,” *Physical Review Letters*, vol. 96, no. 18, p. 186101, 2006.

[155] M. E. Caplan, A. Giri, and P. E. Hopkins, “Analytical model for the effects of wetting on thermal boundary conductance across solid / classical liquid interfaces,” *Journal of Chemical Physics*, vol. 140, p. 154701, 2014.

[156] B. Rethfeld, K. Sokolowski-Tinten, D. von der Linde, and S. I. Anisimov, “Timescales in the response of materials to femtosecond laser excitation,” *Applied Physics A*, vol. 769, pp. 767–769, 2004.

[157] P. E. Hopkins, J. C. Duda, and P. M. Norris, “Anharmonic Phonon Interactions at Interfaces and Contributions to Thermal Boundary Conductance,” *Journal of Heat Transfer*, vol. 133, no. June 2011, pp. 1–11, 2011.

[158] P. E. Hopkins and P. M. Norris, “Relative Contributions of Inelastic and Elastic Diffuse Phonon Scattering to Thermal Boundary Conductance Across Solid,” *Journal of Heat Transfer*, vol. 131, pp. 1–9, 2009.

[159] P. E. Hopkins, “Multiple phonon processes contributing to inelastic scattering during thermal boundary conductance at solid interfaces Multiple phonon processes contributing to inelastic scattering during thermal boundary conductance at solid interfaces,” *Journal of Applied Physics*, vol. 108, no. 013528, 2009.

[160] P. E. Hopkins, P. M. Norris, and R. J. Stevens, “Influence of Inelastic Scattering at Metal-Dielectric Interfaces,” *Journal of Heat Transfer*, vol. 130, no. February 2008, 2008.

[161] H.-k. Lyeo and D. G. Cahill, “Thermal conductance of interfaces between highly dissimilar materials,” *Physical Review B*, vol. 73, no. 144301, pp. 1–6, 2006.

[162] A. Giri, P. E. Hopkins, J. G. Wessel, and J. C. Duda, “Kapitza resistance and the thermal conductivity of amorphous superlattices Kapitza resistance and the thermal conductivity of amorphous superlattices,” *Journal of Applied Physics*, vol. 118, p. 165303, 2016.

[163] A. Giri, B. M. Foley, and P. E. Hopkins, "Influence of Hot Electron Scattering and Electron – Phonon Interactions on Thermal Boundary Conductance at Metal / Nonmetal Interfaces," *Journal of Heat Transfer*, vol. 136, no. September 2014, pp. 1–6, 2014.

[164] G. T. Hohensee, R. Wilson, and D. G. Cahill, "Thermal conductance of metal-diamond interfaces at high pressure," *Nature Communications*, vol. 6, pp. 1–9, 2015.

[165] J. C. Duda, T. E. Beechem, J. L. Smoyer, P. M. Norris, and P. E. Hopkins, "Role of dispersion on phononic thermal boundary conductance," *Journal of Applied Physics*, vol. 108, p. 073515, 2010.

[166] R. J. Stevens, A. N. Smith, and P. M. Norris, "Measurement of Thermal Boundary Conductance of a Series of Metal-Dielectric Interfaces by the Transient Thermoreflectance Technique," *Journal of Heat Transfer*, vol. 127, no. March 2005, pp. 315–322, 2005.

[167] P. M. Norris and P. E. Hopkins, "Examining Interfacial Diffuse Phonon Scattering Through Transient Thermoreflectance Measurements of Thermal Boundary Conductance," *Journal of Heat Transfer*, vol. 131, no. 4, p. 043207, 2009.

[168] M. Shen, W. J. Evans, D. Cahill, and P. Keblinski, "Bonding and pressure-tunable interfacial thermal conductance," *Physical Review B*, vol. 84, no. 195432, pp. 1–6, 2011.

[169] P. J. O'Brien, S. Shenogin, J. Liu, P. K. Chow, D. Laurencin, P. H. Mutin, M. Yamaguchi, P. Keblinski, and G. Ramanath, "Bonding-induced thermal conductance enhancement at inorganic heterointerfaces using nanomolecular monolayers," *Nature Materials*, vol. 12, no. 2, pp. 118–122, 2012.

[170] B. M. Foley, S. C. Herna, J. C. Duda, J. T. Robinson, S. G. Walton, and P. E. Hopkins, "Modifying Surface Energy of Graphene via Plasma-Based Chemical Functionalization to Tune Thermal and Electrical Transport at Metal Interfaces," *Nano Letters*, vol. 15, pp. 4876–4882, 2015.

[171] C. Monachon, G. Schusteritsch, E. Kaxiras, L. Weber, C. Monachon, G. Schusteritsch, E. Kaxiras, and L. Weber, "Qualitative link between work of adhesion and thermal conductance of metal / diamond interfaces," *Journal of Applied Physics*, vol. 115, no. 123509, 2014.

[172] C. L. Kelchner, S. J. Plimpton, and J. C. Hamilton, "Dislocation nucleation and defect structure during surface indentation," *Physical Review B*, vol. 58, no. 17, pp. 85–88, 1998.

[173] M. Ziegler, J. W. Tomm, D. Reeber, T. Elsaesser, U. Zeimer, H. E. Larsen, M. Petersen, P. E. Andersen, H. E. Larsen, P. M. Petersen, and P. E. Andersen, "Catastrophic optical mirror damage in diode lasers monitored during single-pulse operation single-pulse operation," *Applied Physics Letters*, vol. 94, p. 191101, 2010.

[174] C. S. Lee, N. Koumvakalis, and M. Bass, “A theoretical model for multiple-pulse laser-induced damage to metal mirrors,” *Applied Physics Letters*, vol. 54, no. May 1983, p. 5727, 1983.

[175] P. B. Corkum, F. Brunel, N. K. Sherman, and T. Srinivasan-Rao, “Thermal Response of Metals to Ultrashort-Pulse Laser Excitation,” *Physical Review Letters*, vol. 61, no. 25, pp. 2886–2889, 1988.

[176] J.-P. Tourrenc, S. Bouchoule, A. Khadour, J.-C. Harmand, A. Miard, J. Decobert, N. Lagay, X. Lafosse, I. Sagnes, L. Leroy, and J.-L. Oudar, “Thermal optimization of 1.55 um OP-VECSEL with hybrid metal-metamorphic mirror for single-mode high power operation,” *Optical and Quantum Electronics*, vol. 40, pp. 155–165, 2008.

[177] J. Tomko, S. M. O’Malley, C. Trout, J. J. Naddeo, R. Jimenez, J. C. Griepenburg, W. Soliman, and D. M. Bubb, “Cavitation bubble dynamics and nanoparticle size distributions in laser ablation in liquids,” *Colloids and Surfaces A: Physicochemical and Engineering Aspects*, vol. 522, pp. 368–372, 2017.

[178] Y. Shen, J. Gaskins, X. Xie, B. M. Foley, R. Cheaito, P. E. Hopkins, and J. C. Campbell, “Thermal Analysis of High-Power Flip-Chip-Bonded Photodiodes,” *Journal of Lightwave Technology*, vol. 35, no. 19, pp. 4242–4246, 2017.

[179] S. Wilbrandt, O. Stenzel, H. Nakamura, A. Duparré, and N. Kaiser, “Protected and enhanced aluminum mirrors for the VUV,” *Applied Optics*, vol. 53, no. 4, pp. 125–130, 2014.

[180] M. Miles, *Evaporated Aluminum Fluoride as a Barrier Layer to Retard Oxidation of Aluminum Mirrors*. PhD thesis, 2017.

[181] N. Gutiérrez-Luna, B. Perea-Abarca, L. Espinosa-Yáñez, C. Honrado-Benítez, T. de Lis, L. V. Rodríguez-de Marcos, J. A. Aznárez, and J. I. Larruquert, “Temperature dependence of AlF3 protection on far-UV Al mirrors,” *Coatings*, vol. 9, no. 7, p. 428, 2019.

[182] M. Mäntymäki, M. Ritala, and M. Leskelä, “Metal fluorides as lithium-ion battery materials: An atomic layer deposition perspective,” *Coatings*, vol. 8, no. 8, p. 277, 2018.

[183] A. Giri and P. E. Hopkins, “A Review of Experimental and Computational Advances in Thermal Boundary Conductance and Nanoscale Thermal Transport across Solid Interfaces,” *Advanced Functional Materials*, vol. 2019, p. 1903857, aug 2019.

[184] C. S. Gorham, K. Hattar, R. Cheaito, J. C. Duda, J. T. Gaskins, T. E. Beechem, J. F. Ihlefeld, L. B. Biedermann, E. S. Piekos, D. L. Medlin, and P. E. Hopkins, “Ion irradiation of the native oxide/silicon surface increases the thermal boundary conductance across aluminum/silicon interfaces,” *Physical Review B*, vol. 90, p. 24301, 2014.

[185] J. A. Tomko, D. H. Olson, A. Giri, J. T. Gaskins, B. F. Donovan, S. M. O. Malley, and P. E. Hopkins, "Nanoscale Wetting and Energy Transmission at Solid/Liquid Interfaces," *Langmuir*, vol. 35, pp. 2106–2114, 2019.

[186] W. M. Manheimer, R. F. Fernsler, M. Lampe, and R. A. Meger, "No Title," *Plasma Sources Sci. Technol.*, vol. 9, pp. 370–386, 2000.

[187] R. A. Neger, R. F. Fernsler, M. Lampe, and W. Manheimer, "U.S. patent 5,874,807," 1999.

[188] G. M. Petrov, D. R. Boris, E. H. Lock, T. B. Petrova, R. F. Fernsler, and S. G. Walton, "No Title," *J. Phys. D: Appl. Phys.*, vol. 48, pp. 275202–275208, 2015.

[189] S. G. Walton, D. R. Boris, S. C. Hernandez, E. H. Lock, T. B. Petrova, G. M. Petrov, and R. F. Fernsler, "No Title," *ECS Journal of Solid State Science and Technology*, vol. 4, no. 6, pp. N5033–N5040, 2015.

[190] D. R. Boris and S. G. Walton, "Precise control of ion and radical production using electron beam generated plasmas," *J. Vac. Sci. Technol. A.*, vol. 36, no. 6, p. 60601, 2018.

[191] D. R. Boris, R. F. Fernsler, and S. G. Walton, "Measuring the electron density, temperature, and electronegativity in electron beam-generated plasmas produced in argon/SF6 mixtures," *Plasma Sources Science and Technology*, vol. 24, no. 2, p. 25032, 2015.

[192] D. R. Boris, T. B. Petrova, G. M. Petrov, and S. G. Walton, "Atomic fluorine densities in electron beam generated plasmas: A high ion to radical ratio source for etching with atomic level precision," *J. Vac. Sci. Technol. A*, vol. 35, p. 01A104, 2017.

[193] S. M. George and Y. Yee, "Prospects for thermal atomic layer etching using sequential, self-limiting fluorination and ligand-exchange reactions," *ACS Nano*, vol. 10, pp. 4889–4894, 2016.

[194] S. K. Natarajan and S. D. Elliott, "Modeling the chemical mechanism of the thermal atomic layer etch of aluminum oxide: A density functional theory study of reactions during HF exposure," *Chem. Mater.*, vol. 30, pp. 5912–5922, 2018.

[195] S. G. Walton, S. C. Hernandez, D. R. Boris, T. B. Petrova, and G. M. Petrov, "Electron Beam Generated Plasmas for the Processing of Graphene," *J. Phys. D: Applied Physics*, vol. 50, pp. 354001–354017, 2017.

[196] S. G. Walton, E. H. Lock, A. Ni, M. Baraket, R. F. Fernsler, D. D. Pappas, K. E. Strawhecker, and A. A. Buianda, "Study of plasma-polyethylene interactions using electron beam generated plasmas produced in Ar/SF6 mixtures," *J. Appl. Polym. Sci.*, vol. 117, p. 3515, 2010.

[197] J. Lee, J. Lim, and P. Yang, "Ballistic phonon transport in holey silicon," *Nano Letters*, vol. 15, no. 5, pp. 3273–3279, 2015.

[198] C.-C. Lee, M.-C. Liu, M. Kaneko, K. Nakahira, and Y. Takano, "Characterization of AlF3 thin films at 193 nm by thermal evaporation," *Appl. Opt.*, vol. 44, pp. 7333–7338, dec 2005.

[199] W. Heitmann, "Vacuum Evaporated Films of Aluminum Fluoride," *Thin Solid Films*, vol. 800, no. 1970, pp. 61–67, 1969.

[200] K. Iwahori, M. Furuta, Y. Taki, T. Yamamura, and A. Tanaka, "Optical properties of fluoride thin films deposited by RF magnetron sputtering," *Appl. Opt.*, vol. 45, pp. 4598–4602, jul 2006.

[201] G. Tas, J. J. Loomis, H. J. Maris, A. A. Bailes, and L. E. Seiberling, "Picosecond ultrasonics study of the modification of interfacial bonding by ion implantation," *Applied Physics Letters*, vol. 72, no. 18, pp. 2235–2237, 1998.

[202] H. Harikrishna, W. A. Ducker, and S. T. Huxtable, "The influence of interface bonding on thermal transport through solid-liquid interfaces," *Applied Physics Letters*, vol. 102, no. 25, p. 251606, 2013.

[203] C. Thomsen, H. T. Grahn, H. J. Maris, and J. Tauc, "Surface generation and detection of phonons by picosecond light pulses," *Physical Review B*, vol. 34, no. 6, pp. 4129–4138, 1986.

[204] T. B. Reed, *Free Energy of Formation of Binary Compounds.* Cambridge, MA: MIT Press, 1971.

[205] A. V. Jagtiani, H. Miyazoe, J. Chang, D. B. Farmer, M. Engel, D. Neumayer, S.-J. Han, S. U. Engelmann, D. R. Boris, S. C. Hernandez, E. H. Lock, S. G. Walton, and E. A. Joseph, "Initial evaluation and comparison of plasma damage to atomic layer carbon materials using conventional and low Te plasma sources," *J. Vac. Sci. Technol. A*, vol. 34, p. 01B103, 2016.

[206] E. H. Lock, D. Y. Petrovykh, P. Mack, T. Carney, R. G. White, S. G. Walton, and R. F. Fernsler, "Surface composition, chemistry, and structure of polystyrene modified by electron-beam-generated plasma," *Langmuir*, vol. 26, pp. 8857–8868, 2010.

[207] B. J. Orf, S. G. Walton, D. Leonhardt, and G. S. Oehrlein, "Study of photoresist etching and roughness formation in electron-beam generated plasmas," *J. Vac. Sci. Technol. B*, vol. 25, p. 779, 2007.

[208] N. Serpone and A. V. Emeline, "Semiconductor Photocatalysis - Past, Present, and Future Outlook," *The Journal of Physical Chemistry Letters*, vol. 3, pp. 673–677, 2012.

[209] S. M. Kim, L. Hyosun, and J. Y. Park, "Charge Transport in Metal – Oxide Interfaces : Genesis and Detection of Hot Electron Flow and Its Role in Heterogeneous Catalysis," *Catalysis Letters*, vol. 145, pp. 299–308, 2015.

[210] C. Clavero, “Plasmon-induced hot-electron generation at nanoparticle/metal-oxide interfaces for photovoltaic and photocatalytic devices,” *Nature Photonics*, vol. 8, no. January, pp. 95–103, 2014.

[211] M. W. Knight, H. Sobhani, P. Nordlander, and N. J. Halas, “Photodetection with Active Optical Antennas,” *Science*, vol. 332, no. May, pp. 702–705, 2011.

[212] Z. Ji, H. Hong, J. Zhang, Q. Zhang, W. Huang, T. Cao, R. Qiao, C. Liu, J. Liang, C. Jin, L. Jiao, K. Shi, S. Meng, and K. Liu, “Robust Stacking-Independent Ultrafast Charge Transfer in MoS2/WS2 Bilayers,” *ACS Nano*, vol. 11, pp. 12020–12026, dec 2017.

[213] X. Hong, J. Kim, S. F. Shi, Y. Zhang, C. Jin, Y. Sun, S. Tongay, J. Wu, Y. Zhang, and F. Wang, “Ultrafast charge transfer in atomically thin MoS2/WS2 heterostructures,” *Nature Nanotechnology*, vol. 9, no. 9, pp. 682–686, 2014.

[214] R. Asapu, N. Claes, R.-G. Ciocarlan, M. Minjauw, C. Detavernier, P. Cool, S. Bals, and S. W. Verbruggen, “Electron Transfer and Near-Field Mechanisms in Plasmonic Gold-Nanoparticle-Modified TiO2 Photocatalytic Systems,” *ACS Applied Nano Materials*, vol. 2, pp. 4067–4074, jul 2019.

[215] J. J. Chen, J. C. Wu, P. C. Wu, and D. P. Tsai, “Improved photocatalytic activity of shell-isolated plasmonic photocatalyst Au@SiO2/TiO2 by promoted LSPR,” *Journal of Physical Chemistry C*, vol. 116, pp. 26535–26542, dec 2012.

[216] J. B. Priebe, M. Karnahl, H. Junge, M. Beller, D. Hollmann, and A. Brückner, “Water reduction with visible light: Synergy between optical transitions and electron transfer in Au-TiO2catalysts visualized by in situ EPR spectroscopy,” *Angewandte Chemie - International Edition*, vol. 52, pp. 11420–11424, oct 2013.

[217] P. Narang, R. Sundararaman, and H. A. Atwater, “Plasmonic hot carrier dynamics in solid-state and chemical systems for energy conversion,” *Nanophotonics*, vol. 5, pp. 96–111, jun 2016.

[218] M. L. Brongersma, N. J. Halas, and P. Nordlander, “Plasmon-induced hot carrier science and technology,” *Nature Nanotechnology*, vol. 10, pp. 25–34, jan 2015.

[219] R. Sundararaman, P. Narang, A. S. Jermyn, W. A. G. Iii, and H. A. Atwater, “Theoretical predictions for hot-carrier generation from surface plasmon decay,” *Nature Communications*, vol. 5, pp. 1–8, 2014.

[220] K. Wu, J. Chen, J. R. McBride, and T. Lian, “Efficient hot-electron transfer by a plasmon-induced interfacial charge-transfer transition,” *Science*, vol. 349, pp. 632–635, aug 2015.

[221] Y. Yu, V. Sundaresan, and K. A. Willets, “Hot Carriers versus Thermal Effects: Resolving the Enhancement Mechanisms for Plasmon-Mediated Photoelectrochemical Reactions,” *Journal of Physical Chemistry C*, vol. 122, pp. 5040–5048, mar 2018.

[222] D. Kozawa, A. Carvalho, I. Verzhbitskiy, F. Giustiniano, Y. Miyauchi, S. Mouri, A. H. Castro Neto, K. Matsuda, and G. Eda, "Evidence for Fast Interlayer Energy Transfer in MoSe2/WS2 Heterostructures," *Nano Letters*, vol. 16, pp. 4087–4093, jul 2016.

[223] E. Feigenbaum, K. Diest, and H. A. Atwater, "Unity-order index change in transparent conducting oxides at visible frequencies," *Nano Letters*, vol. 10, pp. 2111–2116, jun 2010.

[224] T. G. Folland, L. Nordin, D. Wasserman, and J. D. Caldwell, "Probing polaritons in the mid- to far-infrared Probing polaritons in the mid- to far-infrared," *Journal of Applied Physics*, vol. 125, no. January, p. 191102, 2019.

[225] B. Tandon, A. Agrawal, S. Heo, and D. J. Milliron, "Competition between Depletion Effects and Coupling in the Plasmon Modulation of Doped Metal Oxide Nanocrystals," *Nano Letters*, vol. 19, no. ii, pp. 2012–2019, 2019.

[226] E. Sachet, C. T. Shelton, J. S. Harris, B. E. Gaddy, D. L. Irving, S. Curtarolo, B. F. Donovan, P. E. Hopkins, P. A. Sharma, A. L. Sharma, J. Ihlefeld, S. Franzen, and J.-p. Maria, "Dysprosium-doped cadmium oxide as a gateway material for mid-infrared plasmonics," *Nature Materials*, vol. 14, no. February, pp. 414–420, 2015.

[227] E. L. Runnerstrom, K. P. Kelley, E. Sachet, C. T. Shelton, and J. P. Maria, "Epsilon-near-Zero Modes and Surface Plasmon Resonance in Fluorine-Doped Cadmium Oxide Thin Films," *ACS Photonics*, vol. 4, pp. 1885–1892, aug 2017.

[228] E. L. Runnerstrom, K. P. Kelley, T. G. Folland, J. R. Nolen, N. Engheta, J. D. Caldwell, and J. P. Maria, "Polaritonic Hybrid-Epsilon-near-Zero Modes: Beating the Plasmonic Confinement vs Propagation-Length Trade-Off with Doped Cadmium Oxide Bilayers," *Nano Letters*, vol. 19, pp. 948–957, feb 2019.

[229] G.-M. Choi, R. B. Wilson, and D. G. Cahill, "Indirect heating of Pt by short-pulse laser irradiation of Au in a nanoscale Pt/Au bilayer," *Physical Review B*, vol. 89, p. 64307, 2014.

[230] T. Qiu, T. Juhasz, C. Suarez, W. Bron, and C. Tien, "Femtosecond laser heating of multi-layer metals—II. Experiments," *International Journal of Heat and Mass Transfer*, vol. 37, pp. 2799–2808, nov 1994.

[231] T. Qiu and C. Tien, "Femtosecond laser heating of multi-layer metals—I. Analysis," *International Journal of Heat and Mass Transfer*, vol. 37, pp. 2789–2797, nov 1994.

[232] Y. Yu, K. D. Wijesekara, X. Xi, and K. A. Willets, "Quantifying Wavelength-Dependent Plasmonic Hot Carrier Energy Distributions at Metal/Semiconductor Interfaces," *ACS Nano*, vol. 13, pp. 3629–3637, 2019.

[233] D. C. Ratchford, A. D. Dunkelberger, I. Vurgaftman, C. Owrutsky, and P. E. Pehrsson, "Quantification of Efficient Plasmonic Hot-Electron Injection in Gold Nanoparticle-TiO2 Films," *Nano Letters*, vol. 17, pp. 6047–6055, 2017.

[234] X. Zhou, M. V. Tokina, J. A. Tomko, J. L. Braun, P. E. Hopkins, and O. V. Prezhdo, "Thin Ti adhesion layer breaks bottleneck to hot hole relaxation in Au films," *Journal of Chemical Physics*, vol. 150, no. April, p. 184701, 2019.

[235] Y. Yang, K. Kelley, E. Sachet, S. Campione, T. S. Luk, J.-P. Maria, M. B. Sinclair, and I. Brener, "Femtosecond optical polarization switching using a cadmium oxide-based perfect absorber," *Nature Photonics*, vol. 11, no. 6, pp. 390–395, 2017.

[236] C. P. Liu, Y. Foo, M. Kamruzzaman, C. Y. Ho, J. A. Zapien, W. Zhu, Y. J. Li, W. Walukiewicz, and K. M. Yu, "Effects of Free Carriers on the Optical Properties of Doped CdO for Full-Spectrum Photovoltaics," *Physical Review Applied*, vol. 6, p. 64018, dec 2016.

[237] J. R. Nolen, E. L. Runnerstrom, K. P. Kelley, T. S. Luk, T. G. Folland, A. Cleri, J.-P. Maria, and J. D. Caldwell, "Ultraviolet to Far-Infrared Dielectric Function of n-doped Cadmium Oxide Thin Films," *submitted to Physical Review Materials*, 2019.

[238] J. A. Tomko, A. Pena-Francesch, H. Jung, M. Tyagi, B. D. Allen, M. C. Demirel, and P. E. Hopkins, "Tunable thermal transport and reversible thermal conductivity switching in topologically networked bio-inspired materials," *Nature Nanotechnology*, vol. 13, no. 10, pp. 959–964, 2018.

[239] A. Poynor, L. Hong, I. K. Robinson, S. Granick, Z. Zhang, and P. A. Fenter, "How water meets a hydrophobic surface," *Physical Review Letters*, vol. 97, no. 266101, pp. 1–4, 2006.

[240] S. Chattopadhyay, A. Uysal, B. Stripe, Y. G. Ha, T. J. Marks, E. A. Karapetrova, and P. Dutta, "How water meets a very hydrophobic surface," *Physical Review Letters*, vol. 105, no. 3, pp. 1–4, 2010.

[241] R. Godawat, S. N. Jamadagni, and S. Garde, "Characterizing hydrophobicity of interfaces by using cavity formation, solute binding, and water correlations," *Proceedings of the National Academy of Sciences*, vol. 106, no. 36, pp. 15119–15124, 2009.

[242] C. Sendner, D. Horinek, L. Bocquet, and R. R. Netz, "Interfacial water at hydrophobic and hydrophilic surfaces: Slip, viscosity, and diffusion," *Langmuir*, vol. 25, no. 18, pp. 10768–10781, 2009.

[243] T. A. Ho, D. V. Papavassiliou, L. L. Lee, and A. Striolo, "Liquid water can slip on a hydrophilic surface," *Proceedings of the National Academy of Sciences*, vol. 108, no. 39, pp. 16170–16175, 2011.

[244] D. Lis, E. H. G. Backus, J. Hunger, S. H. Parekh, and M. Bonn, "Liquid flow along a solid surface reversibly alters interfacial chemistry," *Science*, vol. 344, no. 6188, pp. 1138–1142, 2014.

[245] A. Giri and P. E. Hopkins, "Analytical model for thermal boundary conductance and equilibrium thermal accommodation coefficient at solid / gas interfaces," *The Journal of Chemical Physics*, vol. 144, p. 84705, 2016.

[246] K. Trachenko, "Heat capacity of liquids: An approach from the solid phase," *Physical Review B*, vol. 78, no. 10, pp. 1–7, 2008.

[247] D. Bolmatov and K. Trachenko, "Liquid heat capacity in the approach from the solid state: Anharmonic theory," *Physical Review B*, vol. 84, no. 5, pp. 1–7, 2011.

[248] D. Bolmatov, V. Brazhkin, and K. Trachenko, "The phonon theory of liquid thermodynamics," *Scientific Reports*, vol. 2, no. 421, pp. 1–6, 2012.

[249] A. Giri and P. E. Hopkins, "Spectral analysis of thermal boundary conductance across solid/classical liquid interfaces: A molecular dynamics study," *Applied Physics Letters*, vol. 105, no. 3, p. 33106, 2014.

[250] D. Torii, T. Ohara, and K. Ishida, "Molecular-Scale Mechanism of Thermal Resistance at the Solid-Liquid Interfaces: Influence of Interaction Parameters Between Solid and Liquid Molecules," *Journal of Heat Transfer*, vol. 132, no. 1, p. 012402, 2010.

[251] S. Ge and M. Chen, "Vibrational coupling and Kapitza resistance at a solid-liquid interface," *International Journal of Thermophysics*, vol. 34, no. 1, pp. 64–77, 2013.

[252] N. Shenogina, R. Godawat, P. Keblinski, and S. Garde, "How wetting and adhesion affect thermal conductance of a range of hydrophobic to hydrophilic aqueous interfaces," *Physical Review Letters*, vol. 102, no. 15, pp. 1–4, 2009.

[253] S. Murad and I. K. Puri, "Thermal transport across nanoscale solid-fluid interfaces," *Applied Physics Letters*, vol. 92, no. 13, pp. 10–13, 2008.

[254] G. Balasubramanian, S. Banerjee, and I. K. Puri, "Unsteady nanoscale thermal transport across a solid-fluid interface," *Journal of Applied Physics*, vol. 104, no. 6, p. 64306, 2008.

[255] L. Xue, P. Keblinski, S. R. Phillpot, S. U. S. Choi, and J. A. Eastman, "Two regimes of thermal resistance at a liquid-solid interface," *Journal of Chemical Physics*, vol. 118, no. 1, pp. 337–339, 2003.

[256] L. Xue, P. Keblinski, S. R. Phillpot, S. U. S. Choi, and J. A. Eastman, "Effect of liquid layering at the liquid-solid interface on thermal transport," *International Journal of Heat and Mass Transfer*, vol. 47, no. 19-20, pp. 4277–4284, 2004.

[257] J.-L. Barrat and F. Chiaruttini, "Kapitza resistance at the liquid solid interface," *Molecular Physics: An International Journal at the Interface Between Chemistry and Physics*, vol. 101:11, no. June 2015, pp. 1605–1610, 2002.

[258] S. Merabia, S. Shenogin, L. Joly, P. Keblinski, and J.-L. Barrat, "Heat transfer from nanoparticles: A corresponding state analysis," *Proceedings of the National Academy of Sciences*, vol. 106, no. 36, pp. 15113–15118, 2009.

[259] Z. Tian, A. Marconnet, and G. Chen, "Enhancing solid-liquid interface thermal transport using self-assembled monolayers," *Applied Physics Letters*, vol. 106, no. 21, p. 211602, 2015.

[260] S. R. Das, S. Srinivasan, L. R. Stromberg, Q. He, N. Garland, W. E. Straszheim, P. M. Ajayan, G. Balasubramanian, and J. C. Claussen, "Superhydrophobic inkjet printed flexible graphene circuits via direct-pulsed laser writing," *Nanoscale*, vol. 9, pp. 19058–19065, 2017.

[261] E. J. Heilweil and R. M. Hochstrasser, "Nonlinear spectroscopy and picosecond transient grating study of colloidal gold," *The Journal of Chemical Physics*, vol. 82, no. 11, pp. 4762–4770, 1985.

[262] G. Tas and H. J. Maris, "Picosecond ultrasonic study of phonon reflection from solid-liquid interfaces," *Physical Review B*, vol. 55, no. 3, pp. 1852–1857, 1997.

[263] A. J. Schmidt, X. Chen, and G. Chen, "Pulse accumulation, radial heat conduction, and anisotropic thermal conductivity in pump-probe transient thermoreflectance," *Review of Scientific Instruments*, vol. 79, no. 11, p. 114902, 2008.

[264] P. V. Ruijgrok, P. Zijlstra, A. L. Tchebotareva, and M. Orrit, "Damping of acoustic vibrations of single gold nanoparticles optically trapped in water," *Nano Letters*, vol. 12, no. 2, pp. 1063–1069, 2012.

[265] C. Hua, X. Chen, N. K. Ravichandran, and A. J. Minnich, "Experimental metrology to obtain thermal phonon transmission coefficients at solid interfaces," *Physical Review B*, vol. 95, p. 205423, 2017.

[266] A. Dupré, *Théorie mécanique de la chaleur*. 1869.

[267] M. E. Schrader, "Young-Dupre Revisited," *Langmuir*, vol. 11, no. 6, pp. 3585–3589, 1995.

[268] B. Ramos-Alvarado, S. Kumar, and G. P. Peterson, "Solid-Liquid Thermal Transport and Its Relationship with Wettability and the Interfacial Liquid Structure," *Journal of Physical Chemistry Letters*, vol. 7, no. 17, pp. 3497–3501, 2016.

[269] M. Maccarini, R. Steitz, M. Himmelhaus, J. Fick, S. Tatur, M. Wolff, M. Grunze, J. Janecek, and R. R. Netz, "Density depletion at solid-liquid interfaces: A neutron reflectivity study," *Langmuir*, vol. 23, no. 2, pp. 598–608, 2007.

[270] P. Gutfreund, M. Wolff, M. MacCarini, S. Gerth, J. F. Ankner, J. Browning, C. E. Halbert, H. Wacklin, and H. Zabel, "Depletion at solid/liquid interfaces: Flowing hexadecane on functionalized surfaces," *Journal of Chemical Physics*, vol. 134, no. 6, 2011.

[271] P. E. Hopkins, "Thermal transport across solid interfaces with nanoscale imperfections: Effects of roughness, disorder, dislocations, and bonding on thermal boundary conductance," *ISRN Mechanical Engineering*, vol. 2013, no. 1, pp. 1–19, 2013.

[272] J. P. Feser and D. G. Cahill, “Probing anisotropic heat transport using time-domain thermoreflectance with offset laser spots,” *Review of Scientific Instruments*, vol. 83, no. 2012, p. 104901, 2014.

[273] A. Giri and P. E. Hopkins, “Analytical model for thermal boundary conductance and equilibrium thermal accommodation coefficient at solid / gas interfaces,” *The Journal of Chemical Physics*, vol. 144, p. 84705, 2016.

[274] C. J. Morath and H. J. Maris, “Phonon attenuation in amorphous solids studied by picosecond ultrasonics,” *Physical Review B*, vol. 54, p. 203, 1996.

[275] J. A. Tomko, A. Pena-francesch, H. Jung, M. Tyagi, B. D. Allen, M. C. Demirel, and P. E. Hopkins, “Tunable thermal transport and reversible thermal conductivity switching in topologically networked bio-inspired materials,” *Nature Nanotechnology*, vol. 13, no. 10, pp. 959–964, 2018.

[276] J. L. Braun, S. W. King, A. Giri, J. T. Gaskins, M. Sato, T. Fujiseki, and P. E. Hopkins, “Breaking network connectivity leads to ultralow thermal conductivities in fully dense amorphous solids,” *Applied Physics Letters*, vol. 191905, pp. 10–15, 2016.

[277] A. Devos, M. Foret, S. Ayrinhac, P. Emery, and B. Ruffle, “Hypersound damping in vitreous silica measured by picosecond acoustics,” *Physical Review B*, vol. 77, p. 100201(R), 2008.

[278] A. Devos and R. Cote, “Strong oscillations detected by picosecond ultrasonics in silicon: Evidence for an electronic-structure effect,” *Physical Review B*, vol. 70, p. 125208, 2004.

[279] P. Babilotte, P. Ruello, D. Mounier, T. Pezeril, G. Vaudel, M. Edely, J.-M. Breteau, V. Gusev, and K. Blary, “Femtosecond laser generation and detection of high-frequency acoustic phonons in GaAs semiconductors,” *Physical Review B*, vol. 81, p. 245207, 2010.

[280] P.-a. Mante, C. C. Stoumpos, M. G. Kanatzidis, and A. Yartsev, “Electron-acoustic phonon coupling in single crystal CH3NH3PbI3 perovskites revealed by coherent acoustic phonons,” *Nature Communications*, vol. 8, p. 14398, 2017.

[281] R. Legrand, A. Huynh, B. Jusserand, A. Lemaître, and B. Perrin, “Direct measurement of coherent subterahertz acoustic phonons mean free path in GaAs,” *Physical Review B*, vol. 184304, p. 184304, 2016.

[282] R. N. Kini, A. J. Kent, N. M. Stanton, and M. Henini, “Generation and detection of terahertz coherent transverse-polarized acoustic phonons by ultrafast optical excitation of GaAs/AlAs,” *Applied Physics Letters*, vol. 88, p. 134112, 2006.

[283] M. Garfinkel, J. J. Tiemann, and W. E. Engeler, “Piezoreflectivity of the noble metals,” *Physical Review*, vol. 148, no. 2, pp. 695–706, 1966.

[284] W. Ma, T. Miao, X. Zhang, M. Kohno, and Y. Takata, “Comprehensive Study of Thermal Transport and Coherent Acoustic-Phonon Wave Propagation in Thin Metal Film–Substrate by Applying Picosecond Laser Pump–Probe Method,” *The Journal of Physical Chemistry C*, vol. 119, no. 9, pp. 5152–5159, 2015.

[285] J. K. Chen, D. Y. Tzou, and J. E. Beraun, “A semiclassical two-temperature model for ultrafast laser heating,” *International Journal of Heat and Mass Transfer*, vol. 49, no. 1-2, pp. 307–316, 2006.

[286] V. H. Dalvi and P. J. Rossky, “Molecular origins of fluorocarbon hydrophobicity,” *Proceedings of the National Academy of Sciences*, vol. 107, no. 31, pp. 13603–13607, 2010.

[287] J. T. Gaskins, A. Bulusu, A. J. Giordano, J. C. Duda, S. Graham, and P. E. Hopkins, “Thermal Conductance across Phosphonic Acid Molecules and Interfaces: Ballistic versus Diffusive Vibrational Transport in Molecular Monolayers,” *Journal of Physical Chemistry C*, vol. 119, no. 36, pp. 20931–20939, 2015.

[288] D. M. Lemal, “Perspective on Fluorocarbon Chemistry,” *Journal of Organic Chemistry*, vol. 69, no. 1, pp. 1–11, 2004.

[289] L. C. Clark Jr. and F. Gollan, “Survival of Mammals Breathing Organic Liquids Equilibrated with Oxygen at Atmospheric Pressure,” *Science*, vol. 152, no. 3730, pp. 1755–1756, 1966.

[290] J. G. Riess and J. G. Riess, “Oxygen carriers (”blood substitutes”) - Raison d’etre, chemistry, and some physiology,” *Chemical Reviews*, vol. 101, no. 9, pp. 2797–2919, 2001.

[291] Y. Takata, J. H. J. Cho, B. M. Law, and M. Aratono, “Ellipsometric search for vapor layers at liquid-hydrophobic solid surfaces,” *Langmuir*, vol. 22, no. 4, pp. 1715–1721, 2006.

[292] G. Wehmeyer, T. Yabuki, C. Monachon, J. Wu, and C. Dames, “Thermal diodes, regulators, and switches: Physical mechanisms and potential applications,” *Applied Physical Reviews*, vol. 4, p. 41304, 2017.

[293] X. Gou, H. Ping, Q. Ou, H. Xiao, and S. Qing, “A novel thermoelectric generation system with thermal switch,” *Energy Procedia*, vol. 61, no. Supplement C, pp. 1713–1717, 2014.

[294] X. Zhang and L.-D. Zhao, “Thermoelectric materials: Energy conversion between heat and electricity,” *Journal of Materiomics*, vol. 1, no. 2, pp. 92–105, 2015.

[295] M. J. DiPirro and P. J. Shirron, “Heat switches for ADRs,” *Cryogenics*, vol. 62, pp. 172–176, 2014.

[296] Y. Jia and Y. S. Ju, “A solid-state refrigerator based on the electrocaloric effect,” *Applied Physics Letters*, vol. 100, no. 24, p. 242901, 2012.

[297] J. Shin, M. Kang, T. Tsai, C. Leal, P. V. Braun, and D. G. Cahill, "Thermally Functional Liquid Crystal Networks by Magnetic Field Driven Molecular Orientation," *ACS Macro Letters*, vol. 5, no. 8, pp. 955–960, 2016.

[298] J. Cho, M. D. Losego, H. G. Zhang, H. Kim, J. Zuo, I. Petrov, D. G. Cahill, and P. V. Braun, "Electrochemically tunable thermal conductivity of lithium cobalt oxide," *Nature Communications*, vol. 5, no. May, pp. 1–6, 2014.

[299] J. F. Ihlefeld, B. M. Foley, D. A. Scrymgeour, J. R. Michael, B. B. Mckenzie, D. L. Medlin, M. Wallace, S. Trolier-mckinstry, and P. E. Hopkins, "Room-Temperature Voltage Tunable Phonon Thermal Conductivity via Reconfigurable Interfaces in Ferroelectric Thin Films," *Nano Letters*, vol. 15, pp. 1791–1795, 2015.

[300] X. Zhang and M. Hejazi, "From 1D Chain to 3D Network: A New Family of Inorganic-Organic Hybrid Semiconductors MO3(L)x (M=Mo,W; L=Organic Linker) Built on Perovskite-like Structure Modules," *Journal of the American Chemical Society*, vol. 135, no. L, p. 17401, 2013.

[301] S. Shen, A. Henry, J. Tong, R. Zheng, and G. Chen, "Polyethylene nanofibres with very high thermal conductivities," *Nature Nanotechnology*, vol. 5, pp. 251–255, 2010.

[302] V. Singh, T. L. Bougher, A. Weathers, Y. Cai, K. Bi, M. T. Pettes, S. A. McMenamin, W. Lv, D. P. Resler, T. R. Gattuso, D. H. Altman, K. H. Sandhage, L. Shi, A. Henry, and B. A. Cola, "High thermal conductivity of chain-oriented amorphous polythiophene," *Nature Nanotechnology*, vol. 9, pp. 384–390, 2014.

[303] G.-H. Kim, D. Lee, A. Shanker, L. Shao, M. S. Kwon, D. Gidley, J. Kim, and K. P. Pipe, "High thermal conductivity in amorphous polymer blends by engineered interchain interactions," *Nature Materials*, vol. 14, pp. 295–300, 2015.

[304] X. Wang, V. Ho, R. A. Segalman, and D. G. Cahill, "Thermal Conductivity of High-Modulus Polymer Fibers," *Macromolecules*, vol. 46, no. 12, pp. 4937–4943, 2013.

[305] L. Phan, W. G. W. Iv, D. D. Ordinario, E. Karshalev, J.-m. Jocson, A. M. Burke, and A. A. Gorodetsky, "Reconfigurable Infrared Camouflage Coatings from a Cephalopod Protein," *Advanced Materials*, vol. 25, pp. 5621–5625, 2013.

[306] V. Sariola, A. Pena-Francesch, H. Jung, M. Çetinkaya, C. Pacheco, M. Sitti, and M. C. Demirel, "Segmented molecular design of self-healing proteinaceous materials.," *Scientific reports*, vol. 5, p. 13482, 2015.

[307] M. Vural, Y. Lei, A. Pena-francesch, and H. Jung, "Programmable molecular composites of tandem proteins with graphene oxide for efficient bimorph actuators," *Carbon*, vol. 118, pp. 404–412, 2017.

[308] M. C. Demirel, M. Cetinkaya, A. Pena-Francesch, and H. Jung, "Recent advances in nanoscale bioinspired materials," *Macromolecular Bioscience*, vol. 15, no. 3, pp. 300–311, 2015.

[309] A. Pena-Francesch, S. Florez, H. Jung, A. Sebastian, I. Albert, W. Curtis, and M. C. Demirel, “Materials Fabrication from Native and Recombinant Thermoplastic Squid Proteins,” *Advanced Functional Materials*, vol. 24, pp. 7401–7409, 2014.

[310] H. Jung, A. Pena-Francesch, A. Saadat, A. Sebastian, D. H. Kim, R. F. Hamilton, I. Albert, B. D. Allen, and M. C. Demirel, “Molecular tandem repeat strategy for elucidating mechanical properties of high-strength proteins,” *Proceedings of the National Academy of Sciences*, vol. 113, no. 23, pp. 6478–6483, 2016.

[311] M. C. George, M. A. Rodriguez, M. S. Kent, G. L. Brennecka, and P. E. Hopkins, “Thermal conductivity of self-assembling symmetric block copolymer thin films of polystyrene-block-poly(methyl methacrylate),” *Journal of Heat Transfer*, vol. 138, p. 24505, 2016.

[312] M. D. Losego, L. Moh, K. A. Arpin, D. G. Cahill, and P. V. Braun, “Interfacial thermal conductance in spun-cast polymer films and polymer brushes,” *Applied Physics Letters*, vol. 97, p. 11908, 2010.

[313] B. M. Foley, C. S. Gorham, J. C. Duda, R. Cheaito, C. J. Szwejkowski, C. Constantin, B. Kaehr, and P. E. Hopkins, “Protein Thermal Conductivity Measured in the Solid State Reveals Anharmonic Interactions of Vibrations in a Fractal Structure,” *The Journal of Physical Chemistry Letters*, vol. 5, pp. 1077–1082, 2014.

[314] M. G. Ghossoub, J.-H. Lee, O. T. Baris, D. G. Cahill, and S. Sinha, “Percolation of thermal conductivity in amorphous fluorocarbons,” *Physical Review B*, vol. 82, no. 19, p. 195441, 2010.

[315] V. Rashidi, E. J. Coyle, K. Sebeck, J. Kieffer, and K. P. Pipe, “Thermal Conductance in Cross-linked Polymers: Effects of Non-Bonding Interactions,” *Journal of Physical Chemistry B*, vol. 121, no. 17, pp. 4600–4609, 2017.

[316] A. Pena-Francesch, B. Akgun, A. Miserez, W. Zhu, H. Gao, and M. C. Demirel, “Pressure Sensitive Adhesion of an Elastomeric Protein Complex Extracted From Squid Ring Teeth,” *Advanced Functional Materials*, vol. 24, no. 39, pp. 6227–6233, 2014.

[317] P. J. Flory, *Principles of Polymer Chemistry*. Cornell University Press, 1953.

[318] L. R. G. Treloar, *The Physics of Rubber Elasticity*. Oxford University Press, USA, 1975.

[319] A. R. Atilgan, S. R. Durell, R. L. Jernigan, M. C. Demirel, O. Keskin, and I. Bahar, “Anisotropy of Fluctuation Dynamics of Proteins with an Elastic Network Model,” *Biophysical Journal*, vol. 80, pp. 505–515, 2001.

[320] A. Pena-francesch, H. Jung, M. Segad, R. H. Colby, B. D. Allen, and M. C. Demirel, “Mechanical Properties of Tandem-Repeat Proteins Are Governed by Network Defects,” *ACS Biomaterials Science & Engineering*, vol. 4, pp. 884–891, 2018.

[321] V. G. Sakai and A. Arbe, “Quasielastic neutron scattering in soft matter,” *Current Opinion in Colloid & Interface Science*, vol. 14, no. 6, pp. 381–390, 2009.

[322] G. Zaccai, “How Soft Is a Protein? A Protein Dynamics Force Constant Measured by Neutron Scattering,” *Science*, vol. 288, no. 5471, pp. 1604–1607, 2000.

[323] F. Gabel, D. Bicout, U. Lehnert, M. Tehei, M. Weik, and G. Zaccai, “Protein dynamics studied by neutron scattering,” *Quarterly Reviews of Biophysics*, vol. 35, no. 4, pp. 327–367, 2002.

[324] M. Gordon and J. S. Taylor, “Ideal copolymers and the second-order transitions of synthetic rubbers. i. non-crystalline copolymers,” *Journal of Applied Chemistry*, vol. 2, no. 9, pp. 493–500, 1952.

[325] F. Volino and A. J. Dianoux, “Neutron incoherent scattering law for diffusion in a potential of spherical symmetry: general formalism and application to diffusion inside a sphere,” *Molecular Physics*, vol. 41, no. 2, pp. 271–279, 1980.

[326] B. Allen and J. L. Feldman, “Thermal conductivity of disordered harmonic solids,” *Physical Review B*, vol. 48, no. 17, pp. 581–588, 1993.

[327] S. Shenogin, A. Bodapati, P. Keblinski, and A. J. H. McGaughey, “Predicting the thermal conductivity of inorganic and polymeric glasses : The role of anharmonicity,” *Journal of Applied Physics*, vol. 105, p. 34906, 2009.

[328] J. L. Feldman, M. D. Kluge, B. Allen, and F. Wooten, “Thermal conductivity and localization in glasses: Numerical study of a model of amorphous silicon,” *Physical Review B*, vol. 48, no. 17, p. 12589, 1993.

[329] H. Y. Wachman, “The thermal accommodation coefficient: A critical survey,” *American Rocket Society Journal*, 1962.

[330] F. O. Goodman, “Thermal Accomodation Coefficients,” *J. Phys. Chem.*, vol. 84, pp. 1431–1445, 1980.

[331] J. N. Smith and H. Saltsburg, “Atomic-Beam Scattering from Epitaxially Grown Gold Films,” *J. Chem. Phys.*, vol. 40, p. 3585, 1964.

[332] H. Saltsburg and J. N. Smith, “Molecular-Beam Scattering from the (111) Plane of Silver,” *J. Chem. Phys.*, vol. 45, p. 2175, 1966.

[333] R. L. Palmer, J. N. Smith, H. Saltsburg, and D. R. O’Keefe, “Measurements of the Reflection, Adsorption, and Desorption of Gases from Smooth Metal Surfaces,” *J. Chem. Phys.*, vol. 53, p. 1666, 1970.

[334] J. P. Toennies, “Scattering of Molecular Beams from Surfaces,” *Appl. Phys.*, vol. 3, pp. 91–114, 1974.

[335] J. C. Tully, “Dynamics of gas-surface interactions: Thermal desorption of Ar and Xe from platinum,” *Surface Science*, vol. 111, pp. 461–478, 1981.

[336] S. R. Cohen, R. Naaman, and J. Sagiv, "Translational energy transfer from molecules and atoms to adsorbed organic monolayers of long-chain amphiphiles," *Physical Review Letters*, vol. 58, p. 2153, 1987.

[337] A. W. Kleyn, "Molecular beams and chemical dynamics at surfaces," *Chem. Soc. Rev.*, vol. 32, pp. 87–95, 2003.

[338] S. Dou, L. Tao, R. Wang, S. El Hankari, R. Chen, and S. Wang, "Plasma-Assisted Synthesis and Surface Modification of Electrode Materials for Renewable Energy," *Advanced Materials*, vol. 30, p. 1705850, may 2018.

[339] V. M. Donnelly and A. Kornblit, "Plasma etching: Yesterday, today, and tomorrow," *Journal of Vacuum Science & Technology A: Vacuum, Surfaces, and Films*, vol. 31, p. 50825, sep 2013.

[340] P. K. Chu, J. Y. Chen, L. P. Wang, and N. Huang, "Plasma-surface modification of biomaterials," *Materials Science and Engineering: R: Reports*, vol. 36, pp. 143–206, mar 2002.

[341] O. V. Penkov, M. Khadem, W.-S. Lim, and D.-E. Kim, "A review of recent applications of atmospheric pressure plasma jets for materials processing," *J. Coat. Technol. Res.*, vol. 12, pp. 225–235, 2015.

[342] C. Linsmeier, M. Rieth, J. Aktaa, T. Chikada, A. Hoffmann, J. Hoffmann, A. Houben, H. Kurishita, X. Jin, M. Li, A. Litnovsky, S. Matsuo, A. Von Müller, V. Nikolic, T. Palacios, R. Pippan, D. Qu, J. Reiser, J. Riesch, T. Shikama, R. Stieglitz, T. Weber, S. Wurster, J. H. You, and Z. Zhou, "Development of advanced high heat flux and plasma-facing materials," *Nuclear Fusion*, vol. 57, jun 2017.

[343] H. Kersten, H. Deutsch, H. Steffen, G. M. W. Kroesen, and R. Hippler, "The energy balance at substrate surfaces during plasma processing," *Vacuum*, vol. 63, pp. 385–431, aug 2001.

[344] I. H. Hutchinson, *Principles of Plasma Diagnostics*. Cambridge University Press, second edi ed., 1987.

[345] K. Takizawa, K. Sasaki, and A. Kono, "Sensitive measurements of electric field distributions in low-pressure Ar plasmas by laser-induced fluorescence-dip spectroscopy," *Applied Physics Letters*, vol. 84, p. 185, 2004.

[346] D. Staack, Y. Raitses, and N. J. Fisch, "Shielded electrostatic probe for nonperturbing plasma measurements in thrusters," *Review of Scientific Instruments*, vol. 75, p. 393, 2004.

[347] D. B. Graves and P. Brault, "Molecular dynamics for low temperature plasma-surface interaction studies," *Journal of Physics D: Applied Physics*, vol. 42, no. 19, 2009.

[348] M. Warrier, R. Schneider, and X. Bonnin, “Subroutines for some plasma surface interaction processes: Physical sputtering, chemical erosion, radiation enhanced sublimation, backscattering and thermal evaporation,” *Computer Physics Communications*, vol. 160, pp. 46–68, jun 2004.

[349] H. Kersten, H. Deutsch, M. Otte, G. H. P. M. Swinkels, and G. M. W. Kroesen, “Micro-disperse particles as probes for plasma surface interaction,” *Thin Solid Films*, vol. 377-378, pp. 530–536, dec 2000.

[350] A. J. Knoll, P. Luan, E. A. J. Bartis, C. Hart, Y. Raitses, and G. S. Oehrlein, “Real time characterization of polymer surface modifications by an atmospheric pressure plasma jet: Electrically coupled versus remote mode,” *Appl. Phys. Lett*, vol. 105, p. 171601, 2014.

[351] M. Shinohara, T. Kuwano, Y. Akama, Y. Kimura, M. Niwano, H. Ishida, and R. Hatakeyama, “Interaction of hydrogen-terminated Si(100), (110), and (111) surfaces with hydrogen plasma investigated by in situ real-time infrared absorption spectroscopy,” *Citation: Journal of Vacuum Science & Technology A*, vol. 21, p. 25, 2003.

[352] A. Giri, J. T. Gaskins, B. F. Donovan, C. Szwejkowski, R. J. Warzoha, M. A. Rodriguez, J. Ihlefeld, and P. E. Hopkins, “Mechanisms of nonequilibrium electron-phonon coupling and thermal conductance at interfaces,” *Journal of Applied Physics*, vol. 117, p. 105105, 2015.

[353] R. B. Wilson, B. A. Apgar, L. W. Martin, and D. G. Cahill, “Thermoreflectance of metal transducers for optical pump-probe studies of thermal properties,” *Optics Express*, vol. 20, no. 27, pp. 2267–2269, 2012.

[354] G. D. Mahan, “Thermionic refrigeration,” *Journal of Applied Physics*, vol. 4362, no. June 1994, 1994.

[355] D. Vashaee and A. Shakouri, “Improved Thermoelectric Power Factor in Metal-Based Superlattices,” *Physical Review Letters*, vol. 92, p. 106103, 2004.

[356] M. G. Rosul, D. Lee, D. H. Olson, N. Liu, X. Wang, P. E. Hopkins, K. Lee, and M. Zebarjadi, “Thermionic transport across gold-graphene-WSe2 van der Waals heterostructures,” *Science Advances*, vol. 5, p. eaax7827, 2019.

[357] C. Kerse, H. Kalayc, P. Elahi, S. Yava, D. K. Kesim, and Ö. Akçaalan, “Ablation-cooled material removal with ultrafast bursts of pulses,” *Nature*, vol. 537, no. 7618, pp. 84–88, 2016.

[358] J. Freund, J. Halbritter, and J. K. H. Hörber, “How dry are dried samples? Water adsorption measured by STM,” *Microscopy Research and Technique*, vol. 44, no. 5, pp. 327–338, 1999.

[359] G. M. Fleming and J. E. Henderson, "The Energy Losses Attending Field Current and Thermionic Emission of Electrons from Metals," *Physical Review*, vol. 58, p. 887, 1940.

[360] M. Wolf, S. Nettesheim, J. M. White, E. Hasselbrink, and G. Ertl, "Dynamics of the ultraviolet photochemistry of water adsorbed on Pd(111)," *The Journal of Chemical Physics*, vol. 94, no. 6, pp. 4609–4619, 1991.

[361] J. A. Tomko, D. H. Olson, J. L. Braun, A. P. Kelliher, B. Kaehr, and P. E. Hopkins, "Substrate thermal conductivity controls the ability to manufacture microstructures via laser-induced direct write," *Applied Physics Letters*, vol. 112, p. 51906, 2018.

[362] C. M. Rost, T. Borman, M. D. Hossain, M. Lim, K. F. Quiambao-Tomko, J. A. Tomko, D. W. Brenner, J.-P. Maria, and P. E. Hopkins, "Electron and phonon thermal conductivity in high entropy carbides with variable carbon content," *Acta Materialia*, vol. 196, pp. 231–239, 2020.

[363] Y. R. Koh, Z. Cheng, A. Mamun, M. S. Bin Hoque, Z. Liu, T. Bai, K. Hussain, M. E. Liao, R. Li, J. T. Gaskins, A. Giri, J. Tomko, J. L. Braun, M. Gaevski, E. Lee, L. Yates, M. S. Goorsky, T. Luo, A. Khan, S. Graham, and P. E. Hopkins, "Bulk-like Intrinsic Phonon Thermal Conductivity of Micrometer-Thick AlN Films," *ACS Applied Materials and Interfaces*, vol. 12, no. 26, pp. 29443–29450, 2020.

[364] D. H. Olson, V. A. Avincola, C. G. Parker, J. L. Braun, J. T. Gaskins, J. A. Tomko, E. J. Opila, and P. E. Hopkins, "Anisotropic thermal conductivity tensor of β-Y2Si2O7 for orientational control of heat flow on micrometer scales," *Acta Materialia*, vol. 189, pp. 299–305, 2020.

[365] J. Gild, A. Wright, K. Quiambao-Tomko, M. Qin, J. A. Tomko, M. Shafkat bin Hoque, J. L. Braun, B. Bloomfield, D. Martinez, T. Harrington, K. Vecchio, P. E. Hopkins, and J. Luo, "Thermal conductivity and hardness of three single-phase high-entropy metal diborides fabricated by borocarbothermal reduction and spark plasma sintering," *Ceramics International*, vol. 46, pp. 6906–6913, nov 2020.

[366] D. H. Olson, J. T. Gaskins, J. A. Tomko, E. J. Opila, R. A. Golden, G. J. Harrington, A. L. Chamberlain, and P. E. Hopkins, "Local thermal conductivity measurements to determine the fraction of α-cristobalite in thermally grown oxides for aerospace applications," *Scripta Materialia*, vol. 177, pp. 214–217, mar 2020.

[367] T. F. Lu, Y. S. Wang, J. A. Tomko, P. E. Hopkins, H. X. Zhang, and O. V. Prezhdo, "Control of Charge Carrier Dynamics in Plasmonic Au Films by TiOx Substrate Stoichiometry," *Journal of Physical Chemistry Letters*, vol. 11, no. 4, pp. 1419–1427, 2020.

[368] Y.-S. Wang, X. Zhou, J. A. Tomko, A. Giri, P. E. Hopkins, and O. V. Prezhdo, "Electron–Phonon Relaxation at Au/Ti Interfaces Is Robust to Alloying: Ab Initio Nonadiabatic Molecular Dynamics," *The Journal of Physical Chemistry C*, vol. 123, pp. 22842–22850, sep 2019.

[369] C. Kindle, A. Castonguay, S. McGee, J. A. Tomko, P. E. Hopkins, and L. D. Zarzar, "Direct Laser Writing from Aqueous Precursors for Nano to Microscale Topographical Control, Integration, and Synthesis of Nanocrystalline Mixed Metal Oxides," *ACS Applied Nano Materials*, vol. 2, pp. 2581–2586, may 2019.

[370] F. Krahl, A. Giri, J. A. Tomko, T. Tynell, P. E. Hopkins, and M. Karppinen, "Thermal Conductivity Reduction at Inorganic–Organic Interfaces: From Regular Superlattices to Irregular Gradient Layer Sequences," *Advanced Materials Interfaces*, vol. 5, no. 11, p. 1701692, 2018.

[371] W. Jensen, N. Liu, B. Donovan, J. Tomko, P. Hopkins, and J. Floro, "Synthesis and thermal transport of eco-friendly Fe-Si-Ge alloys with eutectic/eutectoid microstructure," *Materials Chemistry and Physics*, vol. 207, pp. 67–75, 2018.

[372] A. Giri, J. Tomko, J. T. Gaskins, and P. E. Hopkins, "Large tunability in the mechanical and thermal properties of carbon nanotube-fullerene hierarchical monoliths," *Nanoscale*, vol. 10, pp. 22166–22172, dec 2018.

[373] A. Giri, J. Braun, J. Tomko, and P. Hopkins, "Reducing the thermal conductivity of chemically ordered binary alloys below the alloy limit via the alteration of phonon dispersion relations," *Applied Physics Letters*, vol. 110, no. 23, p. 233112, 2017.

[374] B. F. Donovan, J. A. Tomko, A. Giri, D. H. Olson, J. L. Braun, J. T. Gaskins, and P. E. Hopkins, "Localized thin film damage sourced and monitored via pump-probe modulated thermoreflectance," *Review of Scientific Instruments*, vol. 88, no. 5, p. 054903, 2017.

[375] H. Jung, C. Szwejkowski, A. Pena-Franchesh, J. Tomko, B. Allen, S. Ozdemir, P. E. Hopkins, and M. C. Demirel, "Ultrafast Laser-Probing Spectroscopy for Studying Molecular Structure of Protein Aggregates," *Analyst*, vol. 142, no. 9, pp. 1434–1441, 2017.

[376] J. Tomko, J. J. Naddeo, R. Jimenez, Y. Tan, M. Steiner, J. M. Fitz-Gerald, D. M. Bubb, and S. M. O'malley, "Size and polydispersity trends found in gold nanoparticles synthesized by laser ablation in liquids," *Phys. Chem. Chem. Phys*, vol. 17, p. 16327, 2015.

[377] J. A. Tomko, R. Jimenez, J. J. Naddeo, D. M. Bubb, and S. M. O'Malley, "Effects of laser polarization and linear surface features on nanoparticle synthesis during laser ablation in liquids," *Laser Physics*, vol. 28, p. 35602, 2018.

[378] S. M. O'Malley, J. Tomko, a. P. D. Pino, C. Logofatu, and E. György, "Resonant Infrared and Ultraviolet Matrix-Assisted Pulsed Laser Evaporation of Titanium Oxide/Graphene Oxide Composites: A Comparative Study," *The Journal of Physical Chemistry C*, vol. 118, pp. 27911–27919, 2014.

[379] M. Ratti, Y. Tan, J. J. Naddeo, J. C. Griepenburg, J. Tomko, C. Trout, S. M. O. Malley, D. M. Bubb, and E. A. Klein, "Irradiation with visible light enhances the

antibacterial toxicity of silver nanoparticles produced by laser ablation," *Applied Physics A*, vol. 122, p. 346, 2016.

[380] Y. S. Touloukian, R. W. Powell, C. Y. Ho, and P. G. Klemens, *Thermophysical Properties of Matter - Specific Heat: {N}onmetallic Solids*, vol. 5. New York, IFI/Plenum, 1970.

[381] Y. S. Touloukian, R. W. Powell, C. Y. Ho, and P. G. Klemens, *Thermophysical Properties of Matter - Thermal Conductivity: {N}onmetallic Solids*, vol. 2. New York, IFI/Plenum, 1970.

[382] L. A. Pettersson, L. S. Roman, and O. Inganäs, "Modeling photocurrent action spectra of photovoltaic devices based on organic thin films," *Journal of Applied Physics*, vol. 86, no. 1, pp. 487–496, 1999.

[383] H. Yilmaz, A. Pena-Francesch, R. Shreiner, H. Jung, Z. Belay, M. C. Demirel, S. K. Ozdemir, and L. Yang, "Structural Protein-Based Whispering Gallery Mode Resonators," *ACS Photonics*, vol. 4, pp. 2179–2186, 2017.

Chapter 9

Appendix

Two-temperature model (TTM)

The analysis of measured temporal dynamics in our pump-probe experiments relies on solving equations for a material's thermal response via a semi-classical two-temperature model (TTM). This TTM is based on the following description of ultrafast laser heating: The incident laser pulse couples and transfers energy directly to electrons. This energy deposition leads to a large increase in the temperature of the electronic subsystem; in doing so, the electrons are now out of equilibrium with the phonon/lattice subsystem which has not gained energy directly from the initial laser interaction. In a sufficiently thin metal film supported by a dielectric substrate, where electron transport out of the initially heated area cannot occur on rapid time scales, equilibrium is achieved through electron-phonon coupling. In thin gold films excited by femtosecond pulses, the electron and phonon subsystem temperatures reach this equilibrium on the order of a few picoseconds, after which energy is conducted by the lattice via 'typical' thermal transport.

We can define the respective temporal evolution of the electron and phonon subsystem temperatures via

$$C_e(T_e)\frac{\delta T_e}{\delta t} = \nabla \cdot (\kappa_e \nabla T_e) - G(T_e - T_p) + S(t) \tag{9.1}$$

$$C_p(T_p)\frac{\delta T_p}{\delta t} = \nabla \cdot (\kappa_p \nabla T_p) + G(T_e - T_p) \tag{9.2}$$

where C_e and C_p are the heat capacities, T_e and T_p are the temperatures, and κ_e and κ_p are the thermal conductivities of the electrons and phonons, respectively. The coupling constant associated with the aforementioned energy transfer between the two subsystems (the electron-phonon coupling constant) is given by G, and the source term, $S(t)$, accounts for the parameters associated with the pump pulse from the ultrafast laser. In metals, the electron heat capacity is well-known to vary linearly with respect to temperature, as given by $C_e = \gamma T_e$. Here, we use a value of $\gamma = 62.9$ J m^{-3} K^{-2}. An example of these calculated temperature evolutions on ultrafast time scales is shown in Fig. 9.1a. As shown, there is an additional steady-state temperature rise that leads to an increase in the 'background' temperature of the system and is not time-dependent; this temperature rise is discussed in more depth in the manuscript as well as later in the Supporting Information.

As the pump pulse has a larger beam waist than that of the probe beam at the sample surface, and the thickness of the Au film is on the order of the optical penetration depth for both the pump and probe beams ($\sim$10 nm), we simply consider the one-dimensional solution to these equations. As such, the laser heat source term, $S(t)$, for the Gaussian beam used in this work does not include a spatial dependence and can be expressed as

$$S(t) = \frac{0.94F_{abs}}{\delta t_p} \exp[4ln(2)(\frac{t-2t_p}{t_p})^2] \tag{9.3}$$

where F_{abs} is the absorbed fluence, δ is the optical penetration depth, and t_p is the pulse width. In this case, as mentioned above, the optical penetration depth is simply equated to the thickness of the Au film (16 nm). As the beam sizes were measured with both an optical beam profiler as well as via knife-edge, the absorbed fluence can be determined by setting the sample at a $\sim$5 degree angle relative to the incident beam and measuring the transmitted and reflected power of the 400 nm pump beam, then subtracting these from the incident power. Measurements regarding the pulse width are discussed in detail later in the Supporting Information.

Clearly, neither the temporal changes of the electron or phonon subsystems, nor the pump source term, account for the well-known fact that following an ultrafast optical excitation, a portion of the gold's electrons are in a non-thermal state and cannot be accurately defined by a Fermi-Dirac distribution for a few hundred femtoseconds. These non-thermalized electrons travel ballistically at approximately the Fermi velocity (on the order of 10^6 m s^{-1}). While the ballistic portion does not play a significant role at these film thicknesses, as the electrons would simply scatter and thermalize at the surface boundary rather than travel to a position below the probed optical penetration depth, these non-thermal electrons will deviate from the scattering rates discussed below. As elucidated by recent work, the weak contribution of this non-thermal electron distribution to changes in reflectivity has essentially subsided within less than 500 fs.[102] Additionally, this same work has shown that within 70 fs of the pump excitation, the step-like function associated with these non-thermal electrons has already reduced to half of its extension in energy-space relative to the Fermi energy. As our cross-correlation of pulses, as discussed later, is greater than the previously measured time necessary to observe changes associated with non-thermal electrons, and the probe pulse is over twice the duration of the observed energy reduction of 70 fs, we can approximate this electron thermalization time as simply an increase in the pulse width. In doing so, we simply substitute the sum of the values to an effective pulse width, i.e., $t_{p,eff} = t_p + t_{ee}$, where t_{ee} is the approximated electron thermalization time, which we assume to be 600 fs, thus using a $t_p = 800$ fs, which is the approximate cross-correlation of the pump and probe pulses in this work.

To solve these equations and determine the temperature evolution of these systems, we utilize the relationship between temperature and the dielectric function of a material as discussed in the manuscript. In short, within the Drude model, the free electron contribution to the dielectric function, ε, of a metal such as gold is given by

$$\varepsilon = 1 - \frac{{\omega_p}^2}{\omega^2 + i\omega\tau^{-1}} \tag{9.4}$$

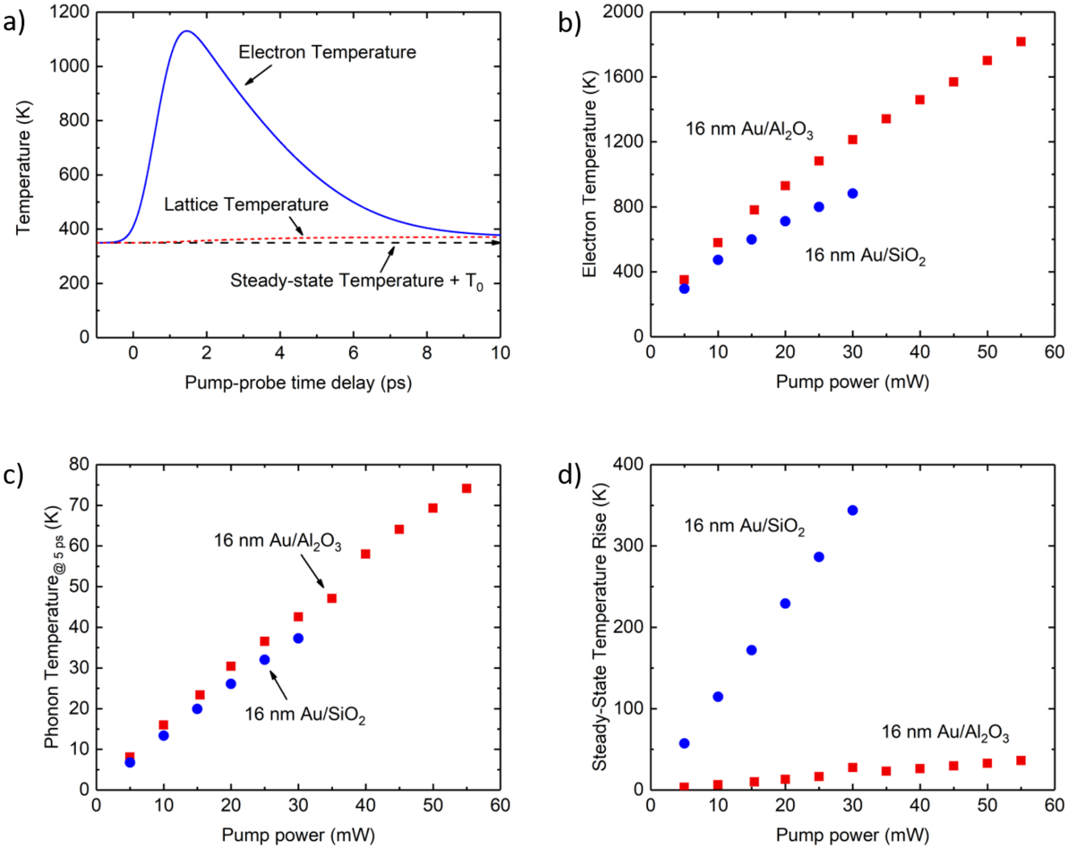

Figure 9.1: a) Temperature evolution of the electron and phonon subsystems following an ultrafast pump as calculated with our two-temperature model. b) Peak electron temperature and c) peak phonon temperature from TTM as a function of incident pump power for 16 nm Au on both a sapphire (red squares) and glass (blue circles) substrate. d) Steady-state temperature rise associated with the high-repetition rate oscillator used in this work as calculated by the cylindrical heat equation.

where ω is the frequency of light. The temperature dependence of this function, and thus the temperature dependence of changes in optical reflectivity, can arise from the other two parameters of this expression, ω_p and τ. As the plasma frequency, ω_p, of a metal is defined by $\omega_p = 4\pi N_e e^2/m^*$, any change in the electronic number density, N_e, or the effective mass of the contributing electrons, m^*, will clearly lead to a change in the dielectric function. As the band structure of a material is directly related to the structure of the atomic lattice, one could expect a change in effective mass for any increase in temperature, as the bond distance will increase due to thermal expansion. Similarly, as the *total* number of electrons associated with each atom is a nominal value, any variation in the atomic spacing of the material (e.g., thermal expansion) will lead to a change in the total volume of the material; this volumetric expansion causes the electron number density, N_e, to decrease with increasing temperature. Thus, the plasma frequency's temperature dependence is directly related to thermal expansion and is given by

$$\omega_p = \frac{\omega_p(T_0)}{\sqrt{1+3\alpha(T_p - T_0)}} \tag{9.5}$$

where α is the linear thermal expansion coefficient of a given material; for Au, $\alpha = 14.2 \times 10^{-6}\ \mathrm{K}^{-1}$.

On the other hand, the scattering rate of electrons, τ, varies as a function of not only phonon/lattice temperature, but also the temperature of the electrons themselves. As discussed in the manuscript, this relaxation time is dependent on both electron-electron scattering processes as well as electron-phonon scattering. Given this, the effective scattering rate can be expressed as $\tau^{-1} = tau_{ee}^{-1} + \tau_{ep}^{-1}$. In the case of free electrons, the dominant carriers in the case of metals such as Au, we make the common assumption that $\tau_{ee}^{-1} = A_{ee}T_e^2$ and $\tau_{ep}^{-1} = B_{ep}T_p$, where A_{ee} and B_{ep} are constants relating to the aforementioned electron-electron and electron-phonon scattering processes. These constants are assumed to have values of $A_{ee} = 1.5 \times 10^7\ \mathrm{K}^{-2}$ and $B_{ep} = 1.7 \times 10^{11}\ \mathrm{K}^{-1}$ for all TTM calculations in this work, unless noted otherwise; these values are in agreement with previous literature values and our dR/R analysis performed at a time delay of 500 ps, as discussed in detail later.

To directly compare the accuracy of our dR/dT_e derivation/expansion from the manuscript with TTM calculations, we do not include the temperature dependence associated with the plasma frequency in our model. To validate this simplification, we can consider the following: If we assume an arbitrary 100 K increase in temperature from ambient conditions ($\sim$300 K) and use the values referenced in the previous paragraph, we see that the plasma frequency varies by $\sim$2%, whereas the scattering rate changes by nearly 34%. Additionally, this assumption relies on an equivalent increase in both the electron and phonon temperatures of the system; the majority of our work is focused on the case of non-equilibrium distributions, where the electron temperature is much greater than the lattice temperature (i.e., $T_e >> T_p$). At the peak electron temperature rise, where dR/dT_e is analyzed, the lattice contribution to changes in reflectivity is negligible as the electrons have not yet coupled to phonons and thus have not transferred energy to the lattice, and the change in reflectivity would be dominated solely by the electron-electron scattering rate as it is the only T_e-dependent variable.

While the addition of a temperature dependent plasma frequency does not alter the peak

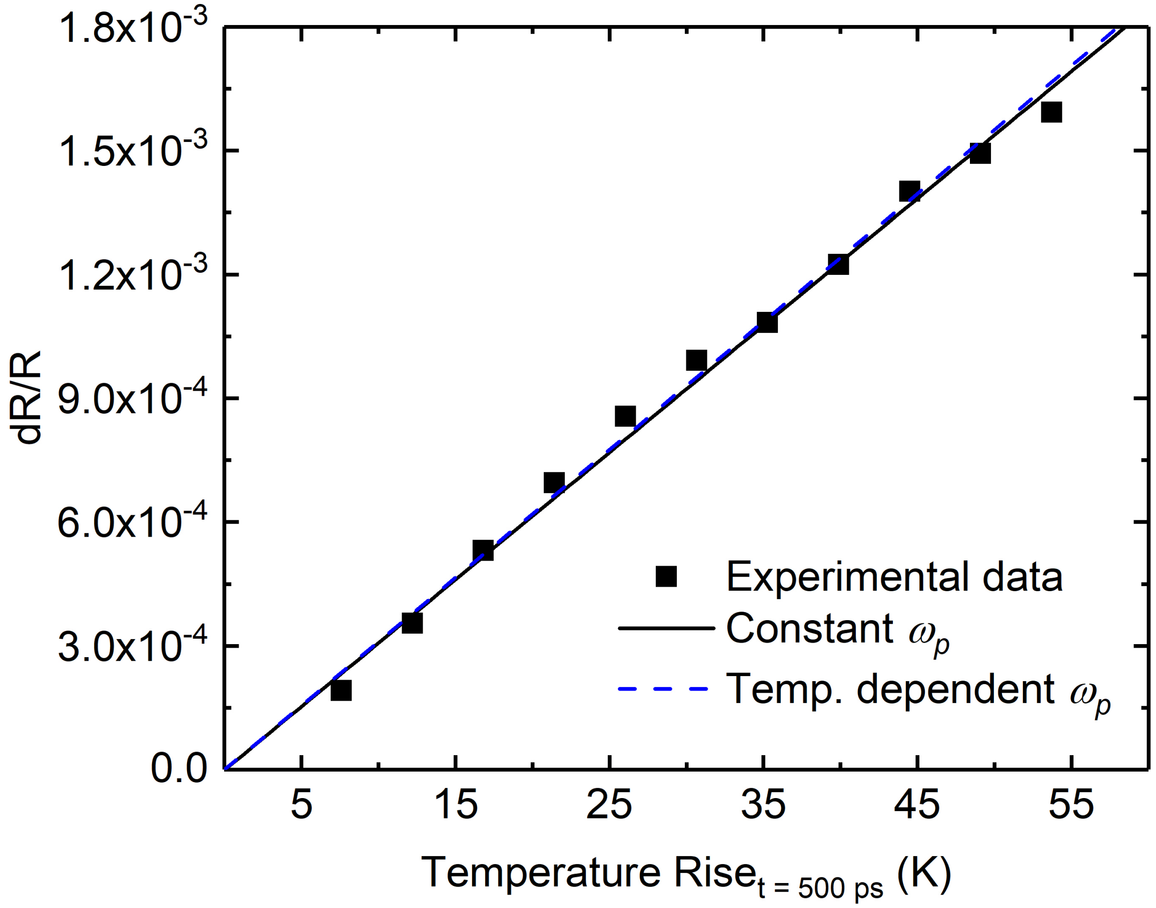

Figure 9.2: Fit of the temperature-dependent dielectric function for extraction of B_{ep} with (black line) and without (blue dashed line) a temperature-dependent plasma frequency, ω_p, to our experimentally measured dR/R as a function of the calculated temperature at 500 ps; $B_{ep} = 2.11 \times 10^{11}$ K^{-1} in both cases.

electron temperature, and thus does not affect the results surrounding the non-equilibrium thermoreflectance coefficient reported here, and also does not significantly affect our data analysis at 500 picoseconds (i.e., when $T_e \approx T_p$) and the associated extraction of the parameters A_{ee} and B_{ep}), we do note that its inclusion to the TTM would drastically affect other works that aim to determine e-p coupling constants via analysis of the time-constant associated with the ultrafast decay over the first few picoseconds. As shown in Fig. 9.2, the addition of a temperature-dependent plasma frequency when extracting B_{ep} negligibly alters the best-fit.

Note, certain experimental configurations can obtain varying sensitivities to the scattering coefficients, τ_{ee} and τ_{ep}, and thus the temperature dependence of ω_p, and hence produce differing results for the reported thermoreflectance coefficient. For example, in the case of infrared reflectivity/absorption measurements where the lattice temperature and electron temperature are not separated (i.e., equilibrium is assumed) and the photon energy is much less than the energy required to induce an interband transition, one can typically neglect the temperature dependence associated witlectron-electron scattering and thus only be dependent upon the lattice temperature (e.g., $\tau^{-1} \approx C \cdot B_{ep}T_p$, where C is a temperature-independent constant related to the e-e scattering rate). Conversely, in the case where the electronic subsystem temperature is in a state of non-equilibrium relative to the lattice temperature (i.e., $T_e >> T_p$), Fermi-smearing occurs and the width of the electron distribution is greatly increased. Although the interband transition threshold under equilibrium conditions is ~2.55 eV in Au, when the electron temperature is sufficient to create holes ~1 eV beneath the Fermi energy, a photon energy of only ~1.55 eV is necessary to transition a d-band electron to near Fermi surface holes. In this case, where near-infrared light, such as the 800 nm probe beam (~1.55 eV), can induce such a transition, its reflectivity becomes highly-dependent on the width of the Fermi-Dirac distribution, and thus highly-dependent on electron temperature. Of course, this 1 eV 'smearing' only occurs at near-melting temperatures for such metals should the electron and lattice have equivalent temperatures, and is why it is only observed under such non-equilibrium conditions. Nonetheless, given the electron temperatures and probe wavelength used in this work, we gain a sensitivity to the electron temperature and the e-e scattering rate associated with it. Attempting to remove this temperature dependence creates an inability to accurately describe the experimental decay curves shown in this work, as shown in the manuscript.

Physically, this electronic scattering rate can be derived from Fermi liquid theory, whereby the relaxation rate is inversely proportional to the square of a given electron's energy relative to the Fermi energy, or $\tau_{ee} = \tau_0(\frac{E_F}{\Delta E})^2$, where ΔE is simply $(E_{electron} - E_F)$, and τ_0 is an intrinsic proportionality constant.[**?**] Under this approximation, the aforementioned Fermi-smearing at elevated temperatures leads to an increased electron population and increased number of hole states above and below the Fermi energy, respectively; the width of this 'smearing' is approximately $\sim 2k_BT_e$ about E_F. Clearly, this creates a number of electrons with $\Delta E \propto T_e$, and thus leads to a scattering time of $\tau_{ee} \propto {T_e}^{-2}$. While one may consider that the classical picture of the Drude model does not explicitly account for electron-electron interactions. Nonetheless, a number of works, particularly the seminal review by Kaveh and Wiser[**?**], have determined that e-e scattering does in fact play a role when considering optical frequencies. This apparent discrepancy can be considered from the fact that the classical Drude model relies on translational symmetry of the electron gas, where local momentum is conserved during e-e scattering processes, hence the model's typical dependence on electron-ion scattering. However, non-spherical Fermi surfaces, higher momentum bands than the nearly-free electron sp-band of Au (i.e., d-band electrons), and perturbations of the electron gas (e.g., short-pulse laser interactions) break this invariance and localized momentum exchange due to electron correlations must be considered; these phenomena are clearly not considered in the classical Drude model.

We numerically solve these equations using an iterative fourth-order Runge-Kutta method, and fit the electron-phonon coupling constant, G, via non-linear least squares fitting. Although G is the fitted-variable, the large sensitivity to A_{ee} and B_{ep} from this model creates a clear lack of agreement between the model and experimental results when there is more than 5% deviation from the values reported here. The peak electron temperature, occurring at $t = 0$, that is used for our reported values of dR/dT_e, along with the maximum phonon temperature, which occurs just after electrons couple to the lattice, that has been calculated via this TTM approach as a function of incident pump power is shown in Fig. 9.1b and c, respectively.

Determination of lattice temperature rise via heat diffusion

While we use the two-temperature model to determine the single-pulse temperature rise when electrons and phonons are out of equilibrium with one another, to calculate the lattice temperature rise at times far after electron relaxation ($t > 100$ ps), we model the temperature rise via the heat diffusion equation. This approach is used to estimate the modulated temperature rise at 500 ps used to determine the thermoreflectance coefficient, as well as the steady-state temperature rise that results from accumulation of heat between pulses. Because the laser beam is Gaussian, it is convenient to solve the radially symmetric form of the heat diffusion equation, given by

$$\kappa_{\mathrm{r}}\left\{\frac{1}{r}\frac{\partial T(z,r,t)}{\partial r}+\frac{\partial^2 T(z,r,t)}{\partial r^2}\right\}+\kappa_{\mathrm{z}}\frac{\partial^2 T(z,r,t)}{\partial z^2}=C_{\mathrm{v}}\frac{\partial T(z,r,t)}{\partial t}, \tag{9.6}$$

where κ_{r} and κ_{z} are in-plane and cross-plane thermal conductivity, respectively, T is the lattice temperature rise, r is the radius, z is the depth, C_{v} is the volumetric heat capacity, and t is the time. We treat the laser heat flux as a surface boundary condition, together with a semi-infinite boundary condition in z and r to solve for the temperature rise at the sample surface. Furthermore, we integrate the radial surface temperature rise induced by the pump over the Gaussian intensity of the probe to obtain a single temperature rise corresponding to the detected change in reflectance. The solution is derived in Ref. [**?**], but we include the relevant equations below. In short, the probe averaged surface temperature rise resulting from a pulsed laser heat source modulated at angular frequency ω_0 is

$$T_{\mathrm{top}}=\frac{A_0}{2\pi}\int_0^{\infty}\sum_{n=-\infty}^{\infty}\left(-\frac{D}{C}\right)_{\omega=\omega_0+n\omega_s}\exp\left(-\frac{k^2(r_0^2+r_1^2)}{8}\right)e^{i(\omega_0+n\omega_s)t}k\,dk, \tag{9.7}$$

where A_0 is the absorbed power from the pump heating, $\omega_s/2\pi$ is the repetition rate of the laser, and r_0 and r_1 are the pump and probe radii, respectively. D and C define the thermal properties of the sample; in this case we use a two-layer model including the gold film layer and bulk substrate, so that

$$C=-q_2\kappa_{\mathrm{z},2}-q_1\kappa_{\mathrm{z},1}\tanh\left(q_1L_1\right)\left(\frac{q_2\kappa_{\mathrm{z},2}}{h_{\mathrm{k}}}+1\right) \tag{9.8}$$

$$D=1+q_2\kappa_{\mathrm{z},2}\left(\frac{1}{q_1\kappa_{\mathrm{z},1}}\tanh\left(q_1L_1\right)+\frac{1}{h_{\mathrm{k}}}\right) \tag{9.9}$$

where subscripts indicate layer number and coordinate direction and L_1 is the thickness of the gold film. q is defined by

$$q_{\mathrm{j}}^2=\frac{1}{\kappa_{\mathrm{z,j}}}(i\omega C_{\mathrm{v,j}}+\kappa_{\mathrm{r,j}}k^2). \tag{9.10}$$

Table 9.1: Room temperature thermal parameters in above calculations

Material	κ_z (W m^{-1} K^{-1})	κ_r (W m^{-1} K^{-1})	C_v (J cm^{-3} K^{-1})	$h_{Au/x}$ (MW m^{-2} K^{-1})
SiO_2	1.35	1.35	1.66 [380]	50
Al_2O_3	35	35	3.06 [380]	50
Au	102	102	2.49 [381]	-

The thermal parameters used for calculation are given in Table 9.1 for Au, Al_2O_3, and SiO_2. Heat capacities were determined via literature values [380, 381] while thermal conductivities were determined experimentally; for Au, 4-point probe resistivity measurements were used and for substrates, TDTR was used to measure both thermal conductivity and thermal boundary conductance.

For steady-state temperature rise measurements, the same heat diffusion equation is used, but the heat source is changed to an equivalent CW source with $\omega_0 = 0$ and having the absorbed power A_0. In practice, this simplifies Eq. 9.7 to

$$T_{SS} = \frac{A_0}{2\pi} \int_0^\infty \frac{-D(k,0)}{C(k,0)} \exp\left(-\frac{k^2(r_0^2+r_1^2)}{8}\right) k\,dk. \tag{9.11}$$

Picosecond acoustics

To determine the thickness of the Au films used in this work, we rely on an inherent aspect of ultrafast pump probe measurements: picosecond acoustics. In such experiments, the intense pump pulse induces a large temperature rise within the optical absorption depth of the Au film. This rapid temperature rise leads to a thermo-elastic stress in the film that launches a coherent acoustic phonon through the metal film towards its supporting substrate. When this acoustic wave reaches the film/substrate interface, it is partially transmitted into the substrate, but also partially reflected back towards the surface of the metal film; as this acoustic wave is essentially a density perturbation within the metal transducer, it leads to a change in the dielectric function/refractive index that can be observed by the probe laser pulse upon arrival at the film surface. As Au has a well-known longitudinal phonon velocity (i.e., sound speed), one can determine the thickness of the metal film, d, from the round-trip period associated with this acoustic wave by the propagation speed of a coherent acoustic phonon by [**?**]

$$d = \frac{\tau * v_{acoustic}}{2} \tag{9.12}$$

where τ is the period of the observed change in reflectivity and $v_{acoustic}$ is the velocity of the longitudinal wave in the metal film; the factor of $\frac{1}{2}$ corresponds to the fact that the acoustic wave is only observed on the probed surface and must traverse the metal film twice before it is detected.

An example of these picosecond acoustic measurements can be seen in Fig. 9.3, where a periodic change in reflectivity of the Au film is observed every ~10 ps due to the arrival

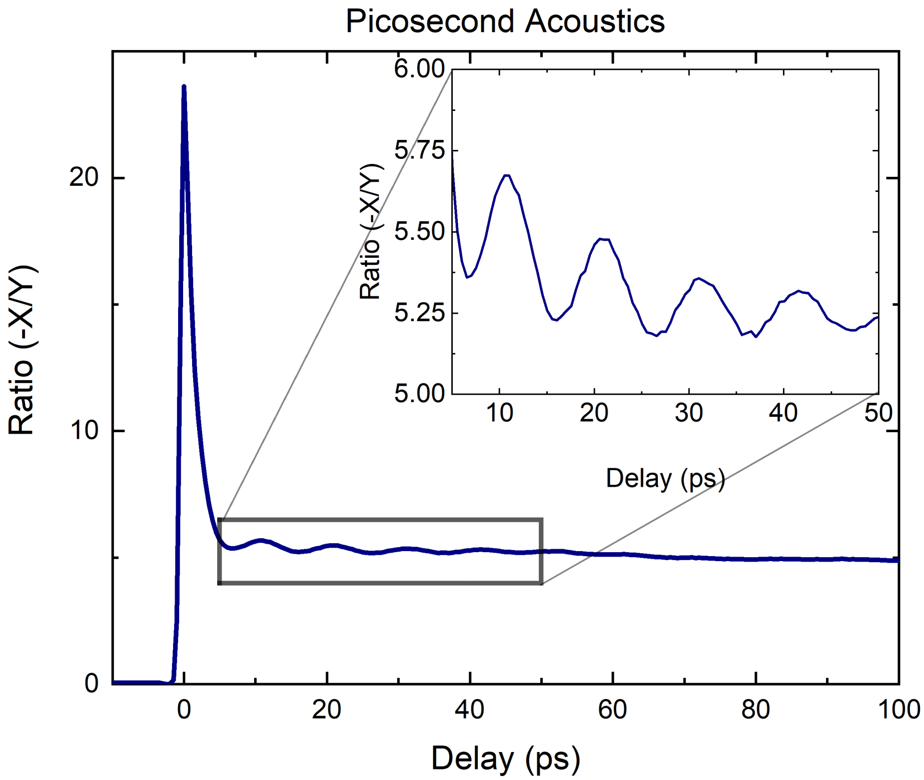

Figure 9.3: Time-domain thermoreflectance (TDTR) data showing the periodic arrival of the pump-induced pressure front on the surface of our thin Au film on a sapphire substrate. The period of these oscillations is measured to be ∼10 picoseconds, corresponding to an Au film thickness of 16 nm.

of this pressure front at the surface of the film. Using a sound speed, $v_{acoustic}$, of 3240 m s^{-1} for Au, the thickness of the metal film is calculated to be 16 nm, which is in great agreement with the thickness obtained from XRR; the results from XRR are discussed later in the Supporting Information. Note, Fig. 9.3 shows the ratio of the in-phase signal from our lock-in amplifier, X, to the out-of-phase signal, Y, as a function of time. At these time scales, the in-phase signal contains the magnitude of change in reflectivity due to heating from the pump-pulse, whereas the out-of-phase signal is physically zero. Thus, any systematic noise in our experiment appears as a perturbation of the out-of-phase signal from its value of zero. Hence, in taking the ratio of these values, this noise can be ‘normalized‘ out of the signal to provide a more accurate representation of these acoustic oscillations.

Pulse width and cross correlation of pulses

The pulse width of the 800 nm probe pulses were measured via the Frequency Resolved Optical Gating (FROG) technique. This technique relies on splitting the probe pulse into two temporally-separated paths that are focused into a second harmonic generation (SHG) medium and measuring the SHG intensity as a function of the temporal offset between the two pulses. In doing so, we determine the probe pulse has a temporal FWHM of 220 ± 20 femtoseconds. As our pump pulse is already frequency-doubled to 400 nm before arrival at the sample surface and is thus greatly reduced in intensity, this process cannot be repeated for measurement of the pump beam’s pulse width. The cross-correlation of the pump and probe pulses were measured in a similar fashion, where a BBO crystal is used as the SHG medium at zero incidence. By adjusting the delay between the pump and probe, we can obtain the cross-correlation of the two pulses; as shown in Fig. 9.4, the cross-correlation of the pump and probe pulses is measured to have a FWHM of 824 ± 20 femtoseconds.

Transfer matrix method (TTM)

To calculate electromagnetic interactions with thin films and nanoscale media, we employ a matrix method approach. In most of the multilayer structures considered here, the layers are isotropic and homogeneous with well defined parallel-plane interfaces, allowing us to describe the propagation of light with a simple 2×2 matrix. Our calculations follow the approach outlined by Pettersson *et al.*, which is described in detail below [382].

Consider a general multilayer structure, with m layers, atop a semi-infinite substrate in ambient conditions (e.g., the multilayer is sandwiched between air and its substrate), where the incident electromagnetic wave is a plane-wave incident upon the surface adjacent to ambient; the direction of incidence will be defined here as the positive x direction. Each layer, j ($j = 1, 2, ..., m$), has a thickness d_j and its optical properties are described by a complex index of refraction $\underline{\bar{n}}_j = n_j + ik_j$. The electric field at any point in the structure can be described by two components that result in the net electric field; one component propagates in the positive x direction and one in the negative x direction, denoted at each position x in layer j as $\boldsymbol{E}_j^+(x)$ and $\boldsymbol{E}_j^-(x)$, respectively.

An refraction matrix then describes each interface in the structure,

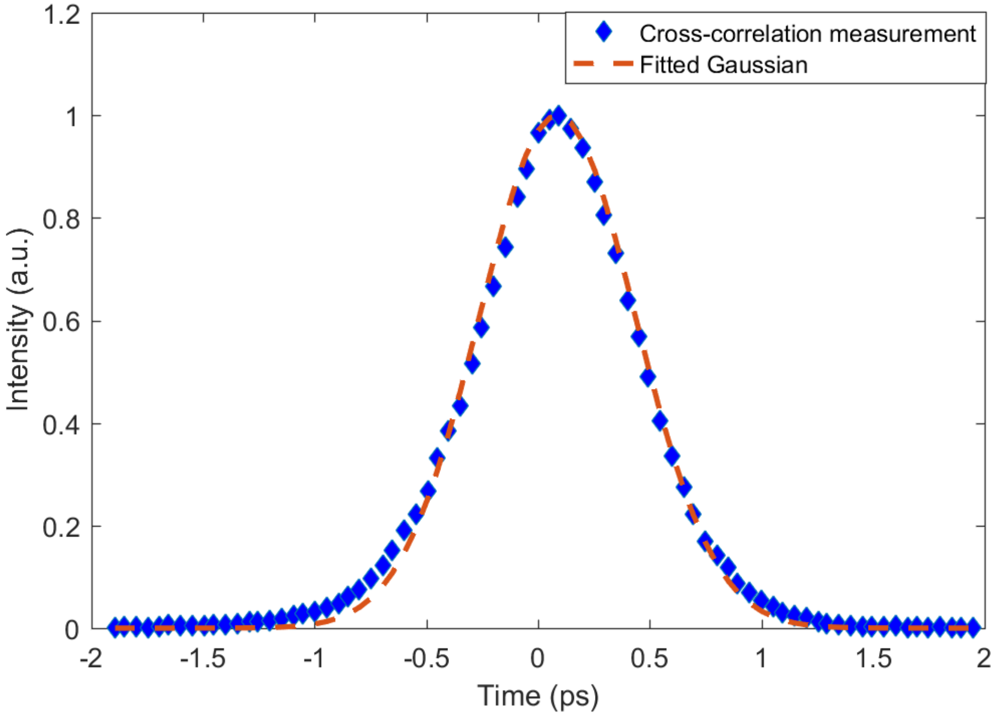

Figure 9.4: Measured second harmonic generation intensity of the pump and probe pulses as a function of the temporal offset between the two pulses. The FWHM of this cross-correlation is measured to be 824 ± 20 femtoseconds.

$$I_{jk} = \frac{1}{t_{jk}} \begin{bmatrix} 1 & r_{jk} \\ r_{jk} & 1 \end{bmatrix}, \tag{9.13}$$

where r_{jk} and t_{jk} are the Fresnel complex reflection and transmission coefficients at interface jk. For s-polarized light, these coefficients are defined by

$$r_{jk} = \frac{q_j - q_k}{q_j + q_k}, \tag{9.14}$$

$$t_{jk} = \frac{2q_{jk}}{q_j + q_k} \tag{9.15}$$

and, for $p-$polarized light, are given as

$$r_{jk} = \frac{\bar{\underline{n}}_k^2 q_j - \bar{\underline{n}}_j^2 q_k}{\bar{\underline{n}}_k^2 q_j + \bar{\underline{n}}_j^2 q_k}, \tag{9.16}$$

$$t_{jk} = \frac{2\bar{\underline{n}}_j \bar{\underline{n}}_k q_j}{\bar{\underline{n}}_k^2 q_j + \bar{\underline{n}}_j^2 q_k}, \tag{9.17}$$

where

$$q_j = \bar{\underline{n}}_j \cos\phi_j = [\bar{\underline{n}}_j^2 - n_0^2 \sin\phi_0]^{1/2} \tag{9.18}$$

and n_0 is the refractive index of air, ϕ_0 is the angle of incidence upon the structure, and ϕ_j is the angle of refraction in layer j.

The phase matrix, which describes the propagation of the field through layer j, is given by

$$L_j = \begin{bmatrix} \exp(-i\zeta_j d_j) & 0 \\ 0 & \exp(i\zeta_j d_j) \end{bmatrix}, \tag{9.19}$$

where $\zeta_j = 2\pi q_j/\lambda$ and $\zeta_j d_j$ is thus the layer phase phase thickness.

By using the interface (9.13) and layer (9.19) matrices, the total scattering matrix, $\boldsymbol{S}$, can be written as

$$\boldsymbol{S} = \begin{bmatrix} S_{11} & S_{12} \\ S_{21} & S_{22} \end{bmatrix} = (\prod_{v=1}^{m} \boldsymbol{I}_{(v-1)v} \boldsymbol{L}_v) \cdot \boldsymbol{I}_{m(m+1)}. \tag{9.20}$$

This scattering matrix allows us to relate the electric field at the ambient and substrate sides of the multilayer structure via

$$\begin{bmatrix} \boldsymbol{E}_0^+ \\ \boldsymbol{E}_0^- \end{bmatrix} = \boldsymbol{S} \begin{bmatrix} \boldsymbol{E}_{m+1}^+ \\ \boldsymbol{E}_{m+1}^- \end{bmatrix}. \tag{9.21}$$

The complex reflection and transmission coefficients for the full structure can now be expressed in terms of the scattering matrix elements:

$$r = \frac{\boldsymbol{E}_0^-}{\boldsymbol{E}_0^+} = \frac{S_{21}}{S_{11}}, \tag{9.22}$$

$$t = \frac{\boldsymbol{E}^{+}_{m+1}}{\boldsymbol{E}^{0}_{0}} = \frac{1}{S_{11}}. \tag{9.23}$$

SRT: Switch times and water content

In the data reported in this work, we conduct TDTR scan once the samples have achieved their "fully on" (hydrated) or "fully off" (ambient) state. Note, throughout this work, we define ambient as being the TR protein in an unsaturated, ambient environment; for our TDTR measurements at the University of Virginia, we measure the relative humidity of our laboratory to be between 28-35%. Conversely, the hydrated measurements are performed on a position of the TR protein film that is fully submerged in an aqeaous environment, as described in the previous section. As a single TDTR scan takes approximately two minutes, we cannot conduct full TDTR scans during the transition from ambient to hydrated to gain insight into the time scale associated with the switching of thermal conductivity in the TR films. However, to quantify the order of magnitude of this thermal conductivity switching time, we instead use the TDTR signal as a relative monitor of the temperature change by monitoring the TDTR signal at a single pump-probe delay time as a function of lab time while manually pipetting of water on and off of the sample to repeatedly hydrate and dry the sample. We have used this this approach of "staring" at the TDTR signal in to observe real time changes in thermal conductivity in various samples previously [299, 374]. We note that in our current case, this procedure does indeed produce variabilities in the absolute switching times due to inadvertent changes in the manual application and removal of the water, along with sample to sample variabilities in film thickness which will change liquid diffusion times through the materials. Thus, while these measurements prevent us from absolutely quantifying the intrinsic switching times of these materials with high precision, this does allow for order of magnitude quantification of the switching times. While we discuss this procedure in more detail below, we note that all reported thermal conductivity values in this work are determined when the system has equilibrated in either the full hydrated or fully ambient states, as previously mentioned. In other words, the full TDTR scans that result in the thermal conductivity data presented in the main manuscript are only performed when there is no temporal fluctuation in the measured lock-in signal.

To give insight into the switching time, we fix our pump-probe delay time to 500 ps and measure the lock-in signal as a function of lab time. From there, we repeatedly hydrate and dry the sample, via manual pipetting of water, over the course of minutes. To convert the measured signal to thermal conductivity as a function of time, we normalize the signal to the measured ratio from TDTR scans for the ambient and hydrated states at 500 ps. The results for the TR films are shown in Fig. 4a of the primary manuscript for TR-n25. Upon hydration, the change in thermal conductivity is on the order of seconds.

Note: the reported thermal conductivity values in this work are when the system has equilibrated in either the ambient or hydrated state. In other words, the TDTR scans are only performed when there is no fluctuation in the magnitude of the lock-in signal.

In an attempt to quantify the role of varying water concentrations associated with this switch, we performed our TDTR measurements on TR-n11 and -n25 up to 92% relative humidity using a custom-built chamber. Although the chamber and sample have excessive condensation, as shown in Fig.9.5b, where water droplets similar to those used for our

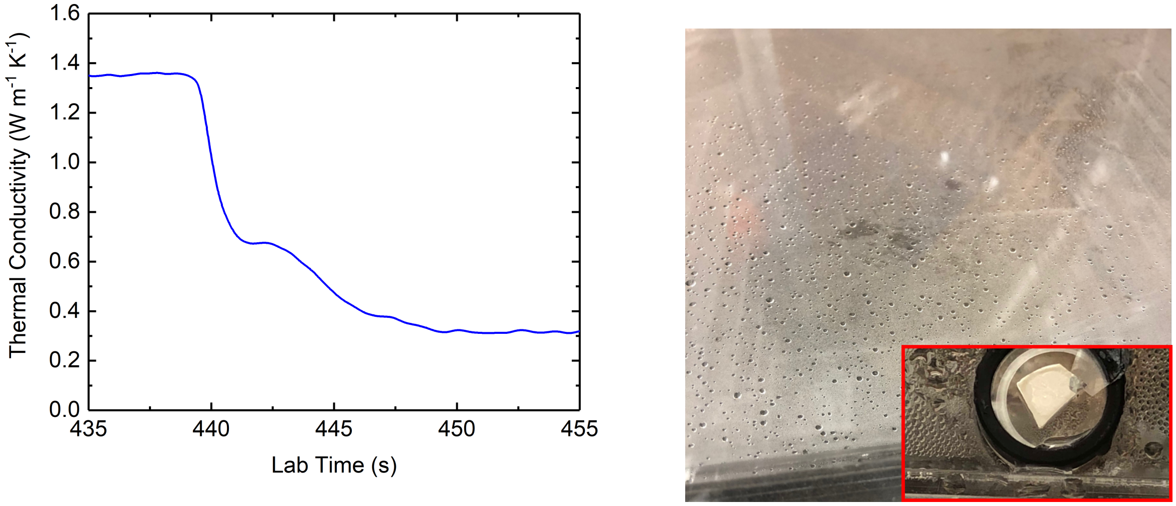

Figure 9.5: a) A zoomed-in view of the measured thermal conductivity as a function of real time for TR-n25, providing insight to the time-scale associated with switching from a hydrated to ambient state. Note, the ambient-to-hydrated switch is consistently within the time constant of our lock-in amplifier (300 ms), thus appearing instantaneous. b) Image of our humidity chamber at a relative humidity of approximately 85%. The inset shows a TR-n11 sample (supported by a 80 nm Al transducer and 1 mm SiO_2 substrate underneath) on the optical window inlet to the chamber. As seen, condensation occurs heavily throughout the chamber.

initial switching experiments are visible on every surface in the chamber including the inset which shows our TR-n11 sample, our probed region remains dry due to localized laser heating. This finding is in conceptual agreement with the rapid switch time found when our sample is dried through manual pipetting of a water droplet; our TDTR measurement leads to a steady-state temperature rise from laser heating, which causes rapid local evaporation from the probed region. In the case of humidity/concentration measurements, this local heating disallows for condensation in the measured area.

SRT: Time-domain Brillouin scattering

We measure the group velocity of coherent acoustic phonons through pump-probe Brillouin scattering measurements using a two-tint version of our TDTR apparatus. In pump-probe reflection measurements, such as TDTR, the initial pump pulse creates a heating event in the transducer; the energy imparted from the laser pulse paired with this temperature rise leads to the formation of coherent acoustic wave within the surrounding media. As a coherent acoustic wave traverses this media, in our case the TR films, the probe beam is partially reflected due to the change in refractive index associated with the pressure gradient; the transmitted portion of the beam continues towards the metal transducer and undergoes thermoreflection as with a traditional TDTR measurement. As described in previous works [262, 274, 284], these two reflected beams will interfere and lead to periodic oscillations in the time-dependent reflectance signal. The intensity of this time-independent signal can be described via

$$I(t,T) = A * \exp(-\Gamma t) * \cos((2\pi/T)t - \delta) - B * \exp(-t/\tau) \tag{9.24}$$

where A, B, and δ are essentially scale factors, Γ is the damping of the acoustic wave-front due to energy dissipation, T is the period of the pressure front, and the second term, $\exp(-t/\tau)$ accounts for the thermal decay associated with traditional thermoreflectance at the metal transducer. When the probe beam is at normal incidence, the frequency, f, (i.e., the inverse of the period, T,) can be related to the sound speed of the partially transparent material via

$$f = \frac{2rv}{\lambda} \tag{9.25}$$

where r is the index of refraction, λ is the wavelength of the probe beam, and v is the velocity of this coherent wave-front. In the case of our TR films, r has been determined in our previous work [383] and our probe beam is 800 nm.

Note, we utilize a two-tint pump-probe apparatus (i.e., the pump beam is also 800 nm) for these measurements to avoid damage of the TR film; as described in our previous work [375], direct interaction between the protein film and the 400 nm pump used in our TDTR measurements leads to gradual degradation of the film. In the hydrated measurements, the sample is fully submerged beneath 3 mm of DI water; the signal-to-noise ratio in the hydrated case is greatly reduced compared to that of the films in ambient conditions. Nonetheless, well-defined peaks remain visible, showing clear reduction in sound velocities compared to the ambient samples. The results from our measurements/calculations are provided in Table 3 at the end of the document.

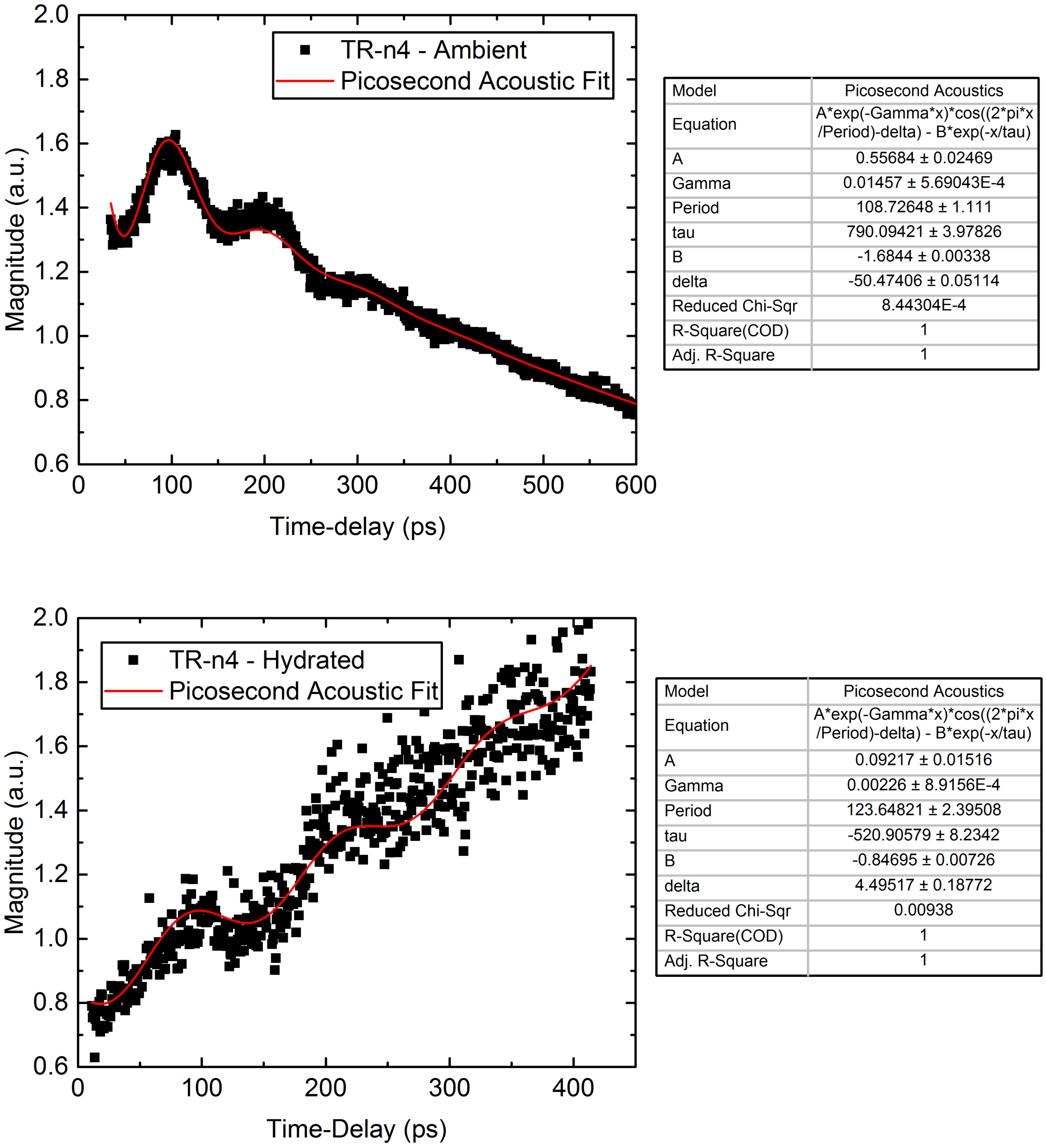

Model	Picosecond Acoustics
Equation	A*exp(-Gamma*x)*cos((2*pi*x /Period)-delta) - B*exp(-x/tau)
A	0.55684 ± 0.02469
Gamma	0.01457 ± 5.69043E-4
Period	108.72648 ± 1.111
tau	790.09421 ± 3.97826
B	-1.6844 ± 0.00338
delta	-50.47406 ± 0.05114
Reduced Chi-Sqr	8.44304E-4
R-Square(COD)	1
Adj. R-Square	1

Model	Picosecond Acoustics
Equation	A*exp(-Gamma*x)*cos((2*pi*x /Period)-delta) - B*exp(-x/tau)
A	0.09217 ± 0.01516
Gamma	0.00226 ± 8.9156E-4
Period	123.64821 ± 2.39508
tau	-520.90579 ± 8.2342
B	-0.84695 ± 0.00726
delta	4.49517 ± 0.18772
Reduced Chi-Sqr	0.00938
R-Square(COD)	1
Adj. R-Square	1

Figure 9.6: Examples of TDBS measurements on n-4 in the ambient (top) and hydrated states (bottom), with values of best fit tabulated for each.

Table 9.2: TDBS measurements

Sample	**TR15 (-n4)**	**T42 (n11)**
Ambient Velocity (m/s)	2374 ± 45	1768 ± 200
Hydrated Velocity (m/s)	2088 ± 291	1805 ± 291
Calculated Switching Ratio	$\sim$3.70	$\sim$4.90